NASA/OHIO SPACE GRANT CONSORTIUM

2023-2024 ANNUAL STUDENT RESEARCH SYMPOSIUM PROCEEDINGS XXXII

A total solar eclipse is seen in Dallas, Texas on Monday, April 8th, 2024.

Photo Courtesy of NASA

March 22, 2024
Held at the Ohio Aerospace Institute
Cleveland, Ohio

Follow OSGC on:

Just click on any name, and it will link you to the page immediately!

TABLE OF CONTENTS

FOREWORD

The Ohio Space Grant Consortium (OSGC), a member of the NASA National Space Grant College and Fellowship Program, awards graduate fellowships and undergraduate scholarships to students working toward degrees in Science, Technology, Engineering and Mathematics (STEM) disciplines at OSGC-member universities. The awards are made to United States citizens, and the students are competitively selected. Since the inception of the program in 1989, over 1,455 undergraduate scholarships and 288 graduate fellowships have been awarded.

Matching funds are provided by the 24 member universities/community colleges, the Ohio Aerospace Institute (OAI), and the Ohio Department of Higher Education (State of Ohio).

By helping more students to graduate with STEM-related degrees, OSGC provides more qualified technical employees to industry. The research conducted for the Master's fellowship must be of interest to NASA. A prime aspect of the scholarship program is the undergraduate research project that the student performs under the mentorship of a faculty member. This research experience is effective in encouraging U. S. undergraduate students to attend graduate school in STEM. The Education scholarship recipients are required to attend a workshop conducted by NASA personnel where they are exposed to NASA educational materials and create a lesson plan for use in their future classrooms.

Research reports of students from the following schools are contained in this publication:

Affiliate Members

- The University of Akron
- Baldwin Wallace University
- Cedarville University
- Central State University
- Cleveland State University
- University of Dayton
- Kent State University
- Marietta College
- Miami University
- Ohio Northern University
- The Ohio State University
- Ohio University
- University of Cincinnati
- Wilberforce University
- Wright State University
- Youngstown State University

Community Colleges

- Cincinnati State Technical and Community College
- Columbus State Community College
- Cuyahoga Community College
- Lorain County Community College

MEMBER INSTITUTIONS

Affiliate Members	***Campus Representative***
• Baldwin Wallace University	James W. McCargar, Ph.D.
• Case Western Reserve University	Christina A. Zorman, Ph.D.
• Cedarville University	Robert Chasnov, Ph.D., P.E.
• Central State University	Augustus Morris, Jr., Ph.D., P.E.
• Cleveland State University	Wei Zhang, Ph.D.
• Kent State University	Joseph D. Ortiz, Ph.D.
• Marietta College	Dr. Andrew Beck
• Miami University	Jeong-Hoi Koo, Ph.D.
• Ohio Northern University	Jed E. Marquart, Ph.D., P.E.
• The Ohio State University	Dr. Mo Samimy
• Ohio University	Dr. Roxanne Male'-Brune
• The University of Akron	Dr. Julie Zhao
• University of Cincinnati	Dr. Kelly Cohen
• University of Dayton	Dr. Kenyan M. Crosson
• The University of Toledo	Dr. Lesley M. Berhan
• Wilberforce University	Deok Hee Nam, Ph.D.
• Wright State University	Mitch Wolff, Ph.D.
• Youngstown State University	Byung-Wook Park, Ph.D.

Community Colleges	***Campus Representative***
• Cincinnati State Technical and Community College	Professor Abigail Yee
• Columbus State Community College	Professor Erik Aagard
• Cuyahoga Community College	Prof. Michelle S. Davis
• Lakeland Community College	Professor Rick Bartlett
• Lorain County Community College	Regan L. Silvestri, Ph.D.
• Sinclair Community College	Eric C. Dunn

NASA Glenn Research Center - Representatives

- Dr. Gerald Volts
- Mr. Robert F LaSalvia

ACKNOWLEDGMENTS

Thank you to all who helped with the OSGC's 32nd Annual Research Symposium!

OSGC Alumni Panel:

★ Ashlie Flegel, NASA Glenn Research Center
★ Ryan Palmer, Lorain County Community College & RPTech
★ Dulci Avouris, University of California
★ Em Williams, Lorain County Community College

Campus Representatives – 4-Year Universities

- Dr. James W. McCargar, Baldwin Wallace University
- Dr. Chris Zorman, Case Western Reserve University
- Robert Chasnov, Ph.D., P.E., Cedarville University
- Augustus Morris, Jr., Ph.D., P.E., Central State University
- Wei Zhang, Ph.D., Cleveland State University
- Dr. Joseph D. Ortiz, Kent State University
- Dr. Andrew Beck, Marietta College
- Jeong-Hoi Koo, Ph.D., Miami University
- Jed E. Marquart, Ph.D., P.E., Ohio Northern University
- Dr. Mo Samimy, The Ohio State University
- Dr. Roxanne Male'-Brune, Ohio University
- Dr. Julie Zhao, The University of Akron
- Dr. Kelly Cohen, University of Cincinnati
- Dr. Rydge Mulford, University of Dayton
- Dr. Lesley M. Berhan, The University of Toledo
- Deok Hee Nam, Ph.D., Wilberforce University
- Mitch Wolff, Ph.D., Wright State University
- Dr. Byung-Wook Park, Youngstown State University

Campus Representatives - Community Colleges

- Professor Abigail Yee, Cincinnati State Technical and Community College
- Professor Erik Aagard, M., Columbus State Community College
- Professor Michelle S. Davis, Cuyahoga Community College
- Professor Rick Bartlett, Lakeland Community College
- Regan L. Silvestri, Ph.D., Lorain County Community College
- Eric C. Dunn, Sinclair Community College

Special thanks go out to the following:

- Dr. John Sankovic, President and CEO – OAI, for supporting the OSGC and hosting this event.
- Mark Cline, Senior Manager, Information Technology – OAI, whose expertise made the hybrid medium not only possible, but a huge success!
- Robert Romero, Director – OSGC, for his enthusiasm and vigor in leading the Ohio Space Grant Consortium.
- Em Williams, Program Assistant – OSGC, for pulling together our rockstar panel and providing a fresh perspective to the program.
- Sam Santos, Program Assistant – OSGC who is on the spot to assist team and students alike throughout the day.
- Jill Marconi, K-12 Specialist – OSGC, who brings in the inner child out in the team and the STEM professional out of our pre-college students.
- All of our presentation evaluators providing insight to our students: Dr. Andrew Beck, Bob Bodi, Emily Clapper, Jill Marconi, Mike Marconi, Jay Reynolds, Dr. Roxanne Male'-Brune, Rydge Mulford, Suzanne Parsons, Dave Van Arsdale, Dr. Abigail Yee, Dr. Julie Zhao

Most importantly, thank you to our students, whose efforts and contribution makes this program possible!

OHIO SPACE GRANT CONSORTIUM

2024 OSGC STUDENT RESEARCH SYMPOSIUM
Hosted By: Ohio Aerospace Institute (OAI)
22800 Cedar Point Road • Cleveland, OH 44142
• (440) 962-3000
Friday, March 22, 2024

AGENDA

8:00 AM – 8:30 AM	Sign-In / Continental Breakfast / Student Portraits (30 minutes)..... Lobby
8:35 AM – 8:40 AM	Welcome to OAI (5 minutes)..... Forum (Lobby Level) *Dr. John Sankovic* President and Chief Executive Officer, Ohio Aerospace Institute
8:40 AM – 8:45 AM	Welcome and Introductions (5 minutes) *Robert Romero* Director, Ohio Space Grant Consortium
8:45 AM – 8:50 AM	Symposium Logistics (5 minutes) *Tim Hale* Program Manager, Ohio Space Grant Consortium
8:50 AM – 9:00 AM	Group Photograph (10 minutes)..... Lobby / Atrium Stairwell
9:00 AM – 11:00 AM	Student Oral Presentations – Senior Scholars and Fellows (120 minutes) • Group 1 ..... Forum (Lobby Level) • Group 2 ..... Presidents' Room (Lower Level) • Group 3 ..... Industry Room A (2nd Floor) • Group 4 ..... Industry Room B (2nd Floor) • Group 5 ..... Board Room (2nd Floor)
11:00 AM – 12:15 PM	Various Displays (75 minutes) • Student Poster Presentations..... Lobby Junior, Community College, and Pre-Service Teacher (Education) Scholars • Industry Displays..... Lobby
12:15 PM – 1:15 PM	Luncheon Buffet (60 minutes) ..... Atrium / Sunroom (Lower Level)
1:20 PM – 2:20 PM	Panel Discussion and Q&A (60 minutes)..... Forum (Lobby Level) *"Launching a STEM Career"*
Panel Members:	• Ashlie Flegel, NASA Glenn Research Center • Ryan Palmer, Lorain County Community College & RPTech • Dulci Avouris, US Geological Survey California Water Science Center • Emily Williams, Lorain County Community College & Ohio Space Grant
2:20 PM – 2:35 PM	Presentation of Best Poster Awards (15 minutes)..... Forum
2:35 PM – 2:40 PM	Closing Remarks
2:40 PM	Symposium Adjourns

OHIO SPACE GRANT CONSORTIUM 32ND ANNUAL RESEARCH SYMPOSIUM

(Left to Right) Collin Schofield, Sydney Maller, Jean Nash (University of Dayton), Lauren Bower (University of Dayton)

Emily Williams (OSGC), Ryan Palmer (LCCC), Ashlie Flegel (NASA), Dulci Avouris (University of California)

Tim Hale (OSGC Program Manager)

Robert Romero (OSGC Program Director)

Ryan Palmer (RPTECH), Jackie Lewyckyj (OAI)

OHIO SPACE GRANT CONSORTIUM STUDENT PRESENTATIONS

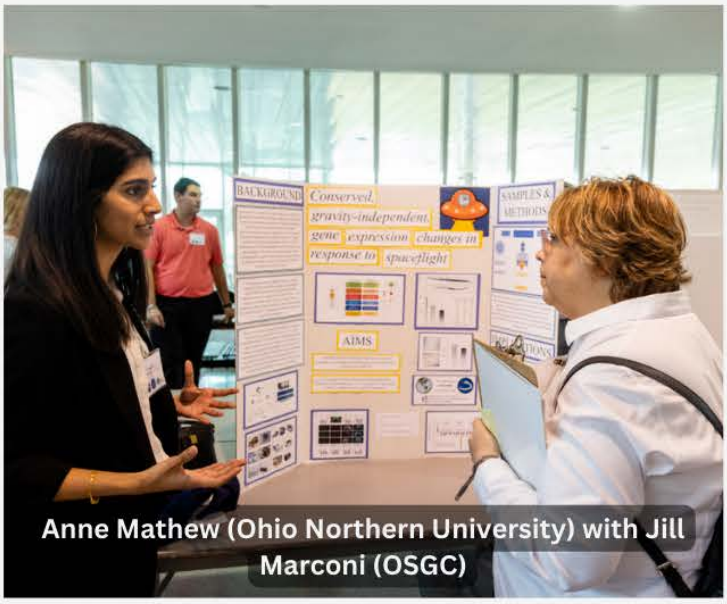

Anne Mathew (Ohio Northern University) with Jill Marconi (OSGC)

Ari Babcock (Cedarville University) with Victoria Swiler (Ohio University)

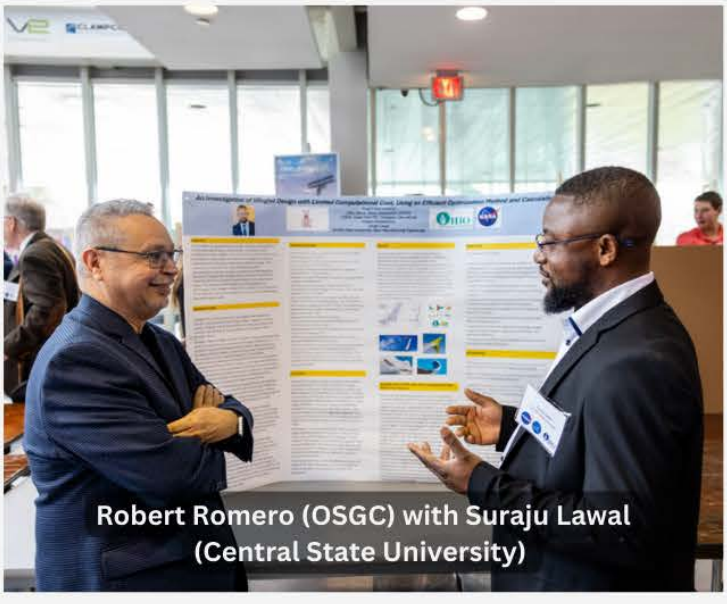
Robert Romero (OSGC) with Suraju Lawal (Central State University)

Monroe Kennedy (LCCC)

OHIO SPACE GRANT CONSORTIUM SENIOR/FELLOW PRESENTATIONS


Lee Nestor (University of Akron)


Michael Siino (Miami University)

Julia Gersey (Baldwin Wallace)


Aimee Ghanem (CWRU)

Alex Dotson (Central State University)


Andrew Porterfield (University of Dayton)


Douglas Baker (Wright State University)

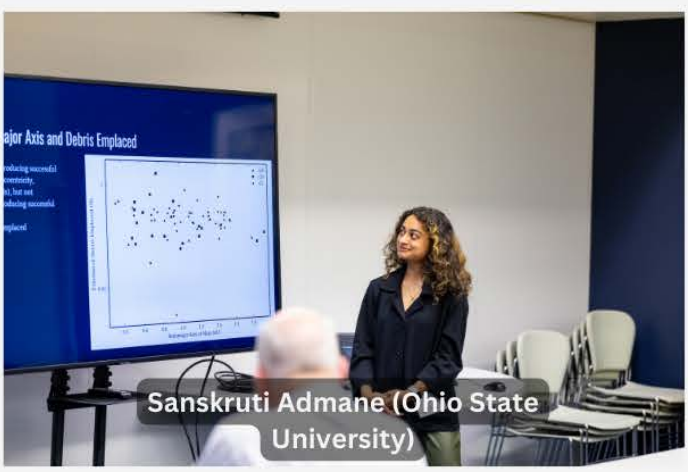

Sanskruti Admane (Ohio State University)

Fellows

Non-faradaic impedimetric determination of cortisol using gold nanoparticle functionalized interdigitated laser induced graphene electrode

Student Researcher: Kyle Duke

Advisor: Dr. Byung-Wook Park

Youngstown State University
Chemical Engineering

Abstract

Wearable biosensors have become a valuable tool for their promising applications in personalized medicine. Cortisol is a biomarker for various diseases and plays a key role in metabolism, blood pressure regulation, and glucose levels. In this study, we fabricated an interdigitated laser-induced graphene (LIG) biosensor for the non-faradaic impedimetric detection of cortisol in sweat. A direct laser writing technique was used to produce the LIG. Gold nanoparticles (AuNPs) were electrochemically deposited onto the surface to enhance impedance response. A Self-Assembled Monolayer (SAM) was formed with on the AuNPs via MPA thiol chemistry. The carboxylic acid (-COOH) groups of the MPA were activated using EDC/NHS chemistry. Following activation, anti-cortisol antibodies were immobilized on the surface. Lastly, the LIG was incubated in the blocking agent bovine serum albumin (BSA) to avoid unwanted detection. Surface characterization of the LIG was performed at each step of modification by Electrochemical impedance spectroscopy (EIS) in a phosphate buffered saline (PBS) solution containing a 5 mM $Fe(CN)^{3-/4-}$ (1:1) redox couple. Further characterization of the modified LIG electrode was achieved through Fourier transform infrared (FT-IR), surfaced-enhanced Raman spectroscopy (SERS), and X-ray diffraction (XRD). The detection experiment using EIS was conducted in increasing concentrations of cortisol (0.1 pM-100 nM) in PBS. The Z_{Mod} decreased logarithmically (R^2=0.97) with a 0.0157 nM limit of detection. Reproducibility was examined by percent change of Z_{Mod} at 100 nM and a 5.93%RSD (n=5) was observed. Additional analysis of sensor specificity and interference studies showed no substantial effect on detection. This research establishes the feasibility of using the gold nanoparticle decorated LIG electrode for flexible, wearable cortisol sensing devices, which would pave the way towards an end-user easy-to-handle biosensors as point-of-care diagnostics.

Project Objectives

The objective of this project is to fabricate and then evaluate the sensors performance through various characterization and detection experiments. The overall goal is to incorporate the sensor into a wearable sensor platform for point-of care applications.

Methods

Fabrication of bare LIG and gold nanoparticle (AuNP) modified LIG electrodes

The LIG electrode was obtained by subjecting PI to CO_2 laser cutter at . After the LIG formation ,the LIG/PI film was rinsed with acetone and 2-propanol followed by oxygen plasma treatment for 30 seconds to increase wettability on the surface[1]. Each LIG electrode was individually treated with a copper foil tape placed over the connection points, and the body of the electrode was insulated with a 5-minute epoxy. To obtain the gold nanoparticle (AuNP) modified laser induced graphene (LIG) electrode, gold nanoparticles (AuNP) were electrochemically deposited on the LIG surface via cyclic voltammetry (CV) for 10 cycles in a 1 mM $HAuCl_4$ in 0.1 M KNO_3 solution.

Immobilization of cortisol antibody on AuNP-LIG

To immobilize anti-cortisol antibody on the AuNP sites on the LIG electrode, thiol chemistry was used. A self-assembled monolayer of MPA thiols was formed on the AuNP by incubating the LIG in a 10 mM MPA ethanol solution for 1 hour and then rinsing with ethanol. Next, the terminal carboxylic acid groups of the MPA were activated to immobilize anti-cortisol antibody through incubating the electrode in a 0.1 M MES buffer containing 40 mM EDC and 100 mM Sulfo-NHS for 1 hour. To obtain the antibody immobilized AuNP-LIG electrode, the sensor was incubated in an anti-cortisol antibody solution at 5 µg/mL in 10 mM PBS for 2 hours. Lastly, to minimize undesired unspecific adsorption on the surface of the LIG, the electrode was incubated in a 1 % BSA in 10 mM PBS.

Electrochemical characterizations using EIS

To verify the LIG underwent surface modification, EIS was performed with a Gamry Interface 1010E Potentiostat. Measurements were performed in a three-electrode system with the modified LIG electrode as the working electrode, a platinum wire counter electrode, and a saturated calomel electrode (SCE) reference electrode. The EIS measurements were carried out in 5 mM $Fe(CN)^{3-}/Fe(CN)^{4-}$ PBS solution as a supporting electrolyte. Impedance spectra were collected over a frequency range of 1 Hz to 100 kHz with a potential amplitude of 10 mV rms at 10 points per decade. EIS results were analyzed by fitting the experimental impedance data to electrical equivalent circuit models.

SEM/EDX

The JIB-4500 MultiBeam integrated with SEM-EDS was used for SEM imaging and EDX analysis on LIG and AuNP/LIG. SEM images were collected at an electron energy of 15kV for 15,000x, 500x, and 100x magnifications for morphology characterization and verification of AuNP electrodeposition. EDS characterization was carried out at 5000x magnification with an electron energy of 138 eV for the elemental analysis of the LIG and AuNP/LIG.

XRD

XRD was performed with a Bruker X8 Prospector Ultra (Billerica, MA, USA) via Cu radiation to characterize the structures of the samples. XRD spectra of PI film, LIG, and AuNP were obtained, and the peaks were analyzed to show the degree of graphitization and defect after formation of the graphitic structure, and further verify the presence of electrodeposited AuNP on the LIG surface.

Raman spectroscopy

Raman spectroscopy is a commonly used technique to examine chemical structure and crystallinity. In this study, Raman spectra were collected using the Horiba iHR320 (Kyoto, Japan) at 531.4 nm laser with a 1800g/mm diffraction gratings to examine the degree of graphitization on the PI film.

Detection of cortisol

To examine the performance of the fully modified sensor, non-faradaic cortisol detection was conducted in a 10 mM PBS solution spiked with increasing cortisol concentrations (0.1 pM-100 nM). 10 uL of the cortisol solution were injected and 30 minutes after each injection of cortisol, EIS was performed and Z_{mod} values at 200 Hz were collected at each concentration. The Z_{mod} values were used to create a calibration plot in terms of the percent change at each concentration compared to the base level (no cortisol injected).

Results and Discussion

Electrochemical characterization for surface modification

The electrochemical characterization of the different electrodes (LIG, AuNP/LIG, Ab/AuNP/LIG, and BSA/Ab/AuNP/LIG) was carried out using EIS from 1-10000 Hz with a 10 mV perturbation and 0 V (DC). All measurements were performed in a redox solution composed of PBS and 5 mM $(Fe(CN)_6)^{3-}$ /$(Fe(CN)_6)^{4-}$ (1:1) solution with the equivalent model shown in Figure 1. At high frequencies, electron charge transfer is prominent as evident by the semi-circle portion of the Nyquist plot. At lower frequencies, diffusion is dominant resulting in an increase in Warburg impedance as depicted by the diffusion tail in the Nyquist plot [2]. The data was fit with a modified Randles circuit and R_{ct} was obtained. The AuNP/LIG electrode showed the lowest R_{ct} (30.98 ±3.59Ω), indicating electrodeposition of AuNP effectively increased the conductivity of the surface. Following the AuNP/LIG, EDC-NHS/AuNP saw an increase with a R_{ct} of 34.83 ± 7.38Ω. The increase can be attributed to the self-assembled monolayers (SAM) immobilization of 3-MPA to the AuNPs, which inhibits the electrolyte/electrode charge transfer. After 3-MPA activation via EDC/NHS, incubation of the anti-cortisol antibody saw an increase of 144% (46.32 ± 2.43), signifying the bonding of large amounts of the antibody to the surface, further impeding charge transfer to the electrode. All steps leading to antibody immobilization resulted in a lower R_{ct} than the bare LIG (50.42± 11.02), further supporting AuNP electrodeposition effectively increased the sensors overall conductivity, thus improving its overall sensitivity and functionality. Finally, the addition of the blocking agent BSA to the Ab/AuNP/LIG saw a further 168% increase in R_{ct} (77.84 ± 4.04) indicating a large portion of the unmodified surface was successfully covered.

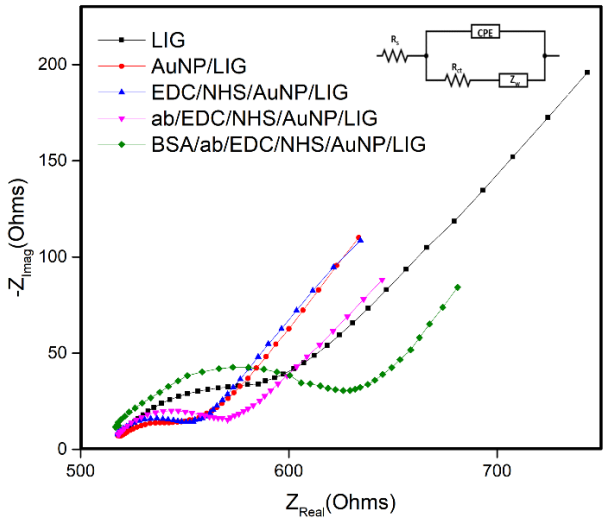

Figure 1: Nyquist plot obtained after surface modification procedures (n=3).

SEM-EDX

The morphology of the LIG and AuNP/LIG surface was examined through SEM imaging at various magnifications with further analysis of the elemental composition achieved by EDX. The porous 3D structure of LIG and AuNP/LIG is clearly exhibited in (Figure 2 A-D). Bright spots were shown (Figure 2D) after the formation of AuNP via electrodeposition. Results from EDS characterization for LIG and AuNP/LIG are shown in (Figure 3). The fabricated LIG is comprised of 100 wt% carbon with AuNP/LIG comprised of 93.54 wt% carbon with the remaining 6.46 wt% gold, further conforming successful electrodeposition of AuNP's. The absence of other elemental peaks indicates a pristine surface with undetectable traces of contaminants.

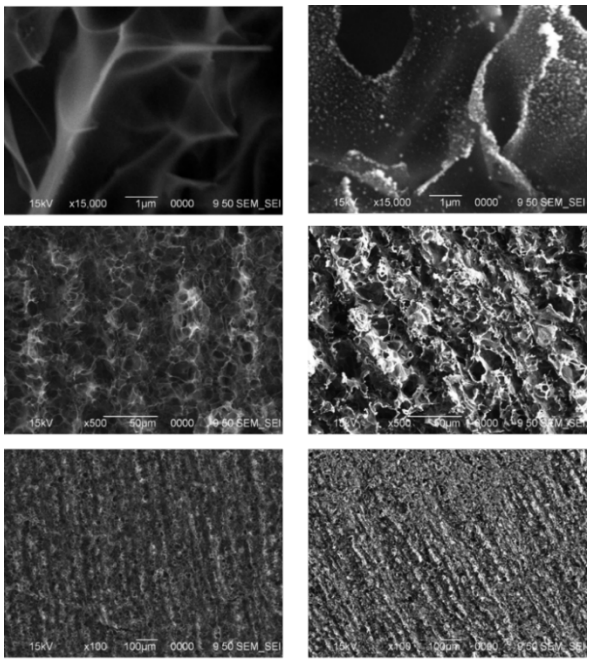

Figure 2. SEM of LIG and AuNP-LIG

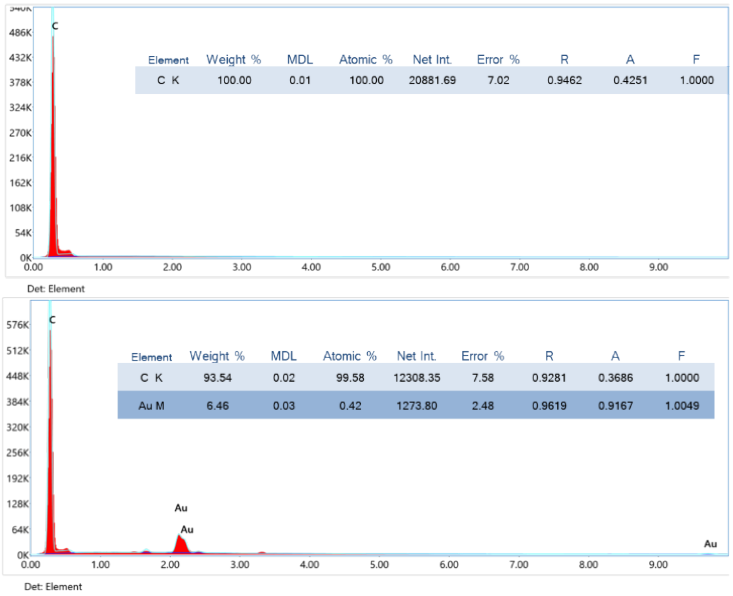

Figure 3. EDS of LIG and AuNP/LIG electrodes.

XRD

Successful graphene formation, and deposition of Au on the LIG is confirmed by X-ray diffraction (XRD). Shown in Figure 4, LIG exhibited a short peak at ~26 ° which is attributed to low crystallinity and low diffraction [3]. AuNP/LIG exhibited reflections of Au face-centered cubic crystallographic structure (38°, 44°, 64°, and 77°) signifying AuNP were successfully deposited on the LIG [4, 5]. The short peak observed at ~26 ° is indicative of a highly graphitized surface, thus increasing the surface area and consequently the available bonding sites for reagents.

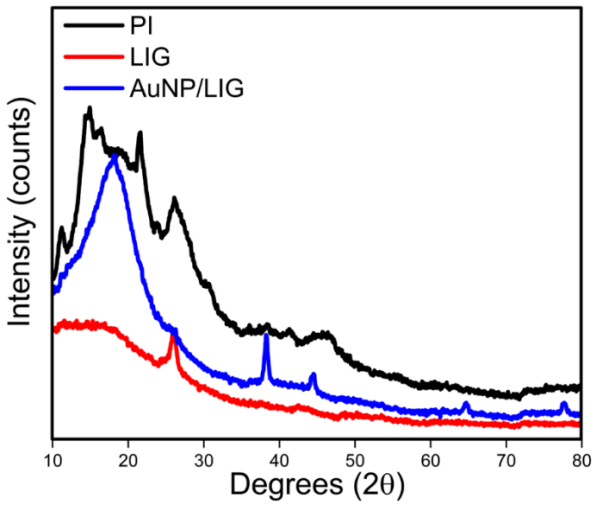

Figure 4: XRD of PI, LIG, and AuNP/LIG.

Raman Spectroscopy

Raman spectra of LIG and AuNP/LIG shows both D (defect states) and G (graphitic states) bands at around 1350 cm^{-1} and 1590 cm^{-1} respectively (Figure 5). The intensity ratio, I_D/I_G, represents the degree of graphitization that occurred, and was found to be 0.475 and 0.548 for LIG and AuNP/LIG. The increase in intensity is the result of interactions between the gold nanoparticles and graphene surface with an increase in disorder of the graphitic structure [6].

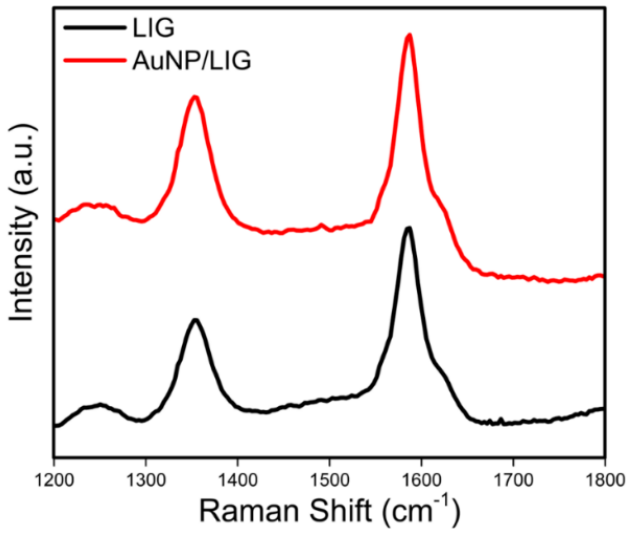

Figure 5: Raman spectra of PI, LIG, and AuNP/LIG.

Detection of cortisol

A modified Randles circuit model was fit to the EIS data to obtain the electrical characteristics of the system (Figure 6(A) inset). Where R_s represents the solution resistance and is parallel to the C_{LIG} and R_{LIG}. Which is in series with a second circuit containing CPE_{dl} and R_{ct} in parallel. The constant phase element (CPE_{dl}) represents the electric double layer capacitance of the system. CPE_{dl} was used to account for non-ideal conditions such as the surface roughness of the LIG, and uneven ion adsorption

onto the electrode surface, allowing for a better representation of the electric double layer capacitance [7, 8].

The resulting Nyquist plot, Bode plot, and model data obtained from cortisol detection are presented in Figure 6(A-B). respectively. As cortisol concentration increases, more antibody-antigen complexes are formed within the electric double layer (EDL). The formation of complexes increases the double layer capacitance (CPE_{dl}), causing the decrease in Z_{Real} observed in Figure 6(A) [9]. Furthermore, the bode plot (Figure 6(B)) exhibited a consistent decrease in impedance for increasing cortisol levels. This phenomenon is exclusive to non-faradaic EIS, where the absence of redox reactions eliminates the parameters in the Randles model associated with electron transfer, such as (R_{ct}) and Warburg impedance (Z_w), as these become negligible. Consequently, in a non-faradaic system, the impedance is inversely proportional to the electrical double layer capacitance [10]. Therefore, the observed decrease in impedance and corresponding increase in CPE_{dl} (Figure 6(D)) can be attributed to the interaction of cortisol with the modified electrode surface.

To obtain a calibration curve, the percent change in Z_{mod} (200 Hz) was calculated at each concentration with respect to the baseline measurement. A 200 Hz frequency was used because it lies in the range of 5-1000 Hz, which is known to represent the electric double layer capacitance [11]. The resulting cortisol dose response is depicted in Figure 6(C). The sensor exhibited a linear fit (log(Concentration)) over the entirety of the tested range with a high goodness of fit (R^2=0.97) and a LOD (3σ/S) of 0.0157 nM.

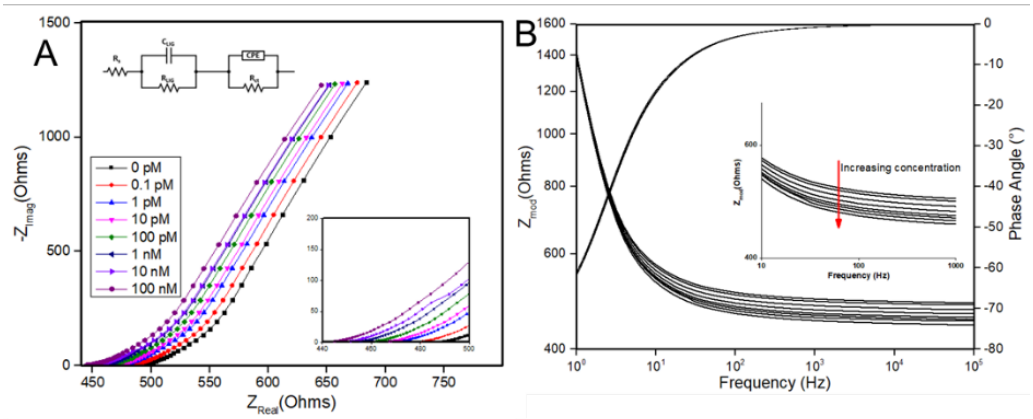

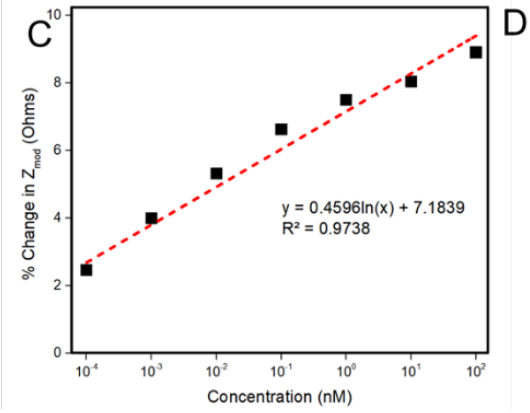

D

Concentration (nM)	CPE-dl
0	9.07E-04
0.0001	1.42E-04
0.001	7.22E-04
0.01	8.53E-04
0.1	1.07E-03
1	1.36E-03
10	1.56E-03
100	1.59E-03

Figure 6: (A) Nyquist plot and (B) Bode plot for increasing cortisol concentrations. (C) Cortisol dose response and corresponding (D) CPE_{dl} values.

Acknowledgments

I would like to thank Dr. Park for his guidance throughout the project and my fellow lab members Natalie, Kyle, and Pari for their support.

References

1. Cheng, C., et al., *Bisphenol A Sensors on Polyimide Fabricated by Laser Direct Writing for Onsite River Water Monitoring at Attomolar Concentration.* ACS Applied Materials & Interfaces, 2016. **8**(28): p. 17784-17792.
2. Park, B.-W., D.-Y. Yoon, and D.-S. Kim, *Formation and modification of a binary self-assembled monolayer on a nano-structured gold electrode and its structural characterization by electrochemical impedance spectroscopy.* Journal of Electroanalytical Chemistry, 2011. **661**(2): p. 329-335.
3. Saleem, H., M. Haneef, and H.Y. Abbasi, *Synthesis route of reduced graphene oxide via thermal reduction of chemically exfoliated graphene oxide.* Materials Chemistry and Physics, 2018. **204**: p. 1-7.
4. Sneha, K., et al., *Yucca-derived synthesis of gold nanomaterial and their catalytic potential.* Nanoscale research letters, 2014. **9**: p. 627.
5. Li, Y., et al. *Intrinsic Catalytic Activity of Gold/Multi-Walled Carbon Nanotubes Composites in Squaric Acid-Iron(II/III) System*. Catalysts, 2018. **8**, DOI: 10.3390/catal8050187.
6. Yang, X., et al., *Graphene uniformly decorated with gold nanodots: in situ synthesis, enhanced dispersibility and applications.* Journal of Materials Chemistry, 2011. **21**(22): p. 8096-8103.
7. Shoute, L.C.T., et al., *Label-free impedimetric immunosensor for point-of-care detection of COVID-19 antibodies.* Microsystems & Nanoengineering, 2023. **9**(1): p. 3.
8. Mark, E., et al., *The Apparent Constant-Phase-Element Behavior of an Ideally Polarized Blocking Electrode.* Journal of the Electrochemical Society, 2007. **154**: p. C81.
9. Kinnamon, D., et al., *Portable biosensor for monitoring cortisol in low-volume perspired human sweat.* Scientific Reports, 2017. **7**(1): p. 13312.
10. Chen, B., et al., *A non-faradaic impedimetric biosensor for monitoring of caspase 9 in mammalian cell culture.* Bioelectrochemistry, 2023. **153**: p. 108456.
11. Radha Shanmugam, N., et al., *Ultrasensitive nanostructure sensor arrays on flexible substrates for multiplexed and simultaneous electrochemical detection of a panel of cardiac biomarkers.* Biosensors and Bioelectronics, 2017. **89**: p. 764-772.

Fuzzy Logic Based Estimator for Enhanced Precision Landing of an Uncrewed Aerial Vehicle

Student Researcher: Rebecca N. Gilligan

Advisor: Dr. Kelly Cohen

University of Cincinnati College
Department of Aerospace Engineering and Engineering Mechanics

Abstract
Uncrewed aerial vehicles (UAV) serve as tools for tasks ranging from aerial imagery/sensing to package delivery and now space exploration with the Ingenuity helicopter [1]. A major limitation of UAVs is safe landing areas; precision landing is a critical technology to enable this. The goal of this research was to improve the safety of precision landing through real-time risk estimation.

Project Objectives
Precision landing guides a UAV during landing using a visual target. Precision landing is useful in UAV operations such as flight over water, landing on elevated platforms, and landing in small or uneven areas. ArduPilot is an autopilot firmware that supports precision landing using an infrared beacon and a specialized camera. The beacon device serves as a target to guide the UAV during precision landing. ArduPilot does not yet have a risk-based failsafe for precision landing. The goal of this research was to improve the safety of precision landing by creating a risk estimation algorithm which could trigger a new failsafe and abort precision landing if conditions become unsafe [2,3].

Methods
Often, risks are addressed procedurally, such as having a safety pilot monitor the precision landing. But autonomous operations require the system to predict these risks and make decisions on its own. In reality, risks are dynamic and difficult to precisely quantify. Fuzzy logic is a soft-computing technique that was used for autonomous risk estimation. Soft-computing is a collection of computational techniques which aim to mimic the human ability to summarize and focus only on decision-relevant information [4]. The goal of soft computing is to exploit the tolerance for imprecision and uncertainty and minimize computation cost. High precision is expensive and not always necessary to make decisions. For example, if an object is falling on someone, one does not care that it is 1500 kg, and moving at 20 m/s; the critical information to yell is “look out” so that the person can move. The numbers 1500 and 20 are crisp values like in traditional logic. Fuzzy logic uses linguistic variables – these are words in natural language such as “small, large”. Fuzzy sets are a group of linguistic variables which have membership functions or degree to which an input belongs to a group [4]. For example, if it is 76 degrees outside, it may be somewhat warm, and somewhat hot, not just one or the other. Fuzzy logic uses linguistic if-then rules.
A fuzzy system was designed to take 2 inputs logged by the autopilot, distance from the target (calculated from relative distance coordinates), and altitude from the rangefinder measurement, shown in Figure 1. These are then fuzzified into membership functions, which classify the distance and altitude into 5 memberships for each input ranging from very low to very high. These then go through a rule base which uses 5 rules. These rules say if the altitude is very low, or distance is very far, then risk is very high as the consequences of maneuvering in ground effect or missing the target are dangerous. The inverse is true; if the altitude is very high or the distance is very close to target, then the risk is very low because little maneuvering is needed and there is plenty of time to do so. Then the center of area

method is used to defuzzify the output back to a crisp risk value on a scale of 0-100. The risk surface is shown in Figure 2.

Results and Discussion

To validate the fuzzy logic-based estimator, logs from previous precision landing flight tests were used. The autopilot logs record the target relative distance to the vehicle, time since startup, rangefinder distance (altitude), and landing states, so these were fed straight into the fuzzy system. The previous flights were known to be successful precision landings. A sample flight, shown in Figure 3 shows that once the precision landing starts, the risk (3rd plot) decreases, then slowly increases as the vehicle descends. The UAV stayed pretty well centered over the target through the entire descent and the risk reached a maximum risk of about 57. So if a failsafe risk threshold was set at 70 for example, the UAV would have been allowed to continue landing.

Integration into ArduPilot requires future work and additional flight testing. This fuzzy risk assessment can be used in creating a new precision landing failsafe. The user can set a maximum risk tolerance and the risk assessment runs each loop of the precision landing controller. If the risk exceeds this threshold, a precision landing failsafe is triggered. Once in the failsafe, failsafe actions such as hold give the operator time to choose to abort precision landing or force landing depending on the operational risk tolerance. Additional future work includes adding more inputs such as windspeed and vehicle attitude, and a genetic algorithm to tune the membership functions.

Figures/Charts

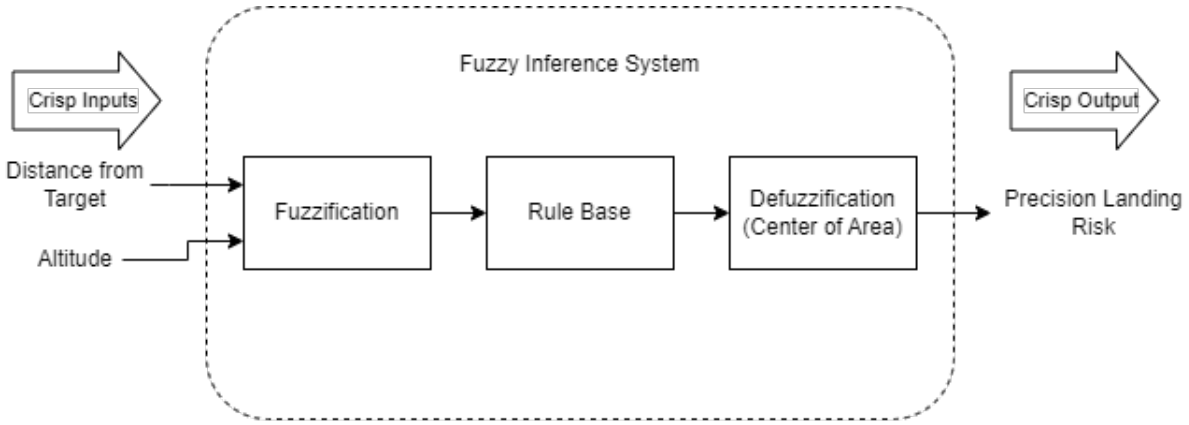

Figure 1: Fuzzy System for Risk Assessment [2,3]

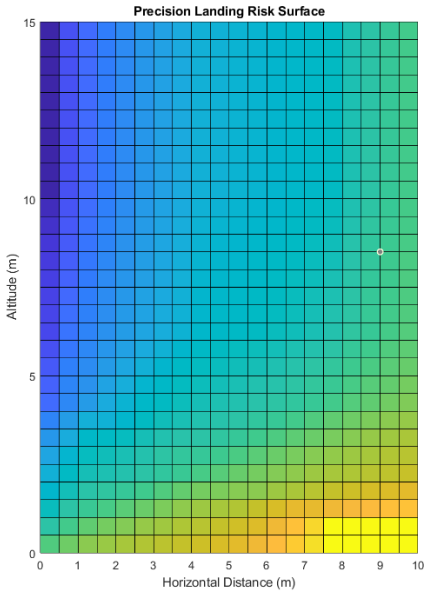

Figure 2: Risk Surface [3]

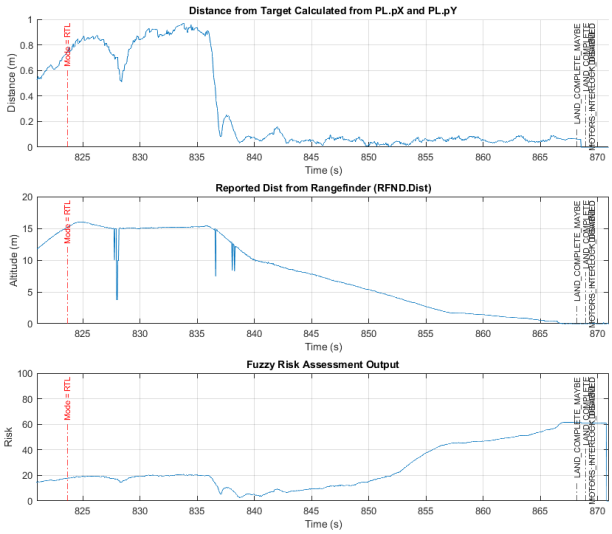

Figure 3: Fuzzy Output of Logged Precision Landing Flight [3]

Acknowledgments

This research would not have been possible without the support of the Ohio Space Grant Consortium, my advisor, Dr. Kelly Cohen, and Justin Ouwerkerk. Thank you!

References

1. NASA. “NASA’s Ingenuity Mars Helicopter Completes 50th Flight.” Accessed 4/17/2023. Apr. 2023. url: https://mars.nasa.gov/news/9381/nasas-ingenuity-mars-helicoptercompletes-50th-flight/.
2. Rebecca N. Gilligan. “Safety Assurance and Risk Estimation for Multi-Rotor Precision Landing”. MS Thesis. 2600 Clifton Ave, Cincinnati, OH 45220: University of Cincinnati, Mar. 2024.
3. Rebecca Gilligan, Justin Ouwerkerk, and Kelly Cohen. “Fuzzy Logic-Based Risk Assessment for Multi-Rotor Precision Landing” Pending publication in Studies in Systems, Decision, and Control by Springer Nature Switzerland AG
4. L.A. Zadeh. “Soft computing and fuzzy logic”. In: IEEE Software 11.6 (1994), pp. 48–56. DOI: 10.1109/52.329401.

Convolutional Deep Learning for Atmospheric Visibility Estimation in Constrained Environments

Student Researcher: Justin Murray

Advisor: Dr. Chad Mourning

Ohio University
Electrical Engineering and Computer Science

Abstract
The safe operation of aircraft requires up to date and accurate weather information. Of particular importance is atmospheric visibility information. Currently, visibility is measured using forward scatter sensors in Automated Weather Observing Systems (AWOS), typically located at airports. While reports from these stations are accurate and reliable, they do not cover areas between the stations. Deploying many forward scatter sensors for this purpose is not viable due to high costs. A solution to this problem would be to create a convolutional deep learning model that can be deployed on small, low-cost devices which can then be placed at regular intervals over an area where visibility information is needed. Existing research on this topic has not focused on the potential constraints for deployment. This project analyzes and compares existing models created for atmospheric visibility estimation. Three models were recreated, trained, and tested using three existing datasets. The accuracy and memory usage of these models were compared before and after applying techniques to reduce memory usage. The data shows that one model stands out as the best candidate for future research on atmospheric visibility estimation for its memory usage, accuracy, and ability to be modified for future improvements. This model will be the focus of future research seeking to improve estimation accuracy so that the model may be used in aviation.

Project Objectives
This project's objective is to explore methods of reducing memory usage of existing convolutional deep learning models created for atmospheric visibility estimation. Memory usage and accuracy of the models are compared to identify a model for future research focused on increasing accuracy so that the model may be used to inform decisions for the safe operation of low-altitude aircraft.

Methods
Three models for atmospheric visibility estimation from existing research were recreated and tested on existing datasets of foggy images. The models used are: VisNet [1], Retrieval of Multiple Environmental Parameters (RMEP) [2], and integrated model [3]. A version of VisNet using fewer nodes in its neural network and smaller convolutional layers was also designed to test VisNet's potential for memory usage reduction. The accuracy and memory usage of these models were compared using three datasets: Foggy Road Sign Images (FROSI) [4], Foggy Cityscapes (FCS) [5,6], and Sub-SkyFinder (SSF) [2]. FROSI and FCS consist of synthetic foggy images, while SSF is made up of real photographs of foggy scenes with matching atmospheric visibility data from nearby weather stations. The SSF dataset is unbalanced, however, with four times as many images with visibility above 10 miles than below. To remedy this issue, a balanced version of dataset was created to get a better measurement of performance across all visibilities.
The metrics used to measure model performance were the R^2 score, mean absolute error (MAE), and root mean squared error (RMSE). Comparison of each model to itself during training and testing was done based on the R^2 score of the model. Comparison of performance between models was done using the MAE and RMSE.

Methods for reducing memory usage mainly focused on quantization, where the number of possible values of the model weights is reduced to use up to 75% less memory. Modification of the neural

network architecture was also tested in the case of VisNet. To measure the minimum memory usage of each model, a utility was used to limit the memory usage of the program during model inference until it crashed due to a lack of memory. The file size of each model was also recorded, as it may provide a better comparison between models since it does not include memory overhead from the PyTorch library used for running the models.

Results and Discussion

The results for each model trained on each dataset can be seen in Tables 1-5, but Tables 2, 3, and 5 are of the most interest. Looking at tables 2 and 3, it can be seen that VisNet and its reduced version have the greatest reduction in model size when quantized, while RMEP has no reduction in model size or memory usage when quantized. Additionally, quantization had no significant effect on the performance of the models. Quantization greatly reduces memory usage in some cases and should be used if possible. Looking at all the results except for Table 5, all models seem to have very similar performance. This would make the best model the one with the smallest size depending on the dimensions of the input. However, Table 5 shows that on a balanced dataset of real photographs of foggy scenes, VisNet and its reduced version have the best performance. While their MAE and RMSE are not significantly lower, their R^2 scores are significantly less reduced from the unbalanced set compared to the other models. In field testing, the models trained on the balanced dataset appeared more accurate.

Each of the three models uses a different number of input images. RMEP only takes the original image as input. The integrated model uses an additional pseudocolored image. In addition to the inputs the integrated model uses, VisNet uses a high pass filtered image. VisNet has an advantage due to its three inputs, as it means there is more opportunity to modify how these images are processed. Better methods for processing the images can be tested without significantly modifying the model architecture and potentially increasing memory usage.

Based on the results discussed, VisNet is the best model for further development to increase accuracy and reduce memory usage for use in constrained environments.

Figures

A B C

Figure 1. Example images from the FROSI (A), FCS (B), and SSF (C) datasets.

FROSI

Model	Dimensions	Loss	Accuracy	Model Size (MiB)	Memory Usage (MiB)
RMEP	3x140x60	0.000	1.000	33.9	285
VisNet	3x140x60	0.013	0.996	130.3	365
VisNet Reduced	3x140x60	0.029	0.991	32.7	250
Integrated	3x140x60	0.026	0.996	147.3	401

Table 1. Performance metrics of the four models when trained and tested on the FROSI dataset.

FCS

Model	Dimensions	Loss	Accuracy	Model Size (MiB)	Memory Usage (MiB)
RMEP	3x256x256	0.306	0.912	33.9	315
VisNet	3x200x200	0.310	0.889	421.2	692
VisNet Reduced	3x112x112	0.336	0.889	41.6	406
Integrated	3x400x200	0.338	0.913	245.3	582

Table 2. Performance metrics of the four models when trained and tested on the FCS dataset.

FCS (Using Quantized Models)

Model	Dimensions	Loss	Accuracy	Model Size (MiB)	Memory Usage (MiB)
RMEP	3x256x256	0.306	0.912	33.9	315
VisNet	3x200x200	0.310	0.889	112.9	437
VisNet Reduced	3x112x112	0.336	0.884	12.3	258
Integrated	3x400x200	0.338	0.917	163.0	483

Table 3. Performance metrics of the four models after quantization when trained and tested on the FCS dataset.

SSF

Model	Dimensions	R^2	MAE	RMSE	Model Size (MiB)	Memory Usage (MiB)
RMEP	3x160x120	0.688	0.884	2.23	33.9	274
VisNet	3x160x120	0.689	1.09	2.28	62.7	365
VisNet Reduced	3x160x120	0.680	1.10	2.32	55.1	292
Integrated	3x160x120	0.688	0.911	2.23	160	431

Table 4. Performance metrics of the four models when trained and tested on the SSF dataset.

Balanced SSF

Model	Dimensions	R^2	MAE	RMSE	Model Size (MiB)	Memory Usage (MiB)
RMEP	3x160x120	0.214	2.18	3.26	33.9	272
VisNet	3x160x120	0.344	2.01	3.09	220	465
VisNet Reduced	3x160x120	0.329	2.08	3.06	55.1	290
Integrated	3x160x120	0.277	2.10	3.17	160	423

Table 5. Performance metrics of the four models when trained and tested on the balanced version of the SSF dataset.

Acknowledgments

Ohio Federal Research Network Project 502 Low Altitude Weather Network.

References

1. Palvanov, Akmaljon, and Young Im Cho. 2019. "VisNet: Deep Convolutional Neural Networks for Forecasting Atmospheric Visibility" Sensors 19, no. 6: 1343. https://doi.org/10.3390/s19061343

2. P. Su et al., "Retrieval of Multiple Atmospheric Environmental Parameters From Images With Deep Learning," in IEEE Geoscience and Remote Sensing Letters, vol. 19, pp. 1-5, 2022, Art no. 1005005, DOI: 10.1109/LGRS.2022.3149045.
3. Zhen Liu, Yihan Chen, Xingyu Gu, Justin K.W. Yeoh, Qipeng Zhang, Visibility classification and influencing-factors analysis of airport: A deep learning approach, Atmospheric Environment, Volume 278, 2022, 119085, DOI: 10.1016/j.atmosenv.2022.119085.
4. R. Belaroussi and D. Gruyer, "Impact of reduced visibility from fog on traffic sign detection," 2014 IEEE Intelligent Vehicles Symposium Proceedings, Dearborn, MI, USA, 2014, pp. 1302-1306, DOI: 10.1109/IVS.2014.6856535.
5. Sakaridis, C., Dai, D. & Van Gool, L. Semantic Foggy Scene Understanding with Synthetic Data. Int J Comput Vis 126, 973–992 (2018). https://doi.org/10.1007/s11263-018-1072-8.
6. M. Cordts, M. Omran, S. Ramos, T. Rehfeld, M. Enzweiler, R. Benenson, U. Franke, S. Roth, and B. Schiele, “The Cityscapes Dataset for Semantic Urban Scene Understanding,” in Proc. of the IEEE Conference on Computer Vision and Pattern Recognition (CVPR), 2016.

Discrete Vortical Gust Encounter and Mitigation using Closed Loop Control

Student Researcher: Andrew Porterfield

Advisor: Dr. Sidaard Gunasekaran

University of Dayton
Aerospace Engineering

Abstract
The open and closed-loop response of a wing to discrete vortical gusts were characterized using Time Resolved Particle Image Velocimetry (TR-PIV) in the University of Dayton Water Tunnel (UD-WaT). Discrete vortical gusts were generated by rapidly pitching a flat plate gust generator upstream of the wing. Simultaneous Time Resolved Particle Image Velocimetry (TR-PIV) and force measurements on the flat plate wing downstream of the gust generator were collected. A closed loop Proportional Integral Derivative (PID) control system was used to correlate the flow physics responsible for the force histories experienced by the wing. Peak-to-peak and average gust mitigation using closed loop control were quantified based on the derivations from open-loop results. The controller reduced the force transients during the gust entry by an average of 67% whereas the gust exit transients were only reduced by an average of 6%.

Project Objectives
The goal of this project was to characterize the strength, size, and trajectory of a series of discrete vortical gusts. By varying gust generator amplitude and pitch rate, varying strength gusts were created and allowed to convect downstream where they impinged on a wing. The effectiveness of a PID based closed loop controller was quantified by the percent mitigation achieved during the wing gust encounter.

Methods
A flat plate gust generator was pitched to 30 and 20 degrees at a rate of 165 and 110 (degrees/s). Particle Image Velocimetry (PIV) was used to identify the gust as it moves through the field of view. Initial tests without the wing were conducted in order to quantify the unobstructed gust strength. Each case was tested 6 times and ensemble averaged. The PIV image processing software Fluere was used to correlate the images into a vector field.[1] The circulation and vorticity of the gust were calculated using the resulting vector field. The vortex center was tracked through the field of view in order to establish the vortex trajectory. For the open-loop cases, a flat plate glass wing was installed 5 chords downstream from the gust generator. The gust was allowed to interact with the wing while being held at an angle of attack of 0. The forces during the encounter were recorded and averaged across each test. For the closed loop cases, the wing was mounted onto a linear motor outfitted with a rack and pinion gear to allow for active angle of attack adjustments. The lift experienced by the wing during the closed loop case was the feedback in a PID based closed loop controller which actively pitched the wing in order to reduce the effects of the gusts. The effectiveness of the controller was quantified by calculating the percent mitigation between the open and closed loop cases.

Results
The trajectories found in the gust characterization cases both show a vertical offset from the gust generator and wing location at the centerline of the tunnel. While the gust is offset from the centerline of the tunnel, neither trajectory sees significant drift as it passes through the field of view. The gust

entry in the open-loop tests saw the largest C_L peaks. The largest of these peaks was seen in the second case, reaching a C_L of 0.6. The positive peaks occur as the gust approaches the wing, and as the gust impinges on the wing, there is a large C_L fluctuation. The wing sees the negative C_L peak as the gust travels over the trailing edge of the wing. The C_L response in the closed-loop cases is much lower during the gust entry. While the closed loop controller was effective during the gust entry, it proved difficult to achieve the same mitigation during the gust exit. The rapid change in C_L was too large for the PID controller to keep up. The closed loop controller also introduced an interesting oscillation seen throughout the test, but it was exaggerated during the gust exit. The controller was able to achieve a gust entry mitigation of up to 69.27% while the largest gust exit mitigation was only 8.12%. There is a clear difference between the two peak-to-peak mitigations, however the average mitigation across the whole run sits between 45 and 48% according to Table 1. A full test can be seen in Figure 3. The PIV images are frames from each of the open and closed loop peaks during the test. The shaded region in Figure 3 represents the large wake experienced by the wing due to the pitched gust generator remaining at a large angle upstream of the wing. Future testing could change the gust profile in order to reduce the wake seen by the wing while maintaining the isolated gust encounter.

Figures/Tables

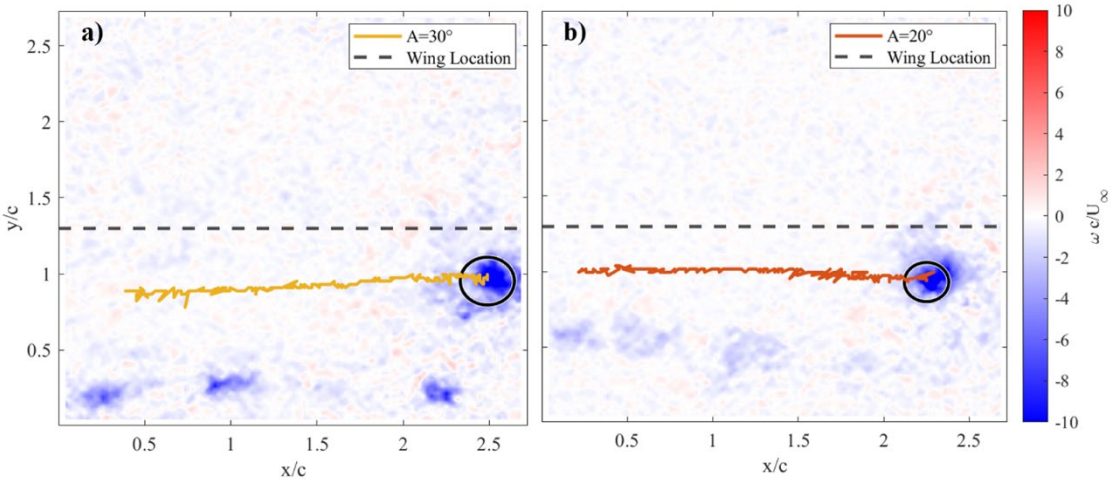

Figure 1. Vortex Trajectories at 165°/s for a) A = 30°, b) A = 20°

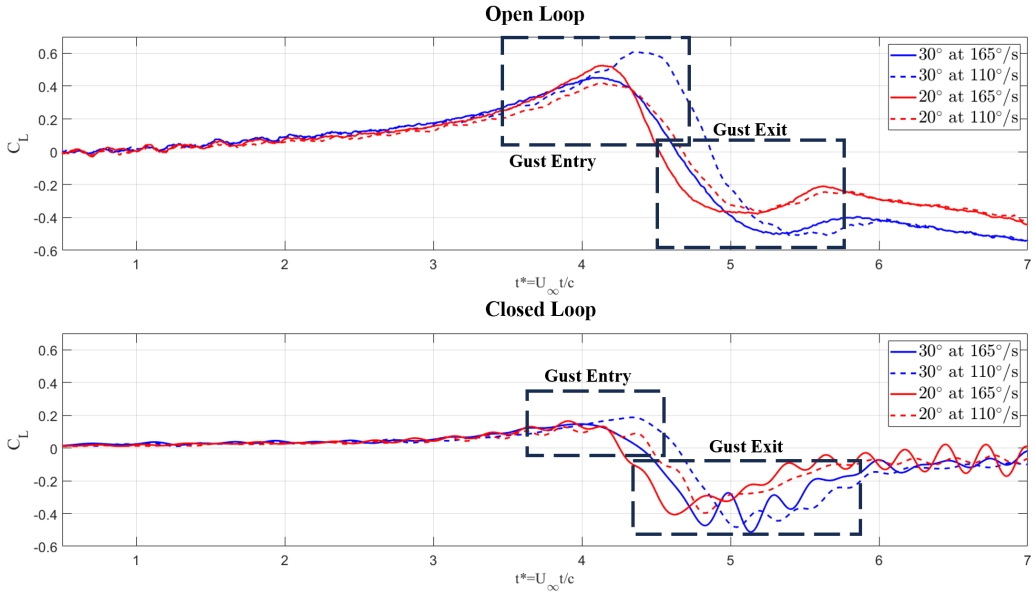

Figure 2. Gust mitigation comparison between open and closed loop cases at different $\dot{\alpha}_N$

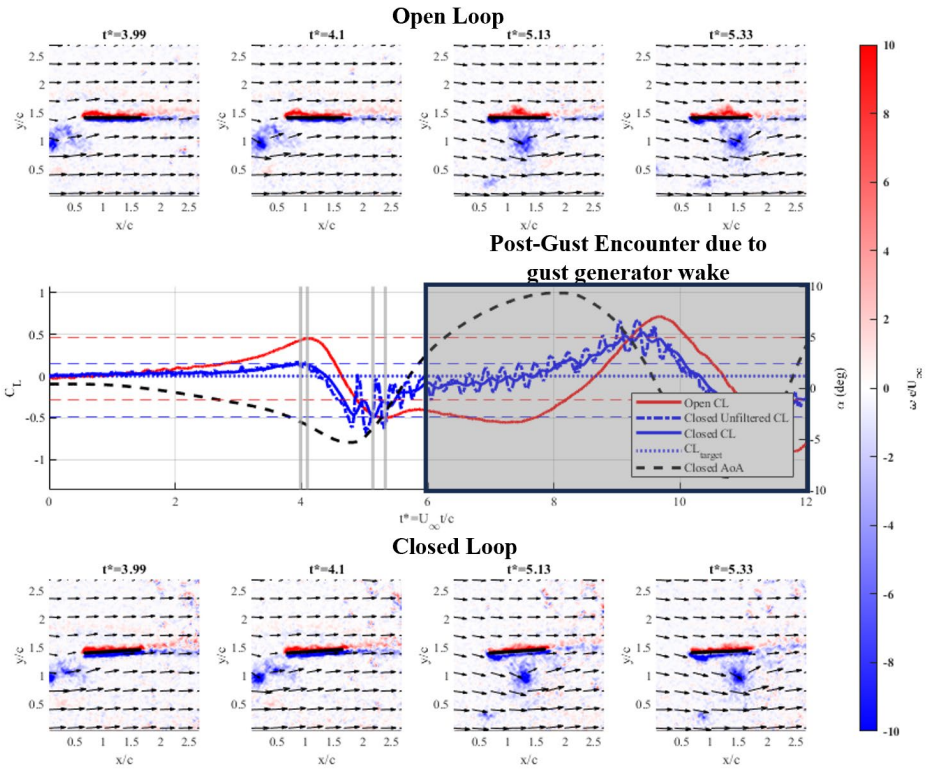

Figure 3. Full Test Gust Mitigation for A = 30°and α.= 165°/s

Table 1. Gust Mitigation

Amplitude	Pitch Rate	Gust Entry Mitigation	Gust Exit Mitigation	Average Mitigation
30°	165°/s	67.55%	1.84%	45.71%
	110°/s	69.27%	5.09%	48.06%
20°	165°/s	68.73%	8.12%	48.96%
	110°/s	67.75%	7.87%	48.04%

Acknowledgments

I would like to thank my advisor Dr. Sidaard Gunasekaran, for assisting me with this research project. I would also like to thank the University of Dayton and the Ohio Space Grant Consortium for giving me the opportunity to conduct research and pursue a graduate degree.

References

[1] Lynch, K. P. "Fluere for Particle Image Velocimetry: User Manual." (2011).

Dynamic Modeling and Testing of Electro-Rheological Haptic Modules

Student Researcher: Michael Siino

Advisor: Dr. Jeong-Hoi Koo

Miami University College of Engineering and Computing
Department of Mechanical and Manufacturing Engineering

Abstract
Widely employed in hand-held devices, haptic feedback technology has been proven to be effective in enhancing the overall user experience by providing additional sensory information to the user. In recent years, the demand for haptics in large touchscreen displays (TSDs) has rapidly grown. However, due to limitations of current haptic actuators used within mobile devices, the technology to implement tactile haptics in larger displays is immature. To address challenges for generating haptic feedback in large touch screen displays, this study proposes a haptic module based on a "smart" fluid called Electro-Rheological (ER) fluid for use in large TSD applications. ER fluid is a fluid whose apparent viscosity is dependent upon electric field; By adjusting the input electric voltage, frequency, or waveform, the ER fluid can be manipulated to shift from liquid to solid behavior.

Project Objectives
In recent years there has been a shift in many industries from conventional user interfaces i.e, screens requiring peripherals such as keyboards and mice, towards touchscreen interfaces due to ease of use. Touchscreens have been the status quo in small scale devices such as mobile phones for over a decade. As such, haptic technology that provides tactile feedback has had time to develop and improve. Meanwhile, as large-scale TSDs become more common in various industries, the required haptic technology remains underdeveloped. Lack of feedback is highly correlated with increased error rates among users [2], and to alleviate this issue further research is necessary to develop new methods of creating haptic technologies for the unique needs of large-scale screens. This study proves the feasibility of using Electro-Rheological fluids, a type of smart fluid, to control vibrations to create a range of tactile haptic sensations in large touch screen displays.

Methodology
To accomplish the project objectives, a prototype haptic module was developed containing Electro-Rheological (ER) Fluid. Consisting of particles suspended in a base fluid, when subjected to an electric field, the particles in the ER fluid line up along field lines, changing the fluids viscosity and providing a resistance to motion [3]. This provides a promising means of providing haptic sensations as when provided with electrical fields, the yield point of the fluid is changed and can reversibly shift from a gel-like fluid to a solid behavior within a millisecond [1].
A prototype haptic module was developed, consisting of a plate electrode, ring electrode, radial spring, aluminum spacers, and a mass. These components are assembled into a haptic module and filled with ER fluid (Fig. 1). To evaluate the dynamics of the system, the module was first analyzed without the ER fluid present. An input vibration is transmitted from the base of the module through the spring and electrodes, and the acceleration is recorded at both the base and output to determine the transmissibility, the ratio of output to input acceleration magnitude, over a range of frequencies from

100-400 Hz. The module was then filled with the ER fluid, and the same data collection was repeated for the inert fluid (no applied electric field).
Following initial testing, data collection was performed on the excited ER fluid. Signals were input into the ER fluid via the two electrodes. These signals, ranging from 1-4 kV and 0-400 Hz were evaluated to demonstrate the performance of the ER fluid haptic module in controlling the vibration input to the system through the base of the module. A study was conducted to determine the impact of the input frequency while holding the input voltage constant. A second study was then conducted to determine the impact of the input voltage was performed while holding the input frequency into the fluid constant.

Results

Impact of Varying Electro-Rheological Fluid Input Frequency

The frequency of the excited ER fluid is demonstrated in Fig. 2 to noticeably affect the output vibration compared to the inert fluid. In Fig. 2 it is evident that an increase to the input frequency to the haptic module has an impactful effect on both the amplitude and response of the output waveform; an increase to the input frequency corresponds to both an increased output amplitude and a waveform more distinct from that of the inactive fluid.

Impact of Increased Voltage Input into Electro-Rheological Fluid

Fig. 3 shows a similar phenomenon for an increase in voltage. As the voltage is increased from 1 kV to 4 kV, a more distinct waveform from the original inert fluid is experienced. Additionally, an increase in amplitude is also observed. These findings are consistent with the expected behavior of the ER fluid, as strengthening the electric field corresponds to a stronger alignment of the particles suspended in the fluid, providing additional resistance to motion and further altering the output waveform.

The overall study is still in progress. These results demonstrate the feasibility of ER fluids for conveying distinctive tactile haptics. However, to demonstrate the ER fluid haptic module's ability to provide tactile haptics to large touchscreen displays the study will be extended to a system consisting of multiple haptic modules attached to a bar interface to demonstrate its ability to control vibrations across a large domain analogous to a large touch screen.

Figures

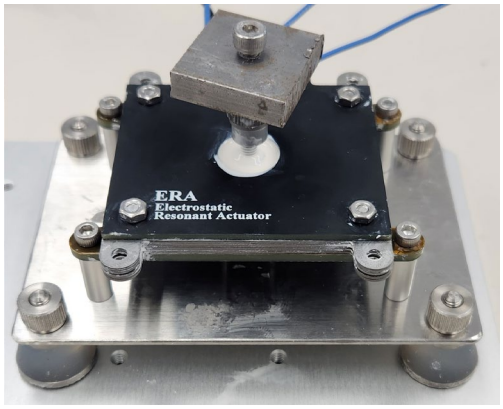

Figure 1: Assembled Haptic Module connected to a damping base. The module consists of two electrodes, radial spring, mass shown on the top of the module, and is filled with Electro-Rheological Fluid.

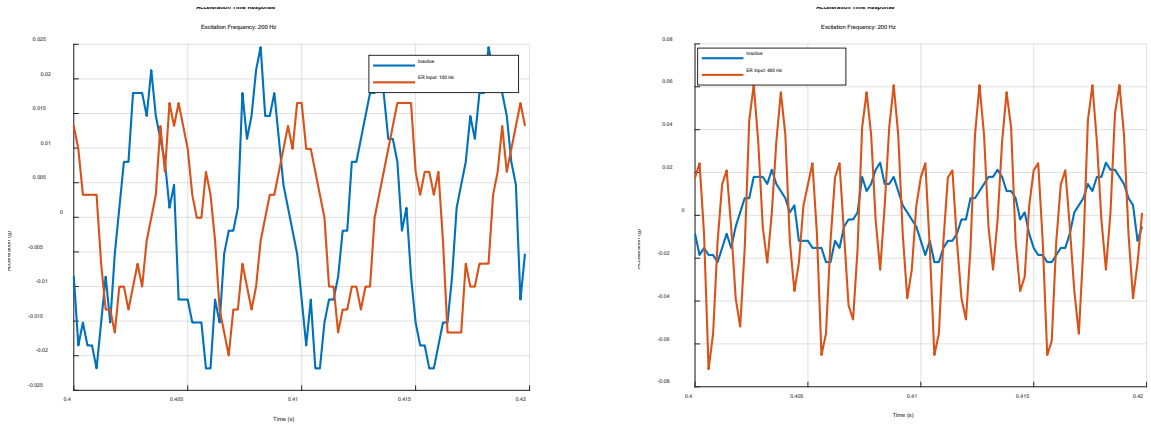

(a) **(b)**

Figure 2: Time response plots showing the impact of input frequency into the ER fluid, **(a)** Input frequency of 100 Hz into ER fluid, **(b)** Input frequency of 400 Hz.

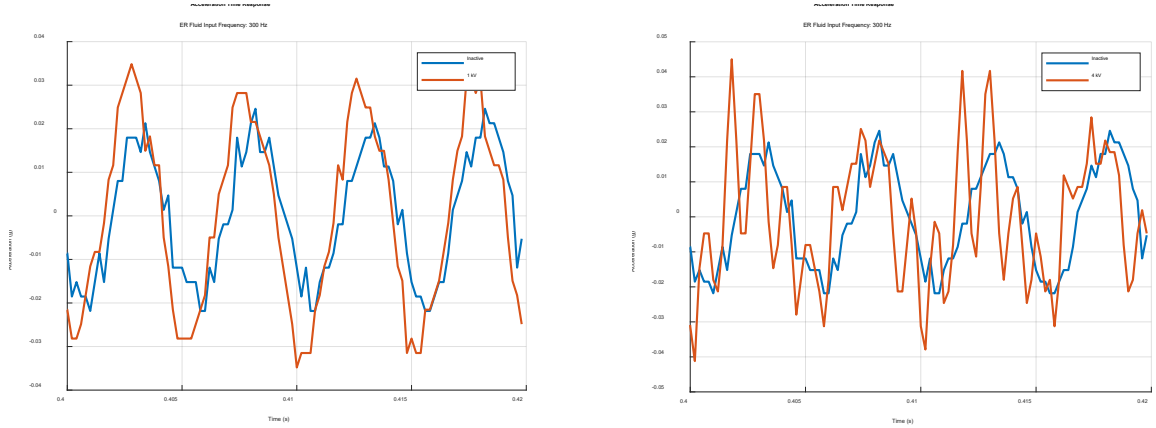

(a) **(b)**

Figure 3: Time response plots showing the impact of voltage input into the ER fluid, **(a)** Input voltage of 1 kV, **(b)** Input voltage of 4 kV.

Acknowledgements

I would like to greatly thank the Ohio Space Grant Consortium for their support throughout the 23-24 academic year, along with my advisor Dr. Jeong-Hoi Koo.

References

[1] Ajit Behera. “Smart Fluid.” *Springer eBooks*, 2021, pp. 193–223. https://doi.org/10.1007/978-3-030-80359-9_6.

[2] Clarkson, E., Clawson, J., Lyons, K., and Starner, T. An Empirical Study of Typing Rates on Mini-QWERTY Keyboards. Presented at the CHI 2005 Conference on Human Factors in Computing System, Portland, OR, USA, 2005.

[3] Fisch, F. J. (2007). *Development and Testing of Haptic Interfaces Using Electro-Rheological Fluids* [Doctoral thesis, Rutgers University – New Brunswick]. Rutgers University Libraries. https://rucore.libraries.rutgers.edu/rutgers-lib/21306/

Applying Current Wireless Security Methods to the Deep Space Network

Student Researcher: John Sipahioglu

Advisor: Dr. Younghun Chae

Kent State University
Department of Computer Science

Abstract
The Deep Space Network (DSN) is the backbone of all communications between Earth and devices beyond its orbit. The DSN consists of three primary ground stations, located in California, Spain, and Australia, as well as the very resource-constrained spacecraft that use it to communicate with Earth [1]. However, the DSN's mission has expanded far beyond its original scope, leading to the network being overburdened by the number of missions it must support [2]. In this research, the aim is to provide a way to ease the burden on the DSN through modifications to its network layer security. Currently, DSN security in the network layer is based on Internet Protocol Security (IPSec) [3], a suite of protocols designed to provide security to the network layer [4]. In this research, the performance of IPSec is compared to a more modern protocol for setting up VPNs, WireGuard, to determine if performance gains can be made by changing the security protocols of the DSN. Specifically, testing of the throughput, CPU usage, RAM usage, configuration difficulty, and file space was conducted. Testing showed that in most cases, WireGuard outperforms IPSec and could be a strong candidate for securing future missions.

Project Objectives
DSN security using IPSec consists of creating a Virtual Private Network (VPN) between the station on Earth and the spacecraft that is being contacted [3]. IPSec has long been one of the primary choices for creating a VPN, however, its cryptographic agility and many configuration options make its implementation highly complex [5]. A recently proposed protocol, WireGuard, offers a simpler and faster solution for setting up VPNs. WireGuard trades the configuration options of IPSec to offer a "common case fast" approach to creating VPNs [5]. By offering the most used features of a VPN as the default and only configuration option, WireGuard reduces the codebase and complexity of its implementation significantly [5], while retaining the performance of IPSec.

In Table 1, the security requirements of the DSN are enumerated [3], and the ways IPSec meets them [4], and how WireGuard could meet them [5], are displayed. To summarize, WireGuard could be capable of meeting all the requirements set forth for DSN security, with some modifications. The first change would be to enable manual rekeying. Rekeying is a change in the public keys used by the parties to communicate are changed to ensure the key is replaced before it can be compromised [6]. However, in mission critical states, rekeying could result in a network lockout, and thus must be disabled at times to ensure the connection is not lost [3]. The other difficulty is with the cryptographic ciphers used. The algorithms used by WireGuard are not included in the list of allowed ciphers for the DSN. The recommended cipher for the DSN is Advanced Encryption Standard (AES) using a 256-bit key [7], with Galois Counter Mode (GCM) using a 128-bit key [7]. WireGuard instead uses ChaCha20-Poly1305 as its Authenticated Encryption with Associated Data (AEAD) [5]. Due to the simplicity of WireGuard's implementation, adding a manual rekeying mode and changing the cryptographic primitives would not be overly difficult, in this author's opinion. Now that it has been established that WireGuard can meet the standards for DSN security, it can be determined if WireGuard offers better performance than IPSec. In this research, the performance of WireGuard is compared to IPSec in terms of its throughput, Central

Processing Unit (CPU) usage and Random Access Memory (RAM) usage. The complexity of setup and amount of storage required to house the files for the protocols is also analyzed.

Methods

The testing consisted of setting up an IPSec VPN network and a WireGuard VPN network between two machines running Ubuntu 22.04 as their operating system. One computer has an Advanced Micro Devices (AMD) Athlon Silver 3050u 2-core, 2-thread processor with 6 GB of RAM. This computer will be referred to as the server going forward. The other computer has an AMD Ryzen 5 2400g 4-core, 8-thread processor with 12 GB of RAM. This computer will be referred to as the client in the rest of this document. Four networks were considered: an unsecured network with no VPN or other security, a network secured by IPSec using AES256-GCM128, one with IPSec using ChaCha20-Poly1305, and one using WireGuard. The two AEDSs used for IPSec allow results to be gathered for the DSN recommended cipher, as well as for the cipher used currently in WireGuard.

Two types of throughput testing were performed, one where a large number of files were transferred successively and the average rate of all the requests represented the throughput, as well as testing the throughput for individual file transfers. The multiple-file transfer test was performed by measuring the data rate when requesting 29,856 megabytes worth of files in series and taking the average. For single file transfers, files of 128, 256, 512, 1024, 2007, 4785, and 10027 megabytes were transferred, and the data rate of the single transfer was used as the measured value. CPU usage was tested by logging the CPU usage with a program running in the background while files were being transferred. RAM usage was tracked in the same manner.

Results and Discussion

In terms of throughput, WireGuard offered performance closer to an unsecured network than it did to IPSec. During the transfer of multiple files, WireGuard outperformed an unsecured network, which was a surprising result to the author. Another surprising result was the CPU usage of WireGuard on the client side. This result, however, did not work in WireGuard's favor, as it performed significantly worse than IPSec with an average CPU usage of 29.25% compared to 17.08% for IPSec using the same ChaCha20-Poly1305 cipher. However, WireGuard performed slightly better than IPSec on the server side, with an average usage of 39.19% compared to 43.30% and 43.45% for IPSec using ChaCha20-Poly1305 and AES256-GCM128, respectively. WireGuard used significantly less RAM than IPSec on both the client and server. Table 2 presents the averages for all of the test cases. Note that RAM usage is in relation to an idle measurement taken when no transfers were taking place. Figures 1 and 2 present the throughput, while Figures 3 and 4 display CPU usage on the client and server, respectively, and Figures 5 and 6 represent the RAM usage on the client and server, respectively. The file space required to install WireGuard was less than IPSec, requiring 345 kilobytes of disk space compared to 8,636 kilobytes. Finally, it is worth noting that WireGuard was much simpler to install, set up, and configure than IPSec. WireGuard only required one package to be installed, whereas the strongSwan implementation of IPSec required several packages. There were also far fewer steps and commands needed to configure the WireGuard VPN, and those steps were much simpler than those for IPSec.

In conclusion, it has been shown that WireGuard offers stronger performance than IPSec in almost all metrics, while still being capable of meeting all of the security requirements for the DSN. The biggest area of concern is the CPU usage on the client, however, since most communication in the DSN is from spacecraft to Earth, most of the time the higher usage will be on Earth where resources are far less limited. More testing should be done to verify the results demonstrated here, as well as to push more toward simulating the very resource constrained nature of spacecraft. Additionally, WireGuard should be tested with the modifications required to fully meet the standards set by the DSN. However,

these results show that WireGuard has potential as a future option for DSN security, as the increased throughput and lower resource usage in most cases could alleviate some strain on the network.

Tables and Figures

Requirement	IPSec	WireGuard
Protocol	Encapsulating Security Payload	WireGuard's default operation offers the same services as ESP
Mode	Tunnel Mode	WireGuard operates as a network tunnel
Authenticated Encryption Service	Required by CCSDS, must be configured	Authenticated Encryption is enabled by default in WireGuard
Integrity	Integrity only service required	WireGuard offers integrity service by default
Manual Key Management	Supported	Not Supported, modification needed
Automatic Key Management	Supported, modified to allow inhibit rekey	Automatic key management is default
Ciphers	Only CCSDS approved ciphers may be used	WireGuard does not use CCSDS ciphers in its current build

Table 1: Comparison of CCSDS standards for IPSec and how WireGuard can meet them.

Single File Throughput				
	No VPN	IPSec ChaCha20-Poly1305	IPSec AES256-GCM128	WireGuard
128 MB	112.00 MB/s	87.52 MB/s	103.28 MB/s	106.80 MB/s
256MB	112.00 MB/s	87.88 MB/s	88.90 MB/s	107.00 MB/s
512 MB	112.00 MB/s	87.40 MB/s	89.58 MB/s	107.00 MB/s
1024 MB	111.80 MB/s	90.64 MB/s	89.08 MB/s	107.00 MB/s
2007 MB	111.60 MB/s	90.88 MB/s	88.28 MB/s	106.60 MB/s
4785 MB	112.00 MB/s	91.50 MB/s	91.94 MB/s	106.60 MB/s
10027 MB	111.41 MB/s	88.90 MB/s	92.12 MB/s	106.22 MB/s
Average	111.83 MB/s	89.25 MB/s	91.88 MB/s	106.75 MB/s
Multiple File Throughput				
Average	82.25 MB/s	65.45 MB/s	75.74 MB/s	87.35 MB/s
CPU Client				
Average	11.47%	17.08%	17.96%	29.25%
CPU Server				
Average	24.77%	43.30%	43.35%	39.19%
RAM Client (Difference from Baseline Measurement)				
Average	7.22 MB	17.70 MB	21.66 MB	5.47 MB
RAM Server (Difference from Baseline Measurement)				
Average	351.86 KB	12.75 MB	11.12 MB	3.31 MB

Table 2: Summary of Data

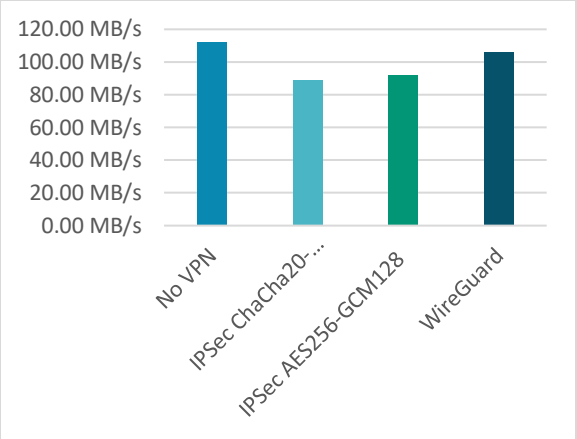

Figure 1: Throughput for Single File Transfer

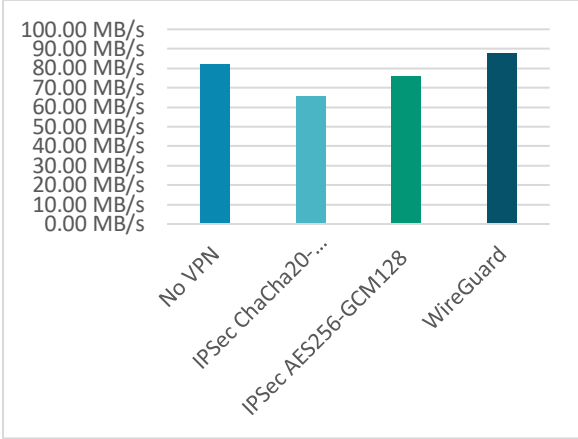

Figure 2: Throughput for Multiple File Transfer

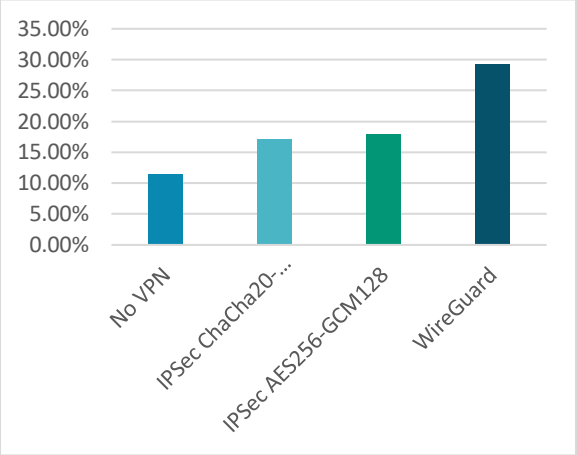

Figure 3: CPU Usage on Client

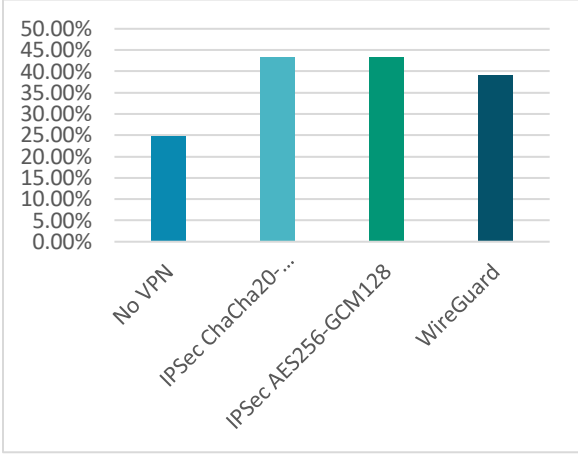

Figure 4: CPU Usage on Server

Figure 5: RAM Usage on Client

Figure 6: RAM Usage on Server

Acknowledgments
Thank you to the Ohio Space Grant Consortium and NASA for providing me with the opportunity to conduct this research. I would also like thank my advisor, Dr. Young Chae, for his guidance through not just this project, but through my other past and present endeavors, as well as Dr. Angela Guercio for informing me of the fellowship.

References

[1] D. J. Mudgway, Uplink-Downlink A History of the Deep Space Network 1957-1997, Washington, D.C.: National Aeronautics and Space Administration Office of External Relations, 2001.
[2] H. H. Means, "The Deep Space Network: Overburdened and underfunded," Physics Today, vol. 76, no. 12, pp. 22-23, December 2023.
[3] CCSDS Report: Recommended Standard for Network Layer Security Adaptation Profile. Recommended Standard, Issue 1. Consultive Committee for Space Data Systems. Washington D.C., United States, Apr. 2023
[4] S. Kent and K. Seo. Security Architecture for the Internet Protocol. RFC 4301. ISOC. Reston, Virginia, Dec. 2005
[5] J. A. Donenfeld, "WireGuard: A Next Generation Kernel Network Tunnel," in Network and Distributed Security Systems Symposium, San Diego, California, USA, 2017.
[6] M. Abdalla and M. Bellare, “Increasing the lifetime of a key: a comparative analysis of the security of re-keying techniques,” in International Conference on the Theory and Application of Cryptology and Information Security. pp. 546-559, 2000
[7] CCSDS Cryptographic Algorithms, Informational Report, Issue 2. Consultive Committee for Space Data Systems. Washington D.C., United States, Apr. 2023

Modeling Thermal Soak Temperature Variation of Electric Aircraft Motors

Student Researcher: Julia Taylor

Advisor: Dr. D Blake Stringer

Kent State University
College of Aeronautics and Engineering/Aerospace Engineering

Abstract
Characterizing thermal performance is essential to optimizing system performance, reducing damage, and enhancing overall reliability and safety, especially in high-powered heat generating applications. In the growing eVTOL (electric Vertical Take-Off and Landing) ecosystem, quantifying and characterizing the thermal performance of new propulsion platforms has resorted to complex, numerical solutions via commercial software. One reason for this is how thermal performance is affected by a phenomenon called thermal soak. Thermal soak is the sudden increase of internal component temperature due to terminating any forced convective cooling from a heat-producing system (i.e., landing and shutdown after hovering). A more accessible thermal soak model was developed and explored with the aim of better understanding heat transfer properties of electric/hybrid motors under VTOL power conditions. Comparisons between the thermal soak model and experimental data from several eVTOL motor and propeller configurations at different power and ambient conditions were made.

Project Objectives
The objective is to provide a working model of thermal soak based upon surface temperature measurements and known characteristics of the motor. The purpose of this is with the mindset of assisting the electrification of aircraft. The research described in this project specifies what model updates have occurred to try and obtain a more reliable thermal soak model.

Methods
There are two components of the methodology used: (1) identifying the theoretical model and (2) collecting data to validate the theory.
The theoretical development of the thermal soak model began making headway during the summer of 2022 under the funding of the U.S. Air Force Research Laboratory (AFRL) Summer Faculty Fellowship Program (SFFP) at the Wright-Patterson Air Force Base. Since the summer of 2022, the founding assumptions and processes have remained consistent while updates to the model have led to further validations of being able to model thermal soak in electric aircraft motors in a laboratory environment.
The following is the steady-state model of the thermal soak model, which was founded by the 1st Law of Thermodynamics and Newton's Law of Cooling:

$$\ddot{T} + 2\zeta\omega_n\dot{T} + \omega_n^2 T = \omega_n^2 T_\infty$$

Where,

$$\omega_n = \sqrt{\frac{1}{\tau_{eff}}\frac{h_n A_s}{mc_p}}$$

$$\zeta = \frac{1}{2\omega_n}\left(\frac{h_n A_s}{mc_p} + \frac{1}{\tau_{eff}}\right)$$

$$T(0) = T_0$$

$$\dot{T}(0) = \dot{T}_0 = \frac{1}{mc_p}\left[\dot{Q}_{eff_0} - h_n A_s \left(T_0 - T_\infty\right)\right] = \frac{A_s}{mc_p}\left(h_f - 2h_n\right)\left(T_0 - T_\infty\right)$$

$$\tau_{eff} = mc_p R_{eff}$$

Nomenclature:

A_s = motor surface area
L = reference length
Q = heat energy
$\dot{Q}$ = rate of heat transfer
R = thermal resistance
T = system temperature
$\dot{T}$ = rate of temperature change
c_p = specific heat at constant pressure
k = thermal conductivity
m = system mass
h = heat transfer coefficient
t = time
δ = damping ratio
τ = time constant
ω_n = natural frequency

Subscripts:

∞ = ambient condition
conv = convective cooling
eff = effective heating
f = forced convective heat transfer
n = natural convective heat transfer
ref = reference
tr = transient region
0 = steady-state value, initial value at start of transient region

The assumptions listed below were also followed:

1. System changes in kinetic and potential energies are negligible.
2. The only energy to cross the system boundaries is heat energy after shutdown (e.g., no work crosses the system boundary).
3. The system can be modeled as a uniform material of constant density.
4. The variation of material properties with temperature is negligible.
5. Heat transfer across the system boundary occurs through convection only.
6. During steady-state operation, heat transfer occurs through forced convection.
7. After system shutdown, heat transfer to system boundary occurs through natural convection.
8. "Trapped" heat will soak into the system via conduction. We will define this as "effective heating" in the next sections. Effective heating decreases as the system temperature increases. It exhibits a first-order decay rate that is negligible at five time-constants [13].

Experiments follow the same general set-up and procedures regardless of the facility at which it was conducted. The data used was from two lab environments, Kent State University's eVTOL Propulsion Lab and the Aeronautics Research Laboratory at the United States Air Force Academy.

From Kent State University's inventory, there are 9 motors and 8 propellers. Based on manufacturing specifications, there were potentially 19 motor-propeller configurations to be tested, with consideration of the power available to be provided to the system. Due to connection compatibility, not all 19 configurations can realistically be assembled on each of the static propulsion test stands.

Tyto Robotics temperature probes for a series 1780 Thrust Stand were used in connection to the branded control board. Using this control board allowed for utilization of the RC Benchmark software, program automated tests, and generate temperature, thrust, torque, ESC, and power data. For each test, there was at least one probe measuring the temperature of the outer motor case and another

measuring the temperature of the copper coils inside the motor. With the orientation of the test stands, the copper coils were almost always easily accessed through the bottom of the motor without interfering with the rotation of the motor.

The test stand at Kent State is a series 1780 Thrust Stand that is quoted for up to 50 lbf of thrust and 50V. 4 12-Volt rechargeable batteries (48V total) are connected in series as the power source for the test stand. The stand is surrounded by a shroud to protect the lab's occupants and is located within the Aeronautics and Engineering Building on Kent's Main Campus.

The test stand used at USAFA was a hybrid of the Tyto Robotics series 1780 and available components from previous experimental setups. Two noticeable differences between the test stand at USAFA and KSU are the orientation of the motor and having a constant power source of 40V.

Another consideration while conducting experiments at different facilities is the adjustment of ambient conditions. The elevation of Kent, Ohio is roughly 1,000ft while the elevation at USAFA, Colorado is approximately 6,000ft. This leads to a significant change in air density which affects the thrust and torque propellers produce. Using the thrust and torque curves for the propellers used, the rotational speed to test at USAFA can be found that is an equivalent to tests at Kent State.

When discussing model updates, the challenge of collecting accurate temperature data at USAFA begged the question of how to confirm the calibration of the temperature probes used on the test stands. The brand of temperature probe did not come with specific instructions on calibration, so we curve fit temperature data taken at various locations on a motor with independent temperature measuring devices, namely an infrared temperature gun. The 3rd degree polynomial fit of the data temperature showed the highest coefficient of determination

Finally, the last consideration for the current model was the objective to identify system parameters from data with the aim of noticing trends of the system that can be applied to potential future systems. System identification is a method for constructing mathematical models of systems using measurements of the system's inputs and outputs. We may not need to know exact specifications of a system, for example the effective thermal resistivity value of the specific motor, to be able to model the thermal soak in electric motors which allows for a more robust and cohesive model that can be used.

MATLAB® was used to first process the data since the collection of temperature data can range from 1 – 4 Hz, depending on the computer used to run RCBenchmark and RCBenchmark version, and there are natural fluctuations from the probe's measurements between these data points. The processed data was then plugged into code which estimated the parameters (ω_n, δ, T_0, $\dot{T}_0$) for an overdamped, second-order system with the same initial conditions of the data set (T_∞ and τ_{tr}). Finally, plots comparing the predicted model's temperature profile and the data's profile were generated and placed in the results.

Results and Discussion

The preliminary model was the first iteration of modeling thermal soak in electric aircraft motors that had data from KSU. The theoretical development along with a few fundamental assumptions, specifically the system's thermal conductivity and specific heat coefficient which makes up the effective thermal resistance (R_{eff}), shaped the preliminary results. For a proof of the model, four datasets of the same motor-propeller configuration ran at power settings that ranged from 1.8-1.9kW. As stated, the lumped parameter assumption made in the theoretical development shows parameters of the entire system rather than by individual thermal material properties. It was because of this assumption that the model was able to proceed with assumptions made for a combined coefficient of specific heat and thermal conductivity. The most effective assumption (a 30-70 ratio of aluminum to copper) came from identifying what materials made up a percentage of the motor and then taking the weighted average of those material's specific heat and thermal conductivity properties. The motors used in this research

have components of copper, iron, aluminum, and air so using this assumption was acceptable to continue with the model but noted as something that needed to be rectified for the next iteration of the model.

The major observation between the first and second iteration of the model is the percent error of the maximum temperature reached by the system and the time it takes the system to reach that temperature after shutdown. While the average percent error of the maximum temperature remained very similar (all less than 1% from Tables 3 and 4), the percent error for the time to reach the maximum temperature drastically increased from iteration one to two (from an error of less than 7% to an error as high as 128%). While having both the maximum temperature and the time to reach the maximum temperature is important, the time component is not as critical as the temperature. Whereas, if the heat within the copper coils inside the motor rises above the heat that can dissipate, the coils can char. If it takes 60 seconds or 120 seconds for the coils to reach the maximum temperature, there is no obvious risk associated with error for this unknown. Thus, from the preliminary model up to the current, updated model, an adequate thermal soak model was created for electric motors used in aircraft.

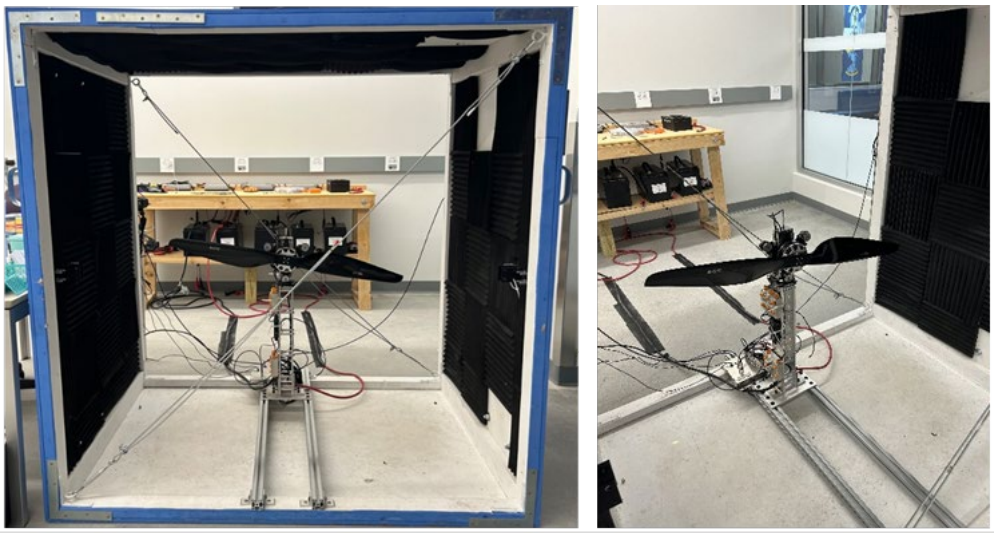

Figure 1: KSU static thrust test stand

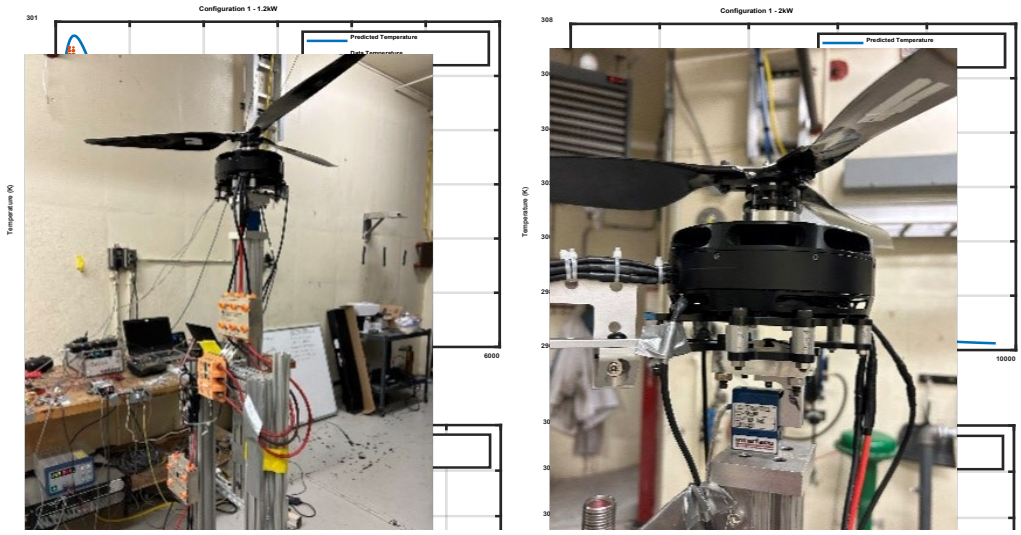

Figure 4: Current model's results

Figure 2: USAFA static thrust test stand

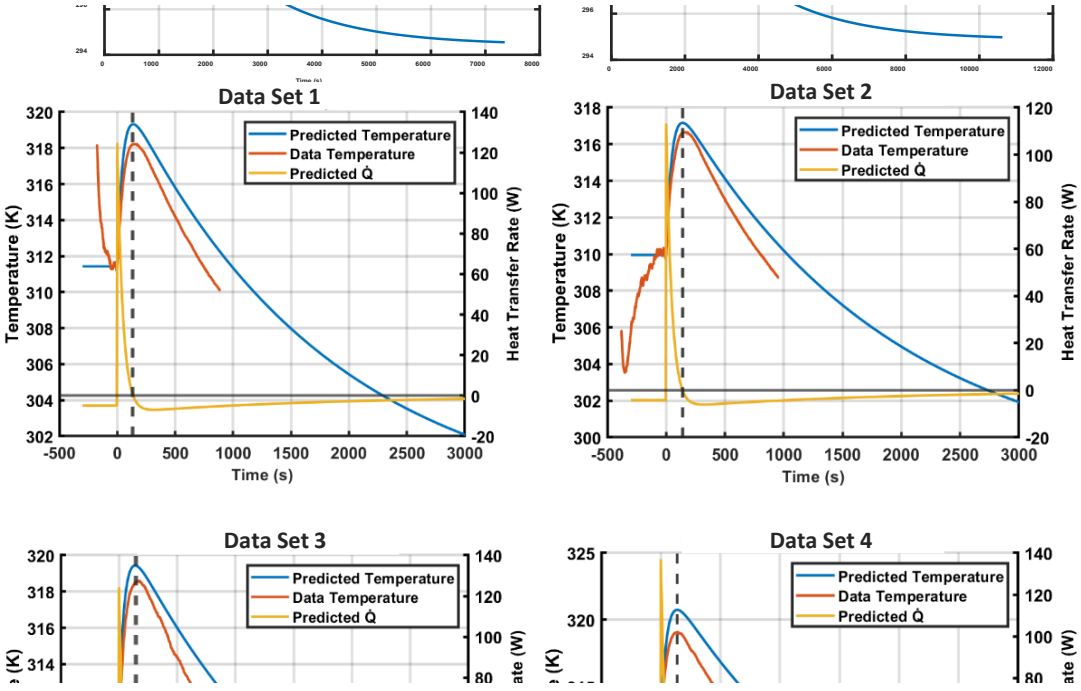

Figure 3: Preliminary results

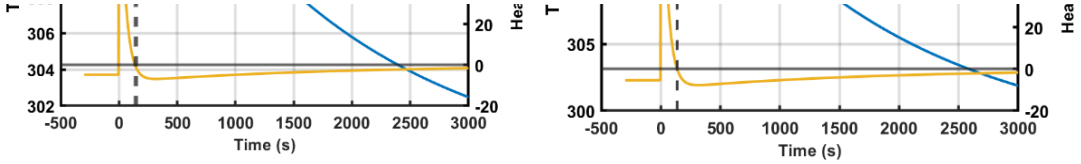

Acknowledgements

I extend my deepest gratitude to my advisor and mentor, Dr. Blake Stringer, for his unwavering support throughout this journey. I am also profoundly grateful for every opportunity that has shaped my path. I am incredibly lucky to have such wonderful people by my side, and I recognize that I would not be where I am today without their support. My heartfelt thanks go to my parents, siblings, and friends.

References

[1] Weidmann, E. P., Binner, T., and Reister, H. “Experimental and Numerical Investigations of Thermal Soak.” Society of Automotive Engineers (SAE) International Journal of Materials and Manufacturing, Vol. 1, No. 1, 2009, pp. 145–153. https://doi.org/10.4271/2008-01-0396.
[2] Agrawal, P., Sepka, S., Aliaga, J., Venkatapathy, E., and Samareh, J. "Thermal Soak Analysis of Earth Entry Vehicles". In 43rd AIAA Thermophysics Conference, No. AIAA 2012-3010, New Orleans, Louisiana, 2012. https://doi.org/10.2514/6.2012-3010.
[3] Harrison, J., Charles, D., Zenker, J., and Frank, E. "Using Multi-Physics System Simulation to Predict Battery Pack Thermal Performance and Risk of Thermal Runaway During EVTOL Aircraft Operations". Presented at the 2019 AIAA/IEEE (Institute of Electrical and Electronics Engineers) Electric Aircraft Technologies Symposium (EATS), 2019. https://doi.org/10.2514/6.2019-4406.
[4] Franchetta, M., Bancroft, T. G., and Suen, K. “Fast Transient Simulation of Vehicle Underhood in Heat Soak.” Society of Automotive Engineers (SAE) Transactions Journal of Passenger Cars: Mechanical Systems, Vol. 115, No. 6, 2006, pp. 1526–1538. https://doi.org/10.4271/2006-01-1606.
[5] Yuan, R., Sivasankaran, S., Dutta, N., Jansen, W., and Ebrahimi, K. “Numerical Investigation of Buoyancy-Driven Heat Transfer within Engine Bay Environment During Thermal Soak.” Applied Thermal Engineering, Vol. 164, 2020. https://doi.org/10.1016/j.applthermaleng.2019.114525.
[6] Kuehbacher, D., Kelleter, A., and Gerling, D. "An Improved Approach for Transient Thermal Modeling Using Lumped Parameter Networks". Presented at the 2013 International Electric Machines & Drives Conference, 2013.https://doi.org/ doi: 10.1109/IEMDC.2013.6556188.
[7] Shah, K., Drake, S. J., Wetz, D. A., Ostanek, J. K., Miller, S. P., Heinzel, J. M., and Jain, A. “An Experimentally Validated Transient Thermal Model for Cylindrical Li-Ion Cells.” Journal of Power Sources, Vol. 271, 2014, pp. 262–268. https://doi.org/10.1016/j.jpowsour.2014.07.118.
[8] Khaled, M., Elrab, M., Habchi, C., Al Shaer, A., Elmarakbi, A., Harambat, F., and Peerhossaini, H. “Analysis and Modeling of the Thermal Soak Phase of a Vehicle—Temperature and Heat Flux Measurements.” International Journal of Automotive Technology, Vol. 16, No. 2, 2015, pp. 221–229. https://doi.org/10.1007/s12239-015-0024-3.
[9] Chakravarthy, B., Cherukuri, H., and Wilhelm, R. “Prediction of Soakout Time Using Analytical Models.” Precision Engineering, Vol. 26, No. 1, 2002, pp. 15–23. https://doi.org/10.1016/S0141-6359(01)00089-7.
[10] Lee, K. “Numerical Prediction of Brake Fluid Temperature Rise During Braking and Heat Soaking.” Journal of Passenger Cars, Part 1, Vol. 108, No. 6, 1999, pp. 897–905. https://doi.org/10.4271/1999-01-0483.
[11] Edmonds, K., Stringer, D. B., and Valco, M. "Experimental Results of Transient Variable Speed Rotor Performance for Small UAS Propulsion Scalability". Presented at the Vertical Flight Society’s 76th Annual Forum & Technology Display, Virtual, 2020. https://doi.org/10.4050/F-0076-2020-16329.
[12] Stringer, D. B., Edmonds, K., and Valco, M. "A Prediction Model of Transient Variable Speed Rotor Performance for Small UAS Propulsion Scalability". Presented at the Vertical Flight Society’s 76th Annual Forum & Technology Display, Virtual, 2020. https://doi.org/10.4050/F-0076-2020-16330.
[13] Kaminski, D. A., and Jensen, M. K. "Introduction to Thermal and Fluids Engineering". John Wiley & Sons, 2017.

[14] Taylor, J., Zirckel, M., and Stringer, D. B. "Laboratory ‘Flight’ Demonstration of High-Endurance Flight Using Alternative Hybrid-Electric Sources". Presented at the AUVSI (Association for Uncrewed Vehicle Systems International) XPONENTIAL, Virtual, 2021.
[15] Edmonds, K., and Stringer, D. B. "Unmanned VTOL Propulsion Research – Scalability of Quadcopter Rotor-Motor Configurations Outside the SUAS Regime". Publication ARL-CR-0848. Army Research Laboratory, 2020.
[16] Laloui, L., and Loria, A. R. "Analysis and Design of Energy Geostructures: Theoretical Essentials and Practical Application". Academic Press, 2019.
[17] Pietrak, K., and Wiśniewski, T. S. “A Review of Models for Effective Thermal Conductivity of Composite Materials.” Journal of Power Technologies, Vol. 95, No. 1, 2015. https://doi.org/Open Access Journal ISN 2083-4187.
[18] Itoh, N., and Mimura, K. "Computational Fluid Dynamics (CFD) Analysis of Membrane Reactors: Simulation of Single-and Multi-Tube Palladium Membrane Reactors for Hydrogen Recovery from Cyclohexane". In Handbook of Membrane Reactors, Elsevier, 2013, pp. 464–495.

Toward Intent Estimation of Non-cooperative Space Objects

Student Researcher: Mark J. Wolf

Advisor: Dr. Mrinal Kumar

The Ohio State University
Department of Mechanical and Aerospace Engineering

Abstract
Space Domain Awareness (SDA) is a major area of interest due to the commercialization of space and the rapid acceleration in the number of objects launched into space. This rapid increase also means there are more actors in space, from governments to private companies, which leads to the need to understand and catalog space activity. However, simply maintaining a catalog of space objects is not enough. It is also necessary to estimate the intent of non-cooperative satellites to ensure the safety of space assets and allow for the best decisions to be made regarding asset maneuvers. This project uses a data-driven approach to understand the behavior of non-cooperative satellites and determine the reason these satellites perform orbital maneuvers. The initial work that has been performed relates to the characterization of perturbations experienced by satellites in orbit. A useful understanding of the perturbations experienced by a satellite is necessary for the accurate forecasting of a satellite's dynamics, thus estimation of its intent. The Adaptative Monte Carlo (AMC) platform developed at the Laboratory for Autonomy in Data-Driven and Complex Systems (LADDCS) is utilized in this project for uncertainty forecasting and parameter determination. Ultimately, this work will help satellite operators in determining future positioning of important assets in space and limiting orbital collisions leading to a decrease in orbital debris generation.

Project Objectives
The future forecasting of satellites' behavior and orbital elements is an important topic of research related to maintaining the safety of space assets. In this work, the Adaptive Monte Carlo (AMC) methodology is utilized for forecasting the sates of a dynamic system, specifically a satellite in orbit [1]. For the realistic modeling of a satellite's dynamics over time, Lagrange's Planetary equations can be used to define the change in orbital elements subject to perturbations. Lagrange's Planetary equations are listed in equations 1-6 [2].

$$\frac{da}{dt} = \frac{2}{n\sqrt{1-e^2}}[Se\sin f + T(1+e\cos f)] \tag{1}$$

$$\frac{de}{dt} = \frac{\sqrt{1-e^2}}{na}[S\sin f + T(\cos f + \cos E)] \tag{2}$$

$$\frac{di}{dt} = \frac{r\cos(\omega+f)}{na^2\sqrt{1-e^2}}W \tag{3}$$

$$\frac{d\Omega}{dt} = \frac{r\sin(\omega+f)}{na^2\sin i\sqrt{1-e^2}}W \tag{4}$$

$$\frac{d\omega}{dt} = \frac{\sqrt{1-e^2}}{nae}\left[-S\cos f + T\left(1+\frac{r}{p}\right)\sin f\right] - \frac{d\Omega}{dt}\cos i \tag{5}$$

$$\frac{dM}{dt} = n - \frac{1}{na}\left[\frac{2r}{a} - \frac{1-e^2}{e}\cos f\right]S - \frac{(1-e^2)}{nae}\left[1+\frac{r}{a(1-e^2)}\right]T\sin f \tag{6}$$

In the equations, a, e, i, Ω, ω, M, and f are the orbital elements (semi-major axis, eccentricity, inclination, longitude of ascending node, argument of perigee, mean anomaly, and true anomaly, respectively). The S, T, and W are the acceleration terms which require a definition of the perturbation acceleration.

To model the perturbation acceleration terms, this project implements the cannonball model for solar radiation pressure (SRP) perturbation, which is a simplified model that assumes the satellite of interest is a perfect sphere [3].

$$\vec{a}_{rad} = -\frac{A}{m}\frac{E}{c}\frac{A_{\oplus}^2}{\left|\vec{r} - \vec{r}_{\odot}\right|^2}\left(\frac{1}{4} + \frac{1}{9}C_d\right)\widehat{S} \tag{7}$$

In equation 7, A is the area, E is the solar flux, c is the speed of light, $A_{\oplus}$ is the astronomical unit, $\vec{r}$ is the satellite position vector, $\vec{r}_{\odot}$ is the Sun position vector, C_d is the diffuse reflection coefficient, and $\widehat{S}$ is the Sun-Satellite position unit vector.

This work assumes that there is known historical measurement data available with some uncertainty, however the area-to-mass ratio (AMR) of the satellite is not known, but an initial guess can be made. Then, using the measurements and the known dynamics of the SRP perturbation, the AMR can be estimated by using a predetermined gain value and comparing the propagation data for the AMC simulation results with the measurement data. The overall problem statement for this project was: can a Monte Carlo simulation be used to estimate the AMR of a space object?

Methods

The AMC platform is utilized in this work to provide propagation estimates for a given time interval when measurement data is available. These estimates are calculated using random samples from probability density functions (pdfs), which are required inputs to the simulation in the form of the initial condition uncertainty. The AMC approach improves upon the traditional Monte Carlo approach in that the accuracy of the simulation results for the specified quantities of interest (QoIs) can be bounded by upper and lower values. The QoIs are the states of the dynamic system that are selected for the evaluation of the accuracy of the simulation. The accuracy guarantee is accomplished through additional sampling of the pdfs to increase the accuracy or by pausing particles to reduce the accuracy to maintain computational efficiency.

In this research, the product of the difference between the known measurement data and the AMC simulation results and a predetermined gain value is used to define a correction factor for the initial guess of the AMR. A new correction factor is calculated at each time step to iteratively improve upon the estimate for the AMR, which increases the accuracy of the AMC simulation. Once the simulation has converged to a useful estimate of the AMR, then the AMC platform can be used to propagate the satellite's orbit for future time intervals and provide information necessary for future decision making on the satellite's position and maneuvering requirements.

Results and Discussion

The initial results from this work are presented in Figures 1-4 and the initial orbit for these results are reported in Table 1. The measurement data used in these results was artificial data generated from a

numerical simulation with a known AMR. These results show that eccentricity as the QoI has poor convergence behavior, however the semi-major axis appears to perform well and provide a useful estimate of the true AMR by the end of the simulation. These gathered results show that there is potential for this approach to provide useful estimation results for the AMR. However, future work will be done to fully characterize the convergence behavior of all the possible QoIs, along with studying how the predetermined gain value affects the estimation results. Additionally, future work will implement real satellite measurement data to show the methods effectiveness in a real propagation scenario.

Table 1. Simulation Initial Conditions

Initial Orbit	
Semi-Major Axis	42,164 km
Eccentricity	0.1
Inclination	10°
Longitude of Ascending Node	0.1°
Argument of Perigee	0.1°
Mean Anomaly	0°
Diffuse Reflection Coefficient	
$C_d = 0.035$	

Figures

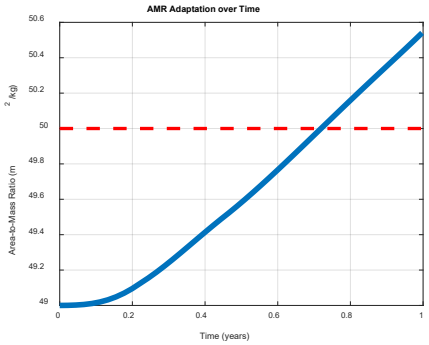

Figure *1*. QoI is eccentricity with a gain of 25

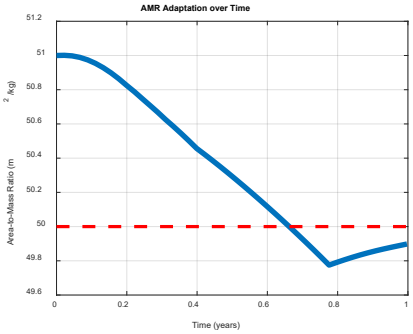

Figure *2*. QoI is eccentricity with a gain of 25

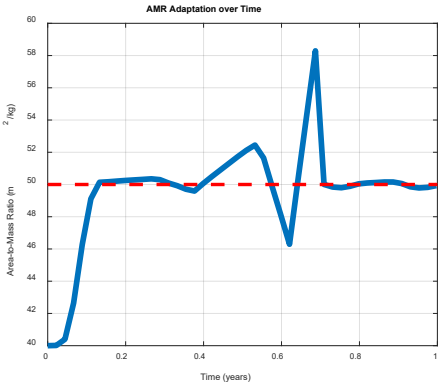

Figure *3*. QoI is Semi-Major Axis with a gain of -0.0025

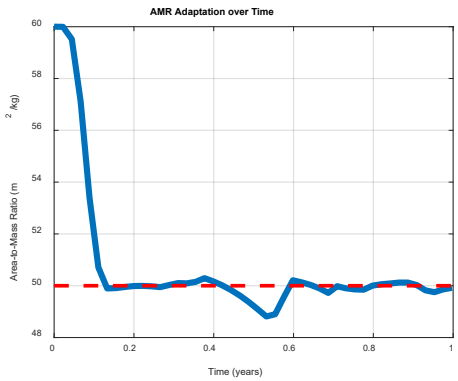

Figure *4*. QoI is Semi-Major Axis with a gain of -0.0025

Acknowledgments
The author thanks Dr. Michael Yakes (Program Officer - Physics of Remote Sensing Program) for supporting this work. This work is supported by the Air Force Office of Scientific Research under Grant No. FA9550-20-1-0083. The author acknowledges his advisor Dr. Mrinal Kumar and his lab mates, specifically Rondale Balo and Sriram Narayanan. The author thanks the Ohio Space Grant Consortium for funding this research. Finally, the author would like to thank his friends, family, and fiancée Vivien for their support and encouragement.

References
[1] A. W. Vanfossen and M. Kumar, "Efficient Adaptive Monte Carlo Uncertainty Forecasting for High Dimensional Nonlinear Dynamic Systems," IEEE Access, Vol. 11, 2023, pp. 12119–12138, 10.1109/ACCESS.2023.3241753.

[2] S. N. Paul, Orbital Perturbations for Space Situational Awareness. PhD thesis, Purdue University, 2020.

[3] C. Fruh, T. M. Kelecy, and M. K. Jah, "Coupled orbit-attitude dynamics of high area-to-mass ratio ¨ (HAMR) objects: influence of solar radiation pressure, Earth's shadow and the visibility in light curves," Celest Mech Dyn Astr, Vol. 117, 2013, p. 385–404, 10.1007/s10569-013-9516-5.

Foreign Object Ingestion Into Composite Fans

Student Researcher: Mitchell Wong

Advisor: Dr. Kiran D'Souza

The Ohio State University

Mechanical and Aerospace Engineering

Abstract

Uncrewed aircraft systems (UASs) have become increasingly popular due to their ease of accessibility to the public and affordable prices. This has increased the risk of a midair collision with a commercial aircraft which has the potential to impart more damage than a soft body impact from a bird. Birds are often modeled to be 70% water [1] while a UAS is considered a hard body with the motor, camera, and battery being identified as key components with them being the hardest. This has led to the development of a UAS model validated for various impact conditions to research the effects of these hard body impacts compared to a soft body impact. First, the DJI Phantom 3 was chosen due to its popularity and then it was tested and validated for static and blunt tests [2]. Second, the UAS was experimentally and computationally validated in the finite element software LS-DYNA for high-speed slicing impacts representing an engine ingestion [3, 4]. Finally, simulations were run on LS-DYNA of a commercial sized generic fan blade impacting a UAS and a bird with the results showing that a UAS will impart more damage than a soft body of a bird of similar size [5]. This work extends on this work using the same generic fan blade design but looks at having a composite fan blade material compared to titanium fan blades. Using a previously validated carbon fiber reinforced fiber material in software LS-DYNA, two different fan blade models were created. One with a full composite fan and another with a titanium leading edge and were subjected to impacts from both hard and soft body impacts. These results were then compared to previous research on impacts onto titanium fan blades.

Project Objectives

The objective of this project was to validate a composite material model previously published to use in a generic commercial sized fan blade model to study foreign object ingestions. Two different projectiles will be considered for the ingestion events. One is a soft body of a bird and the second is a hard body of a UAS. These projectiles would then impact two different fan blade designs of a full composite fan blade design and composite fan blade with a titanium leading edge.

Methods

The material chosen for this study is a carbon fiber reinforced polymer (CFRP) T700 carbon fiber/2510 epoxy prepreg that has been extensively used for general aviation primary structures that has been well documented in the FAA-sponsored AGATE Program (Advanced General Aviation Transport Experiment) [6, 7]. This material was used in a previous study looking at a sinusoidal crush test using the finite element software LS-DYNA where they successfully recreated the crushing behavior using shell elements using MAT_054. To use this material model for this study these results had to be revalidated using our own models. The first step was to conduct a one element test to ensure that the material properties were correctly defined in both the tensile, compressive, and shear directions. Second, a shell model of the sinusoidal crush test was made based on the paper seen in Figure 1. The material properties and initial peak loads of the crush test were looked at to validate that the model was behaving the same as the papers. Finally, a thick shell model was made based on the paper to see how the different element formulation would affect the model behavior. Thick shells were chosen to be implemented into the final

fan blade design due to thick shell elements being formulated like a solid element meaning it has a 3D stress state compared to a 2D stress state of a shell element. Thick shell elements also have the advantage in solid elements when modeling composites as integration points can be added to account for the different number of plies and orientation of the composite layup.

Once the material model is validated, it will be implemented into a generic fan blade model that was previously developed to study hard body impacts of an UAS [5]. Two different fan blades will be considered with one having a full composite fan blade and the other having a titanium leading edge. The generic fan blade model is created by applying a prestress on a two-sector model using cyclic boundary conditions as seen in Figure 2. Then, the two-sector model can then be rotated and combined to create a full fan blade model consisting of twenty-four blades.

With the full fan blade model completed, various ingestion events will then be tested. Impacts from both a hard body of a UAS seen in Figure 3 and a soft body of a bird seen in Figure 4 will be tested at various phases of flight, locations, and orientations. These results will then be compared to see how adding a titanium leading edge to protect the composite fan blades behaves during an engine ingestion event as well as comparing to previous results from impacts on titanium fan blades.

Results and Discussion

This study is still currently ongoing with the material model still being validated and implemented into the two-sector fan blade model. Once this is complete, the full fan model will be developed through the steps described above and the simulations can start. Data will be collected on the effective plastic strain, center of mass of the fan blades, energies, and kinematics of the ingestion events. From these results, the soft body impact of a bird and hard body impact of a UAS on a composite fan blade, composite fan blade with a titanium leading edge, and a full titanium fan blade can be compared.

Figures

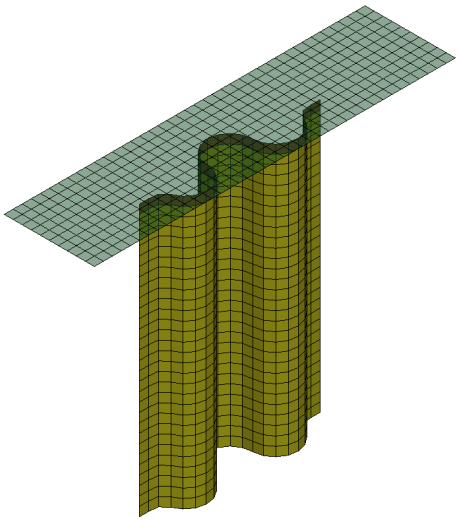

Figure 1: Bird modelled with cylinder with hemispherical ends

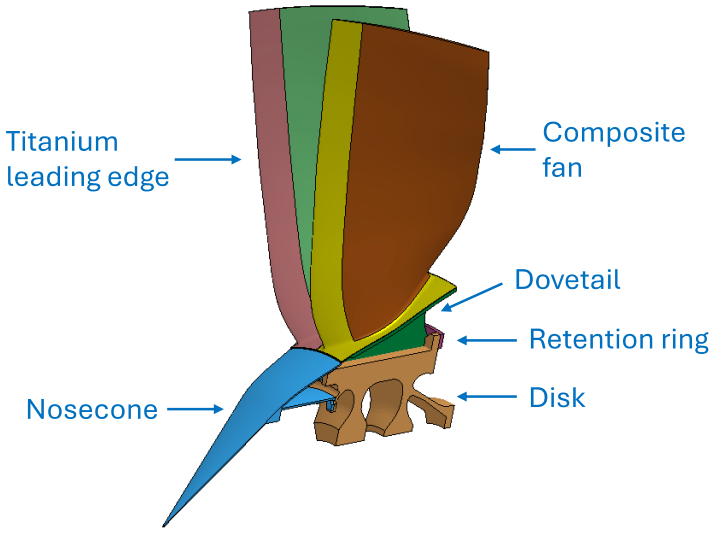

Figure 2: Uncrewed aircraft system of a DJI Phantom 3

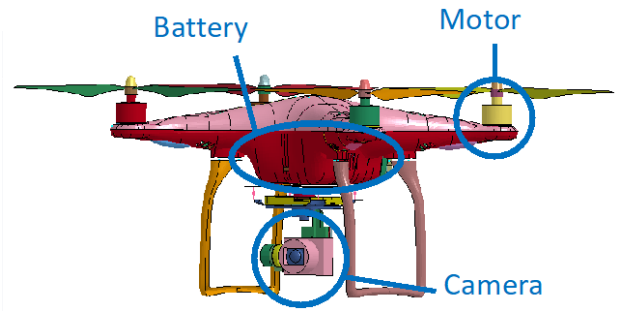

Figure 3: Two-sector composite fan blade model with titanium leading edge

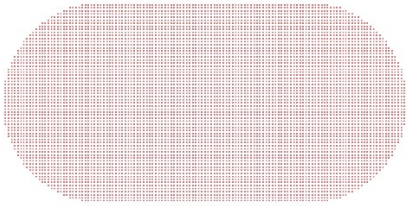

Figure 4: Shell model of sinusoidal crush

Acknowledgments

I would like to thank my advisor Dr. Kiran D'Souza for giving me this opportunity and guiding me through this research process. I would also like to thank Dushyanth Sirivolu a postdoc in my lab who gave his expertise on dynamic nonlinear impacts and modeling techniques.

References

[1] Wilbeck, J., and Rand, J.,"The Development of a Substitute Bird Model," J. Eng. Power 103, 1981.

[2] Olivares, G., Monteros, J., Baldridge, R., Zinzuwadia, C., Gomez, L., "Volume II - UAS Airborne Collision Severity Evaluation - Quadcopter," FAA Report, 2017.

[3] Olivares, G., Gomez, L., and Ly, H., "Annex B to task A17: NIAR/WSU sUAS Numerical Model Validation (Component and Full-Scale Level) for Engine Ingestion Analysis," FAA Report, 2022.

[4] Duling, C., Zweiner, M., and Arteburn, D., "Annex C to Task A17: UAH High Speed Impacts of Full sUAS and Components with Angled Plates," FAA Report, 2022.

[5] D'Souza, K., Sirivolu D., Wong, M., and Kurstak, E., "Annex A to Task A17: OSU Representative Fan Model and UAS Ingestion Studies," FAA Report, 2022.

[6] Feraboli, P., Wade, B., Deleo, F., Rassaian, M., Higgins, M., and Byar, A., "LS-DYNA MAT54 Modeling of the Axial Crushing of a Composite Tape Sinusoidal Specimen," ELSEVIER, 2011.

[7] Tomblin, J., Sherraden, J., Seneviratne, W., and Raju, K.S., "A-Basis and B-Basis Design Allowables for Epoxy-Based Prepreg TORAY T700GC-12K-31E/#2510 Unidirectional Tape," AGATE-WP3.3-033051-132; November 2002.

Scholars

Efficient Early Planetary Ejecta Emplacement in the Main Asteroid Belt Due to Mars

Student Researcher: Sanskruti Admane

Advisor: Dr. Wayne Schlingman

The Ohio State University
Department of Astronomy/ Astronomy Major

Abstract
The giant impact era includes the Moon-forming impact but the overall scope and severity of this phase across the terrestrial planets is unknown. These violent collisions produce ejecta, some of which escape onto heliocentric orbits. Using astrophysical N-body simulations, we show that a remnant fraction of this debris likely survives from the giant impact era of planet formation to today. The capture of impact ejecta onto long-term stable orbits in the main asteroid belt is enabled by gravitational interactions with Mars. Even when considering very different terrestrial planet formation scenarios, impact debris is stranded in the asteroid belt. We study the amount of debris remaining in the asteroid belt after planet formation.

Project Objectives
Our goals are to investigate how much of this debris may survive from the era of planet formation in the asteroid belt today and how the final arrangement of planets impacts these results.

Methods
In the Circular Jupiter and Saturn (CJS) scenario, the giant planets are on compact, circular, and nearly in-plane orbits primed for a Nice model-like giant planet instability following Raymond et al. (2009). The circular orbits of the giant planets in CJS ensure that the stirring they create is at a minimum. Giant planet stirring excites the relative velocities of planetary embryos and increases their collisional velocities. The semimajor axes were 5.45 AU and 8.18 AU respectively, with inclinations 0.00 and 0.5 respectively. In the Eccentric Jupiter and Saturn (EJS) scenario, the giant planets effectively start on their modern day orbits. The higher eccentricities of the giant planets in EJS create a higher amount of stirring than in CJS. Jupiter and Saturn were given parameters following Raymond et. al 2009. In the Grand Tack scenario, Jupiter and Saturn have a specific migration pattern during the proto-planetary phase (Walsh et al. 2011). This truncates the disc of planetesimals and planetary embryos at 1 AU. In Grand Tack, the giant planets enter and exit the terrestrial disk, so stirring is at a maximum. Thus, the giant impacts in these simulations are the most violent. Our simulations follow those detailed by Jacobson and Morbidelli (2014).
Our simulations were run using the gravitational N-body code SYMBA (Duncan et al. 1998), modified to incorporate the effects of the collisional dynamics detailed in Leinhardt and Stewart (2011). The symplectic integrator tracks the movement of each particle, and follows embryo-embryo interactions. The code is modified to model the outcomes of debris-producing collisions using an algorithm that is a function of the giant impact's mass ratio, impact angle and velocity (Leinhardt and Stewart 2011). Collisions considering imperfect accretion were implemented relatively recently, and initially considered two collision types. Chambers (2013) improved simulations further with the implementation of collisional fragmentation, but these did not produce significantly different results. To make the collision outcomes in our simulations more realistic, we consider nine types of outcomes, including debris production and removal.

Results and Discussion

We expect only a small portion of the dynamical space to contain debris - however, it is distributed throughout the region, as seen in the figure below and on the left. Given the figure, it is clear that debris particles are emplaced, but not a lot of mass is actually emplaced in the stable region of the Main Asteroid Belt (< 1% of the debris produced).

We also look at successful simulations, which are those producing two Earth/Venus like planets, and one Mars like planet. We do not strictly differentiate between Earth and Venus like planets because of the difficulty in specifying mass and orbit boundaries (Jacobson and Morbidelli 2014). The apocenter and pericenter establish stability conditions for each analog planet. We found that giant impacts can affect short term stability of debris particles. The Mars embryo may interact with MBA debris, which leads to the particle pericenter being lifted into the asteroid belt. This is especially seen in the figure below and on the right, where the debris particle interacts heavily with Mars and then leaves the planet forming region. Additionally, the timing of last giant impact affects the amount of mass emplaced and long term stability, where later giant impacts lead to more instability in the trajectories of debris particles. These particles are more likely to be removed from the asteroid belt.

Figures/Charts

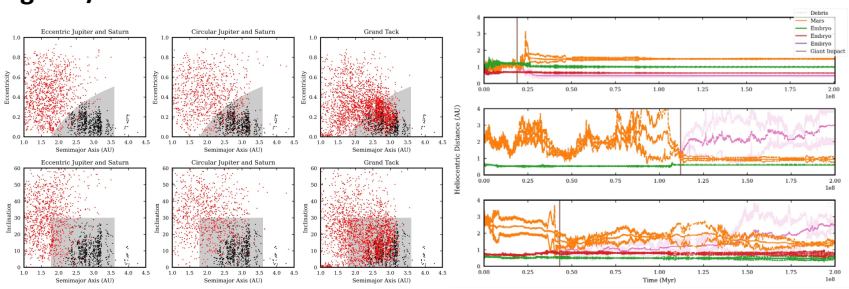

Acknowledgments

Thank you to my advisors, Dr. Wayne Schlingman and Dr. Seth Jacobson, and the ACRES REU (2022).

References

J. Chambers. Late-stage planetary accretion including hit-and-run collisions and fragmentation.

M. J. Duncan, H. F. Levison, and M. H. Lee. A Multiple Time Step Symplectic Algorithm for Integrating Close Encounters.

S. A. Jacobson and A. Morbidelli. Lunar and terrestrial planet formation in the grand tack scenario.

Z. M. Leinhardt and D. C. Richardson. Planetesimals to Protoplanets. I. Effect of Fragmentation on Terrestrial Planet Formation.

Z.M. Leinhardt and S.T. Stewart. COLLISIONS BETWEEN GRAVITY-DOMINATED BODIES. i. OUTCOME REGIMES AND SCALING LAWS.

S. N. Raymond, D. P. O'Brien, A. Morbidelli, and N. A. Kaib. Building the terrestrial planets: Constrained accretion in the inner solar system.

K. J. Walsh, A. Morbidelli, S. N. Raymond, D. P. O'Brien, and A. M. Mandell. A low mass for Mars from Jupiter's early gas-driven migration.

Digital Twin for Manufacturing Purposes

Student Researcher: Rachael Ballentine

Advisor: Dr. Subhashini Ganapathy

Wright State University
Department of Mechanical and Materials Engineering

Abstract
Industry 4.0 and Smart Manufacturing are revolutionizing the field of manufacturing. A push to rethink programming of manufacturing robots using Internet of Things data has come with Industry 4.0, in particular developing and utilizing the digital twin. The concept of a digital twin is a fairly recent development; today, a digital twin can be defined by three significant features: a physical model, a virtual model, and a bidirectional link for data transfer between the two. In this project, the topic of digital twins was explored by examining the history and development of the digital twin, its structure and utilization of Industry 4.0 concepts, and current applications in manufacturing environments. A Yaskawa GP8 robotic arm and the accompanying MotoSim simulation software was used to support this research.

Project Objectives
Two goals were set for this project. The first goal was to conduct a literature review on the concepts behind a digital twin; the second goal was to create a digital model of a robotics cart and accompanying Yaskawa GP-8 robotic arm purchased by Wright State University in 2023.

Methods
University library resources and web search engines were used to gather previous research documents for review. Yaskawa MotoSim software and SolidWorks 3D modeling software were used to create the robot cart model.

Results and Discussion
In 1970, NASA made history when they successfully brought the three astronauts aboard the Apollo 13 home after a catastrophic failure in one of the service module oxygen tanks. Although the term 'digital twin' would not be coined until many years later, the way NASA utilized current data from the spacecraft to modify their 15 training simulators and formulate a return strategy for the Apollo 13 was foreshadowing of today's digital twin concepts [1]. In 2002, the first version of the digital twin was introduced by Michael Grieves at the University of Michigan, in the form of a 'Mirrored Spaces Model' for use in Product Lifecyle Management (PLM) [2], and in 2010, the term 'Digital Twin' was coined and further characterized in NASA's 2010 Technology Roadmap.

The digital twin serves on the forefront of Cyber-Physical System (CPS) integration. One of the identifying characteristics of the digital twin is the live data exchange between the virtual and physical models, where decisions made within the virtual model can be used to change the physical model. To attain this, the digital twin takes advantage of Industry 4.0 technologies such as the Internet of Things (IoT), cloud computing, big data, Artificial Intelligence (AI), and machine learning [3], and includes digital engineering concepts such as Computer Aided Modeling (CAD).

Digital twins can be applied in many different fields and for a variety of purposes. DT can be used for product prototyping, as different model versions can be tested virtually without having to manufacture or destroy a physical prototype and can in turn reduce the amount of time needed for this testing [4]. Product testing for a new product can be done using DT technology, but will still require some physical validation, albeit less than if the entirety of the prototype testing was carried out in the traditional way. Variations on existing products have the potential to be completely prototyped and validated within the DT, if previous products also have DTs that historical data can be pulled from [5].

In 2023, WSU purchased a GP-8 STEM robot cart, intending to use it for STEM outreaches and micro-credential courses. The cart came with several preprogrammed jobs, but it was not clear whether these jobs accounted for

the reduced operation envelope due to the plexiglass shield behind the robot arm. For this reason, a digital model of the robot was desired to run jobs digitally before attempting them with the physical robot.

To create the model, measurements of the physical cart were taken, and a CAD model of the cart was reverse engineered using SolidWorks software. The cart was made as a single-part model rather than an assembly for simplicity. The model was imported into Yaskawa MotoSim software, which included a preprogrammed model of the YRC 1000micro controller used in the GP-8. The cart was reoriented to the correct position and the controller was equipped with tooling matching the physical cart, which was imported from MotoSim's model library.

Figures/Charts

Fig. 1. Physical robot cart

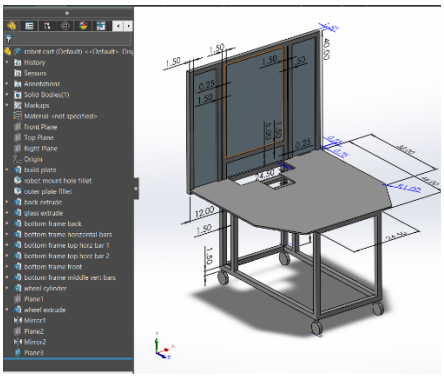

Fig. 2. CAD model of robot cart

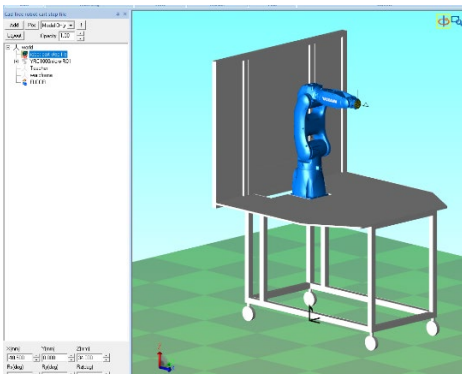

Fig. 3. Completed MotoSim model

Acknowledgments

I would like to thank Dr. Subhashini Ganapathy for advising this project, and Dr. Mitch Wolff for presenting the opportunity to apply for the OSGC scholarship. I would also like to give sincere thanks to Dr. Bob Myers of the Industrial and Systems Engineering department for his guidance and advice throughout the research process.

References

[1] S. Ferguson, "Apollo 13: the first digital twin - SimCenter," *Simcenter*, Mar. 11, 2021. https://blogs.sw.siemens.com/simcenter/apollo-13-the-first-digital-twin/

[2] F. Tao, H. Zhang, A. Liu, and A. Y. C. Nee, "Digital twin in industry: State-of-the-Art," *IEEE Transactions on Industrial Informatics*, vol. 15, no. 4, pp. 2405–2415, Apr. 2019, doi: 10.1109/tii.2018.2873186.

[3] M. Grieves and J. Vickers, "Digital Twin: Mitigating Unpredictable, Undesirable Emergent Behavior in Complex Systems," in *Transdisciplinary Perspectives on Complex Systems*, F.-J. Kahlen, S. Flumerfelt, and A. Alves, Eds. Springer International Publishing, 2017, pp. 85–113. doi: 10.1007/978-3-319-38756-7.

[4] M. Singh, E. Fuenmayor, E. P. Hinchy, Y. Qiao, N. Murray, and D. M. Devine, "Digital Twin: origin to future," *Applied System Innovation*, vol. 4, no. 2, p. 36, May 2021, doi: 10.3390/asi4020036.

[5] S. Huang, G. Wang, L. Dong, and Y. Yan, "Toward digital validation for rapid product development based on digital twin: a framework," *The International Journal of Advanced Manufacturing Technology/International Journal, Advanced Manufacturing Technology*, vol. 119, no. 3–4, pp. 2509–2523, Jan. 2022, doi: 10.1007/s00170-021-08475-4.

Photovoltaic Solar Energy Collection Impacts on Ecology

Student Researcher: Lauren D. Bower

Advisor: Rydge Mulford

University of Dayton
Department of Mechanical Engineering

Abstract
Understanding the effects of renewable and clean energy systems on their surrounding ecology is essential to determining the true level of sustainability of these energy solutions. With the rise in popularity of solar prairies, the effects of this technology on insect and vegetation life in the area must be explored to assess any potential harm from the technology on the environment. The main concern researched in this project was photovoltaic solar panels' adjustment to temperatures of the prairies they reside in. This research determined patterns of temperature change caused by solar panels through tracking multiple locations' temperatures throughout a solar prairie.
During the study, the team found evidence of temperature change caused by the difference in shading from the panels in certain locations. The team also found evidence of heat convection occurring through the metal solar panels throughout the day. This study focused on multiple aspects of shading and heat convection, considering different times of day, weather conditions, and seasons. The nature of photovoltaic solar research requires multiple seasons and years of data to ensure the most accurate and representative results. Therefore, this research will be continued to build further confidence and gain further depth of understanding of the results.

Project Objective
The purpose of this study is to determine the temperature differences at different sections of a solar prairie located in Dayton, OH. Once collected, the team will pass the temperature data on to the university's ecology department for comparison with data on the temperature limitations of local vegetation and animals. The comparison will allow the ecology department to determine how the solar prairies might affect local species.

Methodology
The study used Thermochron iButtons to explore the thermal effects of a solar prairie on local insects using temperature monitoring in Dayton, Ohio. iButtons were carefully placed from row 7 to row 35 in the solar prairie, with three iButtons per row: one in the aisle and another underneath solar panels to assess different shading conditions' effects on insects, and the last in a buffer zone as a control. These placements aim to thoroughly capture temperature variations significant to the study. Data was recorded hourly, reflecting the solar panels' impact over the day.

Results
Upon completion of this segment of the solar ecology research, the team noticed evidence of temperature differences due to potential shading patterns and heat convection from the metal solar panels. Figure 1 demonstrates the extreme temperatures present under the panels throughout the day and the slightly higher temperatures in the buffer brush surrounding the solar prairie than in the aisles between panels. The temperatures under the panels are explained by convection which is also demonstrated in Figure 3 which shows that under the panels is higher during the day and cooler at night as well as in Figure 4 which demonstrates that at 5pm under the panels is consistently highest in temperature. The higher temperatures in the buffer area than in the aisles in Figure 1 and the temperature spikes in certain areas at different parts of the day demonstrated in Figure 2 appears to be explainable due to differences in shading patterns based on positioning. This is noticed because the overall temperatures are lower and the spikes in temperature even out on days that are considered cloudy in Figure 2d.

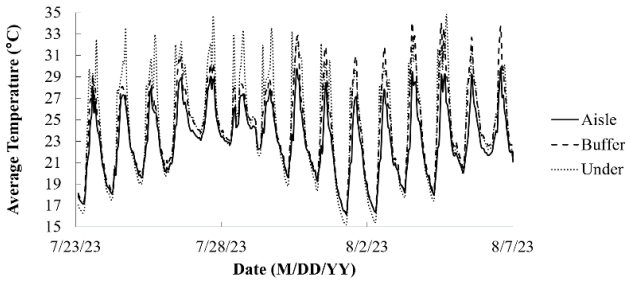

Figure 1: Comparison of Average Temperatures (7/23/23 – 8/06/23)

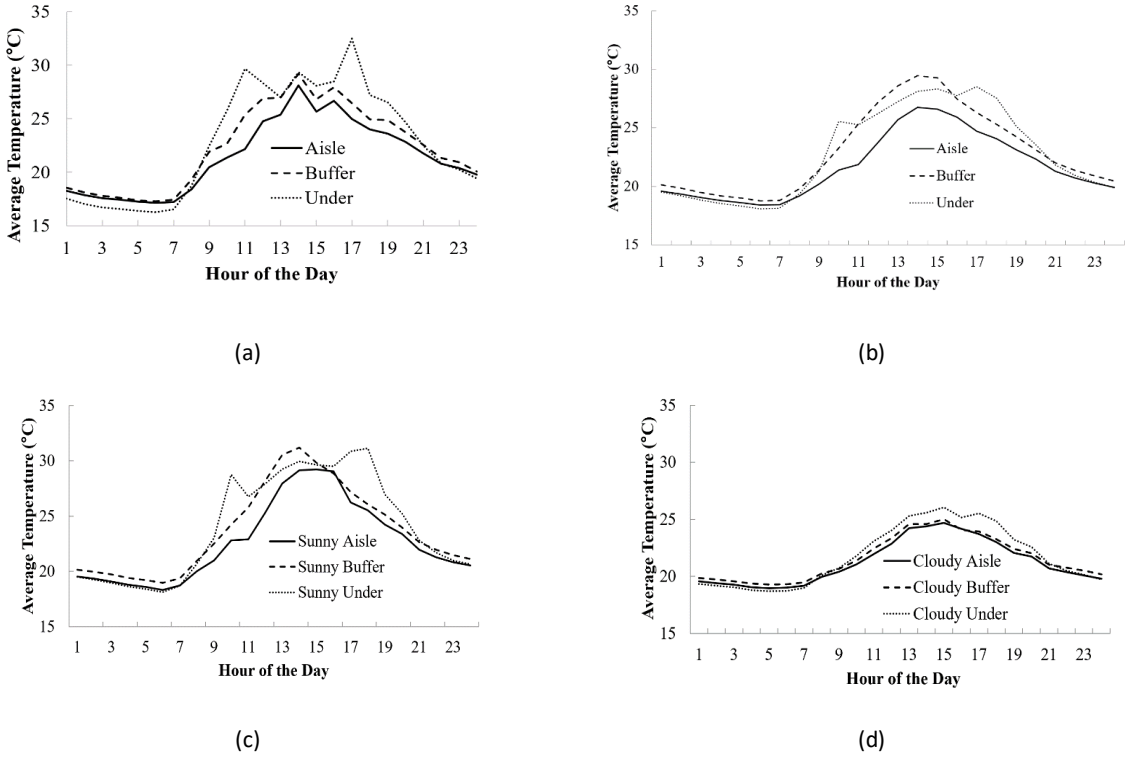

Figure 2 – (a) Aisle Average, Buffer Average, and Under Average (7/23/23) (b) All Days Average 24 Hours (c) Sunny Day Average (6/18/23 – 7/22/23) (d) Cloudy Day Average (6/18/23 – 7/22/23)

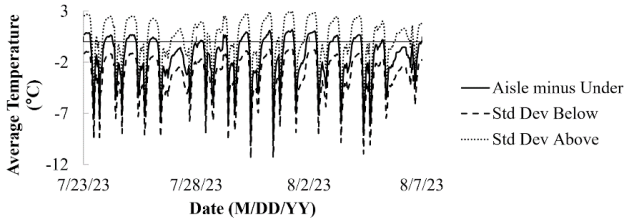

Figure 3: Aisle minus Under Temperature (7/23/23 – 8/6/23)

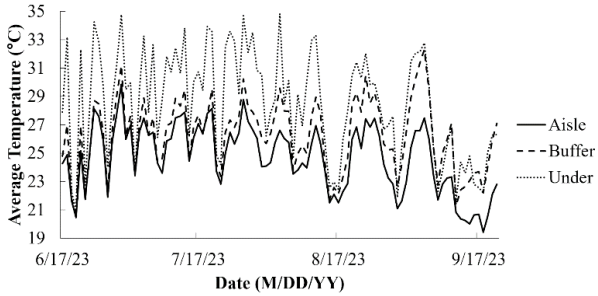

Figure 4: Average Temperature Daily at 5pm Throughout the Summer

Acknowledgements and References

The author would like to thank Dr. Rydge Mulford, her research advisor, for his guidance and Jean Nash, her research partner, for her assistance throughout the study. She would also like to thank Dr. Chelse Prather for her guidance on ecology and input on sensor placement.

[1] Vervloesem, J.; Marcheggiani, E.; Choudhury, M.A.M.; Muys, B. Effects of Photovoltaic Solar Farms on Microclimate and Vegetation Diversity. *Sustainability* **2022**, *14*, 7493. https://doi.org/10.3390/su14127493

CFD Modeling of the Magnus Effect

Student Researcher: Grant Brautigam

Advisor: Dr. Jed Marquart

Ohio Northern University
Mechanical Engineering

Abstract
The magnus effect is a classic aerodynamic phenomenon that describes how spinning objects create lift. Computational fluid dynamics (CFD) is a faster and more cost-effective method to model fluid behavior. Using CFD the magnus effect was modeled on a cylinder in cross flow. The results were then compared with data collected from a wind tunnel. A steeper trend was noticed with the CFD results, however the overall appearance of the data matched. The velocity profiles also represented expected behavior with the flow behind the cylinder dropping at higher rotation rates.

Project Objectives
It was desired to know if the computational fluid dynamics (CFD) methods used at Ohio Northern University (ONU) can accurately represent the magnus effect. To accomplish this a cylinder in cross flow was examined. Validating the CFD methods for the simple case of the cylinder could open the opportunity to investigating rotating cross sections that are not circular.

Methods
A 2D analysis of the cylinder was performed. A grid was generated using Fidelity Pointwise. To accurately represent the flow around the cylinder the flow grid was split into a far-field block and a wake block. The wake block had an increased grid density to help with calculating the higher gradients in the flow around the cylinder. T-rex cells were placed around the cylinder to capture the boundary layer flow. The flow velocity was chosen to give the system a Reynolds number of 82000. This was done so that the results could be compared to the top line in figure 1. Six cases of increasing non-dimensional spin rate were considered. Equation 1 gives the non-dimensional spin rate, R,

$$R = \frac{\omega d}{2V_\infty} \tag{1}$$

where d is the diameter of the cylinder, ω is the rotation rate of the cylinder and V_∞ is the free stream velocity. All four sides of the far-field block were assigned the modified riemann invariants boundary condition. The edge of the cylinder was assigned the general no slip boundary condition. Within this condition the rotation rate of the edge was specified. Cobalt was used as the grid solver. All the solutions were run to convergence in the same number of iterations and CFL drops.

Results and Discussion
Figure 2 shows the coefficient of lift at different non-dimensional spin rates as reported by Cobalt. A similar trend was shown in the data when comparing it with figure 1. However, the trend is steeper and increasing more rapidly. This could be due to the solution only being in two dimensions or that the CFD environment is creating more perfect flow than what was seen in the wind tunnel. Figures 3 and 4 show

the velocity profile over the cylinder with R being set to zero and one respectively. Once the rotation was interduce the wake behind the cylinder dipped down which was expected.

Figures/Charts

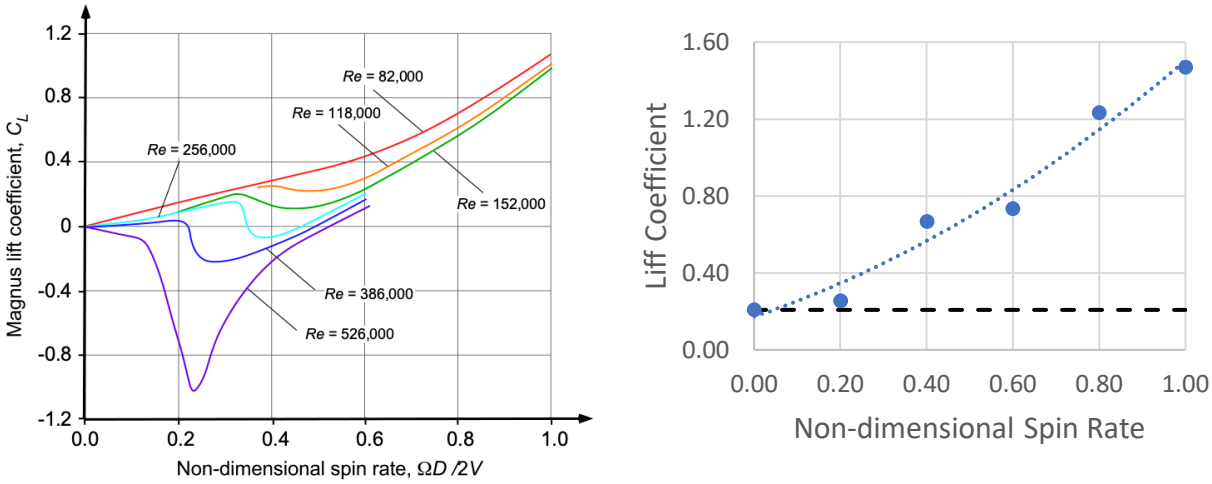

Figure 1 [1] (left): lift coefficient for different spin rates and Reynolds numbers on a cylinder in crossflow determined by wind tunnel testing

Figure 2 (right): lift coefficient for different spin rates on a cylinder in crossflow determined by CFD

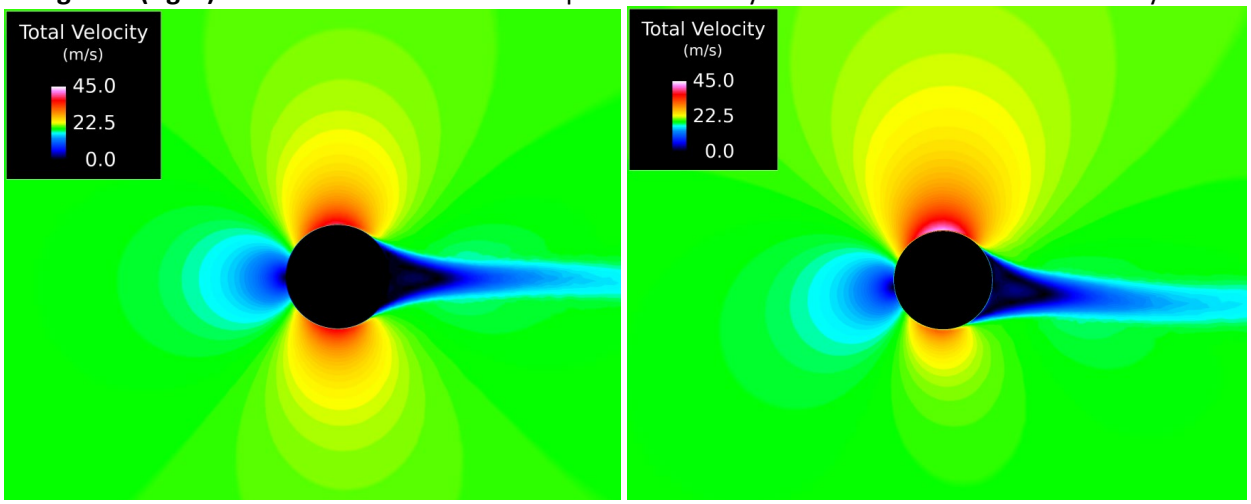

Figure 3 (left): Total velocity profile for rotation rate being set to 0
Figure 4 (right): Total velocity profile for rotation rate being set to 1

Acknowledgments
Thank you to Dr. Marquart for helping guide me through this research project and to OSGC for giving me the opportunity to perform this research.

References

1. J. Gordon Leishman, *Introduction to Aerospace Flight Vehicles*, 2023

Evaluation of Wear and Friction Properties of High Temperature Polymer Blends

Student Researcher: Megan Brockway

Advisor: Dr. Mark Sidebottom

Miami University
Mechanical Engineering

Abstract
Polyimides (PI) are known for their moderate wear (1-8 × 10^{-6} mm^3/Nm), and high upper use temperature (260 °C), and outstanding mechanical and insulating properties [1]. Polytetrafluoroethylene (PTFE) is a linear carbon-fluorine polymer, which has a low coefficient of friction (0.05-0.10) and high upper use temperature (260 °C) but exhibits poor wear (K∼10^{-4} to 10^{-3} mm^3/Nm), and abrasion resistance [2]. Prior studies on PI-PTFE blends have shown excellent friction and wear performance but manufacturing of this blend requires excellent dispersion of PI and PTFE powders before processing begins [1]. Without proper dispersion, this material loses significant mechanical properties and wear resistance. An alternative manufacturing process was used to develop an alternate blend of PI-PTFE. Friction and wear properties new method PI-PTFE will be compared to existing commercially available polymers and polymer composites.

Project Objectives
This project aims to determine if manufacturing processes of PI-PTFE Blends affect its tribological properties (wear rate and coefficient of friction).

Methods
A linear reciprocator flat-on-flat tribometer was used to measure wear rate and the coefficient of friction. Samples were prepared from stock to a uniform size, polished on one face with 400 grit silicon carbide grinding paper, sonicated in methanol to remove contaminants, and measured for reference during testing. The samples were tested with 250 N applied force, 25 mm long sliding stroke, 50 mm/s sliding velocity, and in lab-controlled air (30% RH and 22-25 ^{o}C).

Results and Discussion
Table 1 provides a description for composition and manufacturing processes of the samples. Samples F & G failed to complete the total sliding distance of the rest of the samples due to excessive wear. Sample F ran for 2 km; CoF and wear rate are provided for only that distance. Sample G only ran for 0.5 km, so no experimental values for CoF and K were provided.
Figure 2 shows the steady-state wear rates of each sample. Lower wear rate values are more desirable; values larger than 10^{-4} mm^3/Nm are poor, 10^{-6} mm^3/Nm are acceptable, and 10^{-8} mm^3/Nm are considered excellent. Samples D (3.79x10^{-8} mm^3/Nm), E (5.26x10^{-8} mm^3/Nm), H (2.52x10^{-8} mm^3/Nm), and J (2.09x10^{-8} mm^3/Nm) demonstrated excellent wear rates. Samples C (2.35x10^{-6} mm^3/Nm) and M (2.76x10^{-6} mm^3/Nm) demonstrated acceptable wear rates. Samples F (3.66x10^{-4} mm^3/Nm) and G demonstrated poor wear rates.
Figure 3 shows the experimentally determined average CoF for each sample. Samples E (0.208) and H (0.212) exhibit the highest coefficient of friction. The rest of the samples are within 0.05 of each other, with sample F (0.132) demonstrating the lowest CoF. Generally, a lower CoF is more desirable. Note that while samples E and H are among the least desirable CoF, they demonstrated excellent wear rate (2.5-

5.3 x10^{-8} mm3/Nm). Similarly, sample F has the most desirable CoF but demonstrated the highest wear rate.

Figures/Charts

Table 1: *Summary of samples tested and manufacturing description*

Sample ID	Sample Name	Manufacturing Description
C	*PTFE-PI Blend 1*	*Powders dry mixed and sintered, Novel Method 1*
D	*Commercial Blend 1*	*Unknown*
E	*Commercial Blend 2*	*Unknown*
F	*Unfilled PTFE 1*	*Cold Pressed & Sintered*
G	*Unfilled PTFE 2*	*Unknown*
H	*Commercial Blend 3*	*Unknown*
J	*Commercial Blend 4*	*Unknown*
M	*PTFE-PI Blend 2*	*Dry mixed, sintered, Novel Method 2*

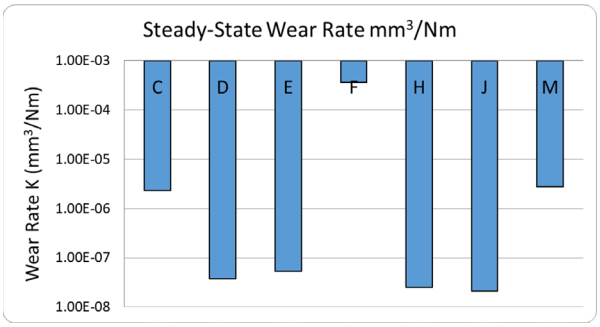

Figure 1: Steady-state wear rates of each sample

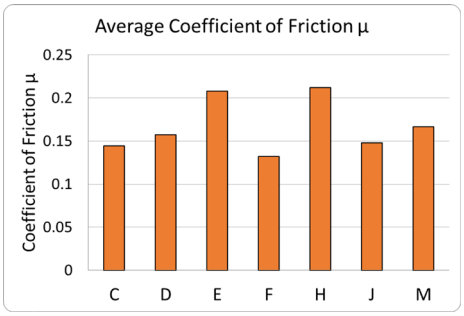

Figure 2: Average CoF of each sample

Acknowledgments

The authors would like to thank the discussion of Dr. Christopher P. Junk of CJIdeas LLC. Additionally, the authors would like to acknowledge the support of OSGC and Miami University through the OSGC Scholarship Program.

References

[1] K. Friedrich,Sliding wear performance of different polyimide formulations, *Tribology International*, Volume 22, Issue 1,1989, Pages 25-31, ISSN 0301-679X, https://doi.org/10.1016/0301-679X(89)90005-4.
[2] S.K. Biswas, Kalyani Vijayan, Friction and wear of PTFE — a review, *Wear*, Volume 158, Issues 1–2, 1992, Pages 193-211, ISSN 0043-1648, https://doi.org/10.1016/0043-1648(92)90039-B.

Predicting Shear Stresses Based on Pressure Data

Student Researcher: McKenzi E. Buttrey

Advisor: Dr. Brian L. Davis

Cleveland State University
Department of Mechanical Engineering

Abstract
This project focused on the human foot, specifically the skin. Foot loading is of paramount importance to astronauts who need to exercise to maintain bone density. In the case of this population, foot loading is dramatically reduced in a microgravity environment. In 1G, however, there are individuals with the opposite problem, specifically patients with plantar pressure profiles and/or shear stress distributions that predispose skin breakdown. These types of patients include those with diabetes. They are at higher risk for increased forces in their feet, which lead to ulcers. In neither population has the relationship between skin pressure (or its spatial derivatives) and shear stress been rigorously investigated. If such a relationship can be determined, then this will offer a potential solution to the vexing problem of assessing skin shearing inside a subject's shoe, without the need for additional in-shoe instrumentation.

Project Objectives
The objective of this research was to determine if there's a relationship between pressure and shear stress by utilizing novel technology at Cleveland State University. This information would help predict where patients are most likely to see the formation of an ulcer, specifically in diabetics' due to being at a higher risk of ulcer development. This then could potentially be used to measure shear on a patient's foot without the need of additional devices.

Methods
For this research, I utilized an ISSI Gait Analysis System. This machine has the ability to measure shear and pressure on the foot during the gait cycle. There is a shear sensor platform with a force plate that measures three forces and three moments' simultaneously. Data analysis utilized MATLAB to determine if shearing stresses can be estimated using pressure data alone. Lastly, ADAMS software was used to create a 3-D model to demonstrate the results of body weight forces applied to the foot and the forces between the skin and floor.
I collected data on several people at the university, I choose subjects with similar characteristics. The data I analyzed was on female college students, in their early 20's. The results from two individuals where chosen to compare results between. Since diabetics are more likely to have skin breakdown, I compared results from a non-diabetic and a diabetic. However, the diabetic did not have any complications related to diabetes and it was well under control therefore, I did not expect to see much variation between the two subjects.

Results and Discussion
After reading a journal written by a Cleveland State University graduate student, I learned that socks cause a 95% error in results of shear stress distributions. Once I finished the journal, I decided to redo all of the data I collected on the subjects, this time with no socks. The actual influence of the sock is unknown so the subjects walked across the platform barefoot to eliminate any potential errors. Other factors that could affect the data include but are not limited to, the weight of the individuals, walking speed, and any turning.
The use of MATLAB algorithms allowed me to determine the spatial derivative. This could offer a potential solution to the problem of assessing skin shearing inside of a subject's shoe without the use of additional instrumentation. The desired outcome was a linear relationship between the spatial derivative and shear. If one of the subjects had uncontrolled diabetes and potentially neuropathy, the results would have varied. The results from a diabetic with neuropathy would differ greatly from the healthy subject.

Figures/Charts

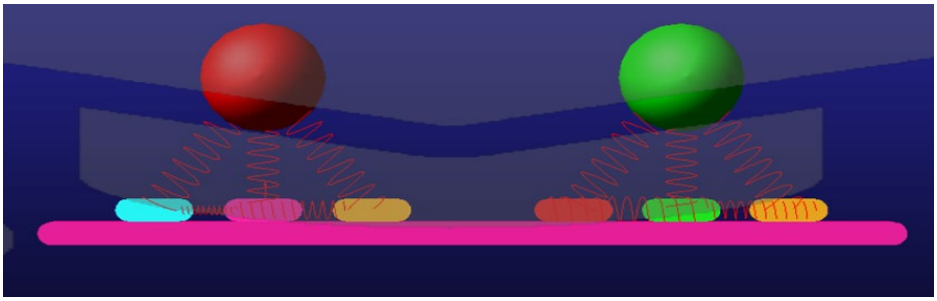

Figure 1: Model to represent the interaction between skin and the floor.

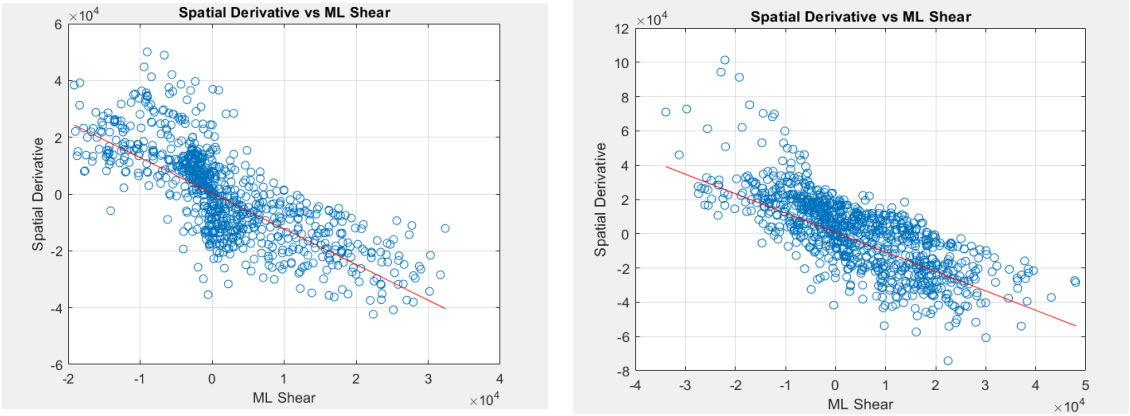

Figure 2: Comparison of actual results collected and analyzed in the lab to theoretical data.

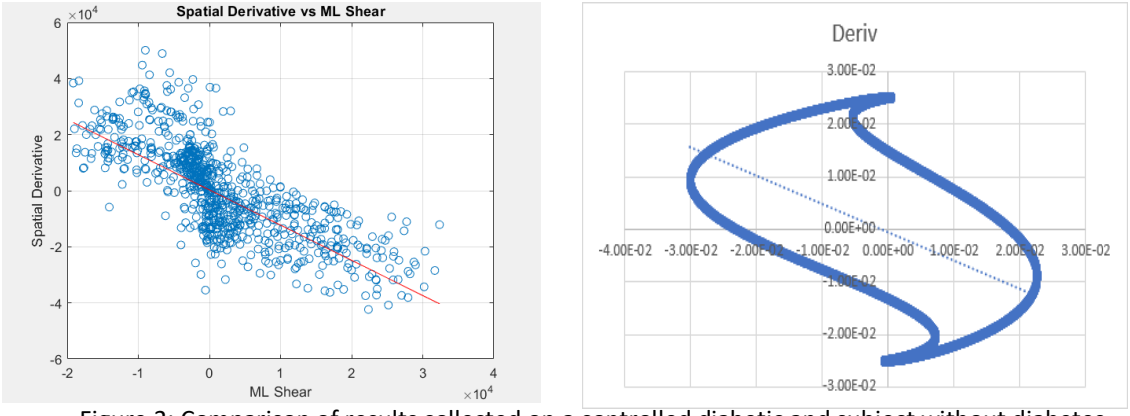

Figure 3: Comparison of results collected on a controlled diabetic and subject without diabetes.

Acknowledgments

I would like to thank my advisor, Dr. Davis for introducing me to this program and guiding me through my research journey. Also, I would like to give a special thank you to the OSGC and everyone who helped organize the symposium!

References

[1] Tiell, S M., S.C., & Davis, B. L (2021). "The effect of frictional coefficients and sock material on plantar surface shear streat management." *Journal of Biomechanics*, 127, 110682. http://doi.org/10.1016/j.jbiomech.2021.110682

A Preliminary Investigation of Jet Thrust Vectoring with Plasma Actuators

Student Researcher: Ethan C. Cartwright

Advisor: Dr. Nathan Webb

The Ohio State University
Department of Mechanical and Aerospace Engineering

Abstract
Improved aircraft performance is a continually active area of research. Altering the angle of jet thrust, known as thrust vectoring (TV), is particularly interesting for its impact on aircraft maneuverability and required takeoff/landing distance. Thrust vectoring is traditionally achieved by mechanical manipulation of nozzle exit geometry, which involves added weight and complexity to the aircraft. An alternative method Coanda-based Thrust Vectoring (CTV), exploits the Coanda effect to attach jet flow to a fixed surface at the nozzle exit which curves away from the jet axis (i.e., a "reaction surface"). This is accomplished by injecting high velocity flow into the exhaust flow shear layer which comes at the cost of a high bleed air requirement. Localized arc-filament plasma actuators (LAFPAs) manipulate natural instabilities in jet flows to control shear layer behavior which could be used, similar to CTV, to attach the jet flow to a curved reaction surface, deflecting the exhaust thrust along the surface. LAFPAs may be particularly suited for this application due to their rapidly variable operational state and low power requirement. LAFPAs have demonstrated success in establishing shear layer control authority for various flow control objectives, but have yet to be applied to thrust vectoring.

Project Objectives
The unification of the demonstrated flow control authority of the LAFPAs and the impact of TV on maneuverability and takeoff/landing distance is promising in terms of the potential aircraft performance gains available. This work serves as a preliminary exploration of jet response to LAFPA/reaction surface control in a broad parameter space, as well as the particular potential of LAFPA operation in thrust vectoring. This is done by sweeping through excitation frequencies of LAFPAs and reaction surface configuration, and documenting jet behavior with pressure measurements, schlieren imaging, and PIV.

Methodology
The Kelvin-Helmholtz instability is an inherent sensitivity of shear layer flows (regions of high velocity gradient) to small perturbations of velocity, temperature, and pressure [1] that cause the shear layer to roll up into large scale structures (LSS) [2]. LAFPAs operate by striking a high voltage arc across pin electrodes which produce local thermal perturbations (1000s of Kelvin) with a relatively low input power (10s of Watts) at a controlled frequency [3,4]. These perturbations are amplified into LSS by the Kelvin-Helmholtz instability, allowing for control authority over LSS formation and development within the shear layer [5]. LSS formation in jet shear layers play a dominant role in several processes such as mixing and entrainment. Past works have applied the control authority over LSS formation afforded by LAFPA's in areas of jet acoustics [6,7], and mixing enhancement [5]. Gonzalez et al. [8,9] demonstrated the LAFPAs' ability to induce asymmetric mixing in a supersonic axisymmetric jet with a straight exit geometry (i.e., no CTV-like reaction surface).
Here, a CTV inspired curved nozzle outlet geometry is paired with embedded LAFPAs to explore the TV capability of the LAFPAs by means of attaching exhaust flow to the curved reaction surface. A 1-inch diameter jet nozzle with a curved reaction surface nozzle (depicted in Fig. 1) is embedded with 8 azimuthally spaced LAFPAs, as well as pressure taps within the reaction surface. A backward facing step was included to situate a shear layer as flow passes the step. The effects of LSS entrainment were explored by altering actuator control frequency. The effect of control on the jet flow was assessed with embedded pressure taps and schlieren imaging (a method of capturing density gradients in fluid flows).
LAFPAs are expected to initiate LSS formation in the shear layer that forms at the step. These LSS naturally entrain fluid as they propagate downstream, but instead attach to the curved reaction surface due to its proximity. An actuation frequency dependent response is expected in the LSS development behavior. At low actuation frequency, LSS are expected to grow naturally as they propagate downstream, while at high actuation frequency, reduced spacing between LSS is expected to cause growth interference and reduce ultimate size. LSS' entrainment—and therefore jet attachment/thrust vectoring capability—is higher for large, coherent structures than for small, rapidly dissipating structures, allowing manipulation of jet attachment location. Using different actuation frequencies for different LAFPAs, LSS size at particular azimuthal locations can be independently controlled, causing an asymmetry in fluid entrainment and subsequent jet attachment/thrust vector deflection along a specified direction.

Results
Excitation was asymmetrically introduced across a range of frequencies along 3 adjacent active actuators. Results in Fig. 2 highlight the azimuthal distribution of suction while Fig. 3 demonstrates the continuity of suction asymmetry across frequencies and limitations in control at the frequency extremes. An expected range of suction profiles is found in response to plasma actuator forcing frequency. Relative to an unforced flow, low forcing frequencies increase suction downstream of active actuators and the opposite is found at higher frequencies. Furthermore, at the lower and upper extremes of the frequency range, impact on suction is reduced as control authority is limited by the time-averaged reduction in excitation and the band of frequencies the shear layer naturally amplifies, respectively.

Figures/Charts

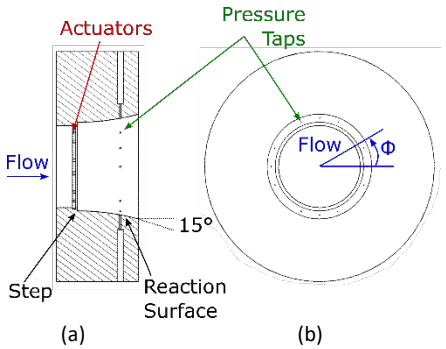

Figure 1: Subsonic axisymmetric jet with reaction surface: (a) Side view (flow left-to-right and (b) Front view (flow out-of-the-page).

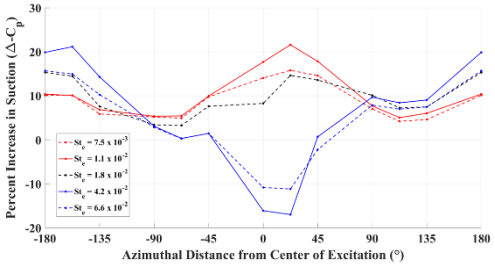

Figure 4.1: Azimuthal Distribution of Suction Coefficient ($-C_p$) Percent Difference from Baseline for an M_j = 0.48 Jet Excited across Various Frequencies (St_e).

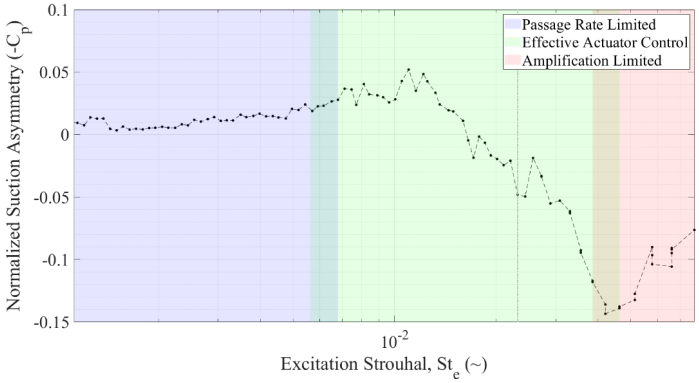

Figure 4.3: Summation of Difference in Suction Coefficient ($-C_p$) from Baseline toward CE for an M_j = 0.48 Jet across Excitation Frequency

References

[1] Moore, C. "The Role of Shear-Layer Instability Waves in Jet Exhaust Noise." Journal of Fluid Mechanics 2 (1977): 321–67.

[2] Michalke, A. "On Spatially Growing Disturbances in an Inviscid Shear Layer." Journal of Fluid Mechanics 3 (1965): 521–44.

[3] Samimy, M., I. Adamovich, B. Webb, J. Kastner, J. Hileman, S. Keshav, and P. Palm. "Development and Characterization of Plasma Actuators for High-Speed Jet Control," Experiments in Fluids, Vol. 37, No. 4 (2004): 577-588.

[4] Samimy, M., N. Webb, and M. Crawley, "Excitation of Free Shear-Layer Instability in High-Speed Flows," AIAA Journal (Invited Paper), Vol. 56, No. 5 (2018): pp. 1770-1791.

[5] Samimy, M., J.-H. Kim, J. Kastner, I. Adamovich, and Y. Utkin. "Active Control of High-Speed and High-Reynolds-Number Jets Using Plasma Actuators." Journal of Fluid Mechanics 578 (2007): 305–30. https://doi.org/10.1017/S0022112007004867.

[6] Kearney-Fischer, M., J.-H. Kim, and M. Samimy. "Noise Control of a High Reynolds Number High Speed Heated Jet Using Plasma Actuators." International Journal of Aeroacoustics 5–6 (2011): 635 – 658.

[7] Kim, J.-H., M. Kearney-Fischer, M. Samimy, and S. Gogineni. "Far-Field Noise Control in Supersonic Jets Using Conical and Contoured Nozzles." ASME Journal of Engineering for Gas Turbine and Power 133 (2011): 081201. https://doi.org/10.1115/1.4002811.

[8] González, D., D. Gaitonde, and M. Lewis. "Large-Eddy Simulation of Plasma-Based Asymmetric Control of Supersonic Round Jets." International Journal of Computational Fluid Dynamics 29, no. 3–5 (2015): 240–56. https://doi.org/10.1080/10618562.2015.1053877.

[9] González, D., D. Gaitonde, and M. Lewis. "Under-Expanded Round Jet Receptivity to Asymmetric Active Control," 2016–1105:1–26. San Diego, CA: AIAA Paper, 2016. https://doi.org/10.2514/6.2016-1105.

The Effects of Surface Roughness on the Macrohardness of 3D Printed Titanium

Student Researcher: Andreas Chaffey

Advisor: Dr. Timothy Norman

Cedarville University
School of Engineering and Computer Science/Mechanical Engineering

Abstract
The goal of the research was to better understand the effects of roughness on macrohardness of three-dimensional (3D) printed grade 23 titanium. 3D printed materials allow for easy surface modification. In this study we manufactured 10 different surfaces by varying frequency and peak magnitude. We also included titanium bar stock polished to industry standards. We defined macrohardness to be the hardness measured using a contact surface of 1/16th of an inch or greater. This is an attempt to measure the hardness experienced initially by another surface interacting with the titanium. We tested all the various samples using the Rockwell Hardness test and three different indenters. Our hypothesis was that as the indenter size increased the macrohardness would decrease and that indenter sized played a large part in the hardness of the material. We found that indenter size has a large influence on the hardness of the material as the larger indenters showed a correlation between the hardness of the surface while the small spheroconical point indenter showed no correlation. Our results show that while the macrohardness the initial surface hardness changed with roughness and interface area for the larger indenters, the actual hardness of the material remained constant when a smaller indenter was applied. We were also able to match our findings with a similar study using electrical discharge machined (EDM) specimens, showing the behavior of the 3D printed material is the same as that of traditionally manufactured material. These findings are useful for designers and manufacturers who plan to use 3D printed metals.

Project Objectives
The primary objective of this research was to determine the effect of customization of 3D printed surface roughness (surface peak magnitude and peak frequency) on macrohardness. An additional objective was to test the effect of different indenters on surfaces with large amplitude peaks for hardness measurements.

Methods
Ten groups of three 3D printed grade 23 titanium samples each of which had a different roughness along with a group of grade 23 bar stock were used in this experiment. Each sample was a circular disc [Ø9.5mm x 2mm Thickness]. There were three peak magnitudes, 0.15 mm, 0.4 mm, and 0.65 mm, and three peak frequencies, 3, 4.5, and 10 peaks/mm^2. Combinations of these parameters provided us with 9 of our 11 groups, while the other two groups were polished bar stock and the unmodified 3D printed control. The 3D printed specimens were manufactured using a GE Additive Concept laser mLab DMLM Fiber Laser printer (Lichtenfels, Germany). This printer uses laser powder bed fusion (LPBF) to create the parts. We used the Rockwell hardness test to measure the roughness of the samples and we used three different Rockwell scales so that we could find the effect of different indenters. The scales used were C scale (spheroconical point; load of 150 kgf), B scale (1/16th carbide ball; load of 100 kgf), and E scale (1/8th carbide ball; load of 100 kgf). All hardness testing was performed to the ASTM International standard test methods for Rockwell hardness. Two machines were used, one for the C scale, and one for the B and E scales. Every sample was tested according to scale and the resulting hardness measurements recorded. One indentation from each indenter was made on every sample. This gave us 3 indentations per sample group per indenter. The statistical mean of these three hardness values were then taken and plotted on Figure 1.

Results and Discussion

The study found that the indenter shape influences the macrohardness of a material if the surface peaks are large and frequent, i.e., the roughness. The regressions with the ball indenters show a decrease in hardness with Ra whereas the hardness with the spheroconical point indenter do not. These micrographs illustrate the effect. Figure 2 shows the conical indentation left by the C scale indenter. While it is difficult to clearly see the point of the indentation is still completely intact much like the indentation left in Figure 4. In Figure 3 we can clearly see gaps between the base of the indentation and the sides of the depression. These gaps are not present in Figure 5 which has a shallow and round depression. Because hardness measurements are found by identing a material and measuring either the depth or the diameter of the indentation, The smaller indenter (spheroconical point) is going deep enough into the surface, that the surface roughness provides no real change in hardness, While the larger indenters (1/16" and 1/8" carbide ball indenters) are greatly affected by the surface features.

Figures/Charts

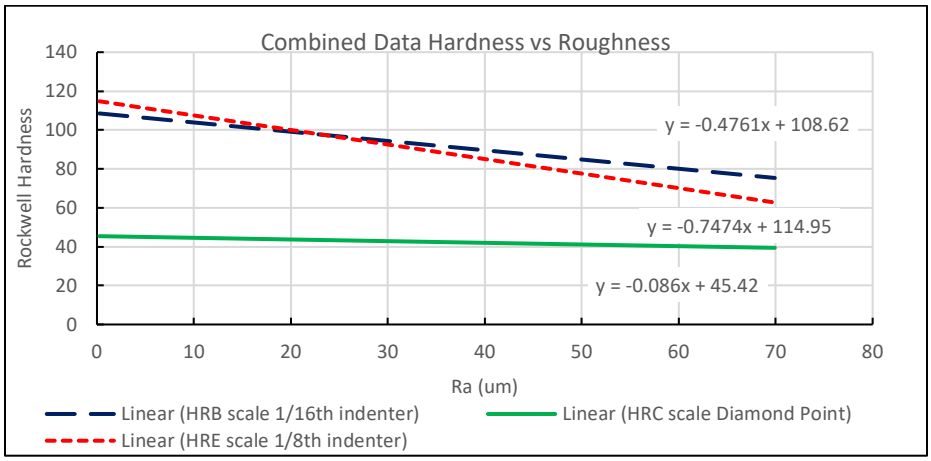

Figure 1. Trendlines for the data of each indenter. Rockwell Hardness numbers vs. Average Surface Roughness

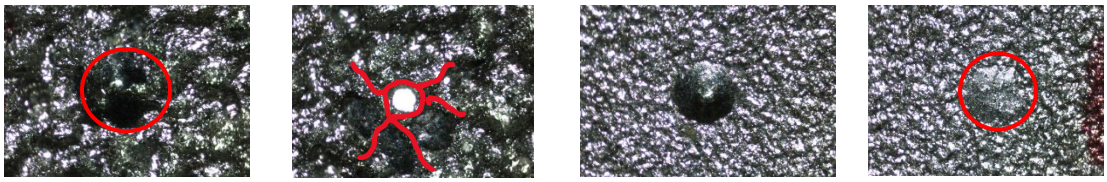

Figures 2-5. Rockwell C scale on .65mm 4.5k specimen, Rockwell E scale on .65mm 4.5k specimen, Rockwell C scale on control specimen, Rockwell E scale on control specimen.1

References

Karbasian, A., Shirazi, M., & Mahmoudi, A. H. (2023). Effect of Surface Roughness on Brinell Hardness and Load-Displacement Curves using a Macro Indentation. International Journal of Engineering, 36(5), 914-924. doi: 10.5829/ije.2023.36.05b.08

Analysis of Paraben Induced Caspase-3 Activation in Human M624 Melanoma Cells versus Normal HaCat Epithelial Cells

Student Researcher: Kennedy L. Couch

Advisor: Dr. Suzanne Parsons

Marietta College
Department of Chemistry and Biochemistry

Abstract
Parabens, a common antimicrobial agent used in a wide variety of industrial, cosmetic, and pharmaceutical products, has been used for many years due to their ability to maintain a neutral pH and their odorless and colorless properties. While parabens have been found in everyday products for a number of years, controversies over their use have arisen as they have been linked to aversive effects and multiple skin cancers including malignant, melanoma, and contact eczema in the last several years. In this study human melanoma cells and normal human epithelial cells were treated with 0.05-10mM paraben solution, consistent with LC_{50} values. Parabens were dissolved in ethanol or methanol solvent and added to complete DMEM for cell treatment. Methylparaben (methyl 4-hydroxybenzoate) and a paraben derivative, helptylparaben, were used. A colorimetric Caspase-3 microplate assay kit was used to assess the ability of these compounds to induce apoptosis. Previous research has shown parabens have induced apoptosis in human melanoma cells, while this study will assess parabens' ability to induce apoptosis in normal human epithelial HaCat cells versus human melanoma M624 cells and provide support for the continued study of paraben as a possible topical treatment for melanoma.

Project Objectives
The primary goal of this particular project was to determine if paraben should be continued to be evaluated as a potential topical treatment for melanoma cells in the presence of normal skin cells. This investigation was the first of its kind to quantify the potential of paraben and paraben derivatives in initiating the apoptotic pathway of both cell types. In the investigation of paraben as a topical melanoma treatment, paraben-induced caspase-3 activation was analyzed in M624 human melanoma cells compared to HaCat normal epithelial cells for support of conclusions.

Methods
Cell Culture
M624 human melanoma cells and normal HCat cells were kept in 100mm cell culture plates with complete media which includes Dulbecco's Modified Eagles Medium (DMEM) with 10% fetal bovine serum, and 1% penicillin-streptomycin. Cells were incubated at 37ºC with humidity and 5% CO_2. Once it was ensured cells were growing without contamination cells were transferred. Trypsin was added, and the plate was incubated for 5-10 minutes for M624 human melanoma cells and 20-25 minutes for normal HCat cells. Complete media was added to the plate and the contents of the plate were washed. New plates were then prepared by adding a small amount of cell and complete media mix to each plate. DMEM was added to each plate and the plates were placed in the incubator. The cells are transferred as needed every 3 to 4 days.
Solvent and Paraben Treatment

Paraben was dissolved in ethanol or methanol solvent as determined through preliminary data. The paraben solution was dissolved in complete DMEM cell growth medium. Control, solvent, and various concentrations of each paraben were prepared. The control treatment group was treated with DMEM only.

Four 10 mm plates of cells at 75-95% confluency were prepared for each treatment group. The regular complete media was removed and DMEM treatment solution was added with solvent or paraben. The plate was then incubated for a designated amount of time determined by previous determination of LC_{50} values with each specific paraben (Table 1).

Paraben	Treatment Time	LC_{50}
Methyl-	6 hours	2.28 mM
Heptyl-	1 hour	0.195 mM

Table 2: LC_{50} values for methylparaben and heptylparaben

Cell Lysis and Caspase-3 Assay
The DMEM containing the dead cells was removed from each plate and placed in centrifuge tubes. PBS was added to each plate and the plate was scrapped using the blunt end of a pipet tip. The collected cells were added to the labeled tube for the control, solvent, and paraben concentration groups. The tubes were centrifuged for 10 minutes, and the supernatant was discarded. 100 ul of lysis buffer was added to the pellet of cells and the pellet was broken up using a pipet tip. The tubes were centrifuged for three minutes. The liquid supernatant is placed into small centrifuge tubes and kept in the freezer until the assay was completed.

The Caspase-3/CPP32 Colorimetric Assay Kit was used to detect and quantify the presence of caspase-3 through recognition of the sequence DEVD. The assay is based on the spectrophotometric detection of the chromophore p-nitroaniline (pNA) after cleavage from the labeled substrate DEVD-pNA. Dilute protein to cell lysis buffer was added to each sample. Reaction buffer was combined with dithiothreitol (DTT) immediately before use. DEVD-pNA substrate was added and incubated at 37 degrees for 1 hour. Cells were then centrifuged for one minute in a standard centrifuge. The supernatant was transferred to a new tube and set on ice for immediate assay.

A Bradford protein assay was completed by creating a dilution series of known protein concertation in mg/mL. Bovine Serum Albumin (BSA) was placed in a tube and centrifuged. The BSA is added to increasing concentrations of water to create a standard protein curve. The sample was performed in triplicate on a 96 well plate and absorbance was measured using spectrophotometer plate reader.

Samples were read in the spectrophotometer at 405nm on a 96 well plate. These results were compared with Bradford protein assay to compare the general protein concentration found in each sample to the amount of Caspase-3 in each sample. Each caspase assay for heptylparaben and methylparaben was standardized to control samples. Statistical analysis was completed using standard deviation and examining p values. P values >.1 were considered statistically significant.

Figures/Charts

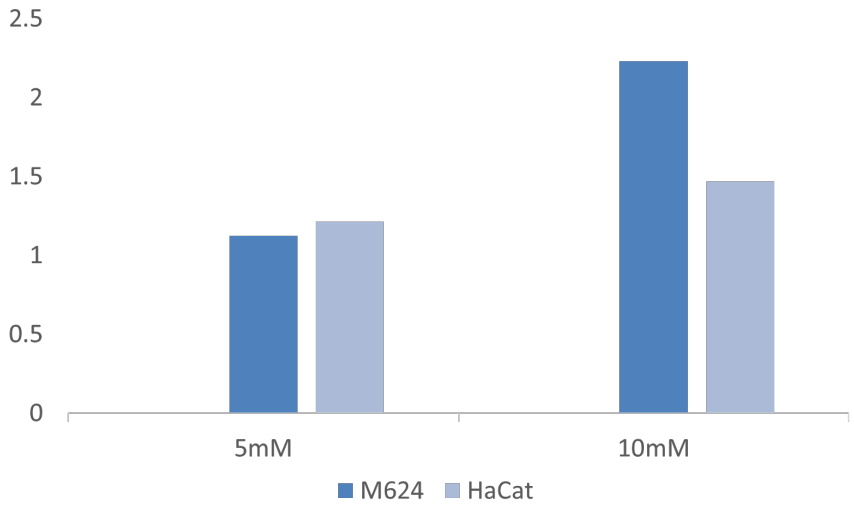

Figure 1: Caspase-3 activation induced by methylparaben standardized to control

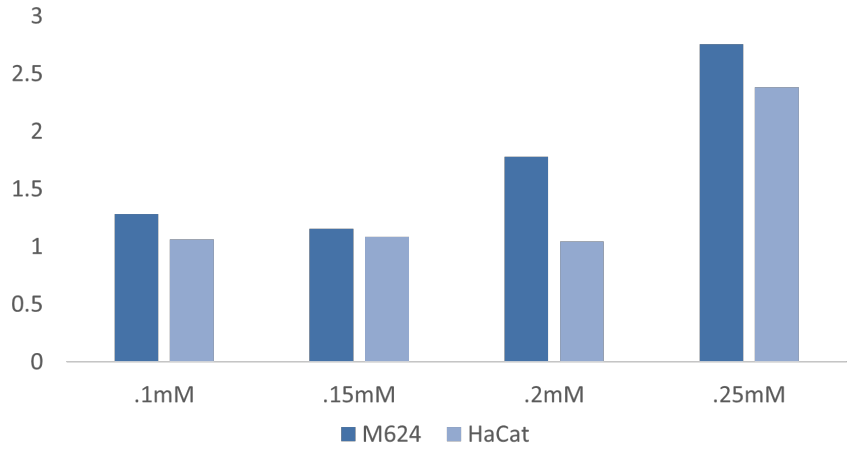

Figure 1: Caspase-3 activation induced by methylparaben standardized to control

Results and Discussion

At LC_{50} concentrations for M624 human melanoma cells, determined through previous studies, no statistically significant difference between the amount of caspase-3 detected in HaCat normal epithelial cells versus M624 melanoma cells was observed. However, increased concentration of both methylparaben and heptylparaben treatment resulted in increased caspsase-3 in M624 cells compared to HaCat, providing evidence that at higher concentration of paraben, these compounds may still be a topical treatment for melanoma.

Experimentation on other apoptotic indicators such as PARP or caspase-9 would provide confirmation of these conclusions. In investigation of paraben as a topical melanoma treatment, paraben-induced caspase-3 activation was analyzed in M624 human melanoma cells compared to HaCat normal epithelial cells. In this preliminary study, results demonstrate that heptylparaben induces higher levels of caspase-3 activation in melanoma cells versus normal cells at concentrations of 0.2mM and higher, while methylparaben is capable of inducing higher levels of caspase-3 activation in melanoma cells than normal cells at 10mM. The lipophilic structure of heptylparaben compared to methylparaben enhances the ability of heptylparaben to penetrate the stratum corneum of the skin to access cancer cells. The activation of caspase-3 protein in melanoma cells demonstrates that apoptosis, healthy cell death, is occurring, and that parabens have the potential to be used at a topical therapeutic.

Acknowledgements
I would like to thank the Ohio Space Grant Consortium, the Chemistry and Biochemistry Department at Marietta College, Dr. Suzanne Parsons, and lab partners Julie, Joel, and Duncan at Marietta College.

References

1. *Centers for Disease Control and Prevention United States Caner Statistics*. https://gis.cdc.gov/Cancer/USCS/?CDC_AA_refVal=https%3A%2F%2Fwww.cdc.gov%2Fcancer%2Fdataviz%2Findex.htm#/AtAGlance/DC (accessed 2023-12-17).
2. Lopes, J.; Rodrigues, C. M. P.; Gaspar, M. M.; Reis, C. P. Melanoma Management: From Epidemiology to Treatment and Latest Advances. *Cancers (Basel.* **2022**, *14* (19), 4652. DOI: 10.3390/cancers14194652.
3. Dzwierzynski, W. W. Melanoma Risk Factors and Prevention. *Sci. Dir.* **2021**, 48 (4), 543-550. DOI: 10.1016.
4. *National Cancer Institute Melanoma Treatment.* https://www.cancer.gov/types/skin/patient/ melanoma-treatment-pdq. (accessed 2023-12-10).
5. Czarnecka, A. M.; Bartnik E.; Fiedorowicz M.; and Rutkowski P. Targeted Therapy in Melanoma and Mechanisms of Resistance. *Int. J. Mol. Sci.* **2020**, 21 (4576), 1-21. DOI: 10.3390/ijms21134576.
6. *Penn State Medine Abramson Cancer Center*. https://www.pennmedicine.org/cancer/types-of-cancer/melanoma/melanoma-treatments/targeted-therapy-for melanoma#:~:text=If%20these %20tests%20show%20that%20a%20tumor%20has,to%20help%20prevent%20cancer%20from%20recurring%20%28coming%20back%29.ted (accessed 2023-12-16).
7. Petri, Z.; Ruzic, J.; Zuntar, I. The controversies of paraben – an overview nowadays. *Sciendo.* **2021**, 71 (1), 17-32. DOI: 10.2478.
8. Darbre, P. D.; Harvey, P. D. Paraben Esters: Review of Recent Studies of Endocrine Toxicity, Absorption, Esterase and Human Exposure, and Discussion of Potential Human Health Risks. *Journal of Applied Toxicology*. **2008**, 28 (5), 561-578. DOI: 10.1002/jat.1358.
9. Lincho, J.; Martins, R. C.; Gomes, J. Paraben Compounds- Part 1: An overview of their characteristics, detection, and impacts. *Applied Sciences.* **2021,** 11 (2307) 1-37. DOI: 10.3390/app11052307.
10. Liao, C.; Liu, F.; Kannan, K. Occurrence of and dietary exposure to parabens in the United States. *Environ. Sci. Technol*. **2013**, 47 (8), 3918–3925. DOI: 10.1021/es400724s/
11. Fransway, A. F.; Fransway, P. J.; Belsito, D. V.; Yiannias, J. A. Paraben toxicology. National Library of Medicine. **2019**, 30 (1), 32-45. DOI: 10.1097/DER.0000000000000428.
12. Final Amended Report on the Safety Assessment of Methylparaben, Ethylparaben, Propylparaben, Isopropylparaben, Buttylparaben, and Benzylparaben as used in Cosmetic Products. International Journal of Toxicology. **2008**, 1-139. DOI: 10.1080/10915810802548359.
13. Schlanz, J. A. Effects of Mononitroparaben on Lipid Content of Melanoma Cells. Honors Thesis, Marietta College, Marietta, OH, 2023. http://rave.ohiolink.edu/etdc/view?acc_nu m=marhonors1683297844540949.
14. Kinney, E. ** revise- need MC access to see paper
15. Subbiah, V.; Baik, C.; and Kirkwood, J. M. Clinical Development of BRAF plus MEK Inhibitor Combinations. Trends in Cancer. 2020, 6 (9), 797-810. DOI: 10.1016/j.trecan.2020.05.009
16. Pollard, T. D.; Earnshaw, W. C.; Lippincott-Schwartz, J.; Johnson, G. T. *Cell Biology,* 3rd ed.; Elsevier: Pennsylvania, 2017; pp 797-815.
17. Eaton, L.; Rogers, K. *Examining Cells*; Britannica Educational Publishing: New York, 2018; pp 222-229.
18. Mor, G.; Alvero, A. B. *Apoptosis and Cancer: Methods and Protocols*, 2nd ed.; Springer: New York, 2008; pp 1-90.
19. Liu, Y.; Jia, Y.; Yang, K.; Wang, Z. Heterogeneous Strategies to Eliminate Intracellular Bacterial Pathogens. Front. Microbiol. [Online] **2020**, *11*, 563. https://pubmed.ncbi. nlm.nih.gov/32390959/.
20. Nelson, L. D.; Cox, M. M. *Lehninger Principles of Biochemistry*, 6th ed.; W.H. Freeman: New York, 2013; pp 762-766.
21. Do, B. H.; Hoang, N. S.; Nguyen, T. P.; Ho, N. Q.; Le, T. L.; and Doan, C. C. Phenolic extraction of *moringa oleifera* leaves induces caspase-dependent and caspase-independent apoptosis through the generation of reactive oxygen species and the activation of intrinsic mitochondrial pathway in human melanoma cells. *Nutrition and Cancer.* [Online] **2020,** *73*, 869–888. https://pubmed.ncbi.nlm.nih.gov/32530312/.
22. Yang, H.; Yi, J.; Pang, S.; Ye, K.; Ye, Z.; Duan, Q.; Yan, Z.; Lian, C.; Yang, Y.; Zhu, L.; Qu, D.-H.; Bao, C. A Light-Driven Molecular Machine Controls K+ Channel Transport and Induces Cancer Cell Apoptosis. *Angew. Chem. Int.* [Online] **2022,** 61, 1-9. https://onlinelibrary.wiley .com/doi/epdf/10.1002/anie.202204605 (accessed Apr 9, 2023).

Thermo-Responsive Bacteria-based Engineered Biohybrid Material Platform

Student Researcher: Natalie M. Dando

Advisor: Dr. Byung-Wook Park

Youngstown State University
College of Science, Technology, Engineering, and Mathematics

Abstract
The combination of multifunctional biomaterials and living cells has given rise to the field of engineered living materials where living cells such as bacteria function as active components of material's design and performance. Genetically modified microorganisms have been encapsulated in hydrogels and used as a part of the living therapeutics for the treatment of skin diseases. On-demand drug delivery is often required for advanced therapeutic applications. In this project, the thermo-responsive bacteria-based engineered biohybrid material platform (EBMP) was developed as a proof of concept transdermal design for production and regulation of green fluorescence protein (GFP) expression has been explored. The thermo-responsive EBMP consists of a hydrogel containing genetically modified probiotic bacteria, Escherichia coli Nissle 1917 (EcN). This study investigates the growth and metabolic activity of bacteria within an associative hydrogel.

Project Objectives
This project aims to answer the question: "Do thermo-responsive EBMPs have the potential to be used for biomedical applications?" So, the objective was to develop an EBMP consisting of a microheater that can heat to 37°C with a low voltage and modified EcN that can survive in the hydrogel, express Green Fluorescent Protein (GFP) protein, and be contained on the microheater in a PDMS spacer.

Methodology
The EBMP consists of an Engineered PEC hydrogel, and a microheater, detailed below:

- Engineered PEC hydrogel
    - 40:60 CHI/ALG hydrogel
    - EcN with modified GFP gene cultured with kanamycin at 25 °C
    - EcN culture diluted with M9 salt medium to OD of 0.284.
- Microheater
    - Composed of Laser Induced Graphene (LIG), silver nanowires coating, copper tape and PI insulation tape
    - Supporting construction for stability
    - PDMS spacer to place the EBMP

Power was supplied to microheaters and temperature was monitored using a thermal camera.

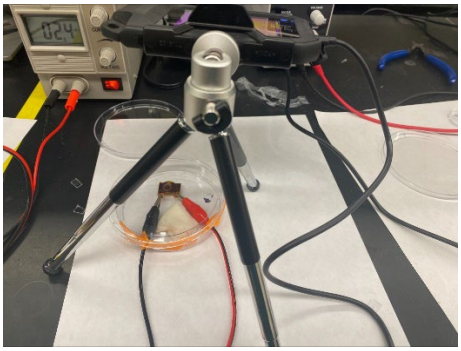

Figure 1. Experimental set up.

Results Obtained
Bacteria heated in EBMP using microheater shown in figure 2 below:

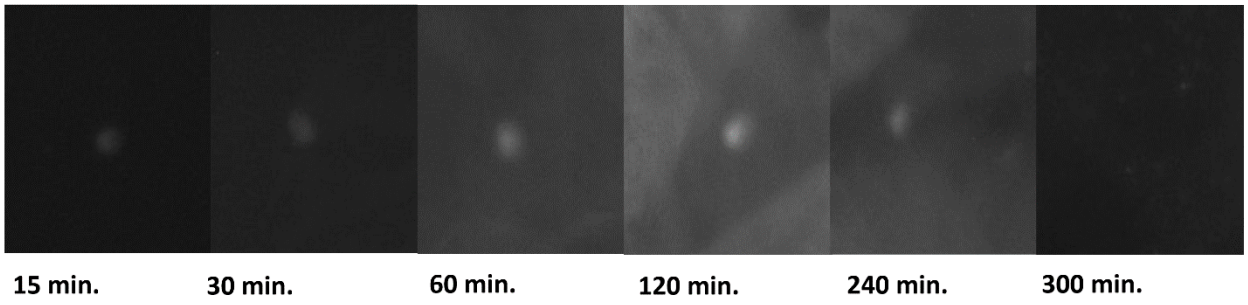

Figure 2. EcN glowing intensity shown at different times.

Modified *E.coli* Nissle 1917 with GFP glows in response to heat, and intensity increases over time. EcN began to glow after 15 minutes, and increased intensity in 0-4 hours when heated in hydrogel using microheater. EcN can be contained in hydrogel and heated with microheater. Supports research question that EBMP may be used for biomedical application, as GFP can be activated with microheater.

Acknowledgments
This work is supported by the OSGC Scholarship program.

The authors acknowledge Dr. Caguiat's lab at YSU for providing us the genetically modified *E.coli* Nissle 1917 for this project.

References
[1] Liu, X.; Wu, M.; Wang, M.; Hu, Q.; Liu, J.; Duan, Y.; Liu, B. Direct Synthesis of Photosensitizable Bacterial Cellulose as Engineered Living Material for Skin Wound Repair. *Advanced Materials* **2022**, *34* (13). https://doi.org/10.1002/adma.202109010.
[2] Sankaran, S.; del Campo, A. Optoregulated Protein Release from an Engineered Living Material. *Advanced Biosystems* **2018**, *3* (2). https://doi.org/10.1002/adbi.201800312.
[3]Lavrador, P.; Esteves, M. R.; Gaspar, V. M.; Mano, J. F. Stimuli-Responsive Nanocomposite Hydrogels for Biomedical Applications. *Advanced Functional Materials* **2020**, *31* (8). https://doi.org/10.1002/adfm.202005941.
[4] Sankaran, S.; Becker, J.; Wittmann, C.; del Campo, A. Optoregulated Drug Release from an Engineered Living Material: Self-Replenishing Drug Depots for Long-Term, Light-Regulated Delivery. *Small* **2018**, *15* (5). https://doi.org/10.1002/smll.201804717

Development of a Pulse Simulator Using a Solenoid System to Reproduce Human Radial Pulse Waveforms

Student Researcher: Simon DeBruin

Advisor: Dr. Jeong-Hoi Koo

Miami University
Mechanical Engineering

Abstract
Radial pulse simulators can play an important role in the advancement of wearable healthcare devices and the modernization of pulse diagnosis methods, which are widely used in Oriental Medicine [1-3]. They can be used to calibrate wrist-worn sensors and train medical professionals for pulse palpations. This study proposes a new, simple, and cost-effective pulse simulator capable of producing a wide range of blood pressure waveforms. It designed and constructed a prototype pulse simulator, consisting of two precision solenoid valves, an air compressor, a pneumatic pressure sensor, and control electronics.

Project Objectives
The primary goal of this project is to replicate radial pulses that are characteristic of a variety of in-vivo human pulses. The project intends to employ a solenoid system to control pressure in a system, creating pressure waveforms that match pulse waveforms. Different inputs will be sent to the solenoid valves to create different waveforms while maintaining the system.

Methodology Used
Figure 1 shows the experimental set up employed in this study. As shown in the figure, an air compressor is linked via a tube to the pressure solenoid. This valve is connected through tubing to both the pressure sensor and the output valve. Both solenoids are connected to a relay, which is interfaced with an Arduino board before data transmission to the computer. A DAQ-IQ board is connected to the computer to read values from the pressure sensor. The pressure tank used is a compact air compressor. Due to the small change of pressure recorded when the system is open, this compressor can be modeled as an infinitely large and unchanging pressure reservoir. It is controlled independently of the rest of the system and is refilled after each run of the system. When fed different duty values, the solenoid valves open and close at different speeds, mimicking a partially opened valve. This allows waveforms with different slopes to be generated.

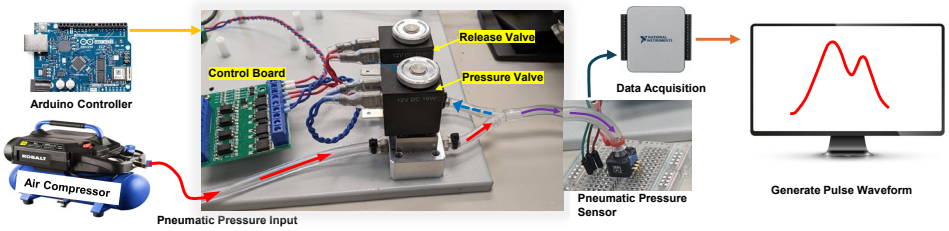

Figure 1. Experimental set-up

Results
Three distinct in-vivo waveforms were chosen to simulate: the waveforms of a 10-year-old, a 50-year-old, and a 90-year-old human. For each of these pressure waveforms, a unique control input was sent to the solenoid valves, regulating their opening and closing times to match the waveform pattern. Figure 2a shows the generated 10-year-old waveform plotted alongside the corresponding in-vivo pulse, which exhibits three peaks.

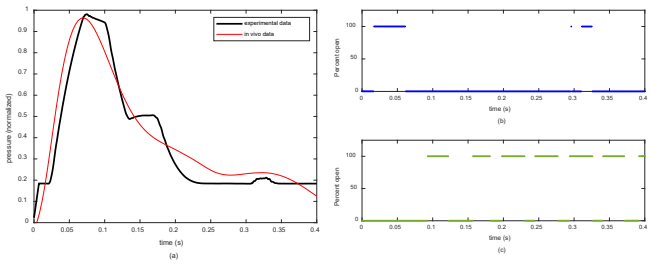

Figure 2. (a) Experimental 10-year-old waveform plotted against in-vivo pulse, (b) Pressure valve control, and (c) Release valve control

Figure 2b shows the periods of time when the input or pressure valve is open, while Figure 2c displays the corresponding periods for the output or release valve. It can be seen that when the input valve was open, a rising slope was recorded, and the opening of the output valve led to a decrease in the pressure in the system.
Figure 3 shows the modeled 50- and 90-year-old pulses plotted against the in-vivo data. It can be seen that the system was able to model both of these waveforms as well, showing evidence that any arbitrary pulse can be modeled with the system. Using root mean square analysis on all 3 waveforms, a percent error of less than 7% was found. As this error is relatively small (<10%), the analysis supports the feasibility of the system accurately modeling arbitrary pule waveforms across various age groups.

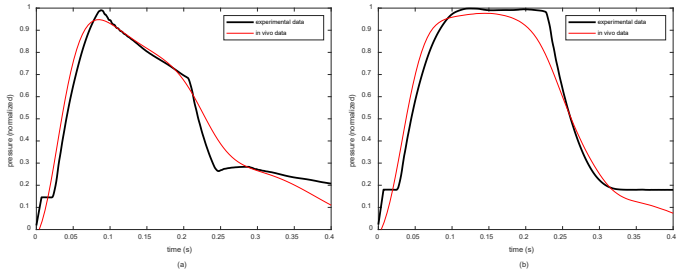

Figure 3. (a) Experimental 50-year-old waveform plotted vs. in-vivo pulse, and (b) Experimental 90-year-old waveform plotted vs. in-vivo pulse

Conclusion and Future Work

This study investigated the feasibility of utilizing a solenoid system to replicate age-related pulses. It demonstrates that the proposed system can generate arbitrary waveforms. Future work includes refining the system by replacing the solenoid valves with more precise alternatives and developing a control method for replicating arbitrary pulses effectively. Overall, the findings of this study offer promising prospects for developing systems that accurately model in-vivo pulses while maintaining simplicity in operation and cost-effectiveness. This could significantly contribute to modernizing pulse diagnosis techniques and advancing sensor technology for wearable healthcare devices.

Acknowledgments

A special thanks to the Ohio Space Grant Consortium for their support in this project. The author would also like to thank Dr. Koo, his advisor, for all of his support and guidance during this research.

References

[1] Velik R. An objective review of the technological developments for radial pulse diagnosis in Traditional Chinese Medicine. Eur J Integr Med. 2015 Aug 1;7(4):321–31.
[2] Yang J, Yang L, Liu W, Du S, Xu L, He G, et al. Analysis of the Radial Pulse Wave and its Clinical Applications: A Survey. IEEE Access. 2021;9:157940–59.
[3] O'Brien KA, Birch S, Abbas E, Movsessian P, Hook M, Komesaroff PA. Traditional East Asian Medical Pulse Diagnosis: A Preliminary Physiologic Investigation. https://home.liebertpub.com/acm [Internet]. 2013 Oct 15 [cited 2024 Apr 23];19(10):793–8. Available from: https://www.liebertpub.com/doi/10.1089/acm.2012.0141

FEA Modal Analysis of a Jet Turbine Blade

Student Researcher: Ryan Dippolito

Advisor: Dr. Manigandan Kannan

University of Akron
Mechanical Engineering

Abstract

Jet turbine blades can be rotated at angular velocities upwards of 25,000 revolutions per minute. These high velocities can lead to a significant amount of vibrational energy being transferred to the structure of the blade, especially when the vibrational frequencies approach the natural frequency of the structure. Hyphen innovations, an Aerospace company based out of Dayton, Ohio, is working with the University of Akron to conduct vibrational testing of their proprietary turbine blade design. Before conducting this physical shake-table testing, preliminary analysis needs completed. Moreover, a Finite Element Analysis (FEA) model needs created to verify the first five vibrational modes and the frequencies associated with these modes. These mode shapes and frequencies will provide preliminary information to Hyphen Innovations on how to conduct the physical shake table testing moving forward

Methodology

The FEA computer program chosen for this project is ABAQUS CEA. This was chosen due to the familiarity of the program from all parties involved with the project. The geometry of the blade is shown in Figure 1 below and is imported into ABAQUS from Solidworks CAD as a VGES file. A second model of interest in this analysis is the same blade, but with a "notch" where the blade meets the base that is fixed on the shake table, where the highest stress concentrations are expected. This model is shown below in Figure 2. This notch, in the physical testing, is meant to simulate a jet turbine blade that has been fractured by debris pulled into the jet engine.

Figure 1 – Turbine Blade Geometry

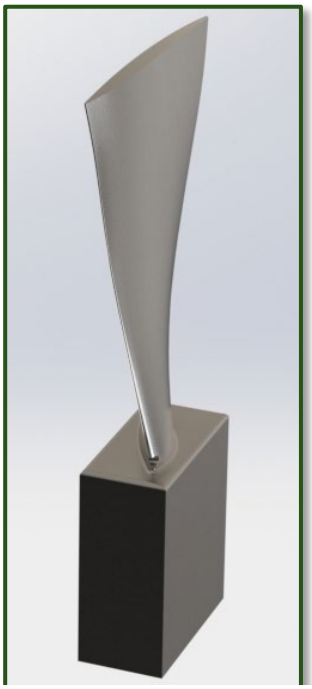

Figure 2 - Turbine Blade Geometry (with Notch)

Figure 3 – Volumetric testing to obtain mass density of Inconel-625

Figure 4 – Dog-bone testing of Inconel-625 Specimen

The material of the blade is Inconel-625. Before this analysis, dog-bone tests and mass density measurements were conducted to gather representative material properties. Pictures of this testing is shown in Figures 3 and 4 below. The material properties of interest are a Young's Modulus of 22737.5 ksi, a Poisson's ratio of 0.3, and a mass density of $7.6\ x\ 10^{-4}\ \frac{lbf*s^2}{in^4}$. These properties were input into the ABAQUS model, which is shown in Figure 5 below.

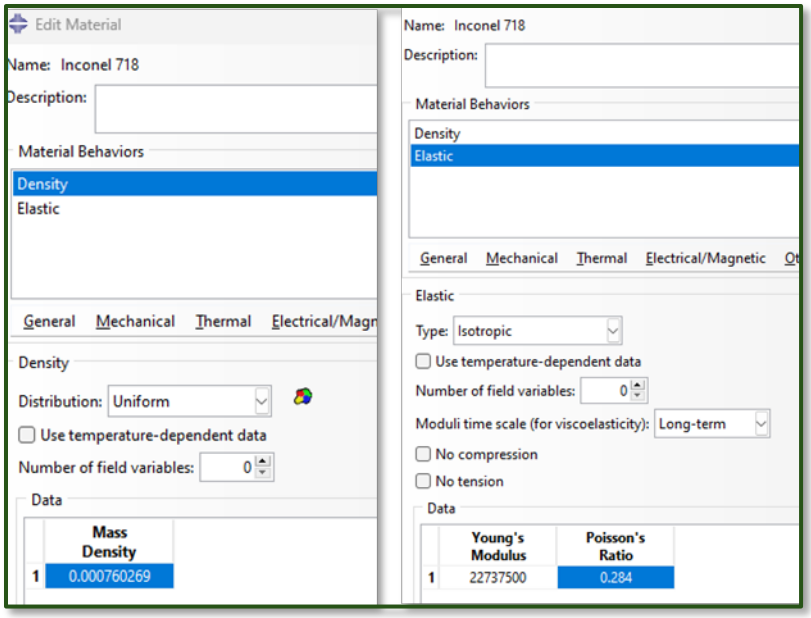

Figure 5 - Materials data input into ABAQUS program

To setup a modal analysis in ABAQUS, a frequency analysis step is added in the step module of the program. Due to this, there are no loads that need added into the model; however, a boundary condition is necessary to constrain the model. A fixed support (all six degrees of freedom locked) on the base of the structure is added to emulate the shake table testing where that portion of the part is fully fixed in a vice grip. This boundary condition is shown in Figure 6 below.

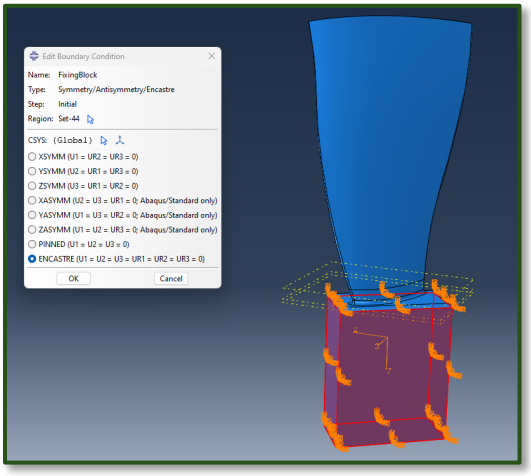

Figure 6 - Fixed boundary condition

Due to the complex geometry of the turbine blade, a quadratic tetrahedron mesh is necessary to run the analysis. Additionally, an eight-node element type was the default in the ABAQUS program and was subsequently used. The blade was partitioned into three sections to provide different mesh sizing. This includes a coarser mesh on the base structure that is not of interest, a fine mesh on the turbine blade, and an extra fine mesh on the high stress bearing part of the blade at the bottom. This mesh is shown in Figure 7 below.

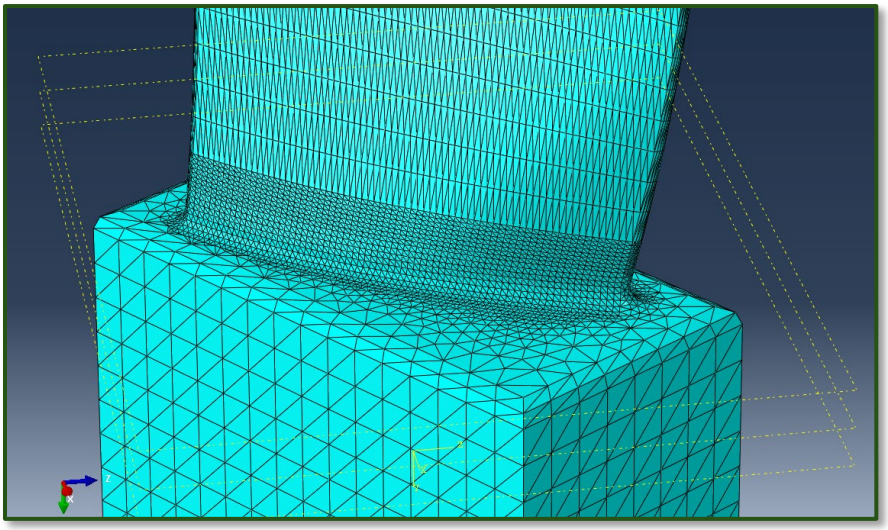

Figure 7 - Refined mesh of turbine blade

Although the vibrational results of the model are of actual use and interest, modal analysis through ABAQUS also provides displacement and subsequent stress values from the vibrations. However, the accuracies of these stress values is widely regarded as inaccurate, but they can be used to make relative

comparisons between multiple designs. For this reason, an extra verification of the model can be completed by verifying that the notched blade has higher stress amplitudes.

Results and Discussion

Shown below in Figures 8 and 9 is the modal frequencies at each mode and the associated mode shape. These results show that the notch in the geometry did not affect the modal frequencies. Additionally, modes 3 and 4 are shown to resemble the parameters of interest most closely for Hyphen Innovations turbine blade application, so they will be used in subsequent shake table testing.

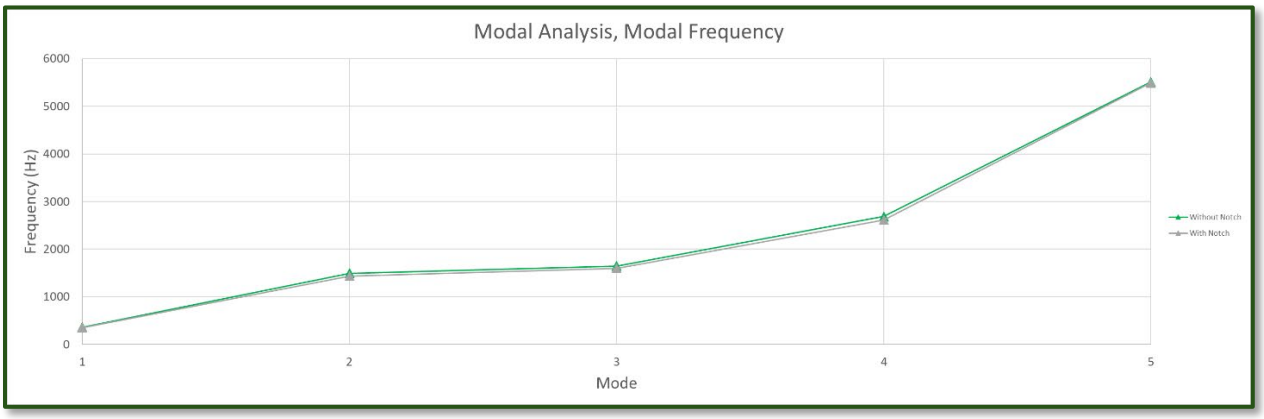

Figure 8 - Modal Frequency results

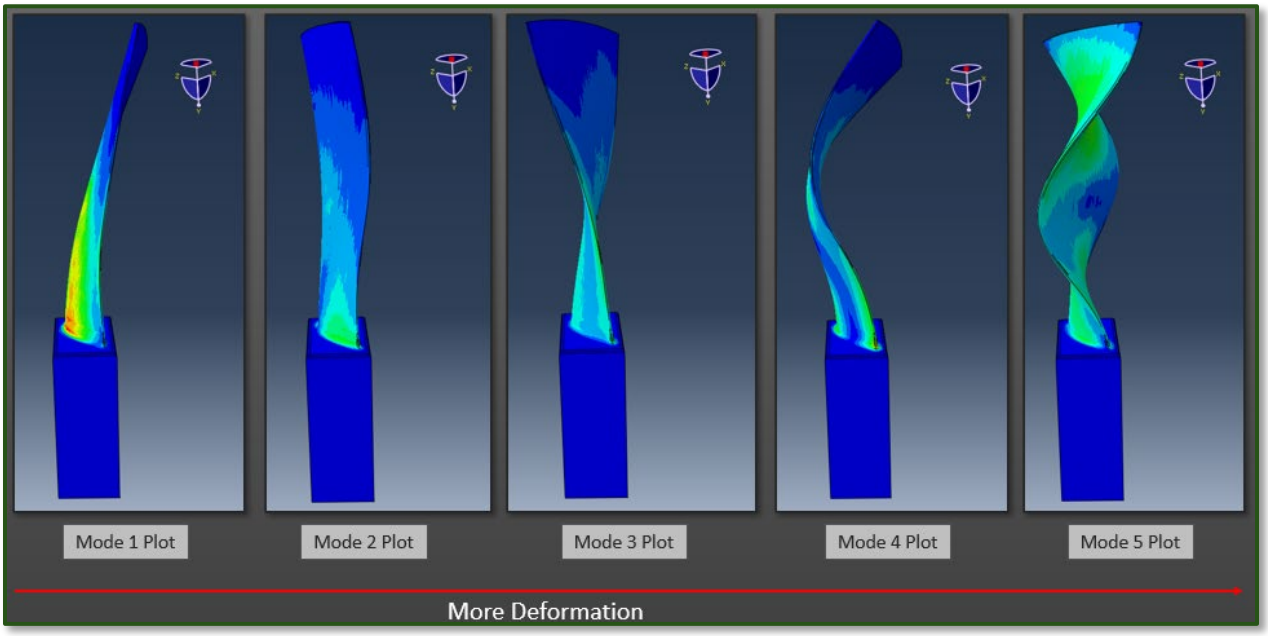

Figure 9 - Mode shapes of turbine blade

Additionally, the results for both principle and von mises stress maximums are shown below graphed in Figures 10 and 11. The maximum values were all located at the notch or notch region for both models. This result shows a direct increase in relative stress experience when adding the notch or fracture which further validates the model.

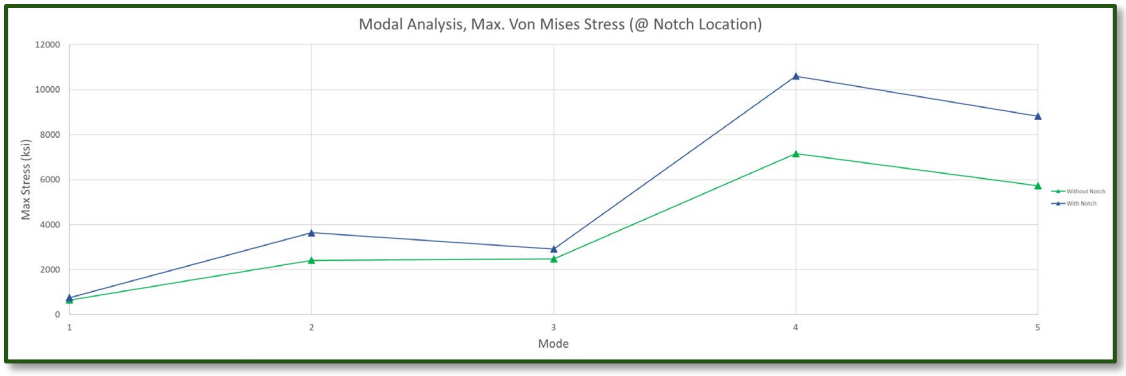

Figure 10 - Von Mises Stress Results

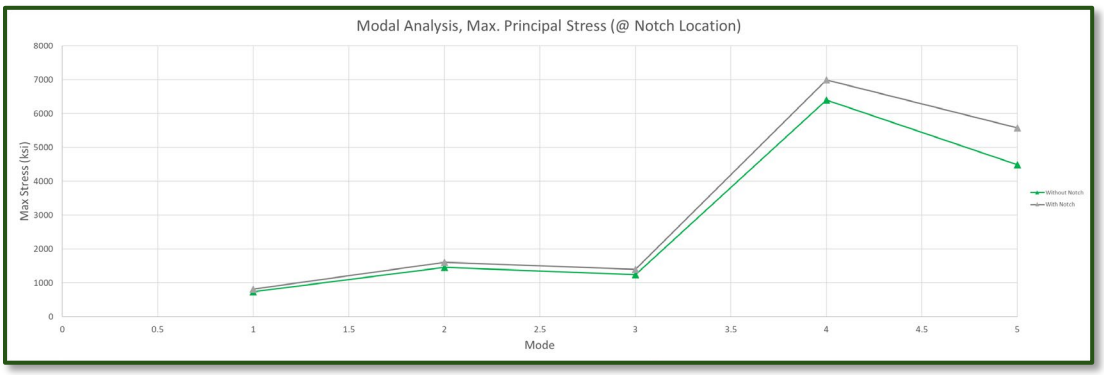

Figure 11 - Principal Stress Results

In this paper, a modal vibrational was completed using the finite element method. The mode shapes and modal frequencies were found and represented. Given this data, Hyphen Innovations will test their turbine blade design to represent modes 3 and 4. The reasoning for this is because the information for modes 3 and 4 match up best with the desired application for the turbine blades they are making. This model was verified using principle and von mises stress numbers that showed a relative change when introducing a “notch” or simulated fracture in the stress bearing geometry of the part.

Acknowledgements

Thank you to Dr. Manigandan Kannan, Dr. Julie Zhao from the University of Akron, Dr. Onome Scott-Emuakpor from Hyphen Innovations, and everyone at the Ohio Aerospace Institute who supports the Ohio Space Grant Consortium.

High Altitude Ballooning/Atmospheric Validation

Student Researcher: Alex Dotson

Central State University
Manufacturing Engineering

Abstract

Atmospheric validation research aims to improve our understanding of atmospheric behavior through the validation of atmospheric models and data. This research involves comparing modeled data with observed data to assess the accuracy of predictions made by atmospheric models. By validating atmospheric models, researchers can improve the reliability of weather forecasts and climate change predictions. Additionally, atmospheric validation research helps identify uncertainties and biases in modeled data, leading to improvements in the representation of atmospheric processes. Through ground-based observations, atmospheric models can be validated across different spatial and temporal scales. Furthermore, atmospheric validation research involves the evaluation of model performance in different atmospheric conditions, such as extreme weather events. By validating atmospheric models, researchers can enhance our ability to predict and understand atmospheric behavior, ultimately leading to advancements in weather forecasting and climate science. Overall, atmospheric validation research plays a crucial role in improving the accuracy and reliability of atmospheric models, ultimately enhancing our understanding of atmospheric behavior.

Objectives

The primary objective when launching a high-altitude balloon is to conduct scientific experiments and observations in the Earth's upper atmosphere. These experiments aim to gather valuable data on various atmospheric parameters, including temperature, humidity, pressure, and composition, at altitudes that are challenging to access through conventional means. The data collected during the high-altitude balloon flight contribute to a better understanding of atmospheric processes, climate dynamics, and environmental changes. This information can be used to validate and refine atmospheric models, improving the accuracy of weather predictions and enhancing our overall understanding of the Earth's atmosphere.

Methodology

This research involves evaluating the accuracy of atmospheric models by comparing their predictions with real-world atmospheric measurements from ground-based instruments and satellite observations. By conducting this comparison, researchers can identify any discrepancies or biases in the model output and improve the representation of atmospheric processes in the models. This methodology helps validate the reliability of atmospheric models, leading to enhancements in weather forecasting accuracy and climate change predictions. Additionally, comparing modeled data with observed data allows researchers to assess the performance of models under different atmospheric conditions, such as extreme weather events, providing valuable insights into atmospheric behavior.

Figures & Charts

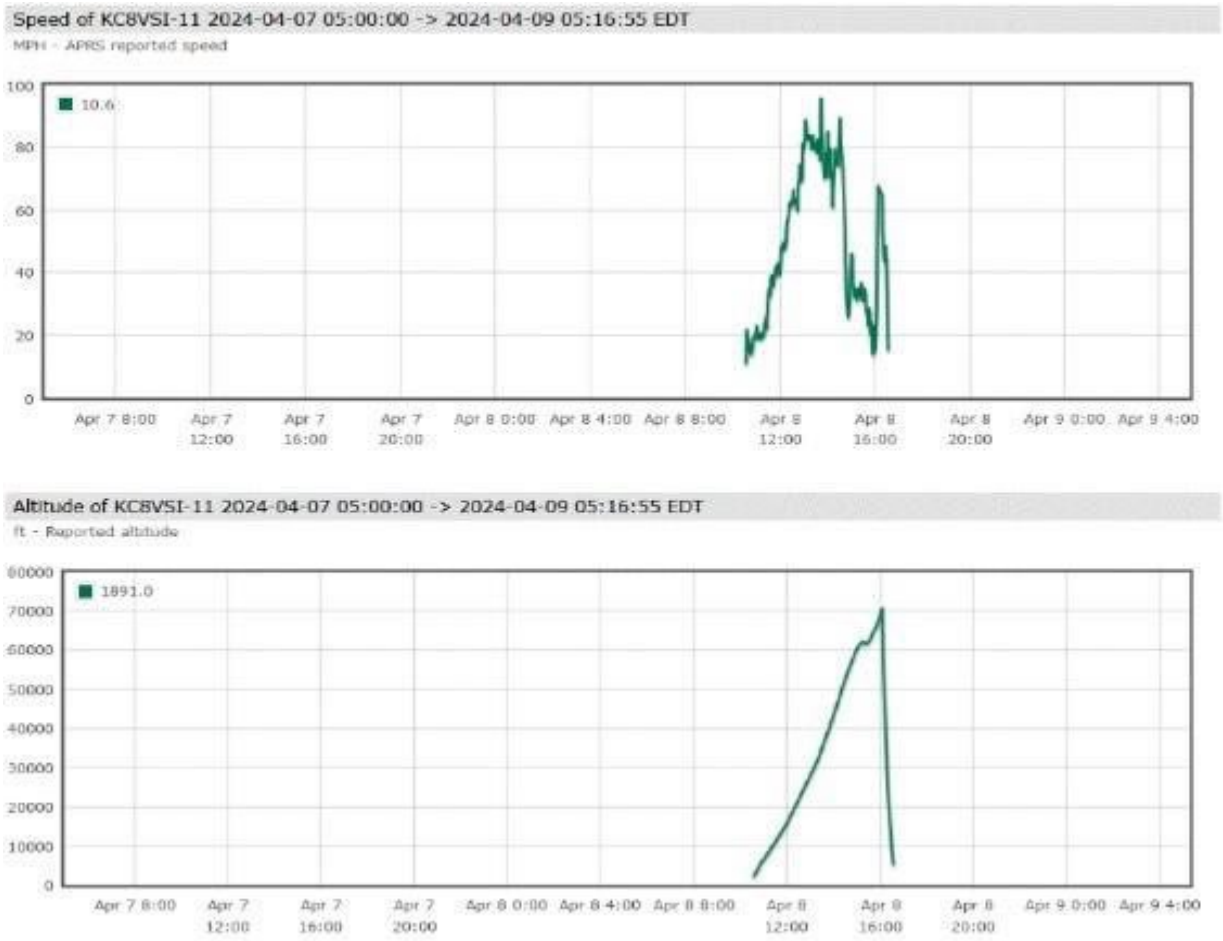

Figure 1: Indicates payload speed and altitude during flight.

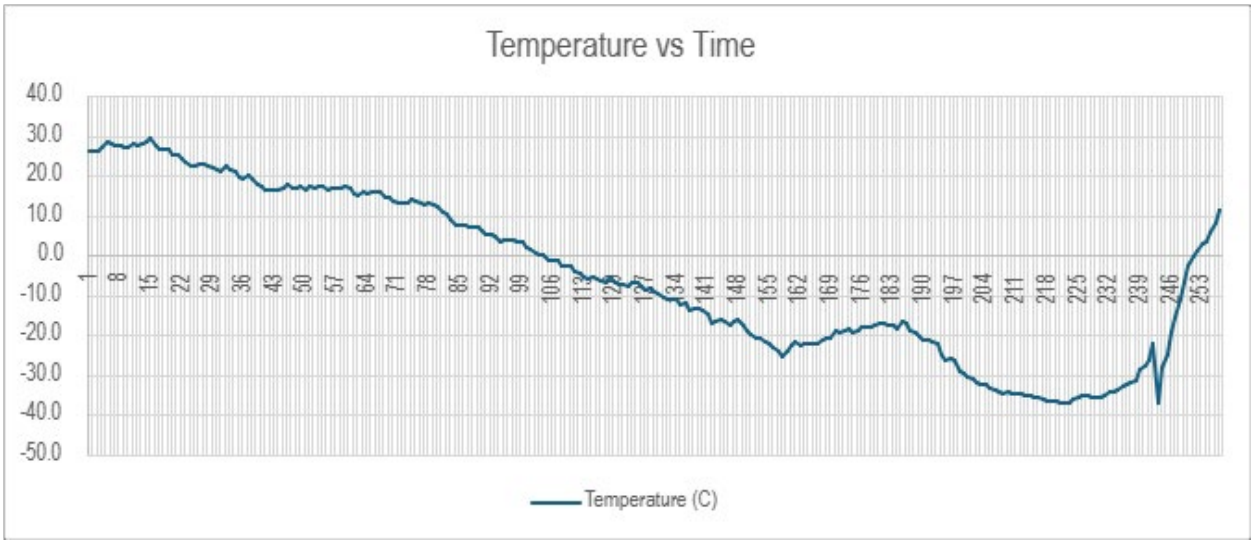

Figure 2: Temperature vs Time chart (time measured in minutes)

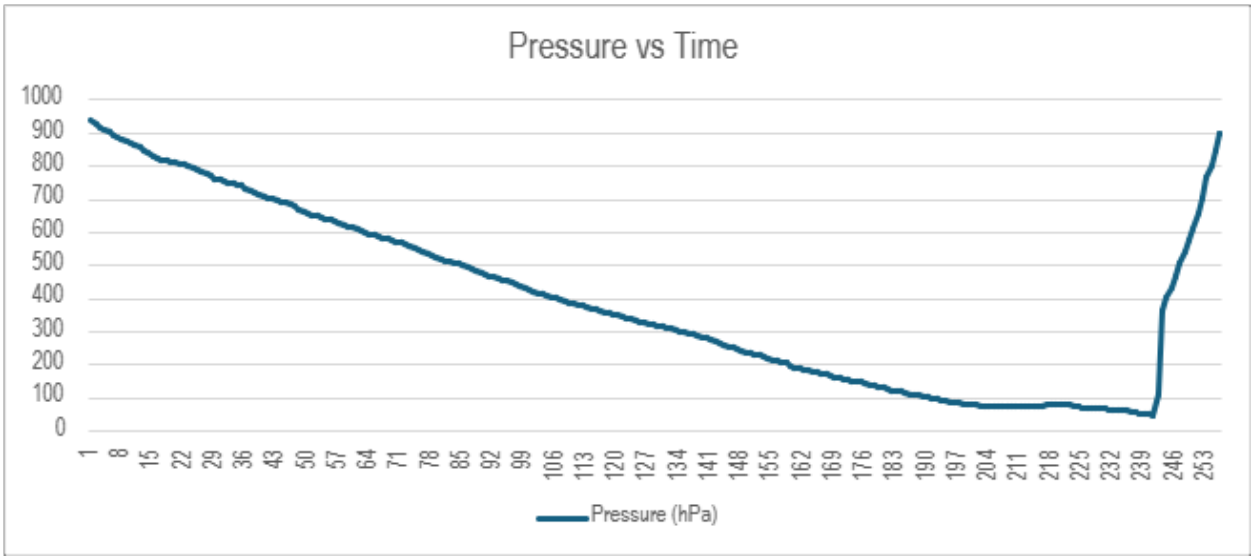

Figure 3: Pressure vs Time chart

Acknowledgements

This project could not have been completed without the help of my advisor Dr. Augustus Morris. I would also like to thank the Ohio Space Grant Consortium and the Ohio Aerospace Institute for hosting the symposium.

References

1. Author links open overlay panelKenjiro S. Lay a, et al. "High Altitude Balloon Testing of Arduino and Environmental Sensors for CubeSat Prototype." *HardwareX*, Elsevier, 16 June 2022, www.sciencedirect.com/science/article/pii/S2468067222000748.
2. "Section 950: Electronics for Atmospheric & Space Measurements." *Associate Dean for Undergraduate Education*, adue.engin.umich.edu/engr100_sections/950-atmosphere-and-space/. Accessed 28 Apr. 2024.

Ethanol-Induced Neural Activity in Male Compared to Female Rats

Student Researcher: Julie M. Dunlap

Advisor: Dr. Clare Mathes

Baldwin Wallace University
Department of Neuroscience

Abstract

The goal of this study was to determine if systemic ethanol administration induces neural activity in brain regions in female rats differently than it does in male rats. Most of the studies reviewed used exclusively male rats (Chang et al., 1995, Criado et al. 2000, Herring et al., 2004, Saalfield et al., 2019, Segovia et al., 2013) and this project aimed to determine if alcohol's impact is different in female rats. This is a problem because the prevalence of alcohol use disorder is increasing in women (White et al., 2015), yet women are underrepresented in basic research. This experiment may be used as preliminary research for future studies in the behavioral neuroscience lab at BW that will focus specifically on female rats.

Project Objectives

We hypothesized that the brains of male and female rats would process alcohol similarly, thus both sexes could be used in future research without concern of confounding sex differences. If there would be alcohol-induced sex differences at a neural level, this could provide information leading to different treatments between men and women with alcohol use disorder.

Methods

To do this, a group of female rats (n=8) and a group of male rats (n=8) were exposed to saline injections before the experiment to acclimate them to the injection so that the stress of the large injection on experiment day did not influence our data. On experiment day, the group of female and group of male rats were either exposed to a concentration of ethanol (20% at 12.5 ml/kg ip, n=4/sex) or saline (n=4/sex). Two hours after the injection, the rats were euthanized and perfused, after which their brains were collected. The brains were sliced and stained through a process known as immunohistochemistry. We evaluated neural activity (as shown by the expression of Fos protein) in brain regions that are part of the limbic system, which processes information and guides behavior based on reward. These brain regions included the central nucleus and basolateral nucleus of the amygdala, the lateral hypothalamus, the lateral septum, and the nucleus accumbens. The data were analyzed to determine if there were differences in Fos levels induced by ethanol between female and male rats.

Results and Discussion

We expected to see significantly more Fos in brain reward regions in at least the male rats that were injected with ethanol compared to those injected with saline. Unfortunately, we found that ethanol injection did not reliably induce Fos in target brain regions when the male data were analyzed separately (Figure 2) or when the male and female data were combined (Figure 3). Thus, we were unable to assess sex differences due to failure to replicate ethanol-induced Fos in male rats. Our data were likely not significant due to low sample size and the qualitative, as opposed to quantitative, scoring of Fos done by students.

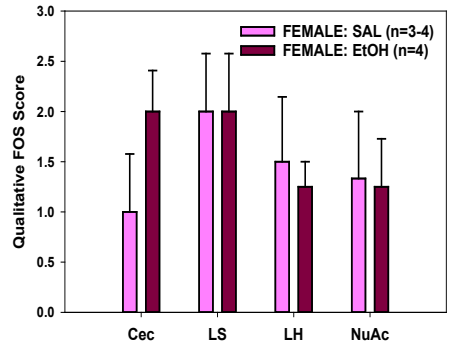

Figure 1. Ethanol did not induce Fos in the target brain regions of female rats.

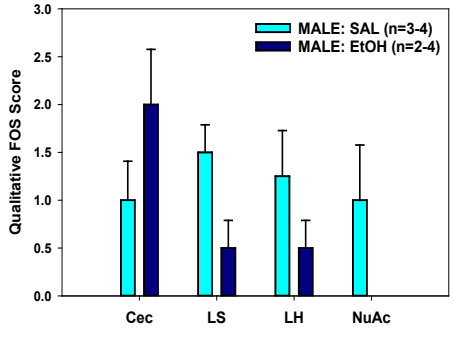

Figure 2. Ethanol did not induce Fos in the target brain regions of male rats.

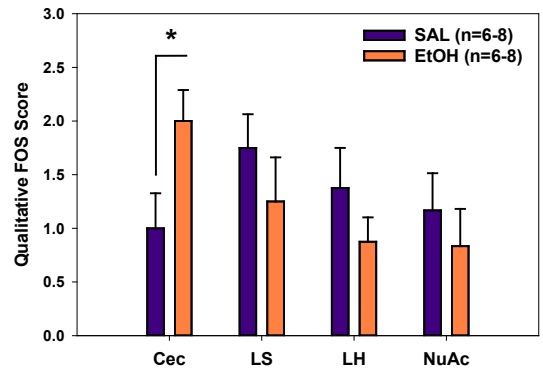

Figure 3. When Fos scores of both male and female rats were combined, ethanol-induced Fos in the CeC in a manner approaching statistical significance (p=0.069), but differences did not emerge in the other brain regions (p>0.05).

Acknowledgments and References

Funding for this project was provided by OSGC and Baldwin Wallace Neuroscience Department. I would like to thank all the students involved in the Fall 2023 and Spring 2024 NRO459: Faculty-Student Collaboration for their help in this project. I acknowledge experimental and technical assistance by Mallory Witt and Gregg DiNuoscio. I am also grateful for the animal care provided by the Neuroscience vivarium staff.

1. Chang SL, Patel NA, Romero AA. Activation and desensitization of Fos immunoreactivity in the rat brain following ethanol administration. Brain Res. 1995 May 8;679(1):89-98. doi: 10.1016/0006-8993(95)00210-h. PMID: 7648269.
2. Criado JR, Morales M. Acute ethanol induction of c-Fos immunoreactivity in pre-pro-enkephalin expressing neurons of the central nucleus of the amygdala. Brain Res. 2000 Apr 7;861(1):173-7. doi: 10.1016/s0006-8993(99)02468-3. PMID: 10751579.
3. Herring BE, Mayfield RD, Camp MC, Alcantara AA. Ethanol-induced Fos immunoreactivity in the extended amygdala and hypothalamus of the rat brain: focus on cholinergic interneurons of the nucleus accumbens. Alcohol Clin Exp Res. 2004 Apr;28(4):588-97. doi: 10.1097/01.alc.0000122765.58324.6d. PMID: 15100610.
4. Saalfield J, Spear L. Fos activation patterns related to acute ethanol and conditioned taste aversion in adolescent and adult rats. Alcohol. 2019 Aug;78:57-68. doi: 10.1016/j.alcohol.2019.02.004. Epub 2019 Feb 22. PMID: 30797833; PMCID: PMC6612301.
5. Segovia KN, Vontell R, López-Cruz L, Salamone JD, Correa M. c-Fos immunoreactivity in prefrontal, basal ganglia and limbic areas of the rat brain after central and peripheral administration of ethanol and its metabolite acetaldehyde. Front Behav Neurosci. 2013 May 24;7:48. doi: 10.3389/fnbeh.2013.00048. PMID: 23745109; PMCID: PMC3662884
6. White A, Castle IJ, Chen CM, Shirley M, Roach D, Hingson R. Converging patterns of alcohol use and related outcomes among females and males in the United States, 2002 to 2012. Alcoholism, clinical and experimental research. 2015. 39(9), 1712–1726. https://doi.org/10.1111/acer.12815

Design Space Exploration For A Novel Self-Healing Elastomer, Informed By Bayesian Optimization

Student Researcher: Grant Eifert

Advisor: Dr. Robert Lowe

University of Dayton
Mechanical Engineering

Introduction

Self-healing elastomers are an emerging class of materials capable of mitigating externally induced damage in soft structures and devices (e.g., soft robots). Recent advancements in polymer chemistry have led to the development of "BeckOHflex," a 3D-prinatble elastomer with real-time autonomous self-healing [1]. BeckOHflex is produced exclusively from commercially available (COTS) precursors, enabling straightforward production at scale. At present, for BeckOHflex and other self-healing elastomers, the trade-offs between virgin mechanical properties and self-healing efficiency enabled by tuning chemical composition are not well known. To address this compelling research opportunity, a Bayesian optimization platform (EBDO+) is utilized to facilitate an experimental design space exploration that investigates the interplay between virgin mechanical properties (hardness and toughness) and self-healing efficiency (ratio of self-healed toughness to virgin toughness) as chemical composition is varied. The use of EBDO+ is expected to generate a well-defined Pareto frontier after tens of experiments out of a possible 2,000+ discrete input parameter combinations.

Methods

The experimental design was constructed by varying the **crosslinker** (hexanediol diacrylate, **HDDA**) and **chain-transfer agent** (pentraerythritol tetrakis, **PETMP**) from 0-10% by volume while holding the molar ratio of acrylate (2-hydroxyethyl acrylate and hexanediol diacrylate) to photoinitiator (phenylbis phosphoine oxide) nearly constant. Informed by previous-iteration experimental inputs (i.e., vol. % HDDA and PETMP) and the resulting outputs from mechanical testing (i.e., virgin hardness, virgin toughness, and self-healing efficiency), an open-source Bayesian optimization platform (EBDO+) was used to suggest next-iteration experimental inputs. For each formulation investigated, component masses were calculated from their respective molar weights and weighed out on an analytical balance with a resolution of +/- 0.001g. Resin was synthesized in 100 mL batches. Test samples were cast in a custom ASTM D412 Type C silicone mold. Using an external UV lamp with a power rating of 0.1974 µW, the samples underwent three cure-rest cycles (10 s cure followed by a 1 min rest) followed by a 4 min continuous cure. After synthesis and curing, the as-cast test samples were stored in a low-humidity nitrogen-purged desiccator (< 10% RH).

A Shore 00 analog durometer was used to measure the **hardness** of all "virgin" (undamaged) samples in their undeformed state prior to tensile testing. Each sample's hardness was interrogated in three locations (gauge section (center) and both grip sections (ends)), recorded after 15 s of contact, and then averaged.

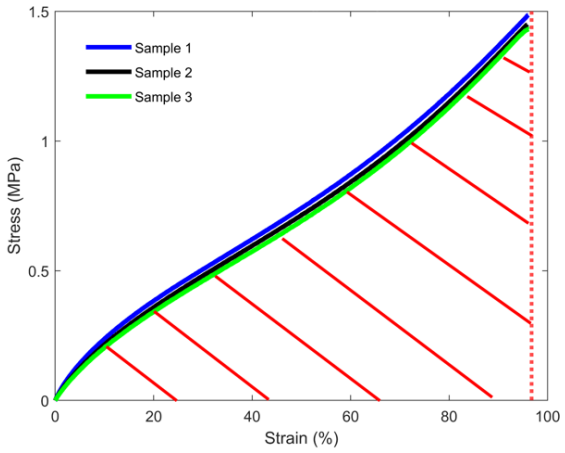

Figure 1: Calculation of toughness (red striped area) from a uniaxial tensile test.

To determine the **toughness** of each "virgin" (undamaged) specimen, uniaxial tension testing was performed on an Instron 3365 universal testing machine equipped with a 2-kN load cell for force measurement and a custom optical setup (FLIR Blackfly 3.0 machine vision camera with a 35-mm lens) to facilitate strain measurement. Tests were performed at a displacement rate of 500 mm/min, with 5 psi of pneumatic grip pressure applied to hold the samples in place. Open-source image processing software and a custom Python code were used to calculate the length-averaged engineering strain between two gage marks. Engineering stress

was calculated as measured force divided by original cross-sectional area (via measurements taken by a digital caliper). As shown in Fig. 1, toughness (area under the engineering stress-strain curve) was calculated through numerical integration. The toughness for each formulation was reported as the mean of four to six different samples.

To determine **self-healing efficiency**, virgin test specimens (four to six per formulation) were cut horizontally across the center of their gage section with a clean razor blade, then allowed to rest for 5 min. Each half of the specimen was then placed back together under nominal manual pressure and allowed to self-heal for 5 min. Post-healing uniaxial tension testing was performed, and the resulting toughness was calculated. The self-healing efficiency of a formulation was calculated by dividing the average toughness of the (four to six) cut-and-healed samples by the average toughness of the (four to six) virgin samples.

Results And Discussions

Thus far, 15 different formulations have been synthesized, cured, and tested to begin populating the design space (blue dots in Fig. 2). The emerging Pareto front in Fig. 2 shows the tradeoffs between the three different properties of interest. While there is currently not enough data for a well-defined 3D surface, a few key trends are emerging.

First, hardness directly correlates with percent volume of crosslinker (HDDA). Self-healing efficiency is highest when there is a higher concentration of chain-transfer agent (PETMP) in the formula. Virgin toughness has generally increased with higher levels of HDDA. Most of these high-HDDA formulations achieved high levels of toughness with very low strain due to the rigidity (stiffness/hardness) of the material. So far, most of the generated formulas across the design space have had higher percent volumes of HDDA, which leaves more room for exploration.

The experimental campaign is shifting towards more emphasis on low-HDDA and high-PETMP compositions, which tend to yield more compliant (less rigid/stiff/hard) materials. These formulations generally show promising self-healing efficiency. As the design space continues to be investigated and more data points are collected, a more well-defined Pareto frontier will form. From there, selected Pareto-optimal formulas will be further interrogated for important not-yet-characterized properties, including 3D printability and viscoelasticity.

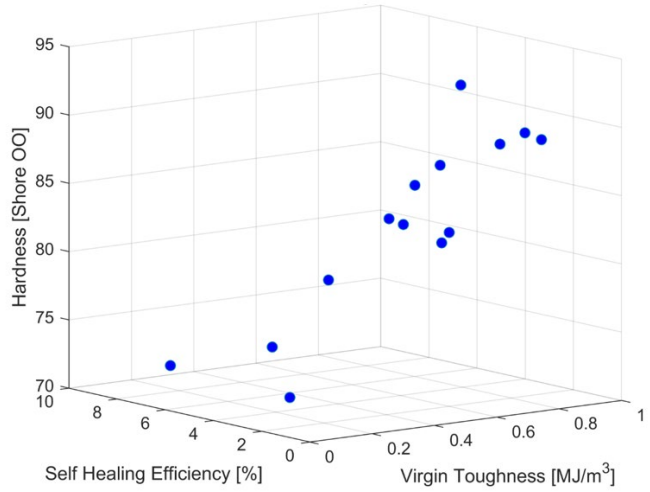

Figure 2: Current design space of formula optimization campaign.

Conclusions

With 15 different formulations tested, the design space is approximately 50% through its initial search. As more data is collected, a clearer Pareto front will allow for better insight into the effect of chemical composition on mechanical properties (hardness and toughness) and self-healing efficiency. From there, specific chemical compositions of BeckOHflex can be further investigated to better understand their suitability for various end-use applications.

Acknowledgements

The authors thank project collaborators Robert “Max” Drexler, Sachin Babu, Luke Baldwin, Anesia Auguste, and Christopher Crouse for their contributions to this work. Thanks to Dr. Vincent Chen for technical support. RLL acknowledges support from an AFRL Summer Faculty Fellowship. Distribution A: Approved for public release; distribution is unlimited (PA # AFRL-2024-1847).

References

Beckett, J., et al. (2024). Tough 3D-printable elastomers for real-time autonomous self-healing in soft devices. *Submitted*.

Modulation of Noxious Stimuli Reactivity and AMPA Receptor Localization in Sensory Neuron Development in a C. elegans Autism Spectrum Disorder Model

Student Researcher: Angelina Gentilin

Advisor: Dr. Jeffrey Zahratka

Baldwin Wallace University
Department of Neuroscience, Department of Psychology, Department of Biology and Geology

Abstract
Neurodevelopmental autism spectrum disorder (ASD) is a common diagnosis, where one in every 100 children is diagnosed globally, typically characterized by aberrant social behaviors and reactions to sensory stimuli. While there is limited research investigating the mutations of this diagnosis, 22q13.3 deletion syndrome, specifically the recurring breakpoint in the Shank3 gene, has been correlated with ASD development. The SHANK3 protein is part of a family of scaffolding proteins involved in excitatory glutamatergic signaling in postsynaptic densities. Some of these signaling pathways target the ionotropic glutamate AMPA receptor, to which the GluA1 subunit of the receptor directly binds to the PDZ domain of SHANK3. Further implications demonstrate decreased AMPA receptor-mediated signaling in a SHANK3 mutant model. While this suggests a basis for one potential neural mechanism behind ASD, the Shank3 mutation needs to reflect similar behavioral patterns. While Shank3 mutant mice models have displayed similar abnormal social and repetitive behaviors, there has been limited research on reactions to nociceptive stimuli. Therefore, we will investigate the model organism Caenorhabditis elegans with a mutation in SHN-1, a SHANK3 protein homolog, to image the localization of AMPA receptors in postsynaptic densities and measure reactions to noxious stimulus presentation to further the knowledge on ASDs.

Project Objectives
Due to the influence of the SHANK family of proteins in autism, specifically SHANK3, their utilization as an ASD model can further the knowledge surrounding the molecular implications of these disorders. C. elegans provide a useful tool due to their established genetic map and identical development, along with their translucence allowing for live imaging. The establishment of SHN-1 as a SHANK3 homologue provides the opportunity to investigate the circuitry involved in this mutation and determine reactivity in response to noxious stimuli. We hope to decrease the knowledge gap surrounding ASDs to potentially allow for more specified treatment of these disorders.

Methods
To investigate this model, behavioral assays and imaging will be conducted to determine the molecular basis and behavioral implications of ASD using two SHN-1 deletion models. SHN-1 is comprised of the ANK domain, PDZ domain, Proline-rich region, and SAM domain, therefore only missing the SH3 domain present in human SHANK3 proteins (Oh et al., 2011). The shn-1(gk181) mutation is a deletion including most of the ANK domain, and the entire PDZ domain—the shn-1(ok1241) mutation includes the entire PDZ domain and Proline-rich region. Since AMPA receptors bind directly to the PDZ domain in SHANK3, the deletion mutations may influence receptor location on the postsynaptic densities. Therefore, as a possible neural mechanism, both mutations will be genetically crossed with a strain modified with green fluorescent protein AMPA receptors (nuIs25 [glr-1p::glr-1::GFP + lin-15(+)]) to conduct live imaging of their location in postsynaptic densities of both SHANK3 mutations. Moreover, due to their identical development and short life span, AMPA receptor localization can be investigated at different development points as characterized by distinct size differences of C. elegans. The SHN-1 mutation and reduced scaffolding protein activity are also expected to influence ASH sensory neurons in C. elegans, the primary nociceptive receptors in both noxious chemosensation and light mechanosensation (Kaplan & Horvitz, 1993). Additionally, ASH neurons signal to interneurons AIB and AVA, which initiate backward locomotion in C. elegans in response to stimulation (Piggott et al., 2011). Therefore, two behavioral assays designed to activate ASH through nociception and initiate backward locomotion, the octanol assay (chemoreception) and nose poke (mechanoreception), will be conducted with both SHN-1 mutations. We hypothesize decreased sensitivity levels to noxious stimuli presentation in shn-1 mutants, through which display a mislocalization of AMPA receptors on the postsynaptic densities of sensory neurons.

Results and Discussion
This study characterized the shn-1 mutants' avoidance responses in both a feeding and nonfeeding state. Previous literature investigating behavioral responses to both avoidance assays has primarily focused on conducting the testing on untreated plates and, therefore, only focused on behavioral responses in a nonfeeding state. However, food-treated plates are not the only treatment that initiates this feeding state; the serotonin-treated plates also accomplish this.
Both shn-1 mutants displayed similar patterns of behavior, where there was no difference in reactivity to the noxious stimuli presentation whether mutants were in a feeding or nonfeeding state. However, considering the animals reacted similarly on

the untreated plate conditionings, the shn-1 mutant strain's ability to avoid a noxious stimulus was established. Both shn-1 deletion animals maintained the ability to respond to chemosensation, but the increased sensitivity levels when placed on treated plates were not present. Therefore, the shn-1 mutations are likely interacting with the ASH sensory neurons in a manner that prevents increased sensitivity levels. Considering that ASH is required for backward locomotion and that the pattern of behavior on treated plates is representative of the untreated plates, ASH's ability to signal to the command interneurons must remain intact. Therefore, the lack of signal amplification abilities likely results from improper signaling involving gpa-11.

Since shn-1 is a scaffolding protein localized in postsynaptic densities, the deletion likely altered the localization of receptors needed to receive the amplification signals from treated plates. Therefore, ASH could not increase sensitivity to the treated plate conditions, and avoidance behavior was not altered. This may result from improper signaling of 5-HT to gpa-11 or gpa-11's signals not being correctly received. The same behavioral test was conducted on all three other mutant strains to determine how signaling was altered.

Due to the similarities between shn-1 mutant animal behaviors and ionotropic glutamate receptor mutant animal behaviors, behavioral testing was also conducted with magi-1(gk657) animals to determine how shn-1 deletions result in behaviors similar to deletions of genes encoding for receptors. Since MAGI-1 encodes two isoforms present in SHN-1's PDZ domain, the results could demonstrate if the decreased reactivity in the behavioral data is a result of the interaction between SHN-1 and GLR-1/NMR-1 since both receptors bind to the PDZ domain (Emtage et al., 2009). The magi-1(gk657) animals displayed the same behavioral pattern as all previous mutants. This further supports the concept that the decreased reactivity is due to improper signaling from ASH. Additionally, the data suggests some type of interaction between altered behaviors as a result of SHN-1 and the two ionotropic glutamate receptors.

Figures/Charts

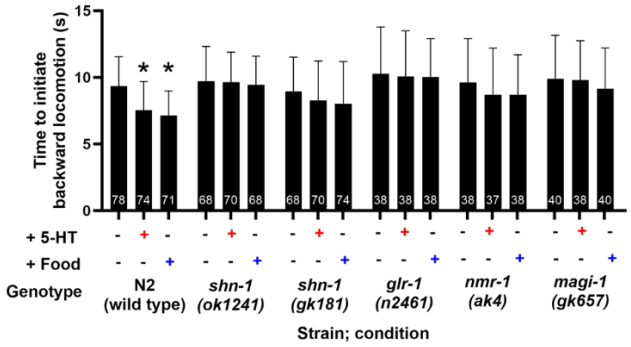

Acknowledgments

I'd firstly like to thank Dr. Zahratka for being my mentor and research advisor for the past three years working on this project and to Manimone Sengvoravong and Jonathan Phillips as my research assistants who helped with data collection. I would also like to thank the BW Department of Neuroscience for funding this project's supplies and equipment, the Edith C. Robinson Grant for Developmental Neuroscience Research, and the Nu Rho Psi Undergraduate Research Grant for additional supplies of financing and equipment. Lastly, I want to thank the Ben Caskey Memorial Scholarship, Ohio Space Grant Consortium (OSCG), and Dr. and Mrs. Lauria for funding my time here at BW and allowing me to continue this research throughout the years

References

Emtage, L., Chang, H., Tiver, R., & Rongo, C. (2009). MAGI-1 Modulates AMPA Receptor Synaptic Localization and Behavioral Plasticity in Response to Prior Experience. *PLoS ONE*, *4*(2), e4613. https://doi.org/10.1371/journal.pone.0004613

Kaplan, J. M., & Horvitz, H. R. (1993). A dual mechanosensory and chemosensory neuron in Caenorhabditis elegans. *Proceedings of the National Academy of Sciences*, *90*(6), 2227–2231. https://doi.org/10.1073/pnas.90.6.2227

Oh, W. C., Song, H.-O., Cho, J. H., & Park, B.-J. (2011). ANK repeat-domain of SHN-1 Is indispensable for in vivo SHN-1 function in C. elegans. *Molecules and Cells*, *31*(1), 79–84. https://doi.org/10.1007/s10059-011-0007-9

Piggott, B. J., Liu, J., Feng, Z., Wescott, S. A., & Xu, X. Z. S. (2011). The Neural Circuits and Synaptic Mechanisms Underlying Motor Initiation in C. elegans. *Cell*, *147*(4), 922–933. https://doi.org/10.1016/j.cell.2011.08.053

Fine-Grained Air Quality Sensing with IoT

Student Researcher: Julia M. Gersey

Advisor: Dr. Brian Krupp

Baldwin Wallace University
Department of Computer Science

Abstract
Air quality is an essential factor for human health. The World Health Organization states there are "4.2 million deaths every year as a result of exposure to ambient (outdoor) air pollution". Additionally, they report that "9 out of 10 people worldwide live in places where air quality exceeds WHO guideline limits". In 2022, Cuyahoga County, an area of 459.07 square miles and a population of 1,245,337 (as of 2020), had only one air quality sensor monitoring Particulate Matter 2.5 levels, proven to be the most dangerous kind for humans to breathe. Particulate Matter 2.5 (PM 2.5) are inhalable particles with a 2.5-micrometer diameter and pose the most significant risk to humans as they can penetrate human lungs and the bloodstream. Long-term exposure can lead to asthma and lung cancer, among other health conditions. Fortunately, since the beginning of this research project (2022), there has been an increase in the number of PM 2.5 sensors. For this project, we specifically use Internet-of-things (IoT) devices to build a network of sensors to capture fine-grained air quality via PM 2.5 levels and report it to our web dashboard. Beyond creating these low-cost microcontrollers, we allow students to learn computer science, engineering, and air quality topics through our curriculum, which allows them to build and deploy their sensors to help their community.

Project Objectives
This project aims to deploy a network of low-cost air quality sensors throughout Cleveland to capture more fine-grained air quality data throughout the city. Additionally, we are building and teaching a curriculum at a local middle school so students can learn important air quality, computer science, and engineering topics.

Sensor Prototype and Testing
Our sensor units were made with four main factors in mind: low-cost, low-power, generally available boards, and accuracy. Commercial-off-the-shelf air quality sensors cost ~$200, and ours cost around $40 per sensor. We also focused on making our sensors low power because power is expensive and limits where these sensors could be placed. Next, we used generally available boards such as Raspberry Pi's and Arduino's, because both are easy for younger computing students to learn. Lastly, accuracy is important in capturing trends in Cleveland's air quality. Although low-cost sensors are less precise than higher-cost alternatives, they can still accurately show general trends in air quality.

Our sensor units active in the field are made up of a Raspberry Pi and Plantower PMS5003 2.5 sensor, and we programmed them to start reporting their PM 2.5 readings to our web dashboard once they have power and connectivity. We partnered with a Cleveland company, PCsForPeople, who provides Wi-Fi hotspots and refurbished electronics to low-income neighborhoods. By leveraging their existing infrastructure and hotspots around Cleveland, we got both power and connectivity for our sensors.

Figure 1. Teaching at Incarnate Wood Academy

Figure 2. Current AQIoT Sensor with Raspberry Pi Pico W

Curriculum Results

Figure 1 above shows two members of the MOPS Research Group, Hannah Ogden and me (Julia Gersey), teaching the after-school program at Incarnate Word Academy. The curriculum was 13 weeks long, with three divided sections: Air Quality, Computer Science, and Engineering. We started by having the students explore current air quality data and trends, specifically in Cleveland, so that they could understand the problem at hand. Next, we entered the Computer Science section, which focused on teaching the students Python and Raspberry Pi microcontrollers. Afterward, we taught them essential engineering topics: power, circuits, 3D printing/modeling, and soldering. The last three sessions were dedicated to coding the sensors since all the hardware components were soldered together, and students could see the live PM 2.5 readings for their sensors.

Deployment Results

Figure 2 shows the current version of our sensor with the Raspberry Pi Pico W and PM 2.5 sensor inside a PVC box. This specific sensor is currently on our Burrell Observatory and has been reading and reporting the real-time PM 2.5 readings to our web server. We are currently building Android and iOS mobile applications and a public-facing website so anybody can go on and get our sensor readings from all around Cleveland. Additionally, we will have our API documentation for the students to use, and we will be able to have their sensors listed on our website's map as well. The mobile applications will serve as a way for Cleveland residents to see the latest readings more easily, as they would when they check the weather on their mobile devices.

Future Work

Our future work is focused on a campus deployment, increasing our sensors around Cleveland, and finalizing our curriculum so we can give it to more schools to use. This academic year allowed us to build out and teach our curriculum; however, we ideally want to have the curriculum available for any teacher to teach to their classes since all our materials are open source. This will allow those kids to learn more about air quality and important computer science topics they otherwise wouldn't.

Acknowledgments and References

I want to thank my advisor, Dr. Brian Krupp, for his continued support and mentorship, PCsForPeople for their partnership and support, Incarnate Word Academy for having us teach our curriculum, and the Ohio Space Grant Consortium for helping make this project possible through their scholarship.

Flow Visualization Studies for the Closed Loop Two-Phase Flow Chill-down Test Module for Future Integration with the Flow Boiling and Condensation Experiment onboard International Space Station

Student Researcher: Aimee Ghanem

Advisor: Chirag R Kharangate

Case Western Reserve University
Department of Mechanical and Aerospace Engineering

Abstract
Success of NASA's future space exploration missions is dependent on cryogenic fluid management systems being able to provide safe, effective, and reliable supply of cryogenic fluid to a variety of systems. A key technological challenge in this, as recognized by NASA, is the line chilldown and transfer process. For understanding chilldown process under microgravity, chilldown tests with a simulant fluid like normal perflourohexane (nPFH) can be conducted in the Flow Boiling and Condensation Experiments (FBCE) module currently available in the International Space Station (ISS). The focus of the present work is to develop and test a chilldown experimental setup under terrestrial conditions in a closed loop with PF-5060 as the working fluid.

Project Objectives
In this project, the study will focus on high-speed imaging of the different flow boiling regimes, viz., film, transition and nucleate boiling regimes during the chilldown of a pyrex tube. The flow regimes will be captured and correlated with the wall heat flux data to better understand and predict the transfer line chilldown process. The results from these ground-based flow visualization experiments are crucial to the development of the flow visualization test section for the space station experiments.

Methods
The experimental schematic is shown in figure 1. The chilldown experiment was carried out with a simulant fluid PF-5060 through SS-316 tubes to mimic the cryogenic transfer line chilldown process and the entire regimes of the chilldown process were captured. Postprocessing data obtained from the experiments conducted using a stainless steel are discussed in the following section. For future work, accurate heat flux can be estimated either by, directly heating the SS tube using an external power supply or using a Nichrome coated heater with Alumina insulating layer to heat the SS tube which allows flow visualizations using the pyrex/sapphire test sections. Currently we are setting up the pyrex tube for experimentation, figure 3. Given the necessity for high voltage/power, our focus lies in evaluating the durability of the connections between the nichrome wire and power source.

Results, and Discussion
The chilldown curves for the stainless-steel (SS) tube experiment (0.6V and 0.7V pump) can be seen in figure 2; the experiment captured all chilldown process regimes for PF-5060. Data was analyzed for 0.4V, 0.5V, 0.6V, 0.7V, 0.8V, 0.9V and 1V pumps and the following was interpreted: because of gravity in the horizontal flow configuration, the liquid re-wets the bottom wall first, hence all the top thermocouples read a higher re-wetting temperature. The propagation of quench front can be clearly visualized in the chilldown curves with the drop in wall temperature readings along the axial direction. Moreover, due to the high inlet subcooling, the curve further drops in the single-phase liquid region which was not present in most cryogenic chilldown experiments. At low inlet liquid subcoolings, the chilldown curves indicate a longer duration film boiling regime which is common for cryogenic chilldown process where the inlet

fluid is near saturation conditions. The duration of single-phase liquid convective regimes reduce as the inlet subcooling decreases. Along the axial direction from the inlet, upstream locations cool down faster compared to downstream locations as the quench front propagates through the tube. In general, the rewetting temperatures, critical heat flux values, regime-specific heat fluxes as well as regime-specific heat transfer coefficients tend to increase with increase in inlet liquid subcooling. The liquid re-wetting temperatures seem to be unaffected by the changes in inlet mass flow rates and the chilldown time decreases with increase in mass flow rate.

Figures/Charts

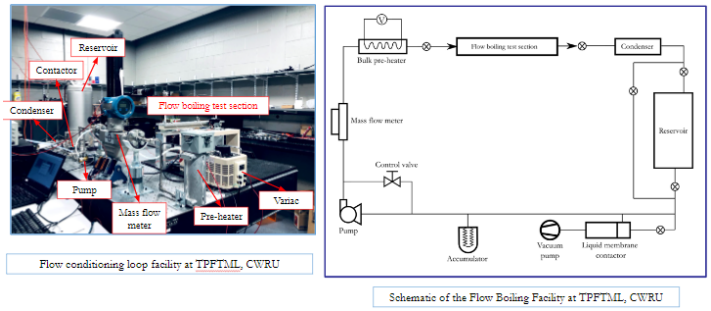

Figure 1: image and schematic of the flow boiling loop facility

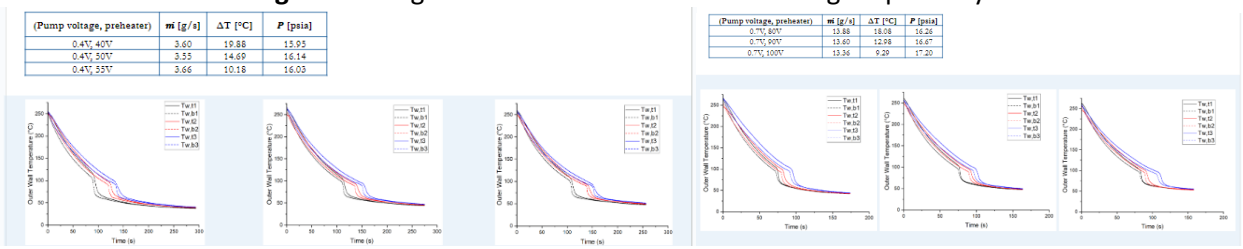

Figure 2: chilldown curves for 0.4V and 0.7V pumps

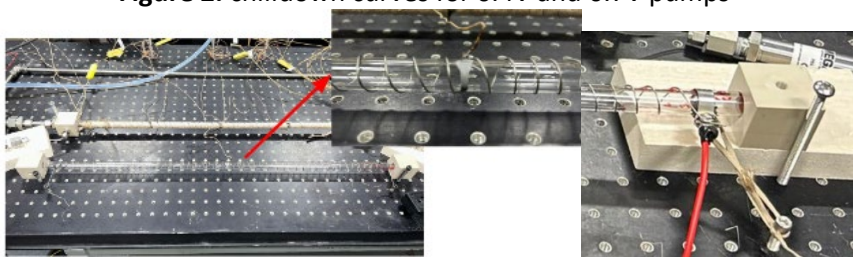

Figure 3: Pyrex tube setup at the facility

Acknowledgments

This research is supported by NASA; Grant #: 80NSSC22M0056. We also acknowledge the machining and fabrication support provided by the Engineering Services Fabrication Center at CWRU.

References

[1] Hartwig, J.W., Hu, H., Styborski, J., and Chung, J. “Comparison of Cryogenic Flow Boiling in Liquid Nitrogen & Liquid Hydrogen” International Journal of Heat & Mass Transfer Volume 88, 662-673. 2015.

[2] Darr, S.R., Hartwig, J.W., Dong, J., Wang, H., Majumdar, A.K., and LeClair, A.C., and Chung, J.N. “Two-Phase Pipe Chilldown Correlations for Liquid Nitrogen and Liquid Hydrogen” ASME Journal of Heat and Mass Transfer 141 (4), 042901. 2019.

[3] Burggraff, O.R. “An Exact Solution of the Inverse Problem in Heat Conduction Theory and Applications” ASME Journal of Heat Transfer 86, 373 – 380. 1964.

Cabin Atmosphere Filtration using Ambient Air Ionization

Student Researcher: Ian Harris

Advisor: Dr. John Horack

The Ohio State University

Department of Aerospace and Mechanical Engineering/Aerospace Engineering, Astrophysics and Astronomy, and Physics – Applied Track

Abstract

The mitigation of microbial life, encompassing bacteria and fungi, in the microgravity environment on the International Space Station presents heightened challenges compared to terrestrial environments. Consequently, astronauts frequently contend with prevalent bacterial and fungal infections due to constant exposure in confined spaces. Addressing this issue necessitates the development of a cost-effective and low-waste mechanism for the continuous neutralization of bacteria and fungi. One promising solution is ambient air ionization. Cabin Atmosphere Filtration using Ambient Air Ionization (CAFAAI) is a specialized ambient air ion thruster created to neutralize microbial life. It operates on a voltage amplifier circuit that converts low-voltage AC into high-voltage, low-current DC. This conversion is crucial for producing an electric field concentrated enough for effective ionization, typically around 10 kV, but with effectiveness increasing up to a certain voltage threshold. This study aims to test CAFAAI's effectiveness in neutralizing *Auerobasidium pullulans*, a fungus found on the International Space Station. Cultures of *A. pullulans* will be nebulized and introduced into agar plates in two distinct manners: direct injection and pre-treatment through CAFAAI. The comparison of the growth of surviving spores on these plates will provide insights into the effectiveness of ambient air ionization for microbial neutralization in microgravity environments.

Project Objectives

The research goal of CAFAAI was to determine the effectiveness of using ambient air ionization for neutralizing microorganisms, mainly fungi, for microgravity applications.

Methods

Prior to fungi testing, agar plates were be made. *A. pullulans* grows well using a potato dextrose solution, where the potato dextrose is made up of potato infusion and dextrose. The potato dextrose broth (PDB) was autoclaved for 45 minutes at 121°C, then the PDB was left to cool overnight. After the PDB cooled to 60°C, Chloramphenicol, which is an anti-bacterial, was added to deter bacteria growth. After the broth had cooled further, 25 mL was added to Petri dishes and left to cool overnight. The yeast stock was an isolate of *A. pullulans* which was collected from buildings on Ohio State's campus. It was stored at -80°C until use. The isolate was revived by adding about 10 L of frozen stock to 25 mL of the PDB. The solution was incubated for 2 days at 25°C while shaken at 180 rpm. This procedure was derived from the paper *Persistence of viable MS2 and Phi6 bacteriophages on carpet and dust*.

For testing, a negative and positive control was needed to validate the results. The negative control shows if there were any contamination in the testing volume and was made by nebulizing the PDB and passing it through CAFAAI while turned on. It was then collected in a potato dextrose agar (PDA) plate. The positive control is the base result to show how much of *A. pullulans* will grow without any ionization introduced; this was made by adding 3 mL of fresh yeast stock to the nebulizer and injecting it directly into a PDA plate. After the controls were made, active testing started. CAFAAI has have 3 stages, each stage consisting of a positive grid and a negative grid. 2 tests were made for 1 stage, 2 stages, and 3 stages attached electrically in parallel. The yeast stock-PDB solution was nebulized for 45 seconds and passed through CAFAAI. Then the nebulizer was turned off and 15 seconds passed with CAFAAI still on. Lastly, CAFAAI was turned off and the contents were allowed to settle for 45 seconds. All plates were then incubated at 25°C for 3 days.

Results and Discussion

In Figure 1, the bottom row of agar plates indicates the results of using 1 stage, the middle row indicates the results of using 2 stages, and the top row indicates using 3 stages. It can be seen there is a clear trend – as the

number of stages increases, the contact time increases as well, killing more fungi. There is also an interesting growth difference for *A. pullulans* when it had more contact time. *A. pullulans* has a dimorphic growth structure, which means it can grow in two different ways: as a yeast-like cluster and as mycelium. For less contact time, *A. pullulans* grew as yeast-like clusters and for more contact time, it grew as mycelium. The reason for fungi to grow mycelia is if they are depleted of nutrients. This implies the nutrient transfer process at the cell membrane, or the ion transport, is not functioning properly. Hence, ambient air ionization affects the ion transport at a cell membrane, effectively damaging it, and with more contact time, killing it.

Figure 1 – Results from active-stage testing. The bottom row, middle row, and top row indicate 1 stage, 2 stages, and 3 stages used during testing, respectively.

Acknowledgments

I would like to thank my advisor, Dr. John Horack, for his endless support as well as Dr. Nick Nastasi for his guidance in this project.

References

[1] B. Alberts, A. Johnson, and J. Lewis. *Molecular Biology of the Cell. 4th edition.* National Library of Medicine - National Institutes of Health, 2002. Accessed: Mar, 2024. [Online]. Available: https://www.ncbi.nlm.nih.gov/books/NBK26910/

[2] B. Crucian, A. Babiak-Vazquez, S. Johnston, D. L. Pierson, C. M. Ott, and C. Sams. *Incidence of clinical symptoms during long-duration orbital spaceflight*. National Library of Medicine - National Institutes of Health, 2016. Accessed: Dec, 2023. [Online]. Available: https://www.ncbi.nlm.nih.gov/pmc/articles/PMC5098747/

[3] G. Horneck, D. M. Klaus, and R. L. Mancinelli. *Space Microbiology*. National Library of Medicine - National Institutes of Health, 2010. Accessed: Aug, 2023. [Online]. Available: https://www.ncbi.nlm.nih.gov/pmc/articles/PMC2832349/#:~:text=In%20general%2C%20microorganisms%20tend%20to,normally%20inhibitory%20levels%20of%20antibiotics.

[4] M. Cortresão, A. de Haas, R. Unterbusch, A. Fujimori, T. Schütze, V. Meyer, and R. Moeller. *Aspergillus niger Spores Are Highly Resistant to Space Radiation*. National Library of Medicine - National Institutes of Health, 2020. Accessed: Mar, 2024. [Online]. Available: https://www.ncbi.nlm.nih.gov/pmc/articles/PMC7146846/#:~:text=Aspergillus%20niger%20Spores%20Are%20Highly%20Resistant%20Toward%20UV%2DC%20Radiation,C%20radiation%20(254%20nm)

[5] N. Nastasi, N. Renninger, A. Bope, S. J. Cochran, J. Greaves, S. R. Haines, N. Balasubrahmaniam, K. Stuart, J. Panescu, K. Bibby, N. M. Hull, and K. C. Dannemiller, *Persistence of viable MS2 and Phi6 bacteriophages on carpet and dust*. John Wiley & Sons A/S, 2021. Accessed: Mar. 3, 2023. [Online]. Available: https://onlinelibrary.wiley.com/doi/epdf/10.1111/ina.12969

[6] S. R. Mehta, S. Johns, P. Stark, and J. Fierer. *Successful treatment of Aureobasidium pullulans central catheter-related fungemia and septic pulmonary emboli*. National Library of Medicine - National Institutes of Health, 2017. Accessed: Feb, 2024. [Online]. Available: https://www.ncbi.nlm.nih.gov/pmc/articles/PMC5607119/#:~:text=pullulans%20grows%20well%20on%20potato,growth%20at%2030%20%C2%B0C.

The Role of KFB in Gravitropism

Student Researcher: Elyse D. Hensley

Advisor: Dr. Sarah Wyatt

Ohio University
Department of Environmental and Plant Biology

Abstract
A plant's perception and response to gravity is necessary for normal growth and survival, but the pathways involved are not fully understood. The Wyatt Lab studies the biochemical components of a plant's gravity response to better understand these pathways. In the BRIC-20 spaceflight experiment, we identified 968 genes that were differentially regulated in spaceflight in 3-day-old etiolated *Arabidopsis thaliana* seedlings, compared to ground control replicates (Kruse et al., 2020). A group of proteins that functions in the ubiquitin pathway, E3 ligases, were differentially expressed. These proteins are involved in the pathway that labels molecules for degradation in the cell. Two of these E3 ligases were later identified to have a role in gravitropism through reorientation experiments conducted on Earth: KFB and PP2-A13. Plants with mutations in these genes displayed a gravitropic phenotype, so they are likely important in gravity signaling pathways. Investigating these proteins will further the knowledge on gravitropism and aim to improve our ability to grow plants in space to fuel long-term spaceflight.

Project Objectives
The objective of this project is to characterize the role of KFB, kelch domain-containing F-box protein, (AT1G23390, *kfb*) in the gravitropic pathway in *A. thaliana* through knockout mutants. Once mutant lines are identified, mutant phenotypes are analyzed through root curvature and gravity persistent signaling (GPS) experiments. These data are then compared to the wild-type response to identify the effect of KFB on gravitropism.
Methods
Recombinant *A. thaliana* seeds were obtained from the Arabidopsis Biological Resource Center (ABRC), containing a tDNA insertion within the transcribed region of *KFB*. These knockout lines were grown and bred to homozygosity, confirmed by DNA extraction and PCR. Plants homozygous for the insertion were then used for experimentation. Two knockout lines, *kfb-1* and *kfb-2*, were studied in this project and compared to the wild type ecotype Col-0. Root curvature experiments are conducted by reorienting 7-day-old *A. thaliana* seedlings, turning them 135° (Figure 1, A). Over 24 hours, their response to the new gravity vector is measured (Figure 1, B). GPS experiments are conducted by placing mature, 8 to 10 cm tall, *A. thaliana* plants on their side in the fridge for an hour, then placing them upright at room temperature (Figure 2, A). Over two hours, their response to the old gravity vector is measured (Figure 2, B). Recovery and response to the current gravity vector is also observed in this timeframe.

Results and Discussion
For the root curvature experiment, there were significant differences between *kfb-2* and Col-0 at time points 5, 7, and 8, and between *kfb-1* and *kfb-2* at time points 3, 4, 5, 6, 7, 8, and 9 at the 0.05 level. *Kfb-1* and Col-0 were not significantly different at any time point. These results indicate that the mutation had a different effect on *kfb-1* than *kfb-2*. Regardless, this data supports the claim that KFB has a role in the gravitropic pathway because mutating it had a significant effect on a plant's gravitropic response. For the GPS experiment, there was no significant difference between any of the genotypes at any of the

time points. This could indicate that KFB has less of a role in shoot gravitropism, compared to root gravitropism.

Figures/Charts

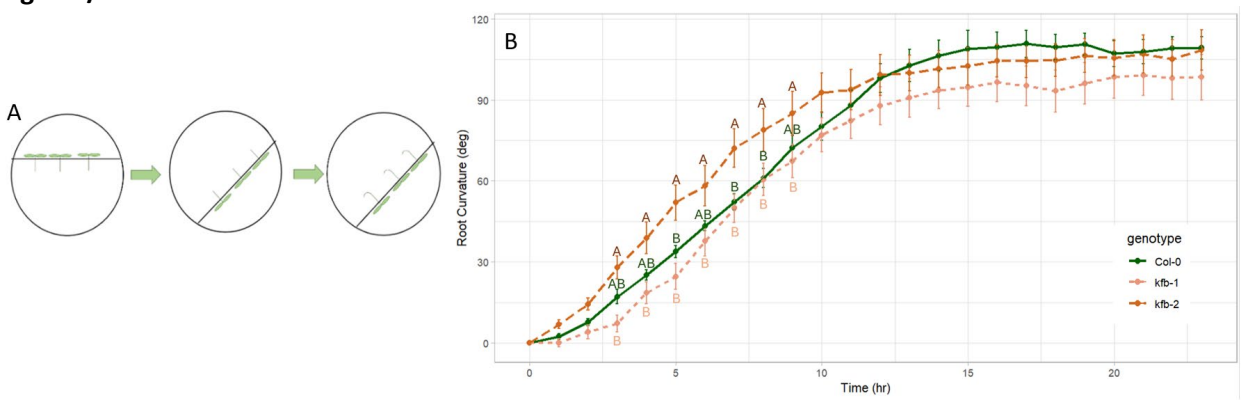

Figure 1. Root curvature setup and results.

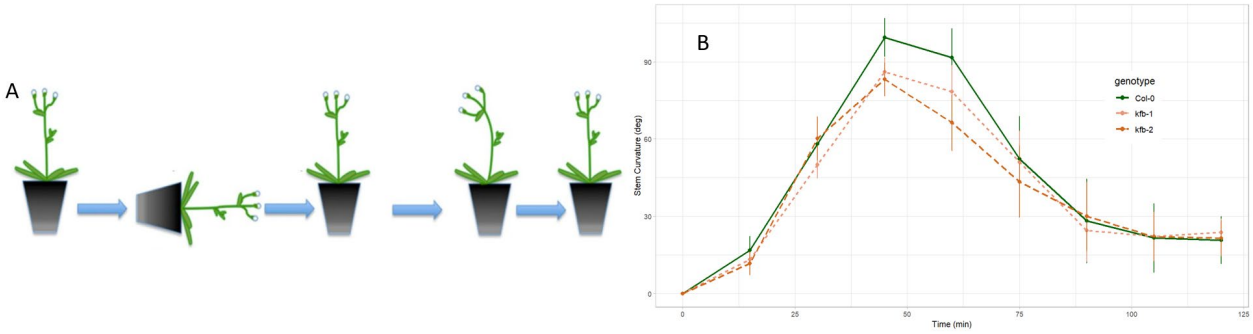

Figure 2. GPS setup and results.

Acknowledgments

I would like to thank the Ohio Space Grant Consortium for funding this project and Victoria Swiler for helping me with figure generation and statistical analyses.

References

Kruse, C. P., Meyers, A. D., Basu, P., Hutchinson, S., Luesse, D. R., & Wyatt, S. E. (2020). Spaceflight induces novel regulatory responses in Arabidopsis seedling as revealed by combined proteomic and transcriptomic analyses. *BMC Plant Biology*, *20*(1). https://doi.org/10.1186/s12870-020-02392-6

Moving Past Chlorophyll for a More Refined Monitoring of Water Quality in the Great Lakes

Student Researcher: Emily Hyland

Advisor: Dr. Brice Grunert

Cleveland State University
Biological, Geological, and Environmental Sciences Department

Abstract
Chlorophyll has long been ubiquitous with water quality. However, individual optical constituents like phytoplankton absorption (related to community composition) and colored dissolved organic matter are more representative of specific ecological processes and water quality stressors, like wastewater inputs or ecosystem state. We can model the contributions of these parameters to satellite-observed reflectance using radiative transfer code to assess how well these components can be observed. This project will build off demonstrations of satellite retrievals of phytoplankton absorption and community composition in Lake Erie, by using select satellite imagery paired with the open-source bio-optics Python package to compare individual biogeochemical components alongside traditional water quality indices (e.g., chlorophyll and harmful algal bloom indicators). Using code and radiative transfer workflows established by Dr. Grunert and others, I will examine the extent to which colored dissolved organic matter and phytoplankton are observable in remote sensing reflectance in Lake Erie to improve our ability to retrieve more advanced ecosystem metrics for the system.

Project Objectives
The main objective of the project was to determine whether global aquatic bio-optical models accurately represent optically complex ecosystems like Sandusky Bay in Lake Erie, including considering how backscattering in the bay affects remote sensing reflectance. Sandusky Bay was identified as an ideal site for this project due to its natural gradient of optical and biogeochemical variability, from highly turbid, sediment rich waters to clearer, productive waters at the mouth of the bay and in coastal Lake Erie.

Methods
The FishTales 3 vessel was used to collect all observations in Sandusky Bay. Data collected included inherent optical properties (IOPs) and apparent optical properties (AOPs), including absorption, backscattering, and remote sensing reflectance. To collect absorption a discrete water sample was collected at each station, stored on ice, then filtered onto 25 mm glass microfiber filters and flash frozen in liquid nitrogen back in the lab at Cleveland State University. Optical density of the filterpad was measured on a Cary 4000 UV-Vis Spectrophotometer following the approach of Cremella et al., 2022 and absorption due to particles, phytoplankton, and non-algal particles was determined following the IOCCG protocols (Volume 1, Neeley & Mannino, 2018). Backscattering data was collected at each site using a hyper-bb hyperspectral backscattering sensor (Sequoia Scientific). The hyper-bb was placed in the water and data was collected within 1m of the surface (0.75-1m actual depth) for five minutes, then a depth profile was collected. Hyper-bb data was processed using MATLAB functions provided by Sequoia Scientific and custom processing code within our lab. Using the IOPs collected for each of the Sandusky Bay sites, the open-source bio-optical Python package was used to re-construct remote sensing reflectance spectra from generic and observed IOPs. The bio-optics package allows for forward and inverse modeling of above water multispectral and hyperspectral observations of natural water bodies, providing an approach to consider the sensitivity of remote sensing reflectance spectra to various IOP combinations.

Results
For this project, we considered whether the default, 'global' parameters used to fit remote sensing reflectance were suitable for optically complex waters such as Sandusky Bay. Specifically, we sought to assess the suitability of using a power law model to represent particulate backscattering, as a power law model is typically assumed when retrieving IOPs from remote sensing reflectance data. We considered all sites, but display data for the first (SB1, most turbid) and last (SB10, most optically transparent) sites to consider the extent to which power law relationships can suitably represent backscattering and effectively reproduce observed reflectance data (Fig. 1). As seen in Figure 1, modeled backscattering using generic bio-optics parameterizations resulted in very poor agreement for the most

turbid site, with improving agreement but still substantial differences for coastal Lake Erie waters where observed backscattering better fits a power law model (Fig. 1a,c). Modeled reflectance closely matched observed reflectance (green and gray lines, respectively); however, when using the observed backscattering data instead of the global model parameterization, reflectance was substantially higher (Fig. 1b,d). Based on these results, we expect the model can be improved through the introduction of regional coefficients and, for waters with more particulate material, by identifying and using models that represent the domed shape of observed backscattering better than a power law model does.

Figures/Charts

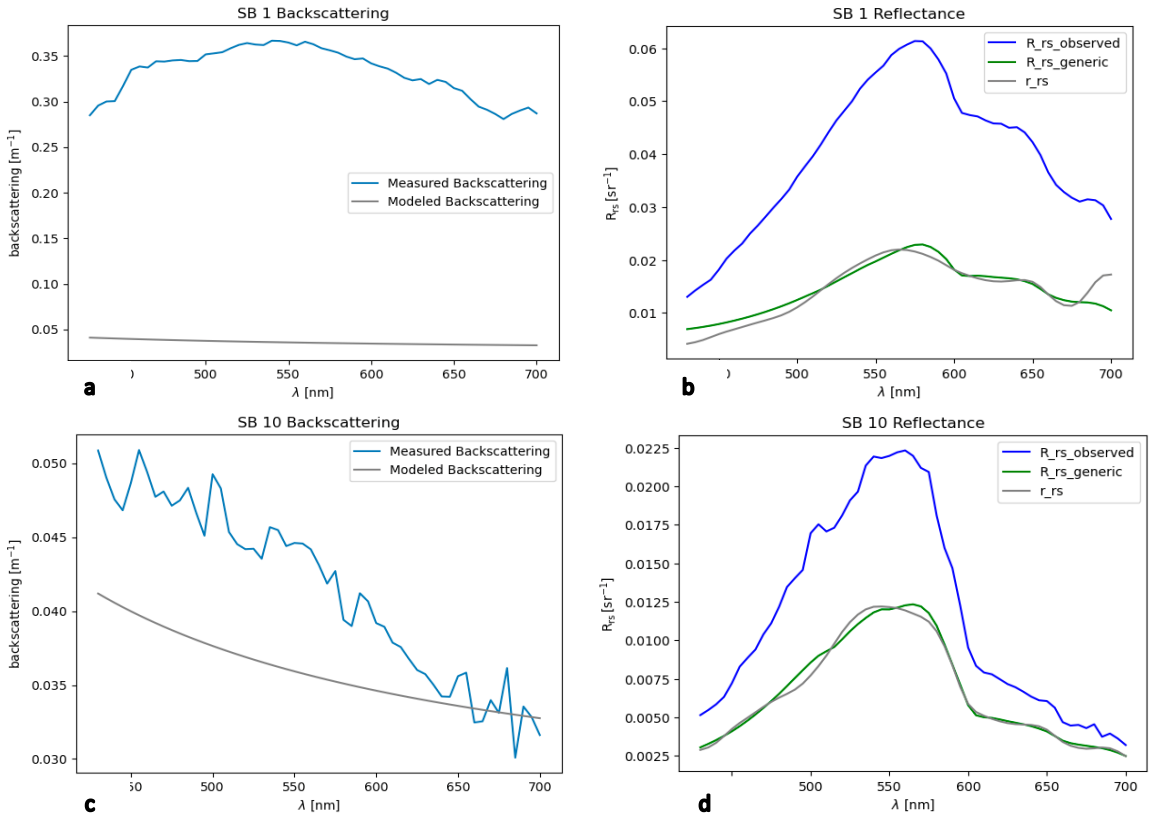

Figure ndusky Bay site 1 and 10 bio-optics model. Modele kscattering is represented in subplots a and c while modeled reflectance is represented in subplots b and d.

Acknowledgments

This work would not have been possible without the support of the Ohio Space Grant Consortium, my advisor, Dr. Brice Grunert, and the entire Carbon and H_2(Optics) lab.

References

Cremella, B., Bélanger, S., & Huot, Y. (2022). Aquatic particulate absorption coefficient combining extraction and bleaching optimized for inland waters. *Limnology and Oceanography: Methods*, *20*(7), 451–465. https://doi.org/10.1002/lom3.10497

König, M., Noel, P., Hondula. K.L., Jamalinia, E., Dai, J., Vaughn, N.R., Asner, G.P. (2023): bio_optics python package (Version x) [Software]. Available from https://github.com/CMLandOcean/bio_optics. [https://doi.org/10.5281/zenodo.10246860]

Neeley, A. R., & Mannino, A. (2018). Ocean Optics and Biogeochemistry Protocols for Satellite Ocean Colour Sensor Validation; Volume 1.0. Inherent Optical Property Measurements and Protocols: Absorption Coefficient.

Developing a Protocol to Examine the Effects of Early-Life Ingestion of Non-Nutritive Sweeteners on Anterior Tongue Taste Bud Morphology

Student Researcher: Cynthia James

Advisor: Clare Mathes

Baldwin Wallace University

Department of Neuroscience, Neuroscience Major

Abstract

Non-nutritive sweeteners (NNS) are promoted as healthier alternatives to caloric sweeteners like sugar. However, their long-term implications on health require further investigation, especially during critical periods of development. Rats provide an informative model of the impact of early-life experiences on health due to their neural and behavioral similarities to humans. We have shown that rats that ingested NNS chronically in their early life lick more avidly across concentrations of the caloric sugar fructose than rats not exposed to NNS while also expressing lower amounts of mRNA that code for a portion of the sweet taste receptor (Taborda et al 2019). NNS-exposed rats also display a smaller taste field on the posterior tongue (e.g., circumvallate papillae, Witt et al 2022). Since a higher density of sweet taste receptors is found on the anterior tongue, early-life NNS exposure may have an even more significant impact in this region. Here, we seek to assess if rats that have chronically ingested NNS early in life have fewer fungiform papillae, which contain taste buds, on the anterior tongue than do unexposed control rats. We are currently piloting on naive rat tongues the process by which to stain and quantify taste pores, which are indicative of an active taste bud, on the anterior tongue. After a transverse cut of the tongue, the mass on the ventral side is removed, and the dorsal surface is stained and flattened between two microscope slides, allowing visualization of the taste pores at 10-20x with a light microscope. We optimized staining and are now assessing how to accurately quantify the taste pores. Once we fully establish the protocol, we plan to assess differences in taste pore number and density in the anterior tongues of rats provided daily with NNS as well as their unexposed littermate controls. We expect to see fewer taste pores across the anterior tongue of NNS-exposed rats. These results would suggest that early-life exposure to NNS can alter the morphology of both the posterior and anterior tongue, which may explain these animal's altered behavior towards caloric sweeteners later in life. Collectively, these results may shed light on the impact of NNS ingestion early in life and influence dietary recommendations, especially for children.

Project Objectives

The purpose of this study was to enhance a staining protocol for the examination and quantification of the morphology of the taste buds on the anterior portion of a rat's tongue.

Methods

Tongues were collected from rats in a previous study within the Baldwin Wallace University Neuroscience Department and were fixed in paraformaldehyde before this project began. The anterior portion of the tongue was first separated from the posterior portion of the tongue using a razor blade. The distinction between the anterior and posterior parts of the tongue was made at the intermolar prominence of the rat's tongue. The anterior portion of the tongue was then placed in distilled water for 30 minutes at room temperature and left out to dry on a paper towel for 25 minutes. After the tongue was left out dry, the tongue's width and length were measured. The tongue was then cut along the transverse plane. The bottom portion was discarded, and the mass of the ventral aspect of the dorsal portion of the tongue was then removed by scrapping and cutting away at the tissue. Once a thin surface of the tongue was achieved, the tongue was submerged in a 0.5% methylene blue dye for 3 seconds. The tongue was then rinsed by submerging it in water to remove excess dye from the surface. After rinsing the tissue, the

tongue was dyed and rinsed twice more to achieve an even coat across the tissue. After the staining process, the tongue tissue was mounted between two slides by a firm pressing and fixed with tape between the slides. The tissue was examined under a microscope at 20x magnification, and taste pores were identified.

Results and Discussion

The protocol was enhanced, and the taste pores that were alive and those that were dead on the anterior portion of the tongue could be recognized under the microscope (Figure 1). The enhancements to the protocol included changes in the thinning of the tongue tissue and the amount of time the tissue was in the dye for the staining procedure. Under the microscope, if the tissue isn't at its thinnest, the layers within the tissue can be seen at different focuses of the microscope, which affects what is being counted/recorded. Also, since the goal is to maximize the visibility of the taste buds/pores on the anterior portion of the tongue, if there isn't enough dye, the taste pores aren't as visible. If there is too much dye, the taste buds blend into the background of the surrounding tissue. Therefore, by enhancing tissue thinnest and staining time, the protocol determined can accurately quantify alive taste pores against dead taste pores on the anterior portion of a rat's tongue.

Figures/Charts

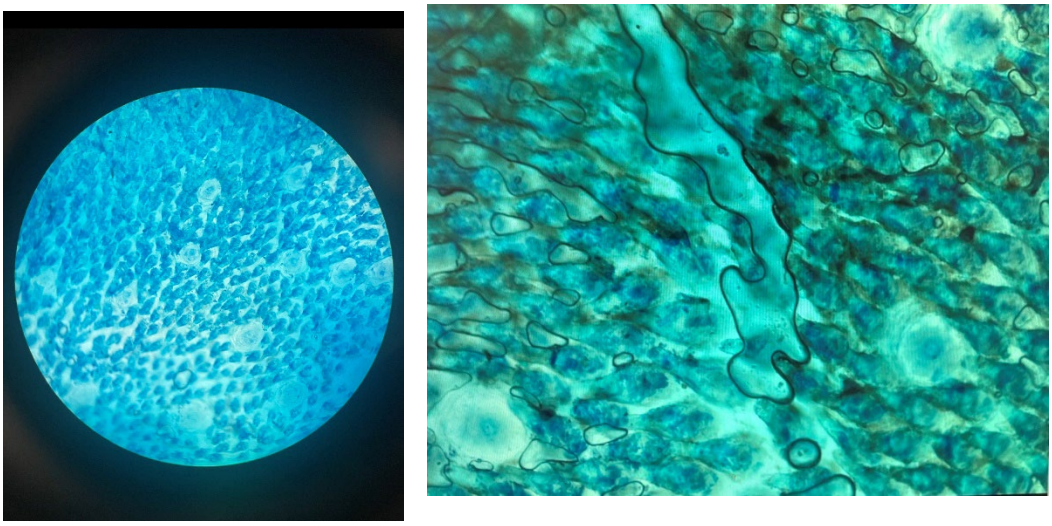

Figure 1: Images of the taste pores found on the anterior portion of the tongue of a rat.

Acknowledgments

I would like to acknowledge Dr. Mathes, the Department of Neuroscience at Baldwin Wallace University, my friends and family. I would also like to thank Baldwin Wallace University and Ohio Space Grant Consortium for funding me and giving me to opportunity to produce this research.

References

Taborda JP, Mendiratta G, Hartswick DR, Chometton S, Schier LA, Mathes CM. *Early-Life Exposure to a Non-Nutritive Sweetener Increases Unconditioned Licking for Fructose and Quinine and Decreases* Tas1r3 *Expression in Adult Food-Restricted Male and Female Rats*, presented as a poster at the April 2022 meeting of the Association for Chemoreception Sciences, Bonita Springs, FL.

Witt MJ, Chometton S, Terrill SJ, Schier LA, Mathes CM. *Early-Life Ingestion of Non-Nutritive Sweetener Associated with Lowered Expression of Sweet Taste Cell Markers in the Circumvallate Lingual Epithelium and Smaller Circumvallate Taste Bud Field Size in Adult Rats*, to be presented as a poster at the November 2023 meeting of the Society for Neuroscience, Washington D.C..

The Impact of Solar Panel Presence on the Biogeochemical Response of Soil Cultures and Their Atmospheric Effects

Student Researcher: Tara Keller

Advisor: Dr. Mark Gathany

Cedarville University

Department of Mathematics and Science, Molecular Biology Major

Abstract

The use of solar energy has increased especially in the past two decades, as the need for renewable energy sources has become increasingly apparent. However, the effect that these solar panels have on the ecosystem, particularly the microhabitats underneath them, is largely under-studied. For this experiment, we are interested in studying the effect that solar panel presence and operation has on soil microbial communities, and consequently the soil-atmosphere exchange of greenhouse gasses. This will be accomplished by quantifying CO2 production in samples from both locations using LI-6400XT with a soil chamber attachment, and further specifying results by selectively inhibiting bacterial and fungal communities using biocidal agents, bronopol and captan respectively.

Results from this study will hopefully provide a greater insight into current contributions of microorganisms in varying microhabitats to greenhouse gases, a broader consideration of the consequences of solar panel land usage, and motivation to take a deeper look into further areas of study such as the effects of increasing temperature or using different biocide agents.

Project Objectives

This project sought to better understand the potential effects of solar panels on the microhabitats where they are established, as this is both an increasingly popular method of renewable energy, but largely understudied from an ecological perspective. This experiment sought to quantify the soil-atmosphere exchange of greenhouse gasses, particularly CO2, through selective inhibition of bacteria and fungi. These results have potential implications for solar panel land usage and other land management considerations.

Methods

We randomly selected solar panels from our university's solar panel field, collecting 4 cores underneath each panel and 4 cores next to it. These cores were dried at 50C for at least 48 hours, ground and sieved to <2mm, and the bulk density was calculated. This bulk density was used to calculate a 70% water fill pore space, in order to uniformly wet each sample prior to biocidal application. At time "-30 minutes", 1000mg of glucose was added to 75% of the determined water amount from the previous step and applied to each sample. Then at time "0 hours", the remaining 25% of the determined water amount was mixed with the appropriate biocide: either 400,000µg captan to inhibit bacteria, 200,000µg bronopol to inhibit fungi, both in the combination group, or none in the control group.

Immediately, the CO2 flux rate was determined using an LI-6400XT chamber. This device calculates the flux rates over consistent intervals over time. The flux rate was measured again at "3 hours" post-biocidal treatment, and again at "6 hours". This was conducted on a total of 68 samples.

Results and Discussion

Using a one way analysis of variance, we found no significant difference in the change in CO_2 efflux rates at 0 and 6 hours of incubation between samples taken from underneath or between solar panels.

The lack of statistical significance shows us that ten years after a solar installation, there is no significant effect on soil respiration rates. This adds a data point to our understanding of the impacts - or lack thereof - on land. We also found no statistical significance in the bulk density of samples taken between versus under panels.

We found that there was no significant difference in CO_2 efflux rates at 0 and 6 hours of incubation between samples among the biocide applications. We noted the *expected trend* of the control responding positively to the addition of glucose over the incubation period. Meanwhile, each biocide treatment had a net negative change in efflux. This indicated that the biocide applications did, on average, reduce the soil respiration rates.

When we dove in a bit further we found that there, again, was no significant interaction between the respective biocides under or between the solar panels. As a group the soils between the solar panels appeared to be most strongly impacted by the biocide inhibition. The interaction effect assesses the slope of the response of the soil source for each biocide. We observed that the biocides had a smaller effect of soil source as compared to the biocide control treatment.

We found the fungal to bacterial ratios to be 0.59 for soils under solar panels and 1.87 for soils between solar panels. This information suggests that soil CO2 efflux is mediated predominantly by bacteria under the panels while fungi were more active between the panels.

IAR, inhibitor additivity values, were 1.02 and 2.36 for soils under and between solar panels, respectively. The closer the IAR is to 1.0, the smaller the overlapping impact a biocide has on a non-target group.

Our study also - out of necessity - used a new approach to assess biocide applications. We found the volume of soil (20x typical) made it difficult to effectively and evenly deliver the biocides and glucose to the sample. As a result this led to a wide range of sample and response variability. The direction of future research in this field should aim to narrow down the sample mass to be able to more effectively and consistently apply the biocides to the entire sample. Using a gas chromatograph could have shown trends in the flux of other greenhouse gasses, as well as the potential effect that changes in temperature could have on these results as well.

Figures/Charts

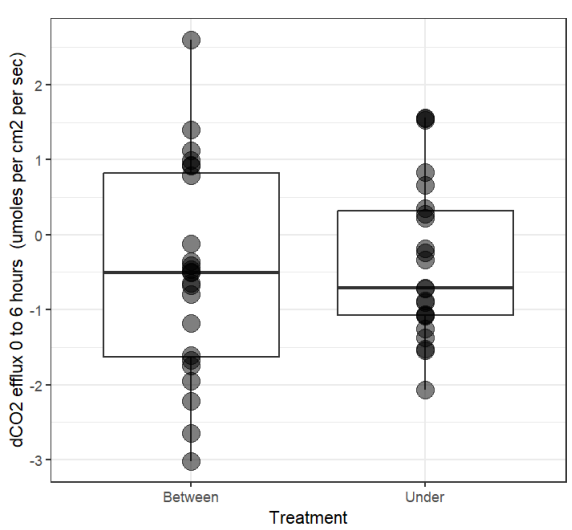

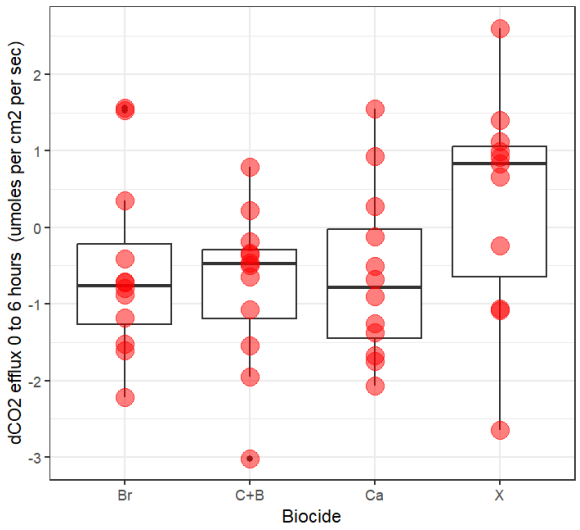

Acknowledgments
I'd like to thank my advisor Dr. Gathany, Cedarville University's Science and Mathematics Department, and the Ohio Space Grant Consortium for the opportunity to explore this field of research.

References
Bailey, V. L., Smith, J. L., & Bolton, H. (2003). Novel antibiotics as inhibitors for the selective respiratory inhibition method of measuring fungal:Bacterial ratios in soil. *Biology and Fertility of Soils, 38*, 154-160. https://doi.org/10.1007/s00374-003-0620-7

Oertel, C., Matschullat, J., Zurba, K., Zimmermann, F., & Erasmi, S. (2016). Greenhouse gas emissions from soils—A review. *Geochemistry, 76*(3), 327-352. https://doi.org/10.1016/j.chemer.2016.04.002

Rousk, J., Demoling, L. A., & Bååth, E. (2009). Contrasting short-term antibiotic effects on respiration and bacterial growth compromises the validity of the selective respiratory inhibition technique to distinguish fungi and bacteria. *Microbial ecology*, *58*(1), 75–85. https://doi.org/10.1007/s00248-008-9444-1

Examining the Effects of Indoor Plants on the Microbiome of a Built Environment

Student Researcher: Abigail Leslie

Advisor: Bridget Hegarty

Case Western Reserve University
Civil and Environmental Engineering / Biochemistry

Abstract
The interplay of green architecture, abiotic factors, and microbiota is not well understood, despite the effects that each have on human well-being. Understanding the interplay of these factors is critical for terrestrial environments, as well as for space flight, where plants may be introduced as a source of fresh food or for bioregenerative life support systems. To better understand how introducing plants into a built environment can influence microbial communities, we quantified the fungal and bacterial communities in the settled dust and potting soil of seven offices in an academic building in Northeast Ohio. Results show that indoor plants have no significant impact on the abiotic factors nor the total concentration of microbes in each office. More sampling is needed to determine if these trends are stable over time. We plan to use these findings to determine the effectiveness of indoor plants and green architecture use for microbiome manufacturing in a built environment.

Project Objectives
Analyze the difference, if any, between the abundance and diversity of fungal DNA and bacterial DNA in an office with an established indoor plant and in an office without any indoor plants.

Methods
Data was collected from seven offices on the same floor in an academic building in Northeastern Ohio. Four offices contained 1-4 plants; 3 offices acted as controls with no plants. Throughout a 3-month period, dust was collected in petri dishes for 4 weeks, then retrieved. Offices that contained plants had soil samples collected every other week. Particulate matter ($PM_{2.5}$), temperature, pressure, and dewpoint were measured once every 30 minutes using a PurpleAir outdoor air quality monitor.
DNA was extracted using the Powersoil Pro kit (Qiagen), according to the manufacturer's instructions. Digital droplet PCR (ddPCR) analysis was performed to quantify the concentration of DNA in each sample.

Results and Discussion
During our sampling period, we detected no significant differences in the abiotic parameters between offices that contained plants when compared to offices without plants. An example of this is particulate matter ($PM_{2.5}$), where rooms with and without plants show similar trends (Figure 1). Little difference was noticed between offices with and without plants for the concentration of bacterial and fungal (Figure 2) DNA over the course of sampling. There was more variability in the total fungal DNA concentrations in the rooms without plants.
While plants in high abundance have been previously shown to induce changes in humidity and air temperature (1), we detected no differences in these parameters based on plant status in this study. Similarly, DNA concentrations were consistent between dust samples regardless of the rooms' plant status. As the offices sampled had at most 4 potted plants, this suggests that the abiotic and biotic factors measured are not influenced by these levels of plant material.

Our findings suggest that low plant densities have negligible effects on abiotic factors and microbial abundances in the built environment. Further sampling is needed to determine if effects can be measured at higher plant densities. Amplicon sequencing may also determine that bacterial and fungal communities are different between built environments with plants versus those with no plants. Identifying a difference would provide a potential mechanism to shape the indoor environment with implications for air quality and human health aboard spacecraft. These future studies will lay the groundw whether indoor plants could modify the microbiome of spacecraft and protect occupant health.

Figures/Charts

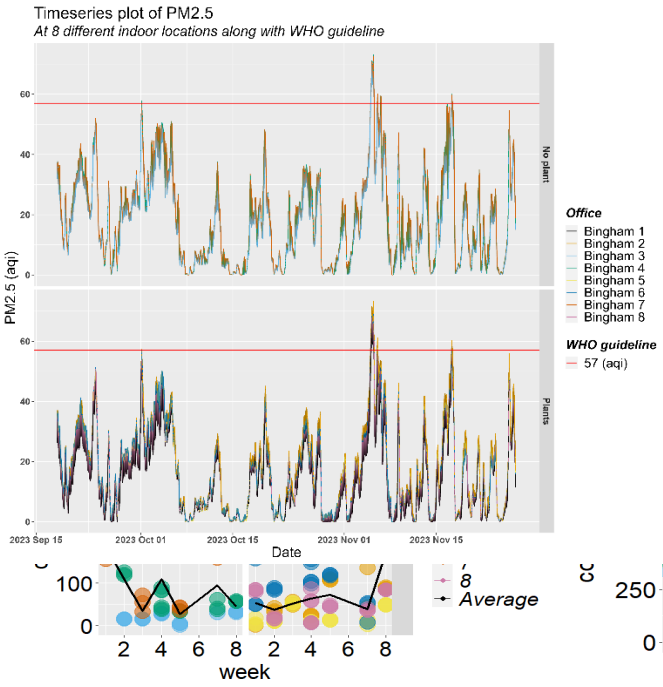

Figure 1. Timeseries of particulate matter (2.5). Data analysis performed showed no correlation between rooms with plants and rooms without plants.

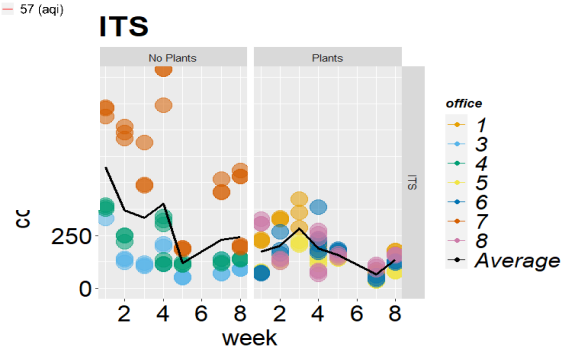

Figure 2. Timeseries data of the bacterial (left) and fungal (right) concentrations in the settled dust samples. An average line is added for all offices without plants or with plants at each week. Week 6 has no data due to sampling issues. Offices labelled based on air quality monitor. Two monitors were in one office, which is why there is no office two.

Acknowledgments

Funding for this work comes from Dr. Bridget Hegarty's start-up. I would like to thank Josh Eagle, Muhtashim Rafiq Chowdhury, Maddie Maduzia, and Sadia Marjia Ferdous for their help with sampling.

References

1. Wahab, I. B. A., and Ismail, L. H. B. A Study on Plant Selection for Green Building Design. *Journal of Science and Technology*

Shape Memory Alloy Adaptive Wing Prototype Model

Student Researcher: James Lyons

Advisor: Dr. Nicholas Garafolo

The University of Akron
Mechanical Engineering

Abstract
This research is being conducted in support of a master's thesis project by University of Akron graduate student Ray Roos studying the development of an adaptive wing. The specific study of this project is the development of a prototype wing model with blended flaps actuated by shape memory alloy. A blended flap can improve aircraft performance in fuel efficiency, aerodynamic performance, and functionality, like a traditional flap system, with the added benefit of maintaining surface integrity and avoiding gaps. Smart material actuators can deliver better power actuation power density than their hydraulic and conventional electromechanical counterparts. These traditional methods use heavy and complex systems to manipulate the wing surface, which has historically added significant weight and drag to the aircraft. The objective of this project is to develop an alternative adaptive wing technology using a shape memory alloy blended flap. Shape memory alloys exhibit mechanical memory whereby temperature manipulation results in a precisely controlled deformation to manipulate the wing flap. Integrated heating can provide control authority of the adaptive wing with significant improvement in weight, maintenance, and complexity, over a hydraulic or conventional electromechanical system.

Project Objectives
The objective of this project is to develop a wind tunnel prototype model to demonstrate blended flap alternative adaptive wing technology. The flap will utilize shape memory alloy actuation. This physical prototype will serve to validate ongoing aerodynamic simulations conducted by the graduate student. Upon completion of a successful test model and convergent CFD simulation, a wind tunnel test campaign will be conducted to provide proof of concept to reinforce the conclusions drawn from the simulation. Following refinement of the scale model through iteration, a larger SMA blended flap will be produced and outfitted onto a large-scale RC plane for flight testing to provide further tangible proof of concept.

Methods
Aerodynamic simulations are being computed using Ansys Fluent. The 3D model being tested is based on the wing of a past Zips Aero Design Team RC plane. To design a physical model the parameters were first selected as follows. A 24-inch model span was determined by the wind tunnel test section available at The University of Akron. Zips Aero flight data was analyzed to determine the loads the model would be subject to, the wind tunnel airspeed was determined analytically. Equivalating Reynolds numbers provided a wind tunnel speed of 92 mph. SolidWorks CAD was then used to develop a solid body 3D model by modifying and scaling the Zips Aero wing planform.
With the model designed, 3D-printing was chosen to achieve precise, strong airfoil contours more simply, cheaply, and quickly than metal or composite construction. Design iteration has yielded a 2-part construction printed from polycarbonate which has successfully withstood the target test conditions in the wind tunnel using a trailing edge mounting tube to interface with the wind tunnel sting mount. 4-inch by 1-inch vacancies for hinged flaps have now been added **Figure 1**.
The next phase of the project included the design and fabrication of a prototype hinge actuated by a small segment of shape-trained nitinol wire. A hinge design was selected from a December 2023 publication that

outlined a torsional shape memory actuator. **(Qiang Liu)** The concept of this hinge is displayed in **Figure 2.** A fixturing method and tempering procedure was developed to successfully shape train small SMA segments. A flap hinge prototype was then designed, printed, and assembled and actuation was achieved through joule heating to induce a localized elevated temperature in the wire **Figure 3**.

Results and Discussion

The 2023-2024 research period has not yielded any quantitative data, but the design progress has been satisfactory. Ongoing development will include refining the flap by filling the gaps with silicone to form a blended wing surface. Then, the flexibility and reliability of this technique will be evaluated to ensure consistent actuation. Afterwards, a LabView VI and physical circuit will be created to control the joule heating through temperature feedback. The SMA flap bench prototype will then be integrated into the scale wing model and subjected to wind tunnel testing to evaluate the design, characterize performance, and validate the aerodynamic simulations. Finally, if the technology is successful, the hinge concept will be scaled to the size of the original reference RC aircraft for flight testing.

Figures/Charts

Figure 1. 3D Printed Wing Model

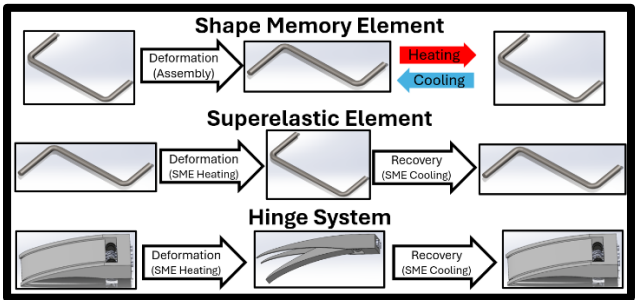

Figure 2. Shape Memory Hinge Function Diagram

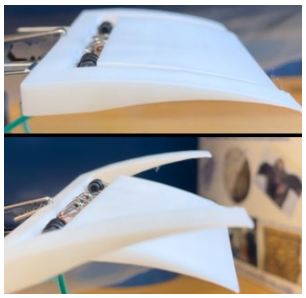

Figure 3. 3D Printed Hinge

Acknowledgments

Materials and guidance provided by Qiang Liu at TU Delft. Lab assistance provided by Dr. Jennifer Lillard

References

McHugh, G. R. (2016). *An Experimental Investigation in the Mitigation of Flutter Oscillation Using Shape Memory Alloys* [Master's thesis, University of Akron]. OhioLINK Electronic Theses and Dissertations Center. http://rave.ohiolink.edu/etdc/view?acc_num=akron1479119992818089

Qiang Liu, Sepideh Ghodrat, and Kaspar M. B. Jansen. 2024. Mimosa: Modular Self-folding Hinges Kit for Creating Shape-changing Objects. In Eighteenth International Conference on Tangible, Embedded, and Embodied Interaction (TEI '24), February 11–14, 2024, Cork, Ireland. ACM, New York, NY, USA, 13 pages. https://doi.org/10.1145/3623509.3633381

Zero Emission Aeronautical Systems using Hydrogen Fuel Cells

Student Researcher: Sydney Maller

Advisor: Dr. Yanhai Du

Kent State University
Aerospace Engineering

Abstract
Developments in aviation are closely associated with performance characteristics, however there are other important advancements to consider. Aviation is consuming a noteworthy amount of our total Carbon Footprint here on Earth with no foreseeable decline. Hydrogen Fuel Cells are a promising alternative to standard jet fuel, with no Carbon Footprint. The objective of this research is to evaluate the potential and viability of hydrogen fuel cell power as an alternative for combustion fuel. The scope of this research is commercial flight; however, the intent of this research is to broaden the implementation to all types of propulsion. Combustion engines are very common in the field of aviation, but in order to properly eliminate emissions, we can no longer rely on the combustion of fuel to propel an aircraft. The implementation of propeller aircraft is a reliable way to turn hydrogen fuel cell generated power into thrust.

Project Objective
The objective of this project is to compile information about Hydrogen Fuel Cells implemented into aeronautical applications. While comparing with current energy sources and other sustainable methods with respect to factors including endurance, range, and cost.

Methods
Research publications were reviewed, and data evaluated to provide comparison of methods. Research Articles were additionally reviewed for their publisher impact factor to ensure credible information.

Results and Discussion
Evaluating current aeronautical fuel technologies and sustainable alternatives, we see four main alternatives in efforts to eliminate standard jet fuel consumption. Most commonly you see sustainable aviation fuel, which is biofuel, which helps address the production concerns, but when consumed produces almost no reduction in NOx emissions and minimal reduction in CO2 emissions. More recent technologies speak on batteries and their ability to store sustainably generated energy and use it when needed in aeronautical applications, many issues have come to light from this method including scaling, efficiency, and the sustainable nature of the battery composition. After review of energy dense substances, hydrogen proved to provide at least twice as much energy per unit of mass, as seen in figure 1. Hydrogen can be harnessed as an energy source in two different ways: the first being combustion of such, as it eliminates carbon emissions, yet NOx emissions are still present; the second being Hydrogen Fuel Cells, which is the primary focus of this research. Hydrogen Fuel Cells use an electrochemical process that results in the sole by product of water and heat. This is a completely zero emission technology, but more goes into this process to implement it into aeronautical applications.
To evaluate the full effects of Hydrogen Fuel Cells we need to consider the following items Hydrogen Production, Hydrogen Containment, Hydrogen Storage, and Transportation. Hydrogen can be produced in a variety of ways, often referred to as the hydrogen rainbow. Zero Emission methods include green from any renewable source, pink from nuclear, and yellow from solar. The most common method is gray

from methane steam reformation. Therefore, to continue our mission, we need to establish a green hydrogen infrastructure, a major setback considering our current infrastructure, H2 Fly has made the first step in building the first Hydrogen Aviation Center at Stuttgart Airport. This type of infrastructure also helps with transportation concerns, if we implement hydrogen production facilities at airports the transport of hydrogen from facility to the aircraft is significantly decreased. Furthermore, the transportation vehicles need to have an aligned mission of zero emissions.
Hydrogen Containment and Storage go hand in hand, through the implementation into the aircraft. Containment refers to the vessel the holds the hydrogen itself, while the storage is locational placement in the aircraft. When dealing with containment, we have two different routes to take with Hydrogen, gaseous and liquid. Perks of liquid are mainly focused on volumetric density as reflected in figure 1. However, liquid hydrogen requires cryogenic cooling, an additional draw of energy. Regardless, both need a vessel capable of withstanding the necessary pressures, which often results in a vessel that weighs more than the actual fuel itself. With the heavy and solid shape of these vessels, this proves to be an issue when replacing current fuel tanks that are stored in the wings of aircraft. By occupying part of the fuselage with fuel, room for payload is decreased, causing decreased profits in airline companies.

Appendix

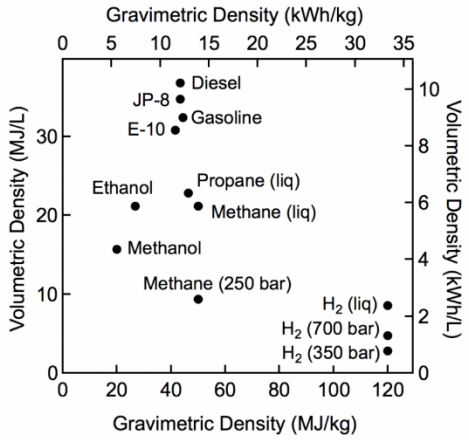

Figure 1: Fuel Energy Density Diagram

Acknowledgments
Special Thanks to Dr. Yanhai Du and the entire Fuel Cell Group at Kent State University for their support.

References
Donateo, Teresa; Ficarella, Anonio; Spedicato, Luigi; Arista, Alessandro; Ferraro, Marco. “A new approach to calculating endurance in electric flight and comparing fuel cells and batteries”. Elservia. May 2016.
Hepperle, Martin J. “Electric Flight - Potentials and Limitations”. Research Gate. October 2012.
“Hydrogen Storage | Department of Energy.” Energy.Gov, www.energy.gov/eere/fuelcells/hydrogen-storage. Accessed 30 Apr. 2024.
IEA (2023), CO2 Emissions in 2022, IEA, Paris https://www.iea.org/reports/co2-emissions-in-2022, Licence: CC BY 4.0
Seyed Ehsan Hosseini & Brayden Butler (2020) An overview of development and challenges in hydrogen powered vehicles, International Journal of Green Energy, 17:1, 13-37, DOI: 10.1080/15435075.2019.1685999

Lunar Navigation System in The AARON System for xEMU

Student Researcher: Sophia Naser Matar

Advisor: Dr. Jong-Hoon Kim

Kent State University
Computer Science Department – Computer Science

Abstract
Space exploration stands at the forefront of human endeavors, pushing the boundaries of our knowledge of the universe. This project introduces a groundbreaking initiative to advance lunar exploration by developing a navigation system. The proposed method offers a broad platform to guide and instruct astronauts, accommodate multi-operator users, and integrate state-of-the-art technologies for autonomous operation. The lunar navigation system is redefining how astronauts navigate and conduct research. Its main objective is to provide astronauts with a versatile and reliable navigation tool that supports various mission objectives.
A necessary feature in the system is the visual interface for multiple robots, addressing the complexities of multi-operator scenarios. This interface enhances situational awareness and allows users to control multiple robots simultaneously, providing a seamless switch between the robots and external perspectives. This unique facet ensures a comprehensive understanding of the lunar environment and mission tasks, fostering a new era of human-machine interactions in space exploration. The lunar navigation system represents a necessary step forward in navigating the challenging and dynamic lunar environment. Beyond facilitating the immediate needs of astronauts, the system contributes to the overarching goal of advancing technology for continued lunar exploration.

Project Objectives
First, this project aims to develop an ultra-modern navigation system with multifunctioning capabilities for lunar missions. It is also added to this; it will be an instrument that guides and provides indispensable instructions to astronauts as they go about on the hard surface of the moon. This will also support multi-operators, easing the ability to coordinate tasks from the lunar surface with counterparts at home base to support mission flexibility and group collaboration.
It will also focus on the latest technologies and algorithms designed for autonomous operations. This will, in turn, further decrease the astronauts' dependence on Earth's commands, hence fastening the decision-making process and increasing mission autonomy. This project worked out a more workable and successful ambitious moon mission aimed at using these technologies for increased efficiency and safety in lunar exploration.

Methods
The Lunar Navigation System is designed as a comprehensive platform, integrating advanced sensors, mapping systems, and sophisticated navigation algorithms. This will provide the system with capabilities such as localizing and mapping lunar terrain with highly required resolutions—a prerequisite for successful navigation during a moonwalk. In addition, the system interfaces manage several robotic assets visually, giving prompt feedback to the operators as they control robots from the optimum distances required.
This adaptability significantly improves operational capabilities, as the system allows for a seamless transition between robot perspectives and external viewpoints. Such flexibility enhances situational

awareness and enables improved decision-making during lunar missions, reassuring operators as they adapt to changing conditions on the surface.

The demonstration component of the Lunar Navigation System was built in Unity to showcase practical use. This present scene features one principal user and three rovers designed with different missions and control layouts to cater to the generic use of the system. Rover, one takes part in a traverse mission, collecting samples and making detailed maps of the local areas it goes over along the lunar surface. Rover Two focuses on a sample-collecting mission, specifically going on missions to look for a specific type of rock within the lunar landscape. The third rover takes part in the rescue mission after getting stranded, waiting for support with its broken axle.

In terms of the user interface, the simulation will let the user switch easily back and forth through the screens of each rover, giving access to particular controls and diagnostics of faults. On that account, this intuitive design in the real system will improve operational efficiency, guaranteeing a response to problems occurring in time that need solving, hence having successful missions for those rovers.

Results and Discussion

The expected effects of the Lunar Navigation System Simulation include several. In this sense, the interface will visually enable the smooth exchange of operators between the several robots and the realization of the Lunar Environment. It will also empower astronauts with autonomy by reducing their reliance on Earth's commands, and hence, it will speed up decision-making on the lunar surface. Its multi-operators' scenario support further enhances mission flexibility, improving coordination during complex tasks. Further, the system ensures user-friendly interfaces, enabling it to respond promptly to operational problems. It is designed in a unity-based simulation, not just to test robustness but also as a form of demonstrating possible developments in technology. Successful outcomes could pave the way for scaling this technology to other planetary explorations, such as missions to Mars, highlighting a broad range of applicational potential.

Figures/Charts

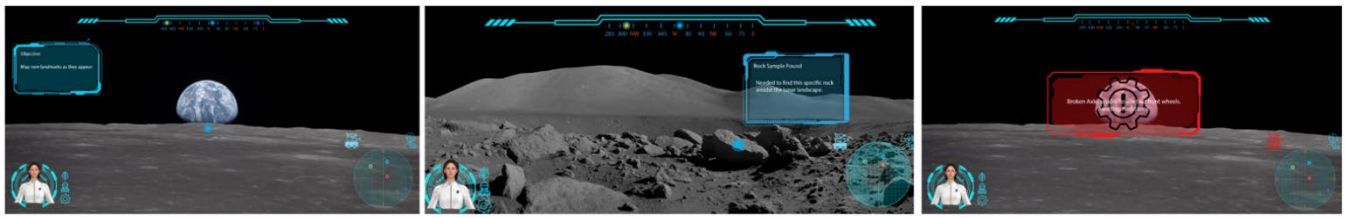

Screenshots of the Lunar Navigation System interface.

Acknowledgments

I want to thank the Ohio Space Grant Consortium for this fantastic opportunity to work on this exciting research project. And thank you to my advisor, Dr. Jong-Hoon Kim, for all his support and guidance.

References

1. Cardenas, Irvin Steve, et al. "AARON: assistive augmented reality operations and navigation system for NASA’s exploration extravehicular mobility unit (xEMU)." Intelligent Human Computer Interaction: 12th International Conference. Springer International Publishing, 2021.

Conserved, gravity-independent, gene expression changes in response to spaceflight

Student Researcher: Anne Mathew

Advisor: Dr. Nathaniel Szewczyk

Ohio University
Neuroscience

Abstract
Recently, investigators have shown that there are gravity-dependent and independent changes in gene expression in response to spaceflight. These changes have been reported in the model systems C. elegans (worms) and Drosophila melanogaster (flies). Interestingly, the gravity-dependent changes have been proposed to be a generic stress response whereas the gravity-independent changes appear to be neuron-specific in flies. Worms, flies, and astronauts all display neuronal defects in response to spaceflight. In flies and astronauts these changes have been proposed to be due to altered oxidative metabolism and altered oxidative metabolism also occurs in worms in space. Thus, the overall goal of my project is to test if there are common gravity-independent changes in gene expression in response to spaceflight in worms and flies.

Project Objectives
My aim is to investigate whether shared, gravity-independent alterations in gene expression occur in response to spaceflight in both C. elegans and Drosophila melanogaster. By comparing the genetic responses of these two model organisms, I aim to identify common mechanisms that transcend species boundaries, thereby shedding light on fundamental genetic adaptations to microgravity conditions in a broader context.

Methods
This research initiative, which began in the fall of 2023, is centered on the comprehensive analysis of gene expression data for Drosophila melanogaster following their spaceflight experience aboard the SpaceX-14 cargo resupply mission. This mission, which commenced on April 2, 2018, involved the launch of experimental subjects to the International Space Station, where they resided from April 4, 2018, until their return to Earth on May 5, 2018.
The dataset for the fruit flies includes specimens from various conditions: male and female ground controls, males and females exposed to microgravity, and males and females exposed to 1g simulated gravity within a centrifuge on spaceflight. This research endeavor used RNA sequencing for transcription profiling. There is also a comprehensive analysis being done for the dataset of C. elegans as they are under similar conditions, so a comparative analysis can take place. This dataset however from from worms cultivated in the Japanese Module of the International Space Station (GSE71770). These worms included: male and female ground controls, males and females exposed to microgravity, and males and females exposed to 1g simulated gravity within a centrifuge on spaceflight. The analytical phase of this project involved acquiring skills in the R programming language, which is tailored for statistical, microarray, and proteomic analysis of the dataset. As this was my first experience in programming I taught myself these skills, starting with the foundational basics and progressively extending to data integration into the R environment. I took the time to learn the basics, which I then could apply to this dataset. I have conducted the normalization and filtering process (shown below) which makes the data more amenable to various statistical techniques and algorithms. The next step

involves conducting differential expression tests. This analysis is fundamental in genomics and transcriptomics to discern which genes or molecular entities exhibit statistically significant differences in expression levels across different experimental conditions or groups.

Results and Discussion

The implications of this research extend far beyond the confines of the laboratory, holding significant implications for human space exploration and the broader field of space biology. By elucidating the molecular impacts of spaceflight on model organisms, this study has the potential to inform strategies for safeguarding the health and well-being of astronauts during extended space missions. Moreover, the findings generated through this research endeavor may pave the way for the development of targeted interventions aimed at mitigating the adverse effects of microgravity on biological systems. Through publications, presentations, and collaborations within the scientific community, the insights gleaned from this study have the power to catalyze advancements in our understanding of space biology, ultimately shaping the future of human space exploration.

Acknowledgments

I am grateful for Dr. Szewzcyk for all his support as I entered this project. Also for Dr. Willis for helping me with my bioinformatics skills.

References

[1]Iyer, J.; Mhatre, S.D.; Gilbert, R.; Bhattacharya, S.
Multi-system responses to altered gravity and spaceflight: Insights from
Drosophila melanogaster. *Neurosci.*
Biobehav. Rev. 2022, *142*,
104880.
[2] Scott, A., Willis, C. R. G., Muratani, M., Higashitani, A., Etheridge, T., Szewczyk, N. J., & Deane, C. S. (2023). Caenorhabditis elegans in microgravity: An omics perspective. iScience, 26(7), 107189. https://doi.org/10.1016/j.isci.2023.107189.
[3] Mhatre SD, Iyer J, Petereit J, Dolling-Boreham RM, Tyryshkina A, Paul AM, Gilbert R, Jensen M, Woolsey RJ, Anand S, Sowa MB, Quilici DR, Costes SV, Girirajan S, Bhattacharya S. Artificial gravity partially protects space-induced neurological deficits in Drosophila melanogaster. Cell Rep. 2022 Sep 6;40(10):111279. doi: 10.1016/j.celrep.2022.111279. PMID: 36070701; PMCID: PMC10503492.
[4] Soni, P., Edwards, H., Anupom, T., Rahman, M., Lesanpezeshki, L., Blawzdziewicz, J., Cope, H., Gharahdaghi, N., Scott, D., Toh, L. S., Williams, P. M., Etheridge, T., Szewczyk, N., Willis, C. R., & Vanapalli, S. A. (2023). Spaceflight Induces Strength Decline in Caenorhabditis elegans. Cells, 12(20), 2470. https://doi.org/10.3390/cells12202470.
[5] Higashibata, A., Hashizume, T., Nemoto, K. et al. Microgravity elicits reproducible alterations in cytoskeletal and metabolic gene and protein expression in space-flown Caenorhabditis elegans. npj Microgravity 2, 15022 (2016). https://doi.org/10.1038/npjmgrav.2015.22

Effect of Geological Conditions on Human Settlement of Different Cities in Ohio

Student Researcher: Ethan Miller

Advisor: Dr. Andrew Beck

Marietta College
Petroleum Engineering

Abstract
I compared the depositional environments, topography, and geologic history of each city I used in my research.

Project Objectives
Determine whether there is any correlation between geological conditions and human settlement.

Methods
Used a web soil survey map to compare the layers of rock underneath the surface to determine depositional environments of each city. Then compared this as to why it was a valuable place to settle

Results and Discussion
In conclusion, the depositional environment of each location in Ohio played a crucial role in shaping human settlement in their own ways by providing fertile land for agriculture, access to transportation and trade routes, valuable natural resources, and influencing the topography and challenges posed by natural hazards. These factors collectively contributed to the development and growth of communities in the region over time, some with greater growth and success than others.

Figures/Charts

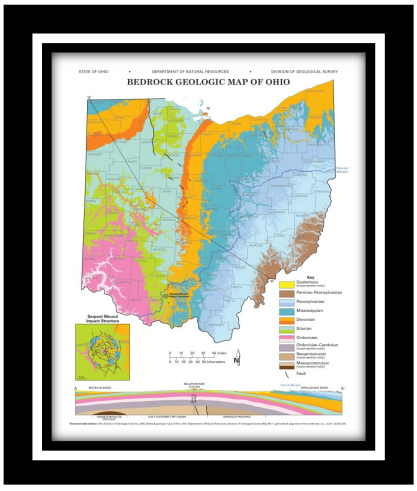

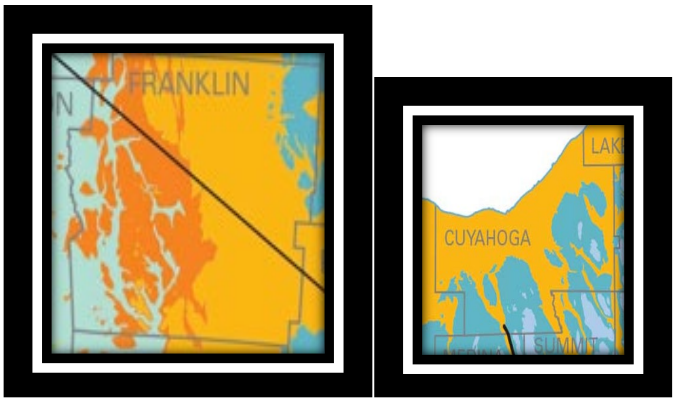

Acknowledgments
Thank you to Dr. Andrew Beck for not only being my supervisor for this project but also helping me with my research every step of the way.

References
https://kiptonquarry.com/about/ohio-sandstone-geology/bedrock-geologic-map-of-ohio/
https://www.researchgate.net/publication/268575394_How_Geology_Shapes_Human_Settlements
https://www.britannica.com/place/Columbus-Ohio
https://www.city-data.com/us-cities/The-Midwest/Cleveland-Geography-and-Climate.html#google_vignette
https://www.britannica.com/place/Cleveland-Ohio
https://www.britannica.com/place/Marietta-Ohio
https://www.nationalgeographic.com/adventure/article/marietta-ohio

Artificial Neural Networks to Predict the Response of High-Temperature Shape Memory Aerospace Actuators

Student Researcher: Madisyn Moore

Advisor: Dr. Josiah S Owusu-Danquah

Cleveland State University
Department of Civil Engineering

Abstract

Shape Memory Alloys (SMAs) have the ability to remember their original shape even after experiencing large inelastic deformations. Although there are many different types and compositions of SMAs, the NiTi and NiTiHf material compositions are common representatives of the conventional and high-temperature alloys, respectively, used for aerospace applications. Their design applications utilize the superelastic and/or shape memory effect properties under thermal or mechanical cycles. From the experimental point of view, investigating the variations in the actuation properties of SMAs under extensive cycles is cumbersome. This highlights the implementation of novel machine learning models, such as Artificial Neural Network, to predict the stress-strain-temperature relationship of shape memory alloys. Artificial Neural Network (ANN) mimics the structure of the brain to predict outcomes by discerning patterns from input data, hence, provides a viable route to predict material performance under the influence of stress, mechanical/thermal cycles and different temperature levels. The overall goal of this project is to develop, test, and enhance the predictive capabilities of a general ANN software for cyclic SMA responses.

Project Objectives.

To achieve the targeted goal, the project is divided into two main specific objectives:

1. Understand the major differences and similarities in the responses of SMAs used in the field of aerospace actuation (e.g. NiTi vs NiTiHf). As part of this step, we will collect extensive data on the cyclic behavior of several different shape memory alloys having distinct transformation characteristics when subjected to thermal cycles and mechanical stresses. This investigation will also highlight the general background of SMAs, their history, applications, and limitations.
2. To learn about the specific aspects of ANN [1] that affects its predictive capabilities. Generally, ANN model contains the following layers: input, hidden, and output. The research here will provide some basic understanding of the effect of the differences in the number of neurons per layer on the prediction accuracy of different ANN architectures. Moreover, prediction outcomes when SMAs are subjected to a certain number of cycles, temperature, and stress will be investigated for NiTi vs NiTiHf under thermal cycles.

Methodology

To begin the project, a deep look at the function and actuation process of SMAs is needed. In this process, preliminary review of scholarly work (thesis, published articles, project reports) was made. The scope of the review covered shape memory alloys, their phase change processes, and their behaviors when high thermal stress is applied. It was observed that there has been a surge in the use of additive manufacturing processes to fabricate SMA components; moreover, methods such as Finite Element Models have been used to predict the responses of SMAs.

Initial testing of various architectures of ANN was made following the previous work of Abdallah et al. [2]. That work focused on NiTi under various stress magnitudes. Through this exercise, I learnt data cleaning, data groupings, and division of the data into various parts for training, verification and validation.

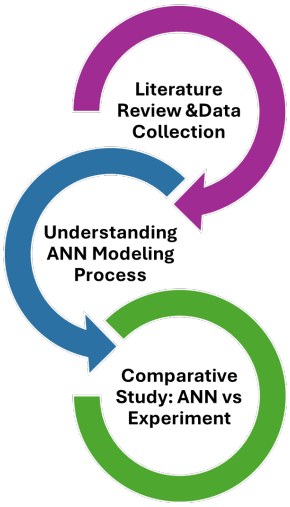

Results and Discussion

Generally, SMAs exhibit superelasticity, one-way or two-way shape memory effect. These alloys will deform and return to their original shape once the applied mechanical loads are removed, and heat is applied. The underlying principle is the martensitic transformation, wherein the alloy undergoes a reversible change in crystal structure from austenite to martensite [3]. A comparison of the cyclic response of NiTi indicated that under constant stress thermal cycles, the material does not return to its prior state after each cycle [4]. In essence there is a loss of actuation strain per thermal cycle until a certain stage when it becomes nearly stable. The number of cycles needed to reach this state of stability is a function of the cycling temperature range, and the amount of stress. On the other hand, NiTiHf has a significant improvement in terms of "early stability" and transformation temperature range when compared to the NiTi. NiTiHf could withstand higher temperatures and return to its initial state proceeding each cycle [4]. As part of this ongoing research, a comparative study will be made to understand the differences in the ANN architectures as we attempt to capture the responses of NiTi and NiTiHf under constant stress thermal cycles.

Acknowledgments.

Thank you OSGC, NASA, and CSU for this opportunity to conduct research as an undergraduate student. The OSGC scholarship has allowed me to apply what I'm learning outside of the classroom and strengthen my qualitative as well as quantitative skills. I look forward to continuing my research and utilizing what I've learned in this experience to future ones.

References

1. Abraham, A. (2005). Artificial neural networks. Handbook of measuring system design.
2. Owusu-Danquah, J. S., Bseiso, A., & Allena, S. (2022). Artificial neural network models to predict the response of 55NiTi shape memory alloy under stress and thermal cycles. Neural Computing and Applications, 1-14.
3. Sadashiva, M., Sheikh, M. Y., Khan, N., Kurbet, R., & Gowda, T. D. (2021). A review on application of shape memory alloys. transformation [TMT], 21, 24.
4. Owusu-Danquah, J., Saleeb, A., Dhakal, B., & Padula, S. (2015). A Comparative Study of NiTi and NiTiHf Tube Actuators. Journal of Materials Engineering & Performance, 24(4).

Solar Panel Tilt Optimization Experimental Validation

Student Researcher: Jean C. Nash

Advisor: Rydge Mulford

University of Dayton
Mechanical Engineering Department

Abstract
This research investigates the optimization of fixed tilt solar panels in Dayton, Ohio, emphasizing the critical role of experimental validation in refining computational models. Departing from traditional approaches, which overlook seasonal variations in sunlight intensity, this study collaborated with Dr. Ridge Mulford to design a year-long experiment comparing two tilt angles. The two tilt angles are 40 degrees as determined by the National Renewable Energy Laboratory due to Dayton's latitude, and 34 degrees as determined by computation analysis previously completed by Dr. Mulford. By constructing mounts for four new 100W solar panels and filling a geographical gap in validation efforts, this research not only enhances understanding of solar dynamics but also empowers future generations to contribute to sustainable energy solutions. This practical journey, presented at the Ohio Space Grant Consortium Symposium, highlights the importance of bridging theoretical models with real-world applications for efficient solar energy utilization.

Project Objectives
The objective of this project is to investigate the optimization of fixed tilt solar panels in Dayton, Ohio, by determining an ideal tilt angle that maximizes energy generation throughout the year. While traditional practice aligns solar panels at a tilt equal to their latitude, we aim to establish a lower tilt angle, particularly suited to harness the increased sunlight and solar intensity during the summer months when the sun is higher in the sky. Given the scarcity of long-term optimization experiments conducted in the United States or at this latitude, this research seeks to fill this gap by conducting a year-long experiment comparing different tilt angles. My personal objective for this research is to design a comprehensive test for a future cohort of researchers to complete in the next year.

Methodology Used
The methodology employed in this study involves conducting a year-long comparative test of two fixed solar panel tilt angles, 34 and 40 degrees, situated on a concrete pad facing south at the University of Dayton Kettering Labs building. The experiment ensures representation across all seasons, with data collection occurring every 15 minutes via a Bluetooth module, resulting in a total of 35,064 data points for each tilt angle. For each tilt angle, two panels at identical tilt angles are connected to one battery and mounted on the tilt mount. To validate results, a control experiment is implemented where all four panels are laid flat for a duration of 30 days prior to ensure uniform performance across the panels. This comprehensive methodology aims to provide data driven insight into the optimal tilt angle for fixed solar panels.

Results Obtained
While the experiment's completion is pending, the expected results anticipate a comparative analysis between the two tilt angles to ascertain the performance superiority of the lower angle. Although the final outcomes remain forthcoming, projections based on computational models suggest promising prospects for the 34-degree tilt angle. It is anticipated that the lower tilt angle will yield approximately 10 kW more power per year compared to its counterpart. As the experiment transitions into the hands of a current freshman and graduate student for the subsequent year, the anticipated results pave the way for further exploration and validation of optimal tilt angles for fixed solar panels, contributing to the advancement of sustainable energy solutions.

Significance and Interpretation of Results
The anticipated results have the potential to inform and guide future decisions regarding solar panel tilt optimization, particularly in regions with similar geographical latitudes to Dayton, Ohio. The expected outcome, indicating a considerable increase in power generation from panels set at a lower tilt angle, underscores the importance of fine-tuning tilt angles to maximize energy capture throughout the year. If confirmed, these results could offer valuable insights for engineering, urban planners, and renewable energy installation companies to enhance the efficiency and sustainability of solar energy systems. Furthermore, the ongoing nature of the experiment highlights its significance for

continuous refinement and validation. Ultimately, the interpretation of these results may catalyze further research endeavors, driving innovation and progress in the pursuit of environmentally friendly energy solutions.

Figures/Charts

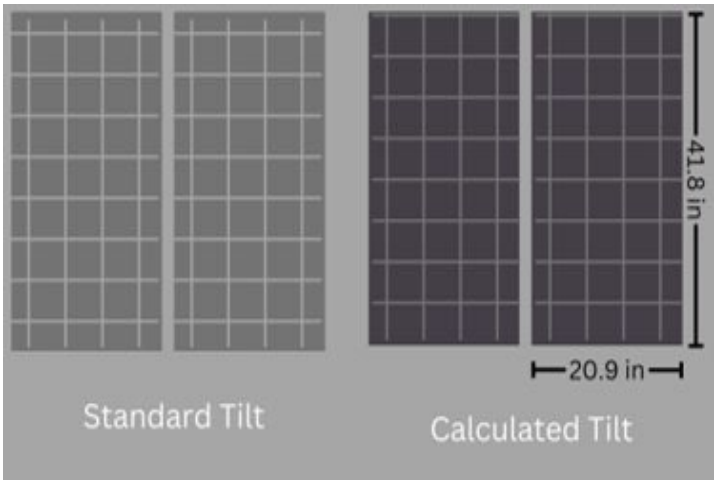

Figure 1. The layout of the solar panels on the concrete pad

Figure 2. 40 degree and 34 degree extruded aluminum tilt mounts

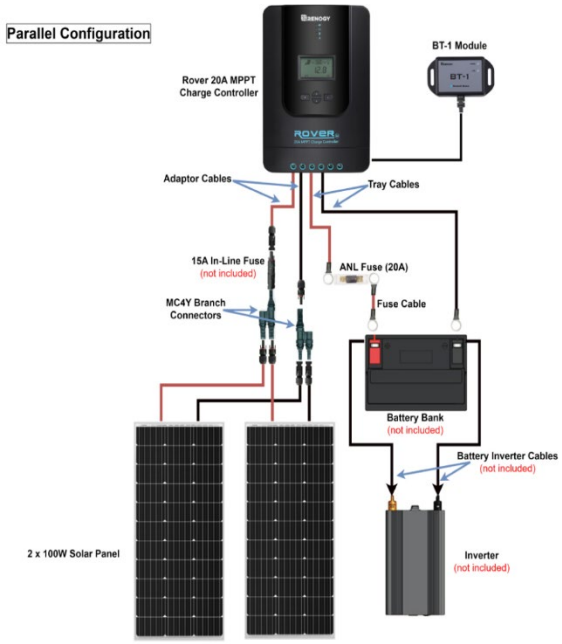

Figure 3. Wiring diagram in parallel configuration of the two solar panels to one battery

Acknowledgments

I would like to express our sincere gratitude to the University of Dayton Thermal Applications Laboratory for their use of their space and materials.

References

Sharma, M. K. (2020). Optimal Tilt Angle Determination for PV Panels Using Real-Time Data Acquisition. Retrieved from: https://www.ncbi.nlm.nih.gov/pmc/articles/PMC7408049/

Krishna, Y. (2021). An Experimental and Mathematical Investigation of Optimal Tilt Angle and Effects of Reflectors on PV Energy Production. Retrieved from: https://www.matec-conferences.org/articles/matecconf/pdf/2021/04/matecconf_eureca2020_03020.pdf

Plasma Induced Active Flow Asymmetric Control for Jets

Student Researcher: Jinit Patel

Advisor: Dr. Mo Samimy and Dr. Nathan Webb

The Ohio State University
Department of Mechanical and Aerospace Engineering

Abstract
The Navy has long been interested in adjusting the angle of thrust from exhaust nozzles on aircraft (thrust vectoring) for diverse applications like hyper-maneuverability and vertical take-off/landing (VTOL). VTOL would facilitate the use of fixed-wing unmanned aerial vehicles (UAVs) from non-flight deck-equipped vessels. Alternative applications of thrust vectoring are extensive. Thrust vectoring is currently produced by a complex, heavy, faceted nozzle design. Another method is Coanda-based Thrust Vectoring (CTV), which utilizes the Coanda effect to attach jets to "reaction surfaces" but can bleed up to 15% of primary air flow. As an alternative, this work explores the use of localized arc-filament plasma actuators (LAFPAs). These exploit flow instabilities to control flow characteristics, offering an energy-efficient, low-power method of thrust vectoring. Similar to a CTV, this ability could enable them to attach/detach flow from a reaction surface.
LAFPAs will initially be mounted on a CTV-inspired reaction surface. Experimental sweeps of excitation frequency and other excitation parameters will be conducted, and the resulting flow interrogated using schlieren and pressure measurements to assess the active flow control concept's (AFCC) jet deflection capability. PIV measurements will confirm thrust vectoring by observing if the AFCC is inducing cross-stream velocity. Time-resolved schlieren will document flow unsteadiness, while PIV over the surface will provide insight into LAFPAs' control mechanism.

Project Objectives
The research aims to explore the potential of LAFPAs for thrust vectoring applications in aircraft. It involves investigating how LAFPAs, when combined with flexible reaction surface nozzle extensions, can enhance maneuverability, and reduce takeoff/landing distances. The study encompasses a broad parameter space; by sweeping over excitation frequencies and spatial modes of LAFPAs and variations in reaction surface configurations, jet behavior will be analyzed. In parallel, the project aims to develop flexible reaction surface nozzle extensions utilizing an SLA resin 3D printer. These extensions will enable rapid and cost-effective testing of nozzle parameters, allowing for the identification of optimal combinations. This innovative approach is expected to streamline the testing process and facilitate the discovery of the most effective thrust vectoring nozzle and to uncover vital information detailing the AFCC's fundamental physics and effectiveness for the potential application.

Methods
The research will be conducted over three years, during which a subsonic, axisymmetric, 1-inch-diameter jet will be designed and manufactured fitted with LAFPAs as depicted in Figure 1. This jet will be tested against a backward-facing step of CTV-inspired reaction surface to evaluate the influence of surface geometry on the flow control effectiveness of the LAFPAs. The primary experimental methodology includes a series of excitation frequency sweeps, documented using schlieren and pressure measurements, to assess the ability of the AFCC to deflect the jet. Additional PIV measurements will be conducted to confirm that observed jet deflections correspond to induced cross-stream velocity, providing a deeper insight into the flow dynamics.
To investigate the dynamic response of the jets, the experiments will initially focus on the effect of excitation on one side of the jet, using time-averaged schlieren and static pressure measurements. These diagnostics will help characterize the baseline and controlled flow states of the jets. The subsequent analysis will delve into the effects of excitation frequency variations and their impact on jet deflection and flow attachment or detachment from the reaction surfaces. This approach aims to determine the optimal operating conditions for the LAFPAs, enhancing their effectiveness in manipulating jet aerodynamics. Further, time-resolved schlieren and excitation-locked PIV measurements will be employed to capture the unsteady behavior of the flow and the evolution of flow structures induced by the LAFPAs. These measurements are crucial for understanding the interaction between the plasma-

induced perturbations and the shear layers in the jet flow. By analyzing the formation and behavior of large-scale vortical structures (LSS), the research will contribute valuable insights into the control mechanisms available through plasma actuation. The results will inform the design of future nozzle configurations and reaction surfaces, potentially leading to more efficient and effective thrust vectoring solutions for aerospace applications.

Results and Discussion

The Plasma Actuators were excited asymmetrically across a range of frequencies and number of active actuators in a subsonic jet facility. After many experimental sweeps, Figure 2 & 3 highlights the baseline case versus the best performing test case yet. For reference, expected asymmetric static pressure distribution is observed with both low and high frequencies, with low frequencies demonstrating increased suction toward active actuators (termed "attachment-based control"), and high frequencies demonstrating increased suction away from active actuators (termed "detachment-based control"). The case at hand uses Actuator Code 131 (LAFPA's 1, 2 & 8) with the center LAFPA aligned with baseline asymmetry, operates at Mach 0.48, and utilizes a detachment-based control. Figures 3 and 4 depict axial velocity and vertical velocity plots for both test cases at hand. It is evident that the DBC-131 test case creates a clear rightwards shift in axial velocity, and a significant downwards shift in vertical velocity, when compared to the baseline results. Further research is needed to comprehend the pressure and velocity profiles at higher Mach numbers, along with the application of measurement techniques such as schlieren imaging and PIV to validate control mechanisms and confirm and quantify thrust vectoring.

Figures/Charts

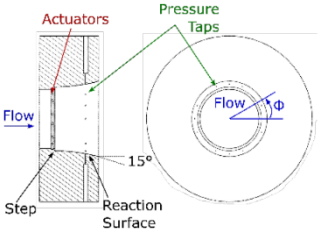

Figure 2. Azimuthal Pressure Reaction Surface, side view (a) and front view (b)

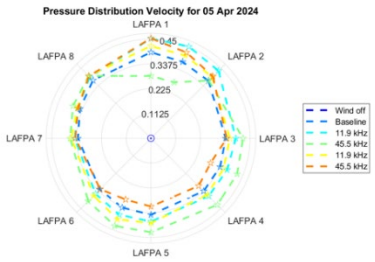

Figure 1. CTV Inspired Distribution Velocity Chart

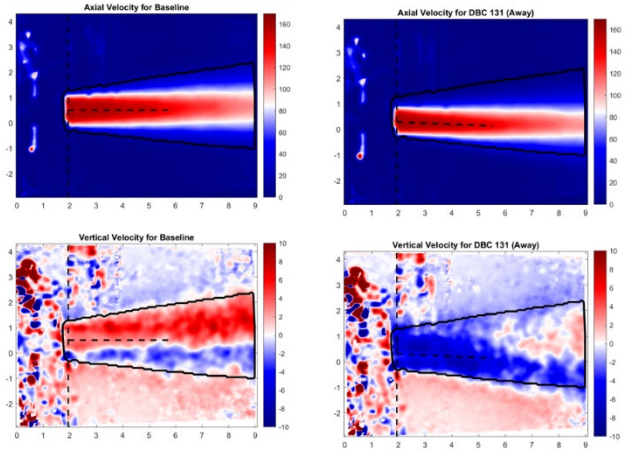

Figure 3. Baseline Case

Figure 4. DBC 131

Acknowledgments & References

Special thanks to Dr. Nathan Webb for his support, advice, and guidance on this project. I would also like to thank The Ohio Space Grant Consortium and NASA for allowing me to take part in this transformative project.

[1] Samimy, M., N. Webb, and M. Crawley, "Excitation of Free Shear-Layer Instability in High-Speed Flows," AIAA Journal (Invited Paper), Vol. 56, No. 5 (2018)
[2] Castañeda, N. Whiting, N. Webb and M. Samimy, "An Experimental Investigation of Deep Dynamic Stall Control Using Plasma Actuators," Springer Link, Volume 63, No. 69, (2022)
[3] N. Webb, D. Mills and Cartwright, "Active Flow Control for Manipulation of Flow Aerodynamics in Jets", (2024)

XR Visualization of OUNPPM and Mars

Student Researcher: Brady Phelps

Advisor: Chad Mourning

Ohio University
Honors Tutorial College, Advanced Computing

Abstract
This project uses XR technologies to establish an immersive environment for the Ohio University Navaid Performance Prediction Model (OUNPPM), catering to public, private, and military runways on Earth, along with navigational aids on Mars. OUNPPM stands as a globally recognized tool pivotal for certifying navigational aid compliance and ensuring airport safety worldwide. Its core function involves calculating multipath interference from nearby structures and generating corresponding error plots. By integrating an XR interface, users are offered an intuitive approach to navigational aid visualizations, enhancing their overall experience by allowing them to interact with these visuals in real-time and real-life. With implications spanning both terrestrial airport safety and missions linked to Mars exploration, this project showcases the potential of XR and OUNPPM in space and aviation.

Methodology
Preliminary Optimization: Before transitioning our existing software to the XR medium, it was imperative to implement optimizations in OUNPPM [1] to avoid certain flaws that would be exaggerated in an XR context. A significant focus was placed on leveraging multithreading, a computer science technique, to enhance the user experience. This optimization notably slashed initial rendering times from over 20 seconds to under 0.1 seconds. With this enhancement, our visualization process became smoother, progressively refining itself towards maximum resolution [2]. This improvement was pivotal, particularly for prototyping airport configurations with a headset, where a 20+ second stall would disrupt user experience, causing the image to no longer synchronize with the user's point of view and potentially causing dizziness, discomfort, and breaking the immersion [3].
OpenXR Integration: To integrate the optimized OUNPPM into the XR medium, the authors used OpenXR, an open standard designed for virtual reality (VR) and augmented reality (AR) development. The integration process began by incorporating the necessary OpenXR libraries and dependencies into the OUNPPM project. Subsequently, the authors established communication between the headset and workstation to facilitate data transmission. With data now flowing from the workstation to the headset and OpenXR successfully implemented alongside OUNPPM optimizations, we could begin the code integration of OUNPPM into the XR environment. After writing the new features, the authors have begun testing the application in a Meta Quest Pro VR headset with promising results.
Creating Mars Terrain from NASA Viking Mission Data: The Mars Terrain visualization was created in the AftrBurner engine [4] by utilizing Mars terrain images and topographic maps sourced from the NASA Viking mission [5] via the USGS website. Notably, this engine shares its foundation with OUNPPM, allowing cross-compatibility. This opens the potential to model future Mars landings using the benefits and tools of OUNPPM.

Results and Discussion
The project has made significant strides in enhancing existing implementations of OUNPPM by laying the groundwork for a complete XR implementation. This innovation not only accelerates engagement and interactivity but also promotes safety and security in airports worldwide. Additionally, the project delves

into Mars 3D visualization techniques, laying a solid foundation for future research in the realm of 3D visualizations and navigational simulations related to Mars exploration. Furthermore, the initiative has propelled advancements in the fields of antenna visualization, navigation, and space science.

Figures

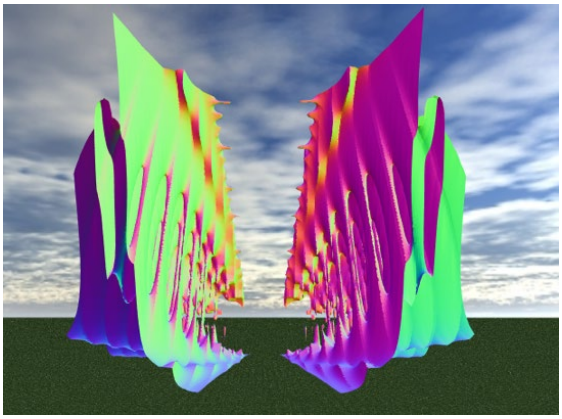

Fig 1. A standard Wilcox 14-10 course array antenna pattern in ideal conditions.

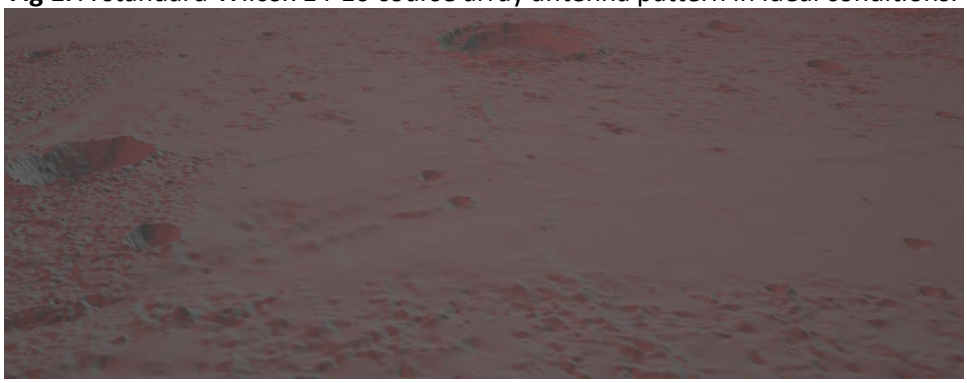

Fig 2. Current renderings of Mars terrain.

References

[1] Mourning, C., and Odunaiya, S., "Dynamic Antenna Pattern Visualization for Aviation Safety Incorporating Multipath and Situational Awareness," Advances in Visual Computing, 2021.

[2] Phelps, B. M., and Mourning, C., Utilizing Parallelism and Multithreading for Iterative Refinement of Antenna Pattern Visualization, 2024. https://doi.org/10.2514/6.2024-0163, URL https://arc.aiaa.org/doi/abs/10.2514/6.2024-0163.

[3] Stauffert, J.-P., Niebling, F., & Latoschik, M. E. (2020). Latency and Cybersickness: Impact, Causes, and Measures. *Frontiers in Virtual Reality*, 1. https://doi.org/10.3389/frvir.2020.582204

[4] Nykl, S., Mourning, C., Leitch, M., Chelberg, D., Franklin, T., & Liu, C. (2008). An overview of the STEAMiE educational game engine. In 2008 38th Annual Frontiers in Education Conference (pp. F3B-21). IEEE.

[5] 1976. Soffen, G. A., Scientific results of the Viking mission, Science, 194, No. 4271, 1274-1276, doi:10.1126/science.

Leveraging a Novel Two-Level Priority Encoder for High-Precision Integer Multiplication

Student Researcher: Maxwell Phillips

Advisors: Dr. Firas Hassan, Dr. Ahmed Ammar

Ohio Northern University
Electrical and Computer Engineering and Computer Science Department

Abstract
Ongoing increases in computing power have decreased the difficulty of decrypting ever larger data, driving a corresponding increase in the size of encryption keys. Multiplication is one common operation necessary for creating and processing such keys, which consist of high-precision (often over 512 bits) binary integers. This work improves upon current hardware for high-precision integer multiplication using an improved priority encoder, which enables skipping all zeroes in the first operand, the multiplier. While priority encoders are traditionally expensive, our novel two-level structure significantly reduces the hardware complexity, and thus cost, of these devices. The proposed algorithm performs no worse than traditional methods in the worst case, is roughly equivalent to contemporary methods in the average case, and is superior to other methods in the best case.

Project Objectives
This work summarizes [1], in which we utilize the two-level priority encoder introduced in [2] and propose a high-precision multiplication algorithm (paralleling the division algorithm also from [2]). Our primary objective is to enhance high-precision encryption by optimizing the arithmetic hardware backing encryption computations. The required precision of encryption keys is continually increasing due to corresponding increases in computing power. For instance, the NIST currently recommends RSA key sizes of at least 2048 bits [3].

Methods
We first reviewed existing multiplication algorithms and hardware, including Booth's algorithm, the Modified Booth Algorithm) Comba scheduling, Karatsuba's method, the traditional shift-and-add method, and improved shift-and-add methods. The proposed algorithm is an improvement on the shift-and-add idea, leveraging the functionality of the priority encoder to skip all zeroes within the multiplier operand. This is the key difference between our method and existing methods, the latter of which must process all bits in the multiplier. Meanwhile, the proposed algorithm must only process the high bits (ones) in the same operand. Notably, the density (in terms of high bits, i.e., Hamming weight) of the *multiplicand* does not matter, only that of the multiplier.

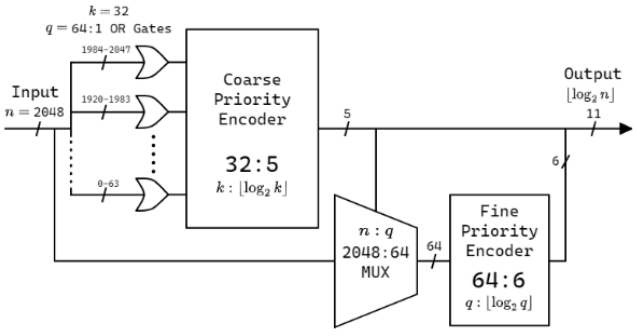

Figure 1: A Block Diagram for a 2048-bit TLPE.

We utilize the two-level priority encoder (2LPE) introduced in [2] and shown in Figure 1 to reduce the complexity of the traditional priority encoder, which makes its usage here feasible. The 2LPE slices the input using multiple OR gates, the outputs of which are passed to the "coarse" PE, which determines which bit slice the most significant high bit (MSHB) is in. The output of the coarse PE is used as the select signal for a multiplexer to select the appropriate bit slice for the fine

encoder, which determines where in that slice the MSHB is in. Concatenating the outputs of the coarse and fine encoders gives the output for the entire encoder.

Finally, a hardware block diagram for the entire multiplication hardware is provided below in Figure 2. The hardware takes the operands (multiplier Mr of length n and multiplicand Md of length m) in sign-and-magnitude form. Each iteration, the priority encoder determines the location of the most significant high bit (or one) in the multiplier. This is the shift amount, Sh_i, which is passed to the decoder and barrel shifter. The latter performs the partial multiplication, shifting the multiplicand by Sh_i. The partial products are accumulated by a carry-look-ahead adder. Meanwhile, the decoder produces a bit vector of all 0s except for a single 1 in the position of the most significant high bit. This is exclusive ORed with the current value of the multiplier to "delete" the most significant high bit, preparing the hardware for the next iteration. The multiplication is complete when the multiplier is all zeroes, and the "Done" signal is generated by a NOR gate. The sign of the product is found by a simple exclusive OR of the signs of the inputs, where 0 represents a positive number, and 1 represents a negative number.

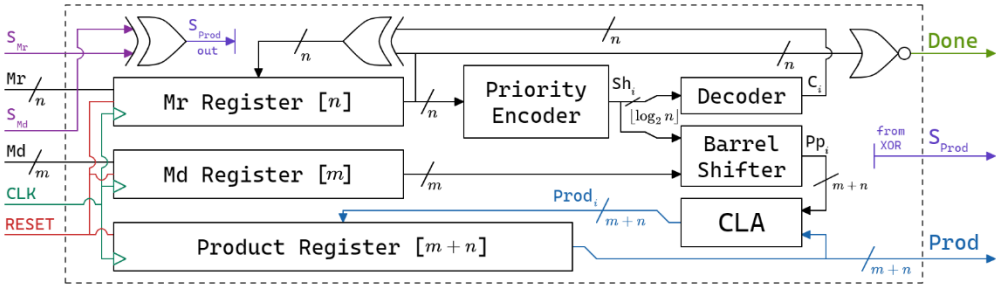

Figure 2: Multiplication Hardware Block Diagram

Results and Discussion

From a theoretical perspective, the proposed algorithm takes a number of clock cycles exactly equal to the number of high bits in the multiplier, denoted h. The best case is when there is only one high bit, so the hardware takes $h = 1$ clock cycles. On average, an n-bit vector has $h = n/2$ ones, which is also the number of iterations necessary for the modified Booth algorithm. In the worst case, the multiplier is all ones, so $h = n$, which is the number of iterations of the traditional shift-and-add algorithm. We implemented our algorithm in hardware for 32 to 2048 bits using VHDL, targeting an FPGA development board. Our source code is available at https://github.com/ALUminaries/Two-Level-Multiplier. We found that our algorithm was far less expensive than competing algorithms. A full analysis is presented in [1].

Acknowledgments and References

Thanks to OSGC and by extension NASA for funding this research and hosting the recent research symposium which I presented at. Special thanks to my advisors, Dr. Firas Hassan and Dr. Ahmed Ammar.

[1] M. Phillips, F. Hassan, A. Ammar, and N. Hagerdorn, "Leveraging a Novel Two-Level Priority Encoder for High-Precision Integer Multiplication," in Proc. IEEE Int. Midwest Symp. Circuits and Systems, 2023, pp. 1118–1122.

[2] A. Ammar, F. Hassan, and H. Drennen, "High-Precision Priority Encoder Based Integer Division Algorithm," in Proc. IEEE Int. Midwest Symp. Circuits and Systems, 2021, pp. 494–497.

[3] H. Ferraiolo and A. Regenscheid, "Cryptographic Algorithms and Key Sizes for Personal Identity Verification," csrc.nist.gov, Sep. 27, 2023. https://csrc.nist.gov/pubs/sp/800/78/5/ipd.

The New Concord Meteorite

Student Researcher: Alex Posey

Advisor: Dr. Andrew Beck

Marietta College
Petroleum Engineering, Geology

Abstract

The meteorite fell on Tuesday, May 1st, 1860, around 12:30 p.m. Over thirty individual meteorite fragments, weighing a combined 230 kg (507 lb.) fell in a broad swath over eastern central the meteorites are named after the town nearest the largest concentration of stones, New Concord, home of Muskingum College and the first American to orbit the Earth, John Glenn. (ASU). The meteorite fragments Scattered over roughly 30 square miles. The largest special specimen weighed 103 pounds and is displayed in the department of geology at Marietta College after being obtained by EB Andrews professor of geology at Marietta College and geologist with the second geology survey of Ohio 1869 to 1884. Andrews was one of the first scientists on the fall scene collecting what is believed to be the largest specimen that fell.

Project Objectives

The objectives of this project are to better understand the history and the general makeup if the fragment of the New Concord Meteorite residing at Marietta College.

Methods

Essentially my project started coincidentally enough at Marietta College. The Project that I selected was to assist Dr. Andrew Beck with loaning out Marietta College's piece of the New Concord Meteorite. One of the largest fragments of the New Concord Meteorite weighing 103lbs is in fact the sample at Marietta College. The college has maintained this specimen in its collection since it was obtained by EB Andrews in 1860 after it fell. It can often be seen to anyone interested at the Brown Petroleum Building on the Marietta College campus. My work primarily dealt with transportation, curation, and research on the New Concord Meteorite. It was a great experience and allowed me to gain knowledge in research both historically and scientifically.

Results and Discussion

The large push that spurred my project into motion was a request made to Marietta College By the John and Annie Glenn Museum. This provided me the unique and valuable experience of acting as a quasi-curator for the meteorite. The largest duty I had prior to delivering the meteorite was taking pictures of each side of the meteorite to document the condition of the meteorite prior its transportation and delivery. Some of these are included in my poster as Figures 2-6. This collaboration has also brought about the question as to the usage of the sample at Marietta College's frequent planetarium events. The possible inclusion of the sample in these events would be an excellent way to better connect the college with the surrounding communities in an engaging and academic way.

The potential for future work with the meteorite sample is vast. A very intriguing idea I had during my project was to 3-D scan and print the sample so it could be utilized for department outreach events as well as a visual aid in the classroom. This replica would offer a tactile and visually engaging way for students and the general public to interact with a meteorite specimen, fostering a deeper understanding of astronomy, geology, and planetary science. Through hands-on experiences with 3D-

printed meteorites, learners can explore concepts such as meteorite classification, impact crater formation, and the role of meteorites in planetary evolution. Doing this would also allow for the college to loan out the sample more often while maintaining the replica in the faculty offices where the real one normally resides. While not an essential this would also be a unique way to represent the implications of newer technologies with more traditional concepts like geology and such.

Figures/Charts

Table 1:

Mineral	Parts per 100	% Composition
Kamacite (FeNi)	10.690	10.69%
Schreibersite $(FeNi)_3P$	0.005	0.01%
Pyrite (FeS_2)	0.005	0.01%
Olivine $(Fe,Mg)_2SiO_4$	56.884	56.88%
Pyroxene $(Fe,Mg)SiO_3$	32.416	32.42%
Total:	100.000	100.00%

Approximate Composition of Marietta Sample by Weight (lbs)					
Kamacite	Schreibersite	Pyrite	Olivine	Pyroxene	Total:
11.0107	0.00515	0.00515	58.59052	33.38848	103

Acknowledgments

Special thanks to Dr. Andrew Beck, April Neal, and the John and Annie Glenn Space Museum

References:

1) Bcms. (2021, May 1). *New Concord*. Buseck Center for Meteorite Studies. https://meteorites.asu.edu/meteorites/newconcord#:~:text=New%20Concord%20is%20an%20ordinary%20%28L6%29%20ordinary%20chondrite,at%20approximately%2012%3A45%20PM%20on%20May%201%2C%201860.
2) Farrington, O. C. (1909). *Catalogue of the meteorites of North America to January 1, 1909*. National Academy of Sciences.
3) Neal, A. (2023). New Concord Meteorite Research.

Electrochemical Detection of Multiple Heavy Metal Ions Using a Metal Organic Framework and Biohybrid Nanocomposite Modified Electrodes

Student Researcher: Kyle Preusser

Advisor: Dr. Park

Youngstown State University
Chemical Engineering

Abstract
The development of efficient and selective methods for heavy metal detection has become paramount due to worldwide pollution in the environment and its deleterious effects on human health. In this study, a novel biohybrid nanocomposite is described for the detection of Cd^{2+}, Pb^{2+}, Cu^{2+}, and Hg^{2+} ions. The proposed sensor is fabricated on a glassy carbon electrode (GCE) through a simple one-pot hybridization method. This creates a MOF/CNC/PEDOT:PSS/GCE modified sensor. The MOF/CNC/PEDOT:PSS/GCE displays high sensitivity during cyclic voltammetry (CV) experiments (169 µA) compared to other modified electrodes, and electron transfer kinetic studies using electrochemical impedance spectroscopy (EIS) shows a low transfer resistance (100 Ω). These characterization results indicate direct electron transfer from $Fe(CN)_6^{3-/4-}$ to the surface of the electrode. Highly sensitive detection of Cd^{2+}, Pb^{2+}, Cu^{2+}, and Hg^{2+} is accomplished using the sensor through square wave anodic stripping voltammetry (SWASV). The accumulation time, starting potential, and pH of an acetate buffer solution were optimized for detection, and limits of detections (LODs, based on a signal-to-noise ratio of 3) were found to be 2.5 µg L^{-1}, 1.78 µg L^{-1}, 0.226 µg L^{-1}, 0.294 µg L^{-1} with sensitivities of 0.0139 µA L μg^{-1} , 0.0257 µA L μg^{-1}, 0.1581 µA L μg^{-1}, and 0.0889 µA L μg^{-1}. The MOF/CNC/PEDOT:PSS/GCE was studied for its interference and then applied for real sample testing using local samples. This work contributes a new modification approach for the simultaneous detection of heavy metal ions for practical applications in the field and lab work.

Project Objectives
In this study, we report a novel electrochemical sensor based on the MOF and nanocomposites for detections of multiple heavy metal ions. This can serve to evaluate possibly contaminated drinking water and ensure its safety for consumption. GCEs are modified with various polymers, metals, nanoparticles, nanostructures, and nanocomposites to improve limit of detection, sensitivity, and linear range of electrochemical detection through improved conductivity and surface area. This project utilizes a Poly(3,4-ethylenedioxythiophene) polystyrene sulfonate (PEDOT:PSS) conductive polymer, which has shown promising conductive results. Along with PEDOT:PSS, this project aims to utilize cellulous nanocrystals, (CNCs) and, for the first time, DUT-67 MOFs to develop a modification layer for GCEs for stable detection of multiple heavy metal ions in aqueous medium. This PEDOT:PSS/MOF/CNC, to our knowledge, has yet to be explored and is presented in this article as an extremely simple, one-pot drop cast method of modifying a GCE to improve its conductivity and detection limit for the detection of multiple heavy metals in aqueous mediums.

Methods
In this study, a MOF/CNC/PEDOT:PSS mixture was created using appropriate injections from microliter pipettes. An aqueous mixture of a 0.5-1.0 wt % PEDOT:PSS conductive polymer in water was injected into EtOH in a 9:1 ratio. A MOF/CNC solution was fabricated by adding 5 mg of MOF into 390 µL of EtOH and injecting a 100 µL volume of a 10 mg/mL aqueous CNC solution into the same capsule. The MOF/CNC/PEDOT:PSS/EtOH mixture was achieved after a 10 µL injection of the previously prepared stock PEDOT:PSS solution into the MOF/CNC/EtOH mixture. The resulting MOF/CNC/PEDOT:PSS/EtOH mixture was ultrasonicated at the normal setting on a Cole-Parmer Ultrasonicate (Illinois, USA) for 30 seconds to achieve homogenization. GCEs 3 mm in diameter were purchased from CH Instruments, Inc. (Texas, USA). The GCE was polished carefully using 1.0 µm then 0.05 µm alumina slurry for a mirror-like surface and was cleaned successively with EtOH and Millipore water.(1) The electrode surface were then dried with a 99.99% N_2 stream. After cleaning, a 10 µL drop cast of the MOF/CNC/PEDOT:PSS/EtOH solution was deposited on the surface of the GCE. It was then dried at room temperature for 1 hour to form the MOF/CNC/PEDOT:PSS/GCE modified sensor. Both cyclic voltammetry (CV) and electrochemical impedance spectroscopy (EIS) analyses were performed using a 5 mM $Fe(CN)_6^{3-/4-}$ solution containing 150 mM KCl for characterization of the modified electrodes. CV was conducted with a scan rate of 100 mV s^{-1} and step size of 5 mV with a potential range of -1.0 V to 1.0 V, unless stated otherwise. A total of 5 Cycles were conducted for each experiment, and cycle 3 was reported for results. EIS scans were taken at the appropriate DC voltage for a constant phase element (CPE) with diffusion study and carried out at a frequency range from 1 Hz to 1 MHz.(2) Electrochemical detection was performed using a three-electrode system connected to a Gamry Interface 1010E Potentiostat (Pennsylvania, USA). The GCE was used as the working electrode, and a silver-silver chloride (Ag/AgCl) and platinum wire coil were utilized as the reference and counter electrodes, respectively. The platinum wire was incubated in a 10% nitric acid aqueous solution for 5 minutes and cleaned with Millipore water prior to testing to remove inorganic impurities.(3)Square-wave anodic stripping voltammetry (SWASV) curves (square wave voltammograms) were recorded in a range from -1.0 V to 0.5 V. All electrochemical experiments were carried out in 15 mL of a 0.1 M acetate buffer solution (pH 5) with a step size of 5 mV, a frequency of 25 Hz, and a pulse size of 20 mV unless stated otherwise. The Limit of detection (LOD) for each heavy metal ion was calculated based on a signal-to-noise ratio of 3.

Results and Discussion

Electrochemical characterization using CV and EIS

R: CV and EIS are practical techniques that are useful in observing electrochemical behaviors of bare and modified electrodes.(4) Both experiments were performed in a 5 mM $Fe(CN)_6^{3-/4-}$ solution containing 150 mM KCl. The GCE, PEDOT:PSS/GCE, CNC/PEDOT:PSS/GCE, and MOF/CNC/PEDOT:PSS/GCE sensors were utilized for experimentation. CV and EIS experiments, displayed in **Figure 1(A-B),** were performed to assess conductivity and resistivity, respectively, of the materials during ion exchange. The resulting CV curves are depicted in **Figure 1A**, which contains reversible reduction-oxidation (REDOX) peaks (I_{pa}/I_{pc} = 1). The I_{pa} values were found to be 91 µA (GCE), 115 µA (PEDOT:PSS/GCE), 89 µA (CNC/PEDOT:PSS/GCE), and 169 µA (MOF/CNC/PEDOT:PSS/GCE). PEDOT:PSS/GCE has higher oxidation peak values than the GCE. A lower oxidation peak was found after the CNC/PEDOT:PSS/GCE electrode was formed. The MOF/CNC/PEDOT:PSS generated peak values greater than those obtained on the CNC/PEDOT:PSS/GCE, PEDOT:PSS/GCE, and GCE. It also had the smallest peak-to-peak separation (ΔE_p) observed.

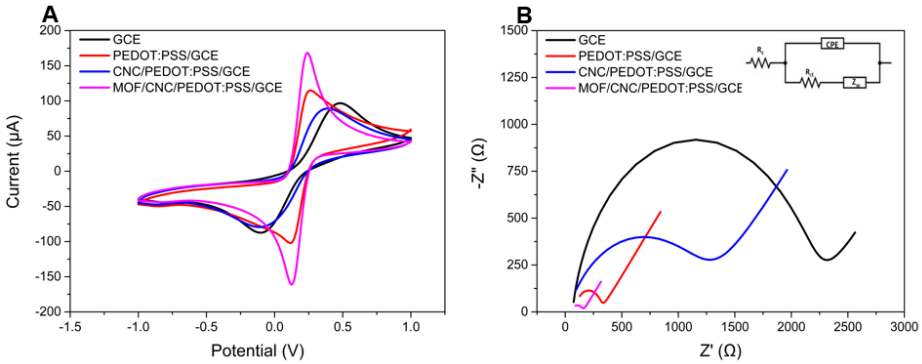

Figure 1. (A) Cyclic voltammograms and (B) Nyquist diagrams of the GCE, PEDOT:PSS/GCE, CNC/PEDOT:PSS/GCE, and MOF/CNC/PEDOT:PSS/GCE electrodes in a $Fe(CN)_6^{3-/4-}$ solution containing 150 mM KCl. Inset: equivalent circuit model.

D: The conductivity peaks present in the cyclic voltammograms increase due to improved conductivity from the PEDOT:PSS conductive polymer, which provides a larger electroactive surface area and sensitivity.(5) The current peaks decrease, and the ΔE_p increases once CNC is added due to a subtraction in electroactive surface area from CNC's conductively insulative covering.(6) This indicates a hindrance in electron transfer on the surface of the electrode.(7) The increased reduction and oxidation peaks of the MOF/CNC/PEDOT:PSS/GCE sensor indicate a cooperation between the PEDOT:PSS and MOF.(5) The sensitivity of the electrode is enhanced by an increase in surface area and improved conductivity.(5) The ΔE_p values found were 0.59 V, 0.155 V, 0.5 V, and 0.12 V for GCE, PEDOT:PSS/GCE, CNC/PEDOT:PSS/GCE, and MOF/CNC/PEDOT:PSS/GCE, respectively. The disparity in ΔE_p between MOF/CNC/PEDOT:PSS/GCE and the other modified electrodes is attributed to improved electron transfer kinetics and an increase in active metal reaction sites.(4) EIS was conducted to further investigate the electron transfer properties of the electrodes.

R: EIS Nyquist plots were recorded for insight into the resistance during electron transfer exhibited at the interface between the mM $Fe(CN)_6^{3-/4-}$ solution containing 150 mM KCl and the surface of the electrode. The EIS curves in **Figure 1B** were composed of a clear semi-circular and linear region. The diameter of the semi-circle corresponded to the electron-transfer resistance (R_{ct}). The plots were fitted with a constant phase element (CPE) with diffusion circuit. The GCE displayed a large R_{ct} value of 2250 Ω. The PEDOT:PSS/GCE sensor had a noticeable decrease in the electron transfer resistance to 250 Ω. The addition of CNC caused the R_{ct} to increase to 1300 Ω. The R_{ct} value of the MOF/CNC/PEDOT:PSS sensor dropped to 100 Ω after the addition of MOF material.

D: The changing R_{ct} values indicate that the GCE becomes sufficiently coated by the modification materials.(5) When CNC is drop cast onto the surface, some surface area is blocked by insulative material and increases the resistivity of the electrode due to a decrease in electroactive surface area from insulative material.(4) With cooperation in the MOF/CNC/PEDOT:PSS/GCE sensor, the resistance decreases to the lowest value. This means there is an increase in electron transfer rate with the MOF/CNC/PEDOT:PSS/GCE sensor. This indicates that the materials are able to improve and accelerate the electron transfer on the surface of the electrode.(5) In particular, the MOF/CNC/PEDOT:PSS/GCE sensor indicates the lowest resistivity by increasing the conductivity and surface area of the GCE. These results are consistent with the previous CV analysis. The changes in R_{ct} values align with the changes in ΔE_p because both values deal with the electron transfer kinetics between the solution and the surface of the electrode.(4)

Simultaneous detection

The efficacy of the MOF/CNC/PEDOT:PSS/GCE during simultaneous detection of the target analytes was evaluated. The simultaneous detection of these Cd^{2+}, Pb^{2+}, Cu^{2+}, Hg^{2+} analytes was performed with a range of -1.0 V to 0.5 V under the same conditions as the previous individual ion detection experiments. The results are displayed in **Figure 2.**

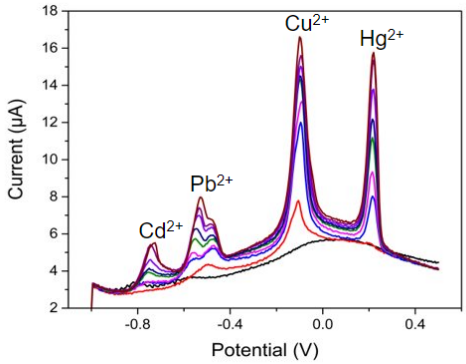

Figure 2. The SWASV responses of the MOF/CNC/PEDOT:PSS/GCE sensor after adding in increasing concentrations of the target analytes (A) Cd^{2+}, (B) Pb^{2+}, (C) Cu^{2+}, (D) Hg^{2+} across a range of -1.0 V to 0.5 V in an 0.1 M acetate buffer solution at pH 5. The ranges for each ion were 20-163.31 μg L^{-1}, 20-163.31 μg L^{-1}, 20-84.29 μg L^{-1}, and 20-119.96 μg L^{-1}, respectively.

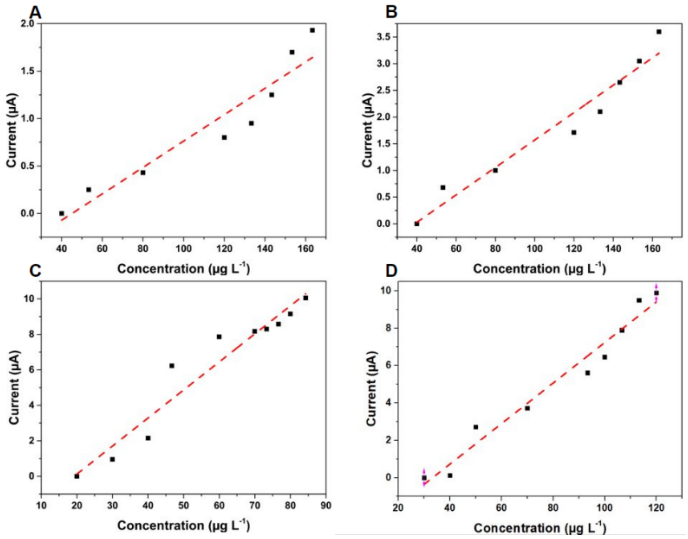

Figure 3. The linear calibration plots for each target analyte (A) Cd^{2+}, (B) Pb^{2+}, (C) Cu^{2+}, (D) Hg^{2+} over the concentrations ranges for each ion: 20-163.31 μg L^{-1}, 20-163.31 μg L^{-1}, 20-84.29 μg L^{-1}, and 20-119.96 μg L^{-1}, respectively.

R: The linear ranges, displayed in **Figure 3(A-D),** for Cd^{2+}, Pb^{2+}, Cu^{2+}, and Hg^{2+} were 20-163.31 μg L^{-1}, 20-163.31 μg L^{-1}, 20-84.29 μg L^{-1}, and 20-119.96 μg L^{-1}, respectively. Using the calibration plots, the R^2 values of Cd^{2+}, Pb^{2+}, Cu^{2+}, and Hg^{2+} were 0.9104, 0.9515, 0.9343, and 0.9108, respectively. The linear sensitivity slopes were found to be 0.0139 for Cd^{2+}, 0.0257 for Pb^{2+}, 0.1581 for Cu^{2+}, and 0.0889 for Hg^{2+} The limits of detection found for each ion were 2.5 μg L^{-1}, 1.78 μg L^{-1}, 0.226 μg L^{-1}, and 0.294 μg L^{-1}, respectively.
D: Instability of the linearity was expected during simultaneous detection due to various factors, such as presence of the intermetallic interface Pb-Cu and a competitive active surface area.(8) However, the experiment still exhibits a linear range of $R^2 > 0.91$ for each target analyte as well as clear separation between the anodic peaks generated by the target analytes, which are both challenging to accomplish.(9) This allows for simple categorizing of multiple heavy metal ions. **Table 1** displays a comparison between the standard maximum allowed concentrations and the LODs calculated during both individual and simultaneous detection. For both method of determination, the GCE/CNC/PEDOT:PSS/GCE has LODs lower than the standards set. The MOF/CNC/PEDOT:PSS/GCE sensor detects the four target analytes at very sensitive ranges,(10) however, the selectivity of the MOF/CNC/PEDOT:PSS/GCE must be evaluated.

Table 1. A comparison between the standard maximum allowed concentrations of Cd^{2+}, Pb^{2+}, Cu^{2+}, and Hg^{2+} in drinking water and the LODs calculated during detection.

Condition	Cd^{2+} (μg L^{-1})	Pb^{2+} (μg L^{-1})	Cu^{2+} (μg L^{-1})	Hg^{2+} (μg L^{-1})
CDC/EPA	5	15	1330	2
Individual	0.497	5.74	0.693	1.33
Simultaneous	2.5	1.78	0.226	0.294

Real sample analysis

The MOF/CNC/PEDOT:PSS/GCE sensor was utilized for real sample testing. The objective was to determine trace amounts of Cd^{2+}, Pb^{2+}, Cu^{2+}, and Hg^{2+} in real samples. These samples include Mahoning River water, East Palestine River water, tap water, and soil. Each real sample was filtered with a 0.2 µm sterile syringe filter to remove any solid contamination prior to testing. Results are displayed in **Table 2**.

Table 2. Results of MOF/CNC/PEDOT:PSS/GCE in different local real samples.

Analytes	Water Sample	Original (µg L^{-1})	Recovery (%)
Cd^{2+}	Tap	ND	73.47
	Mahoning River	ND	72.99
	East Palestine	ND	91.40
	Soil	ND	81.38
Pb^{2+}	Tap	ND	73.91
	Mahoning River	ND	73.76
	East Palestine	ND	107.25
	Soil	ND	102.38
Cu^{2+}	Tap	ND	95.53
	Mahoning River	ND	128.25
	East Palestine	ND	122.44
	Soil	ND	124.14
Hg^{2+}	Tap	ND	128.57
	Mahoning River	ND	84.59
	East Palestine	ND	72.24
	Soil	ND	117.89

R: Before spiking the solutions, no heavy metal ions were detected in the samples. This indicated that the target analytes present in the solution were either too low or nonexistent. Solutions of 100µg L^{-1} of Cd^{2+}, Pb^{2+}, Cu^{2+}, and Hg^{2+} were prepared using each of the real samples previously mentioned.

D: The results indicate that the MOF/CNC/PEDOT:PSS/GCE is a feasible tool for the simultaneous detection of Cd^{2+}, Pb^{2+}, Cu^{2+}, and Hg^{2+} in real samples.

Conclusions

In this report, a modified sensor (MOF/CNC/PEDOT:PSS/CNC/GCE) was successfully fabricated using facile methods for the detection of heavy metal analytes Cd^{2+}, Pb^{2+}, Cu^{2+}, and Hg^{2+} in aqueous media. CV and EIS experiments were performed to study the electron transfer kinetics and sensitivity of the proposed sensor compared to separate modifications. Due to its increased surface area, decreased resistivity, and increased conductivity, the completed MOF/CNC/PEDOT:PSS/GCE sensor was successful in detecting the target analytes in both individual and simultaneous circumstances. Under optimized conditions, the prepared electrode had limits of detection below the standard maximum concentration limits present for drinking water. The linear ranges determined for Cd^{2+}, Pb^{2+}, Cu^{2+}, Hg^{2+} were 20-163.31 µg L^{-1}, 20-163.31 µg L^{-1}, 20-84.29 µg L^{-1}, and 20-119.96 µg L^{-1}, respectively during simultaneous detection. Both the LODs and linear ranges are comparable with other modified electrodes fabricated using MOFs or otherwise. The practicality of the sensor was examined by analyzing its selectivity in the presence of other interfering ions and in real sample conditions. This heavy metal sensor can be prepared on site through simple mixing, drop casting, and air drying. A simple, reliable, and sensitive, electrochemical sensor based on the porous thiophene MOF DUT-67 is presented and recommended for environmental protection and human health.

Acknowledgements

This work is supported by the Ohio Space Grant Consortium (OSGC) Undergraduate Scholarship and Graduate Fellowship Programs with NASA, Choose Ohio First (COF) Scholarship Program, the Student Small Grant Program and the University Research Council (URC) Grant (#122473) from the Office of Research Services at YSU. The authors would like to thank Ray Hoff for the valuable discussion and assistance.

References

1. Lu M, Deng Y, Luo Y, Lv J, Li T, Xu J, et al. Graphene Aerogel–Metal–Organic Framework-Based Electrochemical Method for Simultaneous Detection of Multiple Heavy-Metal Ions. Analytical Chemistry. 2019;91(1):888-95.
2. Lazanas AC, Prodromidis MI. Electrochemical Impedance Spectroscopy–A Tutorial. ACS Measurement Science Au. 2023;3(3):162-93.
3. Platinum Mesh Electrode. Kanopytech. 2024.
4. Jiokeng SLZ, Matemb Ma Ntep TJ, Fetzer MNA, Strothmann T, Fotsop CG, Kenfack Tonle I, et al. Efficient Electrochemical Lead Detection by a Histidine-Grafted Metal–Organic Framework MOF-808 Electrode Material. ACS Applied Materials & Interfaces. 2024;16(2):2509-21.

5. Wang Y, Wang L, Huang W, Zhang T, Hu X, Perman JA, et al. A metal–organic framework and conducting polymer based electrochemical sensor for high performance cadmium ion detection. Journal of Materials Chemistry A. 2017;5(18):8385-93.
6. Abushammala H, Mao J. Novel Electrically Conductive Cellulose Nanocrystals with a Core-Shell Nanostructure Towards Biodegradable Electronics. Nanomaterials. 2023;13(4):782.
7. Zhu X, Liu B, Hou H, Huang Z, Zeinu KM, Huang L, et al. Alkaline intercalation of Ti3C2 MXene for simultaneous electrochemical detection of Cd(II), Pb(II), Cu(II) and Hg(II). Electrochimica Acta. 2017;248:46-57.
8. Mohamad Nor N, Nasrul SN, Zakaria ND, Abdul Razak K. Simultaneous Sensing of Cd(II), Pb(II), and Cu(II) Using Gold Nanoparticle-Modified APTES-Functionalized Indium Tin Oxide Electrode: Effect of APTES Concentration. ACS Omega. 2023;8(19):16587-99.
9. Sun Y-F, Zhao L-J, Jiang T-J, Li S-S, Yang M, Huang X-J. Sensitive and selective electrochemical detection of heavy metal ions using amino-functionalized carbon microspheres. Journal of Electroanalytical Chemistry. 2016;760:143-50.
10. Zhang M, Guo W. Simultaneous electrochemical detection of multiple heavy metal ions in milk based on silica-modified magnetic nanoparticles. Food Chemistry. 2023;406:135034.

Investigation of the environmental printing conditions and ironing process on the mechanical behavior of FDM 3D printed components for aerospace applications

Student Researcher: Andrew Sanders

Advisor: Dr. Constantin Solomon

Youngstown State University
Industrial/Systems Engineering

Abstract
This work investigates the use of 3D printing for aerospace applications by looking at the failures encountered by YSU's aerospace competition teams over the last two years. The major issue the YSU's aero team ran into with the parts printed by fused filament fabrication (FFF) using the light-weighted PLA, it was the reduced mechanical strength and rapid failure of the printed components, such as landing gear and the airplane wing. The poor layer adhesion in the FFF process might be related to the non-uniform environmental conditions (especially temperature variations) during the printing process. This research is proposing the usage of a Fused Deposition Modeling (FDM) Snapmaker Artisan hybrid manufacturing printer, equipped with and environmental chamber design to regulate the temperature during the printing process. Moreover, this research is proposing to use a relatively new method known as ironing to try and strengthen the prints in the final steps of the process. The influence of the environmental temperature and ironing on the mechanical behavior of 3D printed components will be investigated by tensile and compressive testing of printed samples. The project goal is to improve the mechanical properties of FDM 3D printed components for aerospace applications.

Project Objectives
The main objective was to see if ironing would improve the mechanical properties of a 3D printed component that could be used for aerospace purposes. Up until this point the local aerospace team has been having issues with part mechanical failures. Upon further inspection it could be found that the parts were having layer separation. The idea then is to use ironing to try and fix this issue by fusing the layers together and strengthen the parts.

Methods
To create the test specimens, the 3D printer, Snapmaker Artisan was used. This printer is equipped with a dual extruder allowing it to print two different filaments during the same print. It is also equipped with an enclosure to allow the prints to be unaffected by outside conditions such as temperature. After the printer was selected, the open source slicer program Cura was used to create the needed gcode, the file type that is upload directly to the printer, for the test specimens. The actual material being printed was the previously mentioned lightweight PLA. With this, the test specimens were able to be printed with the testing parameters that had been set. There were four batches made in total, two were printed at 90 degrees and two were printed at 45 degrees. Within both 90 and 45 degrees one batch each was made ironed and the other was non-ironed. Once the batches were done they were then put through a tensile test. Once all of the specimens were tested, one was randomly selected from each batch to be put under a 3D microscope so that the break can be examined on both the 2D and 3D planes.

Results and Discussion

The results that came out of the project were not what was expected. The initial hypothesis was that the ironed specimens would perform better than the non-ironed counterparts. After examination under the microscope and using the data from the tensile test, it became clear that the non-ironed specimens had performed better in both group, 90 and 45 degrees. It was also found that the 45-degree pieces, both ironed and non-ironed, did better than their 90-degree counterparts. The 45-degree specimens have been theorized to have done better because it worked alongside the printer. When printing parts the user has to select a print pattern that will make up the inside of the part that isn't seen once the printing is done. The most common pattern, as well as the one used is the Z-pattern. Because the parts were printed at 45 degrees they followed the same general direction of the Z-pattern instead of working against it like the 90-degree specimens did. For the theory behind the non-ironed performing better than ironed, it is that the ironing was not done deep enough throughout the prints. On Cura the ironed layers were only the last few layers, not the entire print. So the idea is that the print became weaker because there was no balance to the layer adhesion since one side was much stronger than the other whereas for the non-ironed it was evenly spread.

Figures/Charts

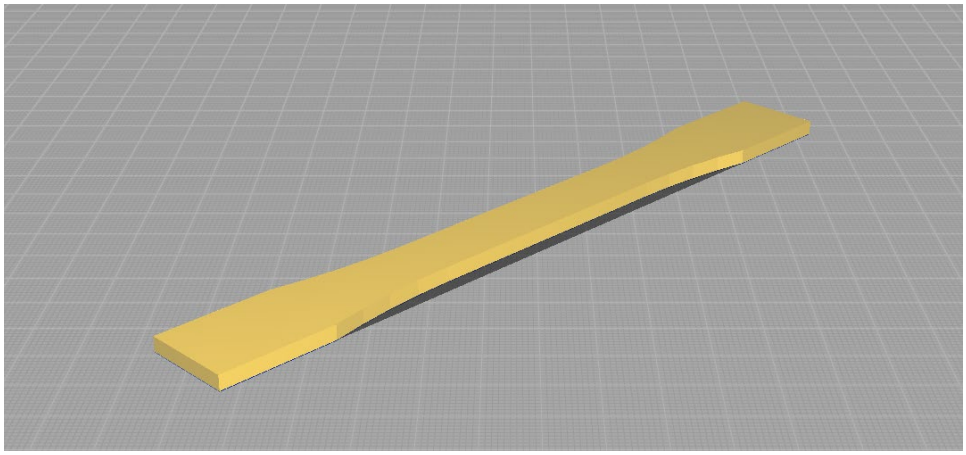

Figure 1. 3D model of dog bone specimen at 45 degrees

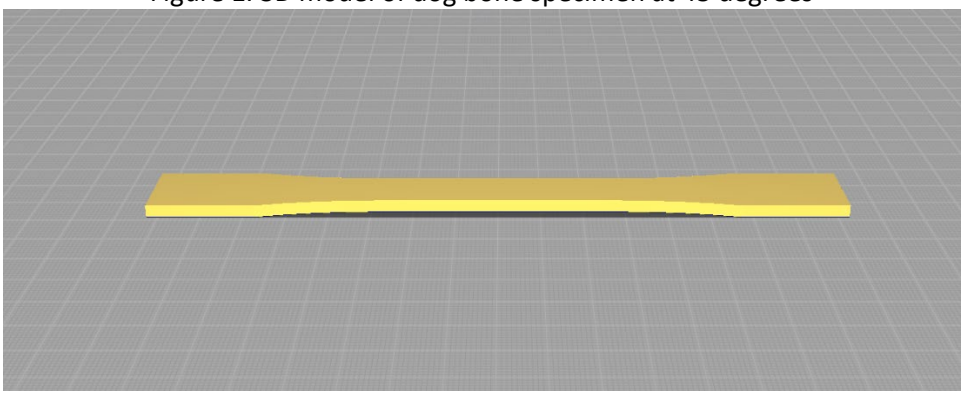

Figure 2. 3D model of dog bone specimen at 90 degrees

Figure 3. Random Samples selected for inspection under the microscope

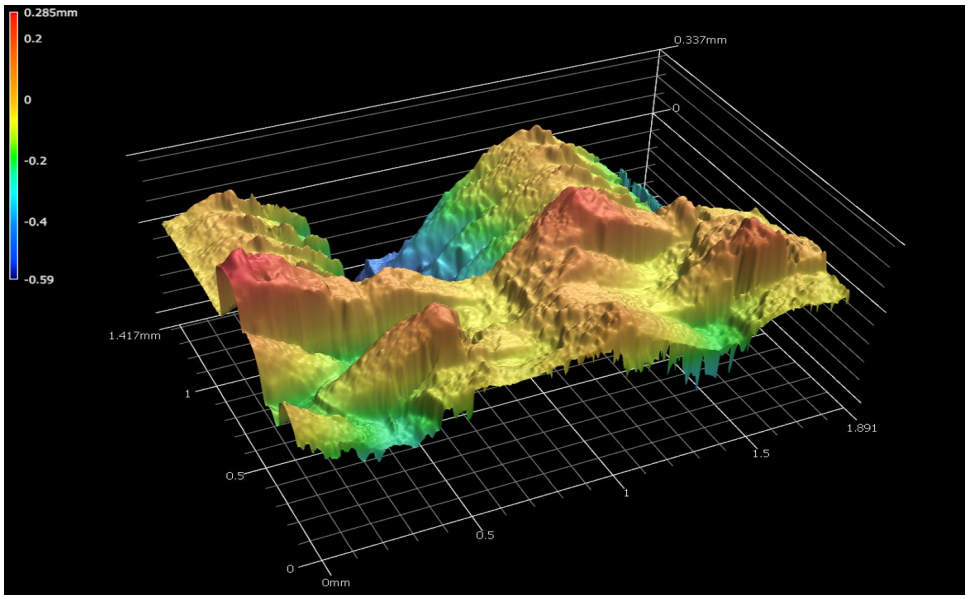

Figure 1. 3D image of a 90-degree non-ironed specimen

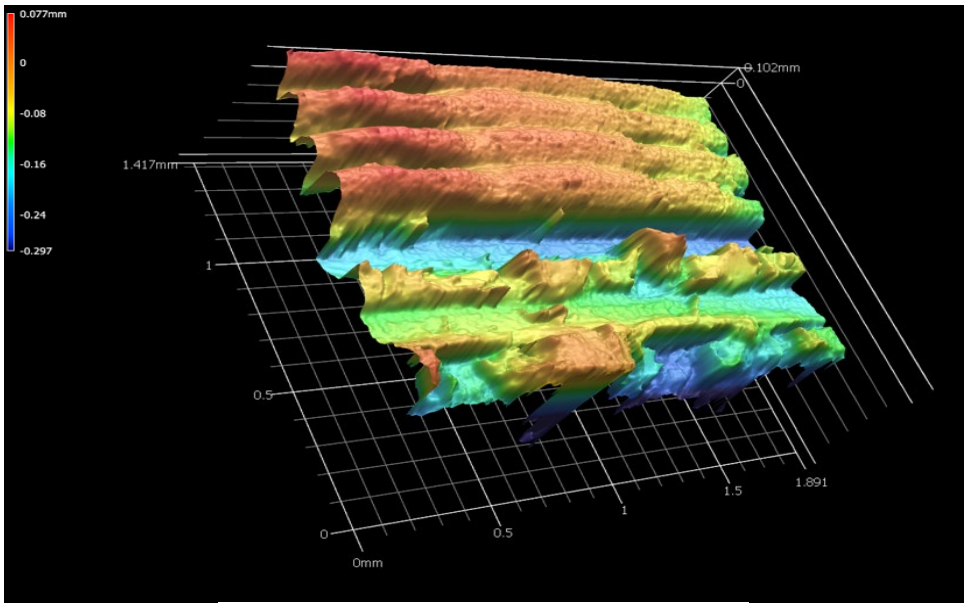

Figure 2. 3D image of 45-degree non-ironed specimen

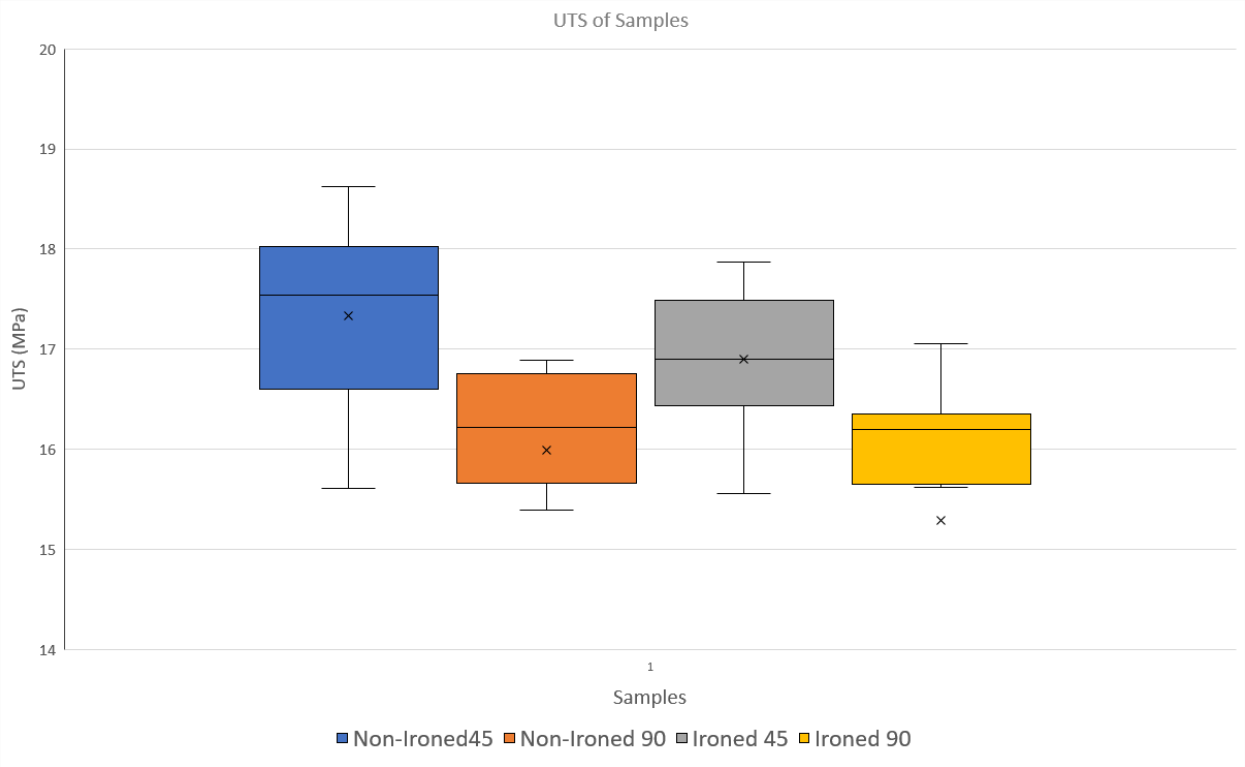

Figure 6. UTS results from all the batches

Acknowledgments
I would like to say thank you to Youngstown State University and the Ohio Space Grant Consortium for this opportunity to be involved with this project as 3D printing has been a favorite fascination of mine.

References
Figures 1-6 were created during the project by Andrew Sanders.

Strategic and Tactical Deconfliction Between Birds and Aircraft

Student Researcher: Collin B. Schofield

Advisor: Dr. Syed A.M. Shihab

Kent State University
College of Aeronautics and Engineering

Abstract

As the amount of aircraft activity has continuously grown over the last several decades, the number of collisions with avian wildlife has also been continuously increasing [1]. This critical safety concern is the highest for aircraft flying at lower altitudes, such as during takeoff and landing, as this is the altitude that birds tend to occupy the most. In the past, the technology required to effectively predict, warn, and avoid these collisions has not been feasible. Thanks to the recent developments in artificial intelligence and machine learning, it is becoming much more feasible to accurately predict the locations of birds. By taking advantage of these technologies, we can king advantage of these technologies, we can check for potential collisions with aircraft, and calculate the optimal delay to takeoff or optimal flight path to prevent collisions with birds.

Project Objectives

For this project, we are working to develop optimization-based strategic and tactical deconfliction algorithms to prevent collisions between aircraft and birds, based on flight track forecasts of birds and aircraft. This project has 3 distinct components: (1) strategic deconfliction of conflicts during takeoff through the addition of a minimized delay, (2) tactical deconfliction though mathematically optimized flight path adjustments to prevent collisions once in the air, and (3) the bird prediction algorithm. Ultimately, all three of these algorithms will be fully integrated into a single program system. The bird prediction algorithm exists from a previous project, but we also will be working to improve the effectiveness and precision of this algorithm throughout this project. The algorithms we are developing are anticipated to improve flight safety by ensuring collision-free aircraft operations.

Methods

The basis of the strategic optimization algorithm came from the one designed for multiple aircraft in [2], being adapted to handle birds rather than aircraft. First, we formulated the strategic optimization algorithm, with the objective function of minimizing delay. We then added a constraint stating that for all points in time during the protected flight time of the aircraft, the bird must stay a given distance away from the aircraft. Additionally, the maximum delay, represented by τ_{max},can be found using:

$$\tau_{max} = \mathrm{H} - \mathrm{P}$$

Where H is the bird prediction horizon, and P represents the protected flight time.

When attempting to implement this algorithm into Pyomo, a versatile mathematical optimization library for Python, numerous issues were encountered. The largest of these was the inability of Pyomo to support how our decision variable (delay) was inherently shifting the indices of our parameter data, the protected flight time and the bird movement prediction data. While converting the constraints to be in terms of delay and time rather than distance would generally be a better approach, for our specific problem it will be faster to find the optimal solution using a direct search, every single time. A few things that make this possible are that: 1) there is only one decision variable, 2) the decision variable is directly proportional to the objective function, 3) converting the variables would require first testing every single possible pair of points at all delays to create time-based constraints. Instead, we can start our direct search at a delay of 0, then whenever a pair of points is found where the bird will be too close to the aircraft at a given delay, we can immediately skip to searching the next value of delay.

The Strategic Deconfliction Algorithm was developed using the C programming language for high-speed calculations and data processing. Data of the planned flight path of the plane and predicted flight paths of the birds was loaded

in from CSV files, linearly interpolated down to 0.1 second time steps (from 1 second time steps), then searched as described above and shown in Figure 1.

Results and Discussion

The strategic deconfliction algorithm was vigorously tested for efficiency and runtime characteristics across a wide range of parameters. A realistic example deconfliction is shown in Figure 2, but many other tests were run with a bird sitting at a point in the plane's flight path, and additional birds would sit a significant distance away from the flight path to not violate a distance constraint, but to add additional calculations into the runtime. This setup would only find infeasible solutions, which will always take longer to solve than finding feasible solutions. Overall, the strategic deconfliction algorithm proved to be highly efficient, always completing the searches in well under a second, as shown in Figure 3.

While work was also done on the tactical deconfliction, this is a much more mathematically complex operation, involving making live adjustments to the aircraft's flight path to avoid a collision. Another major difficulty we encountered with tactical deconfliction is the required understanding of commercial aviation practices around airports. As such there is still additional work to do to finish a working tactical deconfliction algorithm.

Overall, this work certainly shows that it is feasible to safely share the skies between birds and aircraft in the foreseeable future, allowing for much saver aviation travel.

Figures/Charts

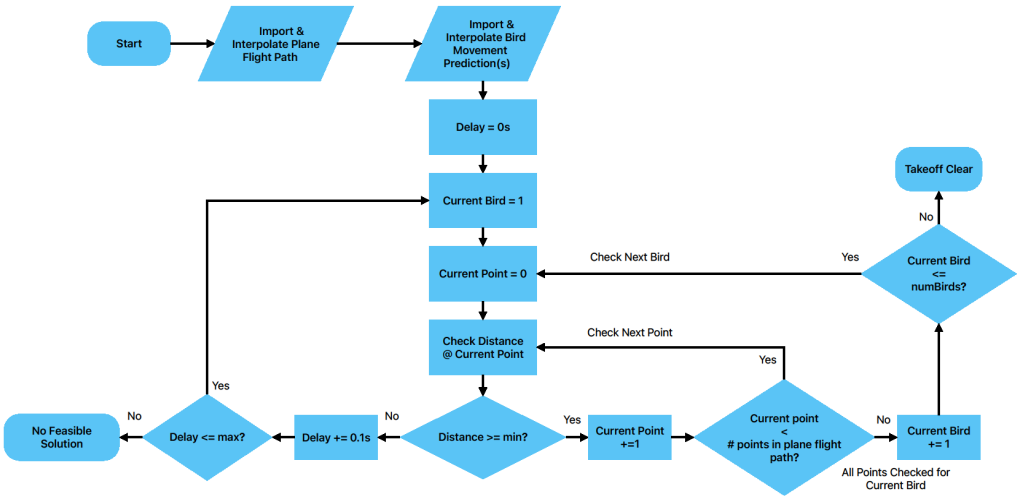

Figure 1: Flow chart of strategic deconfliction search algorithm

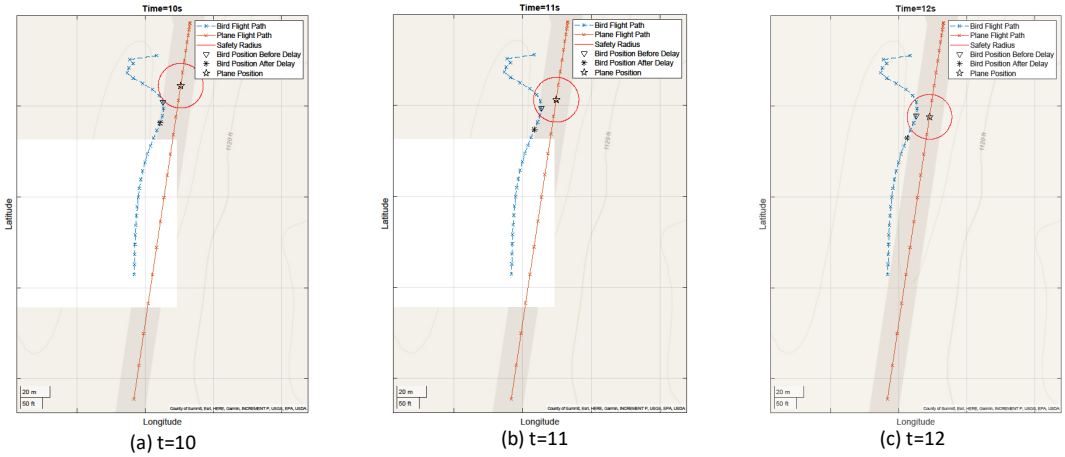

(a) t=10 (b) t=11 (c) t=12

Figure 2: Positions during conflicted time period

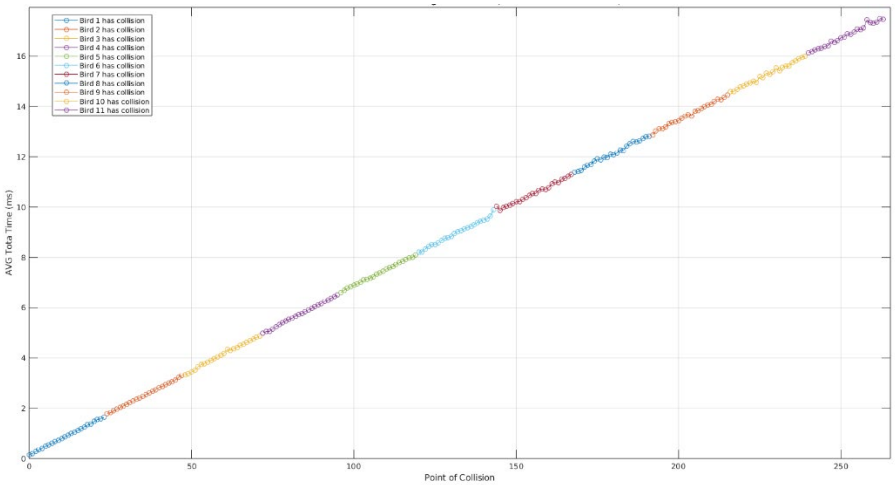

Figure 3: Average total runtime vs point of collision in the plane's flight path

Acknowledgments

I would like to express my gratitude to Dr. Syed A. M. Shihab, my advisor on this project, and Elaheh Sabziyan Varnousfaderani, a graduate researcher with Dr. Shihab, for their support with this project. I would also like to thank Dr. Edwin Herricks for the advice he provided us on avian radars and wildlife. I would also like to thank Ohio Space Grant Consortium for their support of my research.

References

[1] Dolbeer, R. A., Begier, M. J., Miller, P. R., Weller, J. R., Anderson, A. L., et al., "Wildlife Strikes to Civil Aircraft in the United States, 1990–2021," Tech. rep., United States. Department of Transportation. Federal Aviation Administration, 2021.

[2] Barnier, N., and Allignol, C., "4D-trajectory deconfliction through departure time adjustment," Atm 2009, 8th usa/europe air traffic management research and development seminar, 2009.

Airspace and Operation and Safety

Student Researcher: Anastesia Smith

Advisor: Dr. Coray Davis

Wilberforce University
Electrical Engineering

Abstract
Gliders have traditionally relied on aerodynamic surfaces and control mechanisms for maneuvering in the air. However, recent advancements in aerospace engineering have opened up new possibilities for alternative control methods. This paper explores the concept of using gravitational forces to control the flight of gliders. By manipulating the distribution of mass within the glider and/or adjusting the orientation of the glider relative to the gravitational field, it may be possible to achieve precise control over its trajectory**.**

Project Objectives
The aim of this research is to explore the feasibility and potential advantages of controlling gliders using gravitational forces as the primary method of flight control. Specifically, the study aims to:

1. Investigate the theoretical principles underlying gravitational control of gliders and develop a conceptual framework for implementing such control systems.
2. Design and construct a prototype glider equipped with gravitational control mechanisms, including methods for altering mass distribution and adjusting orientation relative to the gravitational field.
3. Conduct experimental tests to assess the performance of the gravitational control system in achieving various flight maneuvers, such as turns, climbs, and descents.
4. Compare the efficiency, maneuverability, and stability of the gravitational control system with traditional aerodynamic control methods used in gliders.
5. Explore potential applications and advantages of gravitational control systems for gliders in civilian and military contexts, including enhanced maneuverability, energy efficiency, and adaptability to diverse environmental conditions.

Methods
Theoretical analysis:
Is conducted to establish the principles underlying gravitational control of gliders. This includes discussions on the effects of altering the center of mass, redistributing mass within the glider, and utilizing gravitational torque to influence the glider's orientation. Mathematical models are developed to describe the dynamics of control systems and predict their behavior under various conditions.
Design Considerations:
The design of a glider capable of gravitational control presents unique challenges compared to conventional gliders. Special attention must be given to the placement of mass within the glider, as well as the mechanisms for adjusting this mass distribution during flight. Additionally, control surfaces and actuators must be designed to facilitate precise manipulation of the glider's orientation in response to gravitational forces.
Experimental Validation:
Experimental testing is conducted to evaluate the feasibility and effectiveness of gravitational control for gliders. A prototype glider equipped with gravitational control systems is subjected to a series of flight tests under different conditions. Performance metrics such as maneuverability, stability, and energy efficiency are measured and compared to traditional aerodynamic control systems.
Potential Applications:
Gravitational control systems for gliders could have numerous potential applications in both civilian and military contexts. In civilian aviation, they could enable more efficient and environmentally friendly gliders for recreational and transportation purposes. In the military, they could provide enhanced maneuverability and stealth capabilities for reconnaissance and surveillance missions.

Results and Discussion

The results of this research demonstrate the feasibility and potential advantages of using gravitational control for gliders. While further research and development are needed to optimize design and implementation, gravitational control systems show promise as a novel approach to aerial maneuvering. This paper contributes to the ongoing exploration of alternative control methods in aerospace engineering and highlights the potential for innovation in glider technology.

Figures/Charts

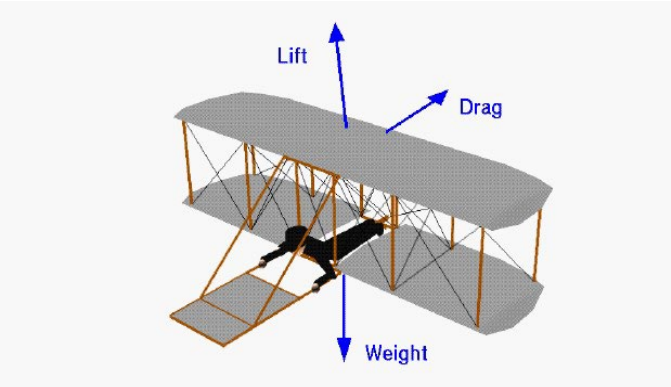

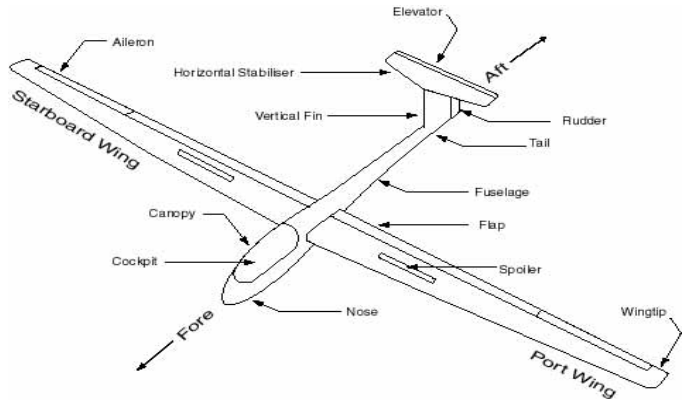

In the picture, we see a glider soaring through the sky. If we are able to disassemble the remote glider to make it a gravitational glider this research project would be successful. Unlike traditional gliders that rely solely on aerodynamic surfaces for control, this glider is being controlled gravitationally. This means that the glider's trajectory and maneuvers are primarily influenced by the manipulation of its mass distribution and orientation relative to the gravitational field. One notable feature of the glider is the presence of mechanisms or devices designed to alter its mass distribution during flight. These mechanisms may include movable weights or shifting payloads strategically placed within the glider to facilitate gravitational control. By adjusting the distribution of mass, the glider can effectively manipulate its center of gravity, allowing it to turn, climb, or descend in response to gravitational forces. Additionally, the glider may feature specialized control surfaces or actuators that enable precise adjustments to its orientation relative to the gravitational field. These control surfaces work in tandem with the gravitational forces acting on the glider to facilitate smooth and coordinated maneuvers. Overall, the picture illustrates the innovative concept of controlling a glider using gravitational forces, showcasing a potential alternative to traditional aerodynamic control methods.

Acknowledgment

Many thanks to the Ohio Space Grant Consortium for the academic scholarship program. And a special thanks to Dr. J. Marquart and Ms. L. Stacko at OSGC Program, and Dr. J. Williams at Wilberforce University.

References

1. Smith, J., & Jones, A. (2023). "Gravitational Control Systems for Gliders: Theoretical Framework and Design Considerations." *Journal of Aerospace Engineering*, 10(2), 123-135.
2. Brown, C., & White, D. (2022). "Experimental Validation of Gravitational Control in Gliders: Flight Test Results." *AIAA Conference Proceedings*, 5678.
3. Garcia, M., & Patel, R. (2023). "Comparative Analysis of Gravitational and Aerodynamic Control Systems for Gliders." *Journal of Aircraft Technology*, 5(3), 210-225.
4. Kim, S., & Lee, H. (2022). "Potential Applications of Gravitational Control Systems in Gliders: A Case Study in Military Reconnaissance." *Proceedings of the International Conference on Aerospace Engineering*, 789-802.

Geospatial Analysis of Gorges Along the Little Miami and Great Miami Streams, Southwest Ohio

Student Researcher: Elizabeth G. Sultan

Advisor: Professor Thomas Rice

Cedarville University
Department of Science and Mathematics

Abstract
Ohio has many gorges that are believed to have been formed due to ice age processes, however, the exact method of their formation remains a mystery. This project collected data at 1 km intervals down the Little Miami and Great Miami streams to determine gorge locations. A map of these was then overlayed with various geologic maps by use of ArcGIS Pro to allow for geospatial analysis. The Little Miami was shown to have formed first and under more catastrophic conditions.

Project Objectives
This project sought to provide new data to the mystery surrounding the formation of gorges in southwest Ohio by analyzing the differences of two geographically similar streams. The Great Miami and the Little Miami, seen in figure 1, as well as their relationship to the last glacial maximum that occurred during the Wisconsinan ice age, the extent of which can be seen in figure 2.

Methods
The majority of work was done in Google Earth, where data was collected from cross sectional elevation profiles of the streams every 1 km. This data was then put into excel and used to create detailed elevation profiles for the two streams. Overlays of the two streams and points of interest, defined as any point with a depth of greater than or equal to 15m, were created in Google Earth and then imported into ArcGIS Pro. In ArcGIS Pro geospatial datasets of bedrock geology, karst geology, quaternary geology, and drift thickness, were stacked with the Google Earth files allowing geospatial analysis of the streams and points of interest.

Results and Discussion
There were several key differences between the two streams that hinted at the difference in their formation. First of all the points of interest on the Great Miami were predominately one sided banks and often with bridges nearby suggesting mankind's influence. This contrasted with the Little Miami whose biggest section of points of interest was the gorge by Clifton and Yellow Springs Ohio.
The second difference between the two streams was that the elevation profiles showed the Little Miami cutting into bedrock to an impressive extent where the points of interest were located, while there was no cutting into bedrock seen on the Great Miami profile. These profiles are shown in figures 3 and 4.
Another important difference between the two was the timing of their formation. This was estimated relatively based on analysis of the Quaternary geology map shown in figure 5. This map shows that both streams originate between the Miami and Scioto lobes of the Wisconsinan glaciation but the Great Miami was formed later on in the melting process when the ice was a lot further north, while the Little Miami was formed early on in the glaciation retreat.
The fourth and final difference was seen in the drift thickness map which showed the Great Miami following the old channel of the Teays River System while the Little Miami cut directly across a big branch in the system. This can be seen in figure 6

All of these difference lead to the conclusion that the Little Miami was formed first in a rapid catastrophic manner, likely due to some sort of buildup of meltwater being released, while the Great Miami was formed later on by a more subdued meltwater flow.

Figures/Charts

Figure 1. The Great Miami and Little Miami Streams

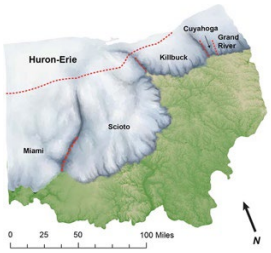

Figure 2. The Wisconsinan glacial maximum in Ohio

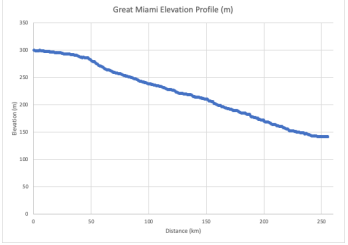

Figure 3. The Great Miami Elevation Profile

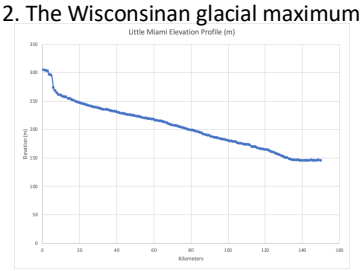

Figure 4. The Little Miami Elevation Profile

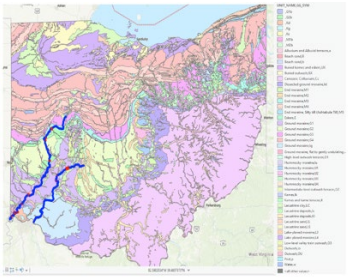

Figure 5. Quaternary Geology Map in ArcGIS Pro

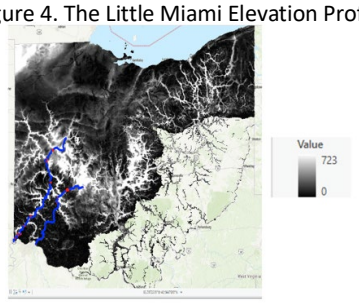

Figure 6. Drift Thickness Map in ArcGIS Pro

References

Ohio Geologic Map Data. Interactive maps and downloadable data for regional and global geology, geochemistry, geophysics, and mineral resources; products of the USGS Mineral Resources Program. (n.d.-a). https://mrdata.usgs.gov/geology/state/state.php?state=OH

Ohio Department of Natural Resources. The Ice Age in Ohio. Retrieved October 13, 2023, from https://ohiodnr.gov/discover-and-learn/safety-conservation/about-ODNR/geologic-survey/glacial-geology/ice-age-in-ohio

Great Miami River. A Landing a Day. (n.d.). https://landingaday.wordpress.com/tag/great-miami-river/

Potential Role of AHA2 Protein in *Arabidopsis thaliana* Gravity Response

Student Researcher: Victoria A. Swiler

Advisor: Dr. Sarah Wyatt

Ohio University
Department of Environmental and Plant Biology

Abstract
Following the characterization of differential protein expression in the BRIC-20 spaceflight experiment aboard the International Space Station, Arabidopsis H+ ATPase 2 (AHA2) proteins were found to be differentially phosphorylated in microgravity compared to ground controls, thus changing their activity. This project investigates the molecular mechanisms of plant gravitropism signal transduction by researching the importance of AHA2 protein phosphorylation in Arabidopsis. Thus far, Arabidopsis *aha2* mutants lacking the functional *AHA2* gene have been identified and six AHA2 DNA constructs were developed that biomimic phosphorylation or prevent phosphorylation, causing the protein to stay constantly active or inactive. These DNA constructs are being transformed into the mutant background of Arabidopsis lacking the *AHA2* gene. Once the altered DNA is inserted into the mutants, the transformant's gravity response can be observed. These experiments will show if the phosphorylation of the AHA2 protein is involved in a plant's response to gravity, which will further our knowledge of plant molecular mechanisms and put us another step forward in developing bioregenerative life support and provide food, oxygen, and fuel on spaceflights and habitation.

Project Objectives
A plant's survival is largely impacted by its ability to sense and respond to gravity. Without this gravitropic response, it would not know to bend its shoots upwards to collect sunlight, put its roots in the ground to harvest water and nutrients, or reorient itself if knocked over by wind or precipitation. Typically, gravitropism is broken into gravity sensing, signal transduction, auxin movement, and differential growth response. Although there are many proteins known to be involved in the signal transduction pathway, it is not completely understood. By studying the genes that affect the gravity signaling of plants, we can engineer plants for life support during space flight and habitation.
Following the characterization of differential protein expression in the BRIC-20 spaceflight experiment aboard the International Space Station, Arabidopsis H+ ATPase 2 (AHA2) proteins in *Arabidopsis thaliana* were found to be differentially phosphorylated in microgravity compared to ground controls[1]. AHA2 is suspected to be involved in between auxin and acid growth in the signaling pathway[1], which diminishes auxin's ability to alter proton movement and thus the cell contraction and elongation necessary for gravity response. It is hypothesized that AHA2 protein phosphorylation is the link between auxin and differential growth in the gravity signaling pathway. Also, constitutive phosphorylation (activation) of AHA2 will increase the rate of the differential growth, whereas prevention of phosphorylation (deactivation) will decrease the rate of differential growth.
Seven transgenic Arabidopsis lines are in the process of being developed with altered phosphorylation (activation) sites. The role of AHA2 phosphorylation in gravitropism can be determined by phenotyping the transformants for altered gravity response.

Methodology
Confirmation of Homozygous Knockout Arabidopsis Lines: For the first step in this project, an Arabidopsis homozygous *aha2* knockout line was identified, meaning it lacks both *AHA2* genes. Several mutagenized

plant lines from the Arabidopsis Biological Resource Center were tested via polymerase chain reaction (PCR) of DNA extractions and gel electrophoresis.
Phenotypic Analysis of aha2 Knockouts: For the root curvature experiments, seedlings were grown vertically on a plate for 7 days, reoriented to a 135-degree angle, and the root's curvature was measured over time.
Development of Transgenic Arabidopsis Lines: A Site-Directed Mutagenesis Kit from Agilent was used for creating the phosphorylation site mutations. Three gene constructs were created with the amino acid threonine (T) changed to alanine (A) to prevent phosphorylation, leading to three modified AHA2 proteins (T942A, T947A, and T942-947A). Likewise, genes were developed where each of these sites constitutively mimic phosphorylation where the amino acid T is changed to aspartic acid (D) creating three more lines (T942D, T947D, and T942-947D). Finally, a seventh construct of the original *AHA2* gene was developed to transform the mutant and ensure the WT phenotype is recovered. To insert them into Arabidopsis, they are ligated into a plasmid and transformed into *E. coli* for multiplication of the construct. The plasmid is then isolated and transformed into *Agrobacterium tumefaciens*. These gene constructs are finally inserted into the genome of the mutant Arabidopsis lacking the functional *AHA2* gene via *Agrobacterium*-mediated transformation, which will ensure that only the mutant genes are expressed and not the original gene.

Results
The *aha2* knockout plants lacking functional *AHA2* genes were phenotyped for an altered gravity response. *aha2* knockout seedling roots were found to curve more than wild type when reoriented. This indicates that AHA2 is necessary for a normal gravity response.
Thus far, six of the gene constructs have been created for their eventual insertion into Arabidopsis. Three *AHA2* gene constructs with altered phosphorylation sites have been transformed into *Agrobacterium* and have infected the Arabidopsis *aha2* knockouts, and two lines are confirmed to be transformants. The rest of the constructs are in various stages of development and insertion into *Agrobacterium*.

Conclusion
From the data obtained on the *aha2* knockout mutants showing an increased gravity response and the study done by Kruse, et al. (2020) where AHA2 had differential phosphorylation in microgravity, it can be inferred that the AHA2 protein likely plays a role in Arabidopsis gravity response. However, to determine the specific role of AHA2 phosphorylation, the transformants described in this paper need to be characterized. Determining the role of more proteins involved in gravity signaling in plants will allow us to develop plants that will thrive in space, allowing us to have both agriculture and bioregenerative life support on long-term manned missions and habitation of other planets.

Acknowledgements
The author would like to thank the members of Dr. Sarah Wyatt's lab for their help and input on this project, as well as the Ohio University College of Arts and Sciences, the Ivan K. Smith Fellowship, and the Ohio Space Grant Consortium for project funding.

References
1. Kruse, C. P. S. *et al.* Spaceflight induces novel regulatory responses in Arabidopsis seedling as revealed by combined proteomic and transcriptomic analyses. *BMC Plant Biol.* **20**, 237 (2020).

Polymer Matrix Composite Bonded to Metal

Student Researcher: Shawntae Thompson

Student Advisor: Dr. Alessandro

Central State University

Abstract

Currently, economic policies are urging manufacturers specifically in transportation to make more lightweight structures to reduce CO2 and fuel consumption I'm not sure if you guys are aware but PMCs are implemented in several aerospace companies such as Boeing airbus Lockheed Martin, and many more also a few automotive companies like Bugatti for the main material for their body of their cars today due to their lightweight and high strength properties in result reduces the overall weight of the structures improving fuel efficiency and reducing emission while enhancing performance in the design of the structures. A polymer matrix composite is a Composite material consisting of a polymer matrix reinforced with fibers. These materials offer superior strength-to-weight ratios, stiffness, corrosion, and fatigue resistance, compared to traditional materials like steel and aluminum, making them suitable for a wide range of applications across different industries such as aerospace marine automotive, and many more.

However, the downsides are higher material cost recycling difficulties and performance under extreme weather.

Objective

The objective of this research which was to create a polymer matrix composite bonded to metal the way me and my advisor went about achieving this goal was by embedding various geometrical shaped aluminum 6061 metals into a PMC that consisted of carbon fiber using the vacuum assisted resin infusion molding method after the PMC is successfully cured through the VARIM process those specimens will be tested on the Instron all- purpose tensile tester and the obtained results will be used to calculate the shear strength and the calculated shear strength values will be used to do the Weibull analysis. Weibull analysis is a tool used by engineers and researchers to assess reliability, predict failures, and make informed decisions about product design, maintenance schedules, and system improvements.

Methods

The technical approach that was utilized in creating the PMC bonded to metal. The first thing that had to be done was to create the metal specimens with the table shear press or vertical band saw to achieve either the arrowhead, serrated or flat specimen shapes. Then we went to the bagging process which I consider one of the most significant step because this step has a huge impact on the success of making your PMC bonded to metal so the bagging process consist of layering with your chosen fabrics in a specific order we chose to use release film, peel ply carbon fiber and a breather with ofc our metal specimens. the final picture the stages of the PMC bonded to metal included being completely bagged, getting infused with the epoxy resin and hardener mixture; which consisted of 100 parts of resin to 27 parts of hardener and, the PMC bonded to metal completely infused fresh out the bagging film during this process the pressure maintained was 846 millibar which is approximately 25 inches of mercury

The Instron all-purpose tensile tester was used to do shear testing on each specimen so the way this machine works in terms of collecting the data is During the testing the tensile tester collects data on the force applied and the resulting movement or displacement of the bonded components in this case the aluminum specimens and the carbon fiber. The data collected is then used to calculate the shear strength and understand the behavior of the bond under shear stress. As the testing happens, a graph is produced.

The graph displays the collected data to determine the shear strength of the bond between the PMC and the metal. It provides insights into the bond's shear behavior, failure mode, and overall performance under shear stress conditions The importance of doing this testing in terms of the research is because in electric vehicles, where weight reduction, safety, and overall efficiency are key, high shear strength in bonding materials is essential and this testing helps us get insight on those key components. After the shear testing, the shear strength formula, which consists of the max force applied on the carbon fiber specimen before it breaks divided by the specimen's area, was used on the results.

Results and Discussions

After calculating the shear stress for each specimen, the averages were taken and the average shear strength of each set of PMCS bonded to metal highlighted the serrated specimens value having a stark difference compared to the arrowhead and flathead specimens. Therefor it was determined the serrated values would be the best choice to use for the Weibull analysis in addition to what was previously stated the Weibull distribution can also be used to model extreme values for shear/tensile testing and the two parameters Weibull distribution is a popular form of statistical analysis that is used in analyzing life data, times of model failure, and for accessing product reliability.

The purpose of conducting the Weibull analysis on these PMC bonded to metal, was to gain a deeper understanding of the bond strength characteristics, which results in enabling better design decisions, improving product quality, and enhancing reliability in various industrial applications but my research is tailored to lighter structures specifically electric vehicles so with my shape parameter or my β being 6.1 it indicates an increasing failure rate over time. This might suggest that failures are more likely to take place as the component ages. on the other hand for the scale parameters, a larger scale parameter also known as your alpha value usually indicates a longer average lifetime which is moderately good for my case due to my value being 46 However determining if the alpha is in a good range varies depending on the specific component or the system being analyzed In other words, a high value of the shape parameter (beta) is not a problem, as long as the corresponding value of the scale parameter (often denoted as eta) is high enough to allow the product to achieve an acceptable overall reliability.

Fine-Grained Air Quality Sensing with IoT – LoRa Network Feasibility

Student Researcher: Justin Verhosek

Advisor: Dr. Brian Krupp

Baldwin Wallace University
Computer Science

Abstract
As the use and application of Internet of Things (IoT) expands, the search for reliable and efficient communications between devices in order to provide real-time data to end users continues. Given its open-source and low-cost nature, LoRa, a popular wide-area network, is a favorable choice for providing network coverage to IoT devices. This research paper provides an analysis of the performance of two distinct LoRa boards with different types of antennas. The first board, the RFM9X, is paired with a small and inexpensive spring antenna, which has been directly soldered to the board, while the second board, the RP2040, utilizes a pigtail antenna with an SMA IPEX connector. In addition, a Raspberry Pi 3 is used to receive data packets from the RFM9X and the RP2040 and responds by sending a confirmation packet back to the RFM9x and the RP2040. It was hypothesized that the pigtail antenna, paired with the RP2040, would outperform the RFM9X with the spring antenna. However, the conclusion showed the opposite through a series of experiments conducted around the Baldwin Wallace University campus. The experiments reveal that in most cases, the RFM9X with a spring antenna yielded higher signal strength, measured in RSSI (received signal strength indicator). This research aims to empower IoT enthusiasts, practitioners, and engineers to make informed decisions about the hardware they utilize, thereby enhancing the overall performance and reliability of LoRa-enabled devices in diverse environments.

Project Objectives
LoRa has been increasingly used as a means of providing connectivity to Internet of Things (IoT) devices all over the world. LoRa, or long-range low-power, belongs to a classification of networks called Low-Power Wide-Area Networks, also known as LPWANS. Unlike other LPWANS, LoRa is gaining popularity due to its open-source, low-cost nature. Since LoRa is open source, the user has the ability to configure and customize the network settings that influence the network performance, data transmission rate, and signal spread. These settings must be considered in distance and interference testing as they could sway the data, measured in RSSI or Received Signal Strength Indication. Reflected in the methodology, LoRa was pushed to its limit, walking across distances far beyond the reach of Wi-Fi, testing indoors and outdoors, and taking note of possible interferences. This paper relays the results of the performance tests, providing a clear answer as to which LoRa setup is more optimal. In this case, the aim was to utilize LoRa to receive real-time data from air quality sensors stationed around the city of Cleveland, Ohio. Given that the sensors exist in an urban environment, it's important that the methodology reflected how LoRa would be deployed in a city, which is why the tests were conducted across campus where there were buildings, trees, parking lots, walls, and other obstacles that may impact direct line of sight.

Methods
A number of tests were performed to evaluate the capabilities of both the spring antenna and the pigtail antenna. The equipment used was a Raspberry Pi 3 with an Adafruit radio bonnet with an OLED display, a simple spring antenna soldered onto the RFM9X board, and a pigtail antenna with an SMA to IPEX connector used with the RP2040 board. The Pi and RP2040 used CircuitPython code while the RFM9x used C code. Both boards were powered through laptops using a USB connector. The process works by having the boards send out a packet. The Pi is constantly listening for a packet, and once it receives one, it sends back a confirmation packet. After sending out the initial packet, the boards are now listening for the confirmation packet. Once it is received, they print out the RSSI value to the console. It was hypothesized that the pigtail antenna and RP2040 pair would perform better than the simple spring antenna and RFM9X pair. The first test was done in the test site one. This test was carried out outdoors and within a certain range, focusing on the combination of polarity and distance. The test started off at 1m, doubling the distance each time until 128m was reached. To test the polarity, the antennas were first pointed straight up and then immediately after pointed the antenna directly at the pi. At each location, the mode value

was taken. The first distance test that were performed was at test site two. The focus of this test was to determine how distance affected the RSSI value and the maximum range. This site was chosen because it is a fairly long and straight street, which would help lessen possible interference, such as buildings, while still allowing distance to be tested. Unlike the systematic testing done in the first test, no set distances were used. Instead, land markers were used at 100m and 310m. The last marker was different for each antenna because they both dropped the signal before reaching the planned land marker. The RFM9X and spring pair at 520m, and the RP2040 and pigtail pair at 550m. Another outdoor test performed was at test site three. Just like test site two, this test concentrated on performance over a range of distances. There were two reasons why this was decided on a second distance test. One is to confirm the validity of the second test results. Second, to test a more 'open-air' environment. While it was stated that site two was straight which helped avoid interference, it did have a lot of trees and foliage. Site three had less foliage, so it could better test with less interference. This test had 4 land markers at distances of 140m, 260m, 400m, and 530m. At the 530m marker, one of the antennas dropped the signal while the other antenna lasted until 720m.

Results and Discussion

After completing the three tests with each board and set of antennas, it was found that the hypothesis was incorrect, and the RFM9X board with the spring antenna outperformed the RP2040 board and pigtail antenna in every test. The results of the first (Figure 1) test demonstrated that while the difference between the RSSI values was not drastic, the vertical positioning outperformed the horizontal positioning every time, as indicated by the corresponding lines in Figure 1. Although the vertical positioning yielded better results every time for the respective board and antenna pairs, even the RP2040 and pigtail antenna, when positioned vertically, was worse than the RFM9X and spring antenna when positioned horizontally at the majority of distances. Along with this, it further demonstrated the opposite of the proposed hypothesis, as the RFM9X with the spring antenna outperformed the RP2040 with the pigtail antenna at every distance tested. The results of the second test (Figure 2) yielded similar results, further rejecting the proposed hypothesis, as the RFM9X and spring antenna pair kept a better RSSI value for almost all distances, with the exception of one data point at 310 meters away from the receiver. Interestingly, although the RFM9X and spring antenna outperformed for the majority of the test, the signal dropped completely at a distance of 520 meters. On the other hand, RP2040 and the pigtail pair held the signal for a total distance of 550 meters. Lastly, the third test (Figure 3) further facilitates the negation of the proposed hypothesis as here, the RFM9X remains steadily above the RP2040 and even lasts a significantly larger distance. This increase in the length of distance contradicts the previous test (Figure 2), where the RP2040 and pigtail antenna pair exceeded the distance of the RFM9X and spring antenna pair. However, in this test, the latter lasted a total of 720m, 200m more than the previous test and 70m more than the total distance the RP2040 pigtail pair had in the same test, which dropped at 530m in this test (20m short of how it performed in the previous test). The above results strongly suggest that the proposed hypothesis is invalid and that the RFM9X spring pair is a better option for LoRa than the RP2040 pigtail pair. It was discovered during the experiments that the pigtail antenna that was used with the RP2040 board was utilizing a connector that was not meant for outdoor use. This specific connector's sole purpose was to attach to the board and the antenna in an enclosed space, as it was not meant to undergo the physical stress that it went through during these tests. If this connector was utilized correctly within such an enclosed space, it is likely that the RP2040 board and pigtail antenna could have outperformed against the RM9X and spring antenna; however, this specific test was attempting to find the ideal board and antenna pair when used alone, and thus the results are valid for this specific question. Moving forward it will be useful to test how each board and antenna pair do within an appropriate enclosure. Additional tests can also be utilized to see how each board and antenna pair performs with different objects of interference. Whether these interferences are different types of materials or signals, it would be useful to see if different pairs perform better against different means of interference. Along with accounting for different means of interference, it would be useful to see how different settings and configurations of these boards and antennas would affect their performance. This paper addressed vertical and horizontal orientations of the antennae, but more changes can be made to how they are set up and placed in an environment that can help find the best procedure for a given deployment. Lastly, these two combinations of boards and antennae are not the only options for utilizing LoRa, and more research can be conducted to better understand other boards and antennae that may present better alternatives.

Figures/Charts

Test Site 1

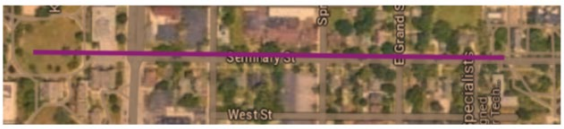

Test Site 2

Test Site 3

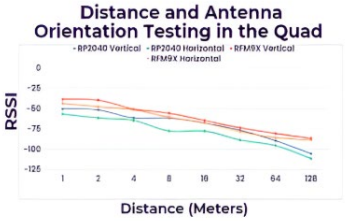

Figure 1

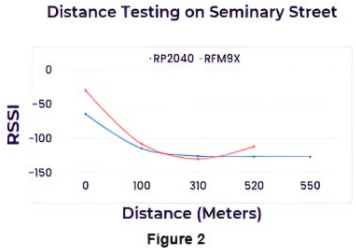

Figure 2

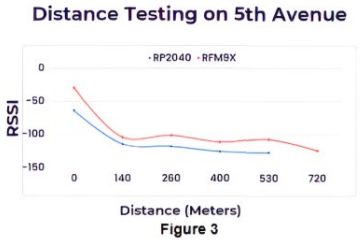

Figure 3

Acknowledgments

This research would not be possible without the funding from the Ohio Space Grant Consortium (OSGC), the help and support from my advisor, Dr. Brian Krupp, and the assistance of Alexandria Macko-Dobrovic, Joshua Buxton, and Dr. David Revta.

Personalized Proactive Assistant for xEMU

Student Researcher: Bailey Wimer

Advisor: Dr. Jong-Hoon Kim

Kent State University
Department of Computer Science

Abstract
As manned space exploration missions extend to unprecedented distances, managing astronauts' health becomes of paramount importance. Studies show that extended times of space travel reduce mental capabilities and increase stress levels, particularly in multitasking scenarios. To address this challenge, this paper introduces the Personalized Proactive Assistant for xEMU (PPAxEMU), an innovative artificial intelligence (AI) system designed to reduce stress during space missions involving task switching. PPAxEMU employs personalized machine learning to adapt directly to each astronaut. By leveraging collected contextual data, PPAxEMU can proactively assist astronauts in completing tasks. This paper outlines the development of PPAxEMU as well as a simulation environment for future use in proving its effectiveness. The proposed solution not only addresses the immediate concerns of space exploration but also showcases the adaptability of proactive AI systems in enhancing human performance and well-being across diverse domains.

Project Objectives
Over the past few decades, space travel technology has improved significantly. Humans can travel safer and farther than they ever have been able to before. As humans prepare to re-enter space and unimaginably long distances, it is important to consider astronauts' mental health as much as their physical health. During extended periods of time in space, studies have found that astronauts' mental performance decreases, and their stress levels increase [1] [2]. Moreover, during these space missions, it is very likely that astronauts are either 1) given multiple tasks to handle at the same time or 2) interrupted during their tasks. Studies unrelated to space travel have shown that individuals who are multitasking or have their tasks interrupted have increased stress levels and decreased output [3] [4]. This paper presents a potential solution for reducing stress during space missions that involve switching between tasks. The Personalized Proactive Assistant for xEMU (PPAxEMU) creates a personalized artificial intelligence (AI) assistant for use in NASA's Exploration Extravehicular Mobility Unit (xEMU). This AI assistant proactively assists astronauts with tasks during space missions.

Background
Previously, the Dr. Jong-Hoon Kim's Advanced Telerobotics Research (ATR) Laboratory (supporting this project) developed the Personalized Proactive Home Robotics (PPHR) System [5]. This system empowers home assistant robots to act proactively by training individual personalized machine learning models for each member of the household. These small models predict each user's desires based on current conditions in the home. The home assistant robot then acts in one of three states (Passive, Active, or Proactive) based on the confidence of the prediction.

Methods
By leveraging the methods of the PPHR System described in [5], the PPAxEMU assistant gathers contextual data from the individual astronaut and the environment. With this data, the system learns combinations of environmental and biometric signifiers to perform different actions to assist the

astronaut. PPAxEMU could be integrated with other systems to gather more detailed information, and perform more mission-specific tasks. The system actively learns over time based on the astronaut's actions.

In order to test the application of PPHR methods with the PPAxEMU system, a simulation environment was created. This virtual reality environment has customizable and repeatable scenarios where a user controls multiple Rovers to complete tasks in a moon-like environment. The user is given five minutes to score as many points as possible by completing tasks. Unexpected events can occur, impeding the user. Some of the possible events include:

1. A Rover breaks down due to a malfunction
2. A space object crashes into a rover
3. An object blocks a rovers path
4. A rover mistakenly goes off course

During the scenario, PPAxEMU collects data from the environment, the user, and the rovers. The assistant can perform tasks to assist the user, including repairing a rover, returning a rover to its course, sending a rover back to its home location, and clearing an obstacle. The assistant begins in an active state and progressively becomes more proactive as it learns about the user.

Results and Discussion

The Personalized Proactive Assistant for xEMU addresses the problem of reduced performance and increased stress in multitasking scenarios. Currently, the development of the PPAxEMU assistant and the simulation environment is complete. The ATR Lab plans to continue this project by leveraging the simulation environment to perform a study with active participants. This study will prove the effectiveness of PPAxEMU at reducing stress levels in a multitasking environment.

Acknowledgments

I would like to thank the Ohio Space Grant Consortium for funding this project and providing an incredible learning opportunity and resources. I would also like to thank Kent State University, as well as my advisor, Dr. Jong-Hoon Kim, for all of his support and guidance throughout the project.

References

1. Manzey, D., & Lorenz, B. (1998). Mental performance during short-term and long-term spaceflight. Brain research reviews, 28(1-2), 215-221.
2. Bartone, P. T., Roland, R., Bartone, J., Krueger, G., Sciaretta, A., & Johnsen, B. H. (2019). Human adaptability for deep space exploration mission: An exploratory study.
3. Wetherell, M. A., & Carter, K. (2014). The multitasking framework: The effects of increasing workload on acute psychobiological stress reactivity. Stress and Health, 30(2), 103-109.
4. Adler, R. F., & Benbunan-Fich, R. (2015). The effects of task difficulty and multitasking on performance. Interacting with Computers, 27(4), 430-439.
5. Wimer, B., Shuvo, M. I. R., Matar, S., & Kim, J. H. (2023, November). PPHR: A Personalized AI System for Proactive Robots. In International Conference on Intelligent Human Computer Interaction (pp. 255-267). Cham: Springer Nature Switzerland.

Human and AI Teaming

Student Researcher: Nikolas Younker

Advisor: Professor Kelly Cohen

University of Cincinnati
Department of Aerospace Engineering and Mechanics/Aerospace Engineering

Abstract
Artificial Intelligence (AI) is becoming a huge part in the modern technological world. Many search engines and even mobile applications are now incorporating AI assistants into their platforms. The underlying issue behind that is, can humans and AI's efficiently trust each other and work together. This study aimed to create a virtual environment where that could be tested. Unreal Engine 5 (UE5) was the platform used to develop the environment for the study to take place, and although UE5 has a lot of their own AI capabilities, our purpose was largely completed using our own methods. We were able to successfully integrate a Fuzzy AI, an AI which does not think binarily, into UE5 using Python, C++, and UE5's own features. The purpose of this AI was to act as a guide for a human player navigating a maze and avoiding an adversary.

Project Objectives
Objectives of this project were mainly focused on the integration and development of the AI and the environment, opposed to the actual study of teamwork (that study was completed by a peer's research project which will contribute to his graduate degree thesis). The objectives for this project were: to learn about the world of AI (specifically Fuzzy AI), apply a fuzzy AI into a digit twin environment, have the fuzzy AI react and take action to evade an enemy or obstacle, program the fuzzy AI into a virtual reality assistant to aid a human player into evading the adversary, and then to create a foundation of knowledge in AI so that I can dive into the deeper projects that Professor Kelly Cohen has ongoing.

Methods
Unreal Engine 5 was chosen suitable for our purposes after taking inspiration from a similar simulation that our lab had already created. Unreal Engine 5 has powerful tools to help backend development which allowed us to utilize our python and C++ knowledge to workaround some of the basic UE5 tools. The platform also has a powerful Blueprint and Blackboard system to create AI's of their own (Figure 1 shows a breakdown of our plan).
Utilizing the blueprints established in UE5 allowed us to leverage our coding capabilities and create custom blueprints in the platform. Using these custom blueprints we were able to create a basic fuzzy AI system in C++ and then integrate it into the platform. After this was done, the AI sensing components (Figure 2) in UE5 were partnered with our custom AI function and tested to see whether an AI could react to a sight and hearing stimulus. These preliminary tests were successful which allowed us to transition to the training section of the project.
Due to system capabilities within UE5, a separate game with the same purpose had to be created to test our AI in. This was done using PyGame within Python and developing a hide-and-seek maze, which was the plan for the final project in UE5. The purpose for this was that the training required a genetic algorithm, and that genetic algorithm acts like human genes and will continually learn and evolve over the course of a training, which would allow it to react the same no matter the layout of the map. These trainings are just simulations ran over and over again, in our case 10000 iterations was ran over the course of a weekend. In this period the AI was able to learn how to avoid adversaries and dead ends by

itself due to the genetic algorithm teaching itself how to play the game. At its best run, the AI was able to survive for 2 minutes long, which was the maximum amount of time we set the run time at.
Once testing was finished, the finished algorithm was implemented back into UE5 and the final map and some minor tweaks needed to be made to the final AI. Those included a delay, which allowed the AI to react to sensing stimuli more efficiently, as well as adding animations to make the AI look less clunky. The project then at this point, was passed onto our peers for further analysis.

Results and Discussion

Almost all of our project objectives were completed. We were able to implement a fuzzy AI into UE5, which was seemingly a new topic, and were able to gather a greater knowledge of AI along the way. Due to timing, the AI was never fully turned into a virtual assistant for a VR version of the game but studies were still ran to show how an AI and human would team together using our model we created. By using a combination of different platforms the goal was achieved. A similar concept could have be done by just utilizing the methods that UE5 had, but it would not have been a true fuzzy AI, since there would be no genetic algorithm or training involved. By using the custom blueprint and then importing a fuzzy system through that, is the most efficient way to import an external AI like that into UE5.

Figures/Charts

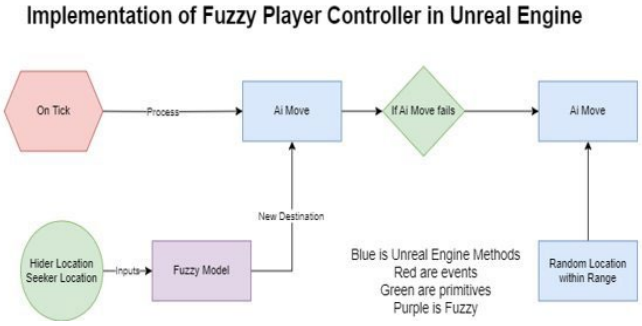

Figure 1. AI Project Workflow

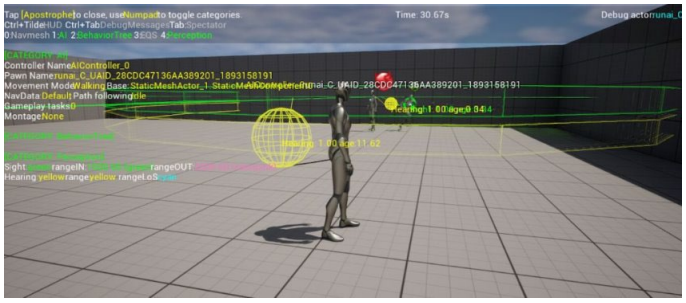

Figure 2. AI Sensing Capabilities

Acknowledgments

I would like to first thank OSGC and NASA for this opportunity, I am very appreciative and hope to continue it in my final semester. Then Professor Cohen for allowing me to work and learn in his lab. Finally, all my collaboritve peers, Kaus Shankar, Wilhelm Louw, Conrad Kent, and Mikhail Nikolaenko.

References

UC AI/BIO Lab Project – VR Hide and Seek

Effect of Airfoil Shape on Lift and Drag

Student Researcher: Jennifer Zayac

Advisor: Dr. Jed Marquart

Ohio Northern University
Mechanical Engineering

Abstract
The impact of various airfoils on the effectiveness and efficiency of an aircraft wing can be significant. Airfoils play an important role in determining the aerodynamic characteristics of an airplane. By altering the shape and design of the airfoil, the lift and drag forces acting on the wing can be altered, which ultimately influences the overall performance of the aircraft. Every aircraft has a different airfoil with distinct properties that affect the performance of the wing for different conditions in flight. Some airfoils are designed for easier maneuvering while others are designed simply for high speed flying. The airfoil selection process depends on several factors, including the weight, size and purpose of the aircraft. The experiment designed will test three separate airfoils in DesignFOIL, to analyze which one provides the most effective performance based on the lift versus drag conditions. The properties of the aircraft used will be based on the Ohio Northern University SAE Aero competition team's aircraft, using the weight, size and slow speeds.

Project Objectives
The objective of this research was to determine the most effective airfoil shape for an aircraft designed towards the SAE Aero Design competition rules based on the lift and drag coefficients as well as the angle of attack.

Methodology
The methodology for this research was conducted using DesignFOIL software and airfoil tools. Multiple airfoils were originally chosen in airfoil tools in order to narrow down the options to three. Once the three airfoil shapes were selected, they were imported into DesignFOIL. The virtual wind tunnel was the main use of this software. Each airfoil shape was examined at 3 and 5 degrees angle of attack using the SAE parameters such as altitude, reference length, etc. The Reynolds number was automatically calculated in the virtual wind tunnel and implemented into the analysis. Pressure, velocity and boundary condition plots were generated and observed and finally, the Eppler and NACA plots were created to determine and compare the lift and drag ratio and coefficients of each airfoil shape.

Results/Discussion/Figures/Charts
Based on the SAE Aero Rules and after performing the experiment and analysis, it was concluded that the GOE448 was the best airfoil shape for angle of attack 3 degrees or less, however, the GOE226 airfoil is the ultimate best choice for an angle of attack between 3 and 8 degrees. A GOE448 airfoil at 3 degrees angle of attack resulted in a L/D ratio of 122.3 and at 5 degrees was 111.1. However, the GOE226 at 3 degrees was 82.6 but at 5 degrees it skyrocketed to have a L/D ratio of 141.4. Figure 1 below shows the NACA plots representing each of the three airfoils coefficient of lift and drag.

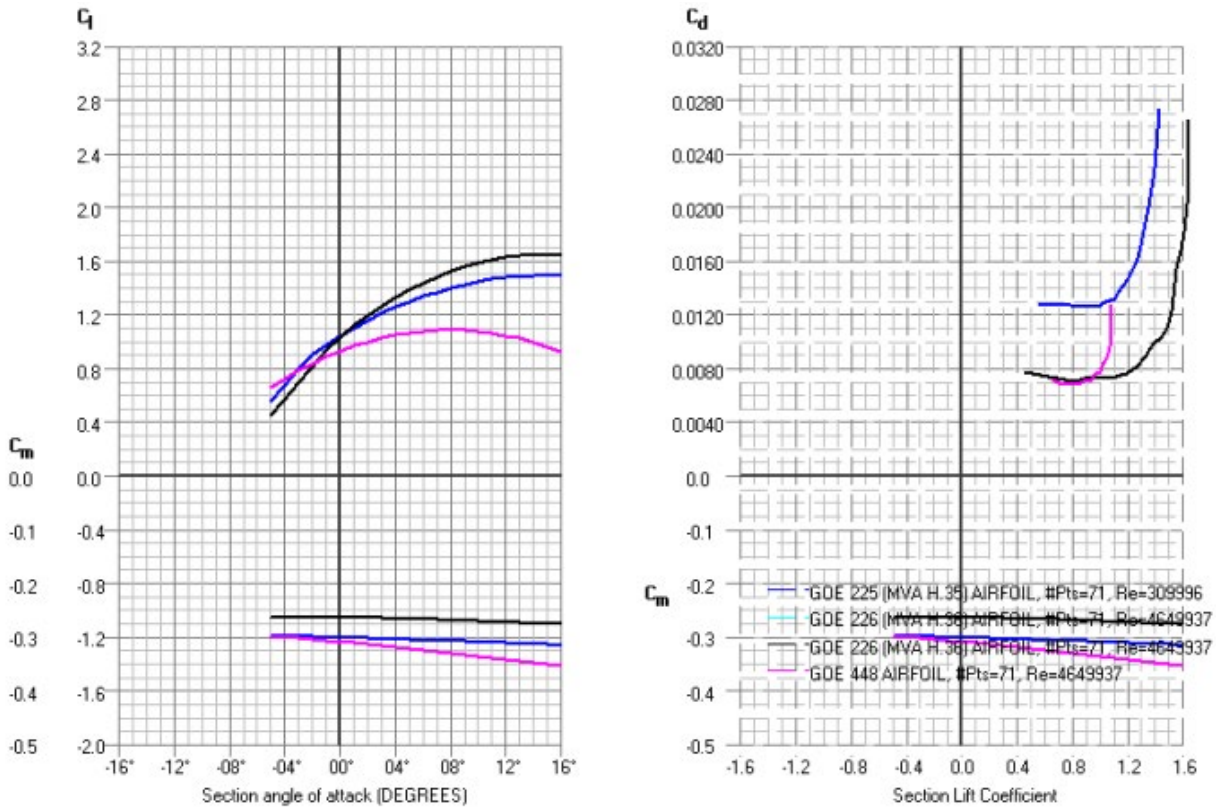

Figure 1: NACA Plots from Virtual Wind Tunnel

It is shown that the GOE225 airfoil has poor performance due to the amount of drag created and gets significantly worse as the angle increases. The GOE448 should be used at lower angle of attack but compared to the GOE226, the drag coefficient starts to increase significantly quicker as the angle increases. After doing the virtual wind tunnel analysis, the best decision for the SAE airfoil to use was the GOE226 airfoil.

Acknowledgments
My advisor Dr. Jed Marquart, OSGC for the amazing scholarship and opportunity

References
[1] “Airfoil database search,” www.airfoiltools.com. http://www.airfoiltools.com/search/index [2] “2024 Aero Design Rules,” www.saeaerodesign.com. https://www.saeaerodesign.com/cdsweb/app/NewsItem.aspx?NewsItemID=79452158-1c85-4e 6e-9031-032440401e8

Community College

In An "Active" Galaxy Far Far Away: Analysis of AGN Emissions through Spectroscopy

Student Researcher: Olivia Bogna

Advisor: Erin Hardy

Lorain County Community College
Universal Sciences

Abstract
An active galaxy is a category of galaxy determined by the presence of an active galactic nucleus (AGN). AGN are defined by their comparatively high activity, emissions and luminosity emitted by the galaxy's compact center, correlating usually with the presence of an accretion-producing supermassive blackhole. There are many categories AGN fall into, with the prominent ones being: Seyfert galaxies, quasars, and blazars. What category a galaxy falls into is determined by their emissions across the electromagnetic spectrum, variability, polarization, luminosity, and viewing angle from Earth.

Project Objectives
The objective of this project is to gather information about the characteristics and emissions of different AGNs, and interpret data from AGN spectra to determine red-shift as well as other characteristics.

Methodology Used
Using NASA/IPAC's Extragalactic Database, University of Alabama Astronomy Databases, and NED's Caltech Glossaries, information was gathered about the properties of AGN and their emissions, as well as why they contained such properties. Simbad, and NED was used to collect spectra.

The three AGN selected to be studied are: 3C 273, NGC 5548 and Markarian 421. Each one falls into a different class of AGN. Spectra was chosen by its categorization as observed, and whether their values allowed for the comparison of either Lyman, Balmer or Paschen series.

To determine redshift, the equation $(\lambda_{observed} - \lambda_{emitted})/\lambda_{emitted} = z$ was used, with $\lambda_{observed}$ being an observed absorption line on the spectra, and $\lambda_{emitted}$ being the calculated value of the absorption line from the corresponding series (Lyman, Balmer or Paschen).

Results Obtained
The spectra of 3C 273 had a Balmer series H-Alpha Line lie at approximately 7600 Angstroms, determining the observed wavelength to have a value of 760 nm. Using the equation $(\lambda_{observed} - \lambda_{emitted})/\lambda_{emitted} = z$, where $\lambda_{emitted}$ = 656 nm, a redshift of 0.158 was calculated for C3 273.

The observed spectra of NGC 5548 had a Paschen H-Beta line around 18750 Angstroms (187.5 nm). Using the Paschen series H-Beta value, an emitted wavelength of 187.56 nm was used in the equation for redshift, producing a redshift of 0.017.

The observed spectra of Markarian 421 had a Balmer H-Alpha line around 6600 Angstroms (527.5 nm). Using the value of 656.0 nm for the rest wavelength and the equation stated above, a redshift of 0.03 was found.

Interpretation of results

Analysis of optical spectra can be determined through many methods, with the method of choice for this study being absorption spectroscopy. Absorption spectroscopy utilizes dark Fraunhofer lines against a colorful background to determine data such as redshift, chemical composition, and distance. These lines appear often as jumps and dips on graphs, coinciding with spectral lines for elements, usually hydrogen. The hydrogen spectral series is often used due to the element's prevalence between spectra, with its values being determined by the energy it takes to make hydrogen electrons to transition energy levels. The values are categorized by the Lyman, Balmer and Paschen series. H-Alpha, H-Beta and H-Gamma lines are found within each series used, but the values differ for each. Lyman series contain values between 950-1216 A, Balmer 4340-6563 A, and Paschen 12821-18756 A. To determine redshift, scientists compare where they compared the observed spectral line value to their rest value.

Absorption spectra have helped scientists determine many aspects of AGN, with some being emissions, chemical composition, and redshift; redshift, the center of this study, is a defining characteristic of some AGN. For many of the radio-loud classes like quasars and blazars, redshift has shown that these galaxies are extremely far away, and due to Hubble Law, has led scientists to believe that radio-loud AGN were common in the early stages of the universe, or were an early step in galactic evolution.

Active galaxies have no unified model, but are usually determined by their accretion disk, angle at which the viewer sees them, the presence of relativistic jets, and the amount of debris that obscures the nucleus. They are often divided into radio-loud and radio-quiet AGN, based upon these observations. The spectra of AGN usually contrast with interstellar bodies around them, with broad emissions lines that set them apart from other galaxies's emissions, and a notable curve in flux that compares to other galactic spectra. Analysis of emission lines in spectra has led to the discovery of AGN emitting vast amounts of radiation across the electromagnetic spectrum, the defining variability and polarization of radio loud AGN, and the ionization of gas clouds in relation to AGN.

Acknowledgements and References

I would like to thank my professor, Dr. Erin Hardy, for the guidance and help she gave me as I did my research. I would also like to thank Amy Jindra, and Dr. Regan Silvestri for their additional assistance.

References

[1] An Introduction to Active Galactic Nuclei. (n.d.). Retrieved March 1, 2024, from ned.ipac.caltech.edu website: https://ned.ipac.caltech.edu/level5/Cambridge/Cambridge1_3.html
[2] Bill Keel's WWW Gallery - Active Galaxies and Quasars. (n.d.). Retrieved March 1, 2024, from pages.astronomy.ua.edu website: https://pages.astronomy.ua.edu/keel/agn/
[3] Home | NASA/IPAC Extragalactic Database. (2018). Retrieved from Caltech.edu website: https://ned.ipac.caltech.edu/
[4] The Hubble Diagram - Redshifts. (2023). Retrieved from Sdss.org website:https://skyserver.sdss.org/dr1/en/proj/advanced/hubble/redhifts.asp
[5] Types of Stars - Absorption Lines. (n.d.). Retrieved March 1, 2024, from cas.sdss.org website: https://cas.sdss.org/dr6/en/proj/basic/spectraltypes/absorption2.asp.

The Future of Biomedical Engineering

Student Researcher: Mickela Harris

Advisor: Abbey Yee

Cincinnati State Technical and Community College
Electrical Engineering Technology- Electronics Systems Major

Abstract
Biomedical engineering is the key to many technological advancements that can help humanity as we know it. A new part of this growth in advancement is bioprinting. Redwire's achievement of successfully fabricating the first human knee meniscus on the International Space Station (ISS) marks an important milestone in this field. Partnered with the Uniformed Services University of the Health Sciences Center for Biotechnology for the BFF-Meniscus-2 investigation. The potential of microgravity research in pharmaceutical drug development and regenerative medicine is endless. Bioprinting, the process of 3D printing with biomaterials to create functional structures, like bones, blood vessels, and tissue. Offers solutions to address issues in organ transplants and tissue engineering. By exploring bioprinting in microgravity environments, this essay aims to explain its life-changing potential and the company's driving innovation in this field.

Project Objectives
The objective of this essay is to examine Redwire's 3D bioprinting breakthrough of the fabrication of a human knee meniscus. Also, the essay aims to elaborate more on the concept of bioprinting, its challenges on earth, and the advantages offered by microgravity conditions. Furthermore, it seeks to highlight the potential of bioprinting.

Methods
A review of relevant sources on bioprinting and the companies associated with bioprinting technology was researched for this essay to help develop an educated understanding of the information provided. Key sources include articles, news reports and company websites for information on Redwire, LambdaVision, and Space Tango.

Results and Discussion
Redwire's achievement of successfully bioprinting a human knee meniscus signifies a significant milestone in biomedical engineering. By using microgravity in space, they aim to advance pharmaceutical drug development and regenerative medicine, with a focus on tissue engineering. Bioprinting offers a promising solution to the waitlist for organ transplants by being able to one day create the organs needed to save lives.

Bioprinting faces challenges, particularly in environments where gravitational forces can compromise the integrity of printed structures. Issues such as the need for scaffolding and the risk of chemical toxicity pose significant hurdles to overcome. That is why microgravity conditions offer an alternative approach, enabling the fabrication of complex structures without the need for scaffolding. This opens new possibilities for those in this field.

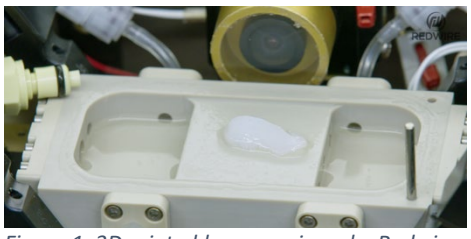

Figure 1: 3D printed knee meniscus by Redwire.

In addition, other companies such as LambdaVision and Space Tango are also driving innovation in bioprinting and microgravity research. LambdaVision's development of an artificial retina and partnership with Space Tango highlight their applications of microgravity in biomedical engineering. Space Tango's expertise in microgravity hardware and automation provides valuable infrastructure to support iterative research and development in fields like tissue engineering and cell culturing.

In conclusion, the achievement of bioprinting a human knee meniscus represents a significant advancement in biomedical engineering. By using this unique environment of space, researchers can overcome challenges associated with earth's gravity when bioprinting and make more progress in regenerative medicine. Bioprinting holds a promising future in addressing the shortage of organs and improving health. With continued innovation and partnerships between companies and hopefully many more like them, the future of biomedical engineering is promising, offering hope for millions of patients in need of life-saving treatments.

Acknowledgments

I would like to thank OSGC, Abbey Yee, Dr. Jeremy Huber, and for all the support.

References

Sarabi, M. R., Yetisen, A. K., & Tasoğlu, S. (2023). Bioprinting in microgravity. ACS Biomaterials Science & Engineering, 9(6), 3074–3083. https://doi.org/10.1021/acsbiomaterials.3c00195

"Redwire's 3D bioprinting breakthrough on the ISS: Printing human knee meniscus in microgravity" – Impact Lab. (2023, September 17). Retrieved from https://www.impactlab.com/2023/09/17/redwires-3d-bioprinting-breakthrough-on-the-iss-printing-human-knee-meniscus-in-microgravity/.

Space Tango. (2023, October 12). Home page - Space Tango. Retrieved from https://spacetango.com/.

Lambda Vision. (2024, March 4). Home - Lambda Vision. Retrieved from https://www.lambdavision.com/.

Determining the Ability of CCR5 Mutants to Serve as a Gene Therapy for AIDS

Student Researcher: Jilyan Hustic

Advisor: Dr. Harry Kestler

Lorain County Community College
Biology

Abstract
AIDS viruses such as HIV-1 require two receptors to enter a cell. Thus, the principal receptor CD4 is not sufficient for infection to occur. In addition to CD4, one of two co-receptors, CCR5 or CXCR4 is required. A mutation in CCR5 has been shown to confer resistance to viral infection. That mutation, CCR5 Δ32, appears to also alter the cell surface expression of the second receptor, CXCR4, as well as the wild-type version of CCR5 in heterozygous individuals and cell culture. The ability to down-modulate co-receptors by the delivery of lentiviral particles containing CCR5 Δ32 will be determined. Lentiviral vector systems were employed to construct viral particles that contained CCR5 wild-type and CCR5 Δ32. Lentiviral vectors have been previously employed as a cure for Sickle Cell Anemia thus the safety of our approach is probable.

Project Objectives
Use CCR5 Δ32 in gene therapy in order to make T cells immune to HIV infection. Additionally, further research will be made on the effectiveness of CCR5 Δ33.

Methods
HEK293ft cells were transfected with pLenti puro HA-ubiquitin plasmids containing the CCR5 wild-type or Δ32 along with two plasmids containing genes needed for viral packaging. We have also constructed a mutation Δ33 that encodes an 11 amino acid deletion. This construct will be used to generate lentiviral particles as well. Stable t-cell lines will be constructed by transducing various alleles of CCR5 into Jurkat, H9, and CEMX174 cells. Flow cytometry and immunofluorescence will be employed to determine the surface expression of CCR5 and CXCR4.

Results and Discussion
The ability of lentiviral particles encoding CCR5Δ32 and CCR5Δ33 to down-modulate wild-type CCR5 and CXCR4 will be determined, both in vitro and in vivo. Should the lentiviral particle encoding CCR5Δ32 or CCR5Δ33 be effective in down-modulating CCR5-wt and CXCR4, a potential gene therapy for HIV/AIDS would be created. Additional doses of the therapy could be delivered if stable stem cells were not obtained in the initial delivery of the gene therapy.

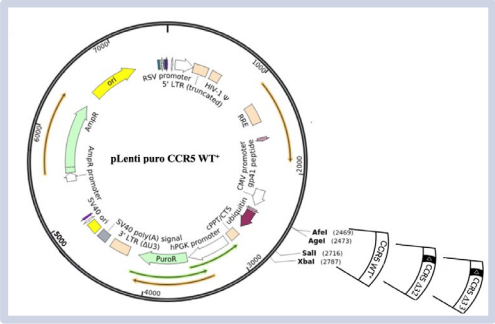

Figure 3. Map of pLenti-CCR5-wt, pLenti-CCR5Δ32, and pLenti-CCR5Δ33 constructed plasmids. pLenti puro HA-Ubiquitin was cut with XbaI and AgeI. PCR fragments were generated, using primers containing the AgeI and XbaI restriction recognition sites from the three different templates. PCR fragments were cloned into pLenti puro.

Figure 4. PCR amplification of fragments used to construct

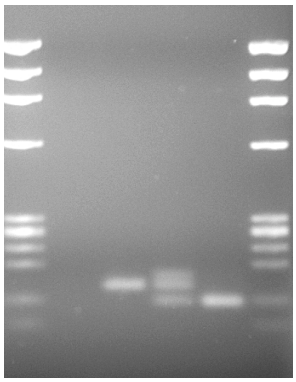

lentiviral particles

1. Φ X174 HaeIII molecular weight marker
2. Negative control
3. PCR of JS1
4. PCR of SD1
5. PCR of AF1
6. Φ X174 HaeIII molecular weight marker

1 2 3 4 5 6

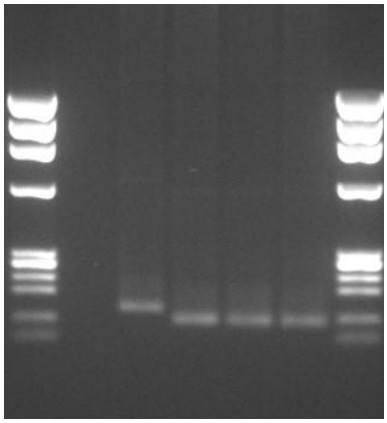

Figure 5. pLenti *ccr5–wt,* pLenti *ccr5Δ32,* and pLenti *ccr5D33* contain
1. Φ X174 HaeIII molecular weight marker
2. PCR negative control
3. PCR of pLenti-CCR5-wt
4. PCR of pLenti-CCR5Δ32
5. PCR of pLenti-CCR5Δ33a
6. PCR of pLenti-CCR5Δ33b
7. Φ X174 HaeIII molecular weight marker

1 2 3 4 5 6 7

Acknowledgments

I would like to thank my advisor, Dr. Harry Kestler, for teaching me the skills I need for research in our lab. He has helped me significantly along the way and has helped me have a greater appreciation for microbiology.

References

Koen K. A. van Rompay, et al. “Attenuated Retrovirus Vaccines and AIDS.” Science, vol. 270, no. 5239, 1995, pp. 1218–22. JSTOR.

Gardner, Matthew R et al. “AAV-expressed eCD4-Ig provides durable protection from multiple SHIV challenges.” Nature vol. 519,7541 (2015): 87-91. doi:10.1038/nature14264

Evaluation of Growing Rod Used in Pediatric Scoliosis Surgeries by Finite Element Analysis

Student Researcher: John Martin

Advisor: Dr. Regan Silvestri

Lorain County Community College
Universal Science

Abstract
This project uses SolidWorks to develop a simple model of a surgical back implant, and run a stress analysis test on the construct using Finite Element Analysis (FEM). The FEM software used is Abaqus CAE Student Edition, which can determine the deformation and stress distribution across the model.

Project Objectives
The greatest challenge in treating pediatric scoliosis is the development of back implants that can grow alongside the patient without mechanical failure. This project aims at demonstrating a means of routinely testing various models quickly and efficiently, and with minimal cost.

Methods
In Abaqus, the CAD model is imported, and sections are assigned to each part of the model. Materials are then assigned to each section, and boundary conditions are set. The bottom-most surface of the model becomes fixed, and a load is applied to the top surface of the model. The model is then seeded and meshed, and the job is run.

Results and Discussion
The Student Edition of Abaqus CAE restricts the number of nodes to 1000. Due to the node restriction, a large seed size was used, resulting in the greatest distance between nodes that the program would allow for the imported geometry. Due to the nature of the mesh generation, an asymmetrical mesh skewed the results, despite the boundary conditions, load, and imported geometry all being left/right symmetrical. The stress was concentrated on the rightmost rod (See Figure 1). While high stress was present on the anterior side of the rod (Figure 2), stress was more heavily concentrated and distributed on the posterior side of the rod, leading to the conclusion that the posterior side of the rod would break first. The geometry used to calculate stress distribution is that of the mesh, which is determined by node count. Hence, the greater the node count, the smaller the error. Therefore, a greater node count is required for further testing to produce a more accurate stress distribution. This will determine if the stress on the anterior side of the rod is indeed greater than that of the posterior side. Furthermore, with a higher node count, the stress will likely be more evenly distributed across the left and right halves of the model.

Figures/Charts

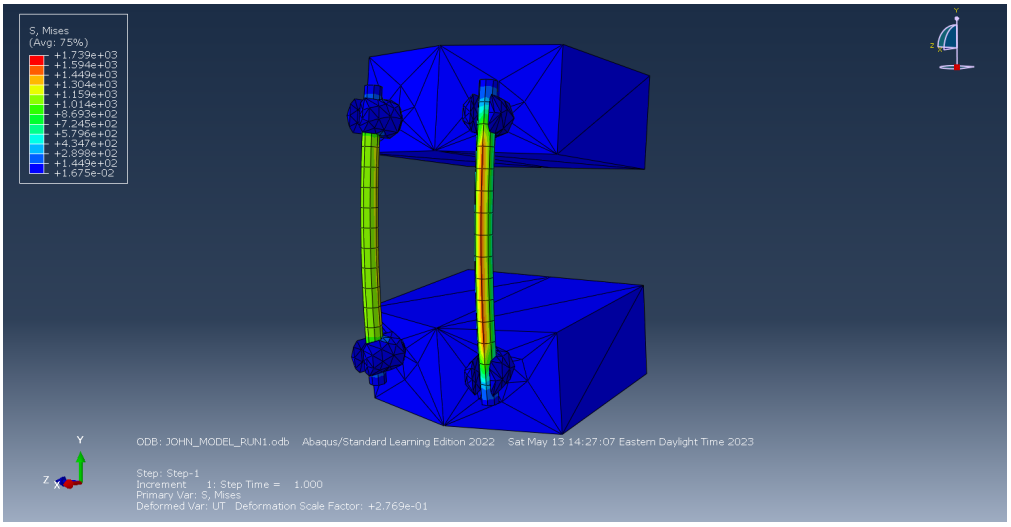

Figure 1: Deformed image of the working model from the posterior-right view.

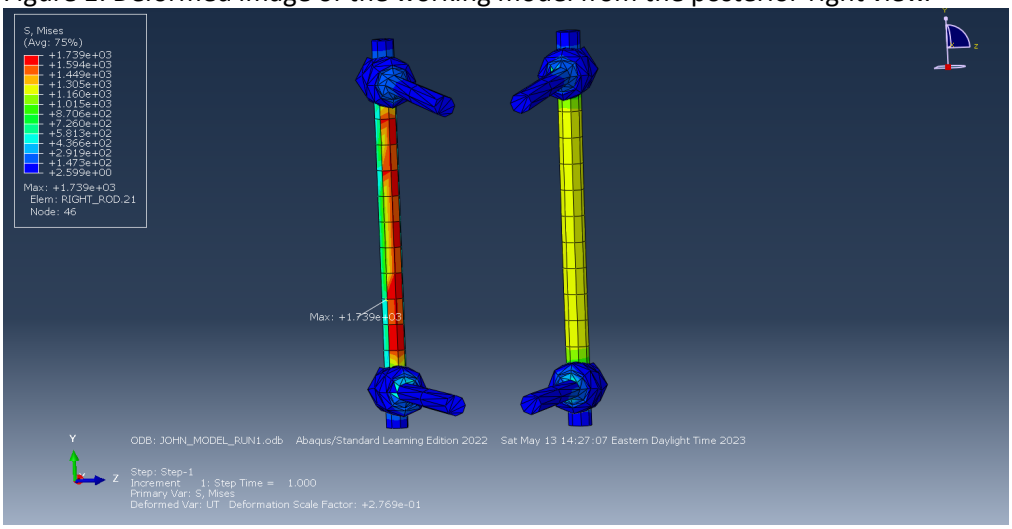

Figure 2: Deformed image of the working model from the anterior view. Top and bottom blocks are hidden to aid the visibility of the rods.

Acknowledgements

Lorain County Community College Student Researchers: John Martin, Eva Wanek, Mallory Alvarez, and Nicholas Valescu

Lorain County Community College Faculty Advisor: Professor Regan Silvestri

University of Toledo Mentors: Manoj Kodigudla, Sudharshan Tripathi, and Amey Kelkar

University of Toledo Faculty Advisor: Professor Vijay Goel

References

Figures 1-5: (2023) Evaluation of Growing Rod Surgical Implants Used in the Treatment of Pediatric Scoliosis by Finite Element Analysis. Page 4

Software Displayed: Abaqus/CAE Student Edition 2021

Magnetism as Simulated Gravity and the Effect on Interplanetary Propagation

Student Researcher: Ashley Meyer

Advisor: Dr. Jeremy Huber, Ph.D.

Cincinnati State Community and Technical College
Chemical Engineering Technology/Pre-Engineering

Abstract
Propagation has been a goal for the International Space Station for several years. A major obstacle in this process is the lack of gravity, and this research aims to find probable solutions using electromagnets and small pieces of iron dispersed in the soil.
Plants use a process called gravitropism to know which direction to grow roots, and which direction to grow stems and leaves. There are currently two theories on how exactly plants utilize gravity, and this research is based on the most likely theory —seeds determine the direction of gravity by tiny pressure changes in the plasma membrane, and direct root growth toward increasing pressures.
There are two possible ways to execute this hypothesis, but both operate on the same basic principles:

- The magnetic attraction on small pieces of metal in the soil work to simulate gravity
- Iron pieces diffused into the soil will allow the electromagnet to apply an even downward attraction, while the tiny, magnetized bits of iron provide higher pressure closer to the electromagnet

Project Objectives
This research aims to find probable solutions using electromagnets and small pieces of iron dispersed in the soil. There are two potential solutions:

Hypothesis A: The most effective method to simulate gravity with electromagnetism is to increase the concentration of dissolved ferrous iron (Fe^{2+}) in the water.

Hypothesis B: The most effective method to simulate gravity with electromagnetism is to habitually add non-dissolved elemental iron pieces to the soil, and rotate periodically to avoid settling.

Methods
This research was exclusively theoretical, and was conducted using literature resources. Throughout the course of the research, it was determined that while hypothesis A may potentially work, it would require extensive steps and additives to prevent iron toxicity, while the dissolved iron ions may not be large enough to induce the magnetism needed to simulate gravity. The majority of this research focuses on hypothesis B.

Results
Hypothesis B utilizes larger pieces of iron, which will result in a stronger induced magnetism on each individual piece. In addition, iron remembers magnetism that has been induced in it, and can be reused up to the point of saturation. The proposed process looks like this: (1) iron filings would be sprinkled on the top of the soil (2) after a predetermined amount of time, the filings will have been pulled toward the magnet, and a new set of filings are sprinkled on top (3) This continues until filings have reached the bottom of the pot, and the electromagnet is turned off and the tray emptied (4) the iron filings are then reused, and the degree of magnetism in increased up to saturation with each trip through the soil.
The size of the iron filings and frequency of “stirring” is key to the functionality of this hypothesis. The size of the iron filings needs to be the perfect balance between optimal magnetism and evenly distributed pressure. The frequency of “stirring” would need to happen often enough to prevent settling and provide a consistent downward magnetic attraction. A few complications with this proposed theory: (1) larger pieces

of iron act as stronger individual magnets, but are less evenly dispersed, resulting in uneven pressures throughout the soil (2) using larger insoluble pieces of iron will require more frequent labor and observations, as the iron cannot be allowed to settle at the bottom.

Discussion

Several determinations must be made to determine the plausibility of these hypotheses:

1) the strength of the electromagnetic field needed to generate a force similar to earth's gravity. This could potentially be done theoretically using this formula:

$$B(z) = \frac{N\mu_0 I R^2}{2(R^2 + z^2)^{3/2}}$$

but would be much more efficient to determine these values experimentally.

2) the pressure induced on the soil as a result of the magnetism on each particle of iron at a specific point. This could again be determined theoretically by a cross product of the strength of the magnetic field (B) crossed with the cross-sectional area of a specific iron filling (M)—

$$\vec{F} = \vec{B} \times \vec{M}$$

but would be much easier to determine this experimentally.

Within those two unknowns, the size of the iron fillings would need to be determined for an optimal balance between overall applied pressure and individual magnetic attraction.

Figures/Charts

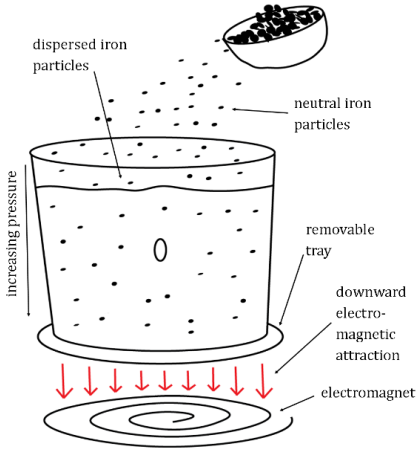

Figure 1: diagram of proposed process for hypothesis B

Acknowledgments

I would like to thank Dr. Jeremy Huber, Ph.D. for his guidance throughout the course of this research.

References

Dr. Jeremy Huber, Ph.D., personal communication, March 11, 2024

Griffiths, D. J. (2024). *Introduction to Electrodynamics*. Cambridge University Press.

Li, G., Kronzucker, H. J., & Shi, W. (2015, November 30). *Root developmental adaptation to Fe toxicity: Mechanisms and management*. National Library of Medicine. https://www.ncbi.nlm.nih.gov/pmc/articles/PMC4871668/

Ling, S. J., Moebs, W., & Sanny, J. (2016). In *University Physics Volume 2* (Vol. 2). essay, OpenStax. Retrieved March 5, 2024, from https://openstax.org/books/university-physics-volume-2/pages/12-introduction.

Niklas, K. J., & Spatz, H.-C. (2012). 2.8 Gravitropism. In *Plant Physics* (pp. 59–61). chapter, The University of Chicago Press.

Modernization of Solar Power: Exploring the Development and Trajectory of Solar Panels and Technology

Student Researcher: Maryam Rababah

Advisor(s): Dean Bortz

Columbus State Community College
Department of Engineering Technology

Abstract
Generally, a solar panel is made with a base layer of tempered, followed by a layer of encapsulant, a module solar of cells, another layer of encapsulant, and a back sheet. The structure is held together using polymer and an aluminum frame, with external wiring located in a junction box on the bottom of the panel [3]. These cells are strung together in rows of fingers and columns of busbars. [1]

Solar energy comes from the absorption of photons by the cell modules of the panel. The cell includes two types of poly silicon, the N-side (negative) and the P-side (positive). The N-side contains negatively charged electrons, while the P-side contains positively charged holes. When a photon is absorbed by a cell it knocks an electron off its atom, exciting it and making it move around. This allows for the flow of electrons, or electricity, and it is only possible within a solar panel when the P/N junction directs the flow of electrons. The P/N junction is created when the negatively charged electrons meet the positively charged holes and create a neutral zone. The electrons follow the path due to it having the least amount of resistance, the electrons are then taken into a load then back out. The electrons are released into the positive side where they meet a hole and are neutralized. These flow back up to the P/N junction and the cycle, photovoltaics, continues [4]. There are multiple advantages to this process, it is self-sufficient and does not require a lot of maintenance besides clean up and pest control. The problems arise when energy loss increases throughout the lifespan of the panel.

Project Objectives
The production of solar panels is designed with two factors in mind: cost and efficient use of materials. However, the production process completely disregards the recyclability and sustainability of manufacturing a panel and prevents solar energy from functioning on a national scale. Inverter and battery technology is in its infancy, and the price of a solar panel, despite having seen significant reductions over the past few years, is still an unfeasible investment for the average household. When considering these factors, solar can seem like a waste of time, money, and effort, yet it is still a necessary step for reducing carbon emissions. Solar energy alone is not the solution, but it is a step in the right direction and a critical component in the fight for a cleaner planet. With a multitude of clean energy sources available today, the best option is using an effective combination of each based off location, resources, and necessity. The objective is to determine the best solution for absorption issues and panel recycling.

Methodology Used
Solar power was theorized to have first been used in the 7th century BC, with the first production of a solar panel being done by Charels Fritts in 1873 [5]. The history of PV is what brought along the modern solar panel, and in turn, the great leaps in innovation. The best way to approach this research was to filter through various sources, including experiments and federal records.

Results Obtained
As of current, the most efficient solar panel has an absorption rating of just over 22% [2]. This does not seem great at first glance, but energy systems' ratings are normally below 60%. There are a multitude of methods being tested to improve this rating, including perovskites, and bifacial panels. Perovskites are a mix of synthetic material identifiable by their crystallographic structure. Perovskites have shown a 25% increase just by working in tandem with the cell. [6] They bolster for the panel, though they are known for their degradation in sunlight they are valuable enough to warrant further research.

As of now the reason for discarding a solar panel is typically monetary and it is in fact a smarter financial decision to replace your panel prior to the end of its lifespan. This is because of the natural decline of absorption efficiency

throughout its life, as well as the cash back you receive from the local government when some of that electricity gets delivered back into the powergrid. The 'Solar Trash Wave' shows the amount of unnecessary waste that is to be expected by 2050. Solar panels are made with precious materials including polysilicon, aluminum and silver [7]. They also contain hazardous materials such as sulfuric acid and hydrogen fluoride [8]. There are companies that plan to fight this wave, this includes We Recycle Solar. We Recycle Solar is a company based in Australia developing a microwave technology that makes it easier to pull apart the panel layers by heating the polymers that stick those layers together. This marks the beginning of a market that specializes in taking apart used panels and selling the materials to make new ones, completing the cycle of a fully sustainable energy source.

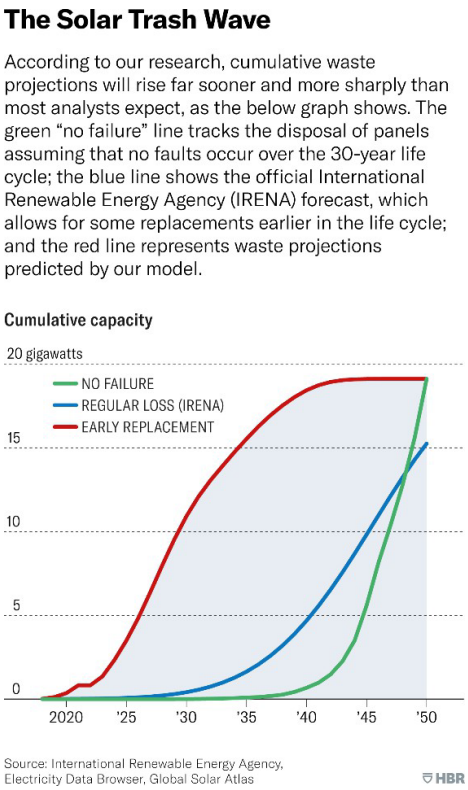

Acknowledgements and References

[8] "Environmental impacts of solar power," Union of Concerned Scientists, https://www.ucsusa.org/resources/environmental-impacts-solar-power (accessed Apr. 30, 2024).

[7] C. Hoffs Former Contributor et al., "Mining raw materials for solar panels: Problems and solutions," The Equation, https://blog.ucsusa.org/charlie-hoffs/mining-raw-materials-for-solar-panels-problems-and- solutions/ (accessed Apr. 30, 2024).

[6] "Perovskite solar cells | Department of Energy," energy.gov, https://www.energy.gov/eere/solar/perovskite- solar-cells (accessed May 1, 2024).

[5] "Solar history: Timeline & invention of solar panels," EnergySage, https://www.energysage.com/about-clean-energy/solar/the-history-and-invention-of-solar-panel-technology/ (accessed Apr. 30, 2024).

[4] "How solar panels work," Union of Concerned Scientists, https://www.ucsusa.org/resources/how-solar- panels-work (accessed Apr. 30, 2024).

[3] "Solar panels," Solar Panels - A guide to solar panels and solar batteries, https://www.renewableenergyhub.co.uk/main/solar-panels (accessed Apr. 30, 2024).

[2] J. Svarc, "Most efficient solar panels 2024," Clean Energy Reviews, https://www.cleanenergyreviews.info/blog/most-efficient-solar-panels (accessed Apr. 30, 2024).

[1] Solar Photovoltaic Manufacturing Basics | Department of Energy, https://www.energy.gov/eere/solar/solar- photovoltaic-manufacturing-basics (accessed May 1, 2024).

Mitigation of Global Warming and Ozone Depletion

Student Researcher: Joseph Tamburello

Advisor: Christopher Huhnke

Cuyahoga Community College
Construction Engineering

Abstract
Rational and sustainable abatement and healing of earth's atmospheric integrity

Project Objectives
To investigate payload, delivery, efficacy, and replicability of operations from low gravity on Earth

Methods
1. What program can be adopted to provide routine delivery of payload.
2. Is there a material which would effectively negate the effects of caustichydrochlorofluorocarbons (HCFC's).
3. Terrestrial impact of the life cycle of this material.

Results and Discussion
1. Rockets launched in the falcon/dragon configuration are equipped to deliver payload to satellites in L1 orbit.
2. By first harvesting brine and in turn removing the chlorine from the salinated material, a reflective material which would be chemically compatible with the atmospheric HCFC.
3. The precipitate of this material would be molecularly similar to the brine solution (pre-dechlorinization) and could only be as caustic as the source material.

Figures/Charts

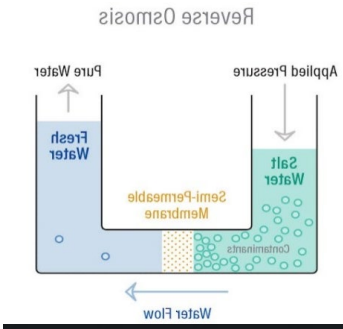

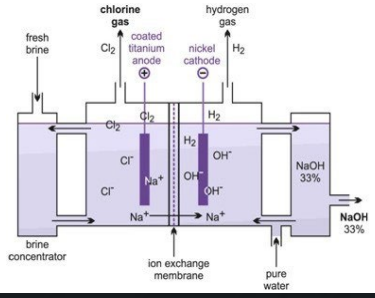

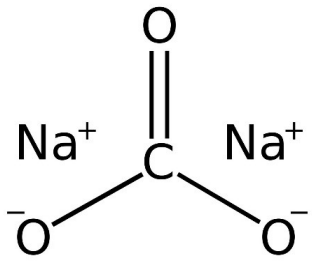

Acknowledgments

Thanks to those with their heads in the stars for all the inspiration they discover. Thanks to Tri-C, the OSGC, Tim Hale, and Christopher Huhnke for facilitating the research for not just myself but the entire consortium.

Strength of Woven Materials

Student Researcher: Emily T. Williams

Advisor: David Van Arsdale

Lorain County Community College
Engineering Information Business Technology - Micro Electromechanical Systems (MEMS)

Abstract
Fabrics of various materials have been worn by humans as clothing for millennia with purposes such as identification, insulation, and protection from the environment. While clothing in the modern world is typically selected for comfort and fashion, the utilization of fabric coverings protecting the body is often overlooked in the selection of everyday outfits. This investigation studies the ability of various fabric materials to withstand shock of a projectile without excessive deformation or rupture of the material.

Objective
The project objective is to determine which fabric of three tested fabrics best withstands impact from a launched projectile. Based on an interest in fabric and fiber with hopes of raising awareness of alternative fabric uses for personal protection in daily wear.

Measuring the independent variables such as thread strength, elasticity, and thread diameter of several fabric swatches to identify which variable had the most significance in the deformation of the swatch's dependent variable, the depth of penetration.

Methodology Used
Several different fabric swatches were tested with. Of the three fabrics used, one titled Heavy Blue is made of 100% polypropylene, Blue Gingham is made of 60% cotton and 40% rayon, and Peach made of a cotton crinoline.

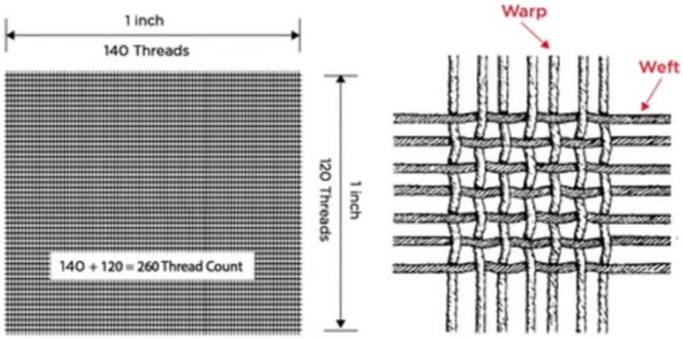

The thread count was calculated as the sum of the warp and the weft with Heavy Blue being 13 threads per centimeter, Blue Gingham being 61/cm, and Peach being 85/cm.

Young's Modulus describes the elasticity of a material when stretched. The tensile strength is the maximum stress a material can endure while being stretched before breaking. These were measured using a force sensor attached to one end of a thread as the other end was fixed in place. As the force sensor stretched the thread, the thread's extension was also measured until the thread fractured. This data was used to determine both the Young's modulus and the tensile strength of the thread material.

A ballistic pendulum, to measure the projectile's velocity, was constructed using an air compressor at a consistent 70 psi to launch a 4.3mm BB through a 4.4mm horizontal barrel. The BB was launched at a hanging target of smooth putty covered with a small swatch of tested fabric. The pendulum swung forward after impact. The swing distance was recorded by measuring the distance a small dowel rod was moved by the swinging

pendulum after resting inside a tube. The deformation of the fabric swatch was determined by placing a digital caliper in the putty crater left by the launched projectile to measure the depth of penetration.

Interpretation and Significance of Results

While a goal of this investigation was to find a fabric that does not break when impacted by a high velocity projectile, it was concluded that it is of equal importance that the fabric does not stretch so much upon impact that both the fabric *and* the projectile became lodged deep within the putty. The concept of "bruise, not break" applies.

Conclusion

Neither the tensile strength nor Young's modulus appeared to have a more significant effect than another in this investigation. Thread count, the reciprocal of thread diameter, was found to have the most significance of the three variables in testing of the three fabric swatches.

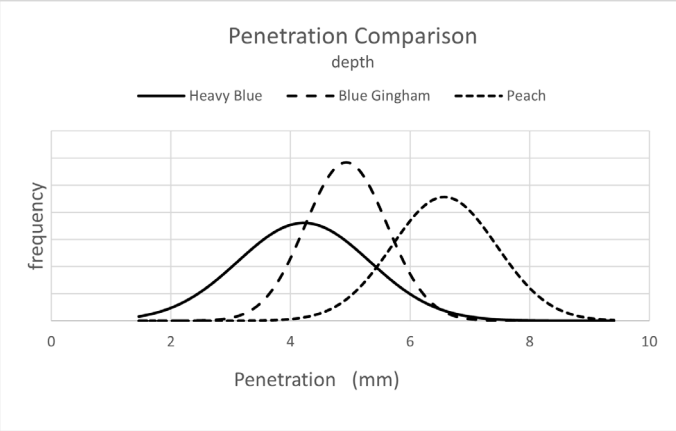

As can be seen in the graph, all three fabrics showed similar variance in depth of penetration. The graph demonstrates the Peach material allowed the greatest penetration at an average of 6.6mm and the Heavy Blue showed the least at 4.2mm. The Blue Gingham had an average of 4.9mm.

A video demonstration of the projectile launch and tensile strength test can be found in the public access link here:

https://drive.google.com/drive/folders/1Mh38BPl0zqGFLQGKqQkSPWWvL6iAuvCZ?usp=drive_link

With Additional Time…

With additional time for continual testing, a more diverse selection of woven materials such as fine copper thread or spider silk, using homogeneous organic materials rather than polyesters and polymers could be studied. By increasing the diameter and speed of the launched projectile it will allow a more accurate assessment of the deformation of the impacted materials, to ultimately determine if there *is* or *is not* a variable in fabrics that can increase the capability of withstanding shock.

Ideally, additional testing might identify the most affordable fiber or woven blend that fits the goal of "bruise, not break." Such a fabric could be incorporated into the wardrobe of those looking to optimize functionality and protection in clothing for daily wear.

Acknowledgements

I would like to express gratitude towards my project advisor, Dave Van Arsdale, for significant contributions in helping develop this project from concept to reality. I am extremely proud of the work we did together. To Johnny Vanderford, for supporting and encouraging my academic journey over the years; teaching me never to settle for less than what I can achieve. To my parents and grandparents, for being my biggest fans and favorite people to come home to.

Finally, I would like to share gratitude towards the Ohio Space Grant Consortium for the opportunity to have written and published three NASA affiliated student research projects. I am grateful to have been selected to work with the OSGC as a Program Assistant and to have served this incredible program.

Education Scholars

Beyond Earth: Space's Effects on the Human Body

Student Researcher: Ari Babcock

Advisor: Dr. Jones

Cedarville University
Middle Childhood Education (Math & Science)

Abstract

In the year 2015, Astronaut Scott Kelly went up into space to fulfill a one-year low-Earth atmosphere mission. Data was collected regarding the human body's reaction and adaptation to long exposure to the space environment. This data is extremely interesting when looking at the results of Astronaut Kelly's journey compared to the data taken from his twin Astronaut Mark Kelly (who stayed on earth and provided an ideal control group to which to compare the results).

In this lesson, students will look at the effects of space travel/orbit on the human body and compare that to human health on Earth. Students will be looking at different aspects of human health, in addition to how space travel would impact the health of a human determining if these effects are detrimental or beneficial. Students will be using inquiry and group discussions to pinpoint the cause of these conditions and look for ways to alter these effects. Students will use research given by NASA, to support their ideas to better human health in space. Their findings and ideas will then be presented in a multimedia format of their choosing.

Project Objectives

- Students will discover the effects of space travel on the human body
- Students will develop a method to test and collect data
- Students will summarize in 4-5 sentences their results.

Methodology Used

This lesson is based on the inquiry approach to learning. IN this learning style students discover how the world around them works based on real world experiences. Students, through the use of a guided lab, will come up with their own method of investigation. As they try to answer the question "how does space affect the human body?".

Students will spend two weeks learning about space travel and basic human anatomy. Students will then put together both topics in a guided lab to demonstrate their knowledge to their peers and educators. Guided labs are labs where students develop procedures, methods of data collection and data interpretation that results in a generalized concept or principle. Inquiry

Investigation:Engage: Students will be introduced to the story of NASA Astronauts, identical twins Scott and Mark Kelly. Scott Kelly spent a year on the space station while Mark was on Earth. Their data gave NASA insight into the human body's reaction and adaptation to long exposure to the space environment.

Explore: Students will spend 2-3 weeks researching the phases of space travel and learning about human anatomy

Explain: Students will keep a logbook to explain their research/discoveries.

Elaborate: Students will take their knowledge and apply it to a guided lab where they will develop a method to test their hypotheses.

Evaluate: Students will decide on a multimedia format to present their results, and take an assessment covering: topics discussed in class, their own research, and the research of their peers.
At the end of this unit students will be assessed in their ability to use the methods of science in order to develop their own questions, and find answers to that question in a guided lab format.

Discussion Points

Students discussed (both in small group, and whole class settings) questions such as: What methods did you use to try to answer the questions ``How does space travel affect the human body", which methods worked well? Which methods did not work well? How do your results compare to your peers? What would you change if you were to do this lab again? And how do your results make you feel about space travel?

Acknowledgments

I would like to acknowledge the Ohio Space Grant Consortium and OAI for the resources and opportunity to grow in my research and teaching skills. Special thanks to Dr. Lori Ferguson, and Dr. Bill Jones for always believing in me and giving me the tools to be a successful educator and individual. To my peers Olivia Marlowe, Lauren Conner, and Emeline Reid, without them student teaching would be filled with less laughter, and joy. And lastly, thank you to my family for instilling in me a love of science and learning.

References

NASA. (2023a, September 20). Twins study. NASA. https://www.nasa.gov/humans-in-space/twins-study/

NASA. (2023b, September 25). Follow the blood: NASA Labs Process Astronaut Blood for Twins study. NASA. https://www.nasa.gov/humans-in-space/follow-the-blood-nasa-labs-process-astronaut-blood-for-twins-study/

NASA. (2024, April 16). The human body in space. NASA. https://www.nasa.gov/humans-in-space/the-human-body-in-space/

The Power of the Sun Student

Student Researcher: Ruthie Curry

Advisor: Dr. Brandi Seither

Baldwin Wallace University
Department of Education

Abstract
Students in the 2nd grade class learned the types of energy that the sun provides relating to the Ohio learning standard 1.ESS.1; The sun is the principal source of energy. By the end of the learning segment students were able to provide two things that heat and light energy from the sun do for us on Earth. Using multiple resources from NASA as well as hands-on ways of showing learning students expressed that they enjoyed this unit about the sun. This learning segment occurred in March of 2024 and was a good transition into talking about the total solar eclipse that would be happening in Cleveland, Ohio which is where my class is located.

Project Objectives
By the end of the learning segment students will be able to and have completed
➔ Notice and Wonder about the Sun
➔ Students think-pair-share about how Earth would feel without the Sun.
➔ Identify the types of energy that the Sun provides.
➔ Brainstorm a list of things that heat energy from the sun does for us on Earth.
➔ Brainstorm a list of things that light energy from the sun does for us on Earth.
➔ Complete a craft of the sun, pictured in the results, that included a topic sentence and two ways the sun provides energy for us on Earth.

Methodology
The notice and wonder about the sun was completed using a NASA resource titled “A Decade of the Sun.” Students expressed enjoyment while watching this video and talked about how different the sun looks from our perspective on Earth. Asking students the question “What would Earth feel like without the sun?” was a question that led to our main topic and objective of the learning segment, heat and light energy. Student answers varied, but ultimately landed on the fact that Earth would be dark and cold without the sun.

After brainstorming multiple ways that the Sun provides energy for us on Earth students completed a craft. Students were given sentence frames to write three sentences and then they colored the rays of the sun, putting them in order to spell “energy.” The beginning sentence frame was “The sun gives us ____ energy.” Students were given a point if they wrote heat, light, or both heat and light in the blank. Students then wrote two more sentences about examples of the energy provided.

Results
All students were able to complete this activity independently in the 2nd grade general education classroom setting. Figure one shows student A’s work. She wrote on her craft that “The sun gives us heat and energy. The heat gives us food, water, grass, and dirt. And the plants grow and give us air and food.”

Acknowledgements
I appreciate the Ohio Space Grant Consortium for granting me an academic scholarship and for providing me with resources to complete this project. Additionally, I would like to thank my field placement teacher for allowing me to integrate this learning segment into our school day leading up to the week of the solar eclipse.

References
NASA Goddard. “A Decade of Sun.” YouTube, 24 June 2020, www.youtube.com/watch?v=l3QQQu7QLoM

Water, Water, Everywhere!

Student Researcher: Roemello Davis

Advisor: Brandi Seither

Baldwin Wallace University
Department of Education, Mild/Moderate (K-12) Education

Abstract
This research/project aims to teach students a lesson on how valuable water is. This will be accomplished by teaching the water cycle process, specifically focusing on the subject of Earth Science. The lesson will address that water is presented within the atmosphere. More specifically, as a water vapor. As a result, when water becomes a vapor in the atmosphere, it can form clouds, snow, fog, rain, and much more. Students will conduct hands-on experiments to learn about the 3 different phases of the water cycle (condensation, evaporation, and precipitation). At the end of the lesson, students will learn why water is an important and valuable resource within our atmosphere and make the connections between how water is involved in our daily lives. Within the lesson, students will also be asked the main essential question, which is how are global precipitation, evaporation, and the cycle of water changing?

Project Objectives
By the end of the lesson, students will….

- Learn what condensation is
- Learn what evaporation is
- Learn what precipitation is
- Experience a hands-on experiment of the 3 stages
- Identify the 3 stages of the water cycle

Methods

1. Students will first watch an introduction of the water cycle (the water cycle song).
2. After listening to the water cycle song, the students will complete a writing activity about the different purposes of water (how we use water on a daily basis).
3. Before reviewing the water cycle diagram, the students will watch the NASA video called “A tour of the water cycle.”
4. After watching the video, the students will review the water cycle diagram (learn about each stage of the water cycle and how it is all connected).
5. The students will review the diagram again the next day and watch a new NASA video called “The fresh (water) connection.”
6. The students will complete hands-on experiments, experiencing the 3 stages of the water cycle.

Results and Discussion
By the end of the 3-day learning segment, the students were able to….

- Identify the 3 stages of the water cycle and explain what each stage is.
- Explain the connection between the 3 stages of the water cycle and the importance of water in our daily lives.
- Explain how the 3 stages of the water cycle affect the weather and how water is an important resource.

Acknowledgments/References
I would like to thank NASA for providing all of the supports and resources I needed to create my learning segment for my students. Without NASA's resources and supports, I wouldn't have been able to create this project the way I wanted to present it.
https://gpm.nasa.gov/education/water-cycle

Using Knowledge of Human Anatomy to Determine the Effects of Longterm Space Exploration

Student Researcher: Cora L. Gill

Advisor: Laura Dell

The University of Cincinnati
Secondary Education Integrated Sciences: Chemistry

Abstract
This lesson would be for a senior or AP anatomy class. The lesson would be based on the different anatomical systems in the body and how they would be affected by extended time in space. This would be an end-of-the-year project that fully encompasses what the students have learned throughout the year. There are 10 body systems: skeletal, muscular, nervous, endocrine, cardiovascular, lymphatic, respiratory, digestive, urinary, and reproductive. The students would be split up into equal groups of two or three and assigned one of the body systems to research. The students would have to use what they learned throughout the year and what they found in books and websites. Students will be expected to use at least two NASA resources to obtain their information. Students will also be expected to present what they found in a formal presentation to their peers and a written group report of their findings and any data they may have used to justify what they found. The final part of the project is students will have to theorize a way to prevent the effects of space on the body. If prevention is not possible, that should be included in their reports.

Project Objectives
- Students will recall the subject matter on their assigned body system
- Students will be able to explain the effects of space on their body system

Lesson Plan
This is an end-of-the-year project for a senior/AP Anatomy and Physiology class. Students will have to rely on previous lecture notes and information they gather from NASA websites and other reliable sources.

The Project
Students will be split into 10 groups of 2-3. Each group will be assigned a different body system to research. Students will have to use NASA resources and other reliable sources to explain the effects of space on their body system. Students will have to present possible ways to prevent any problems that may be caused by extended time in space. Students will present their findings in a formal presentation to the class.

Conclusion
The goal of this lesson is three-fold. First, students are asked to recall information from previous lectures on their body system. Next, students would have to work with their partners and find credible sources of information for their body system to support their prior knowledge. Specifically, students will have to use NASA resources to support their findings. Finally, students will have to think critically and come up with a possible solution for the effects of space on their body system. All of these things, in conjunction, would push students to the limits fo their knowledge and further their understanding of their body system and the human body on Earth and in space.

Humans in Space

Student Researcher: Molly MacLochlan

Advisor: Karen Henning

Youngstown State University

Beeghly College of Arts and Liberal Science

Abstract

Human space exploration is an essential tool to address fundamental questions about Earth's position in the universe, along with the history of the solar system. These fundamental questions include: Why are we here? Are we alone? How did it all begin? What comes next? These fundamental questions are an inspiration on why humans choose to study space by exploration. However, in order for human space exploration to be successful, The National Aeronautics and Space Administration (NASA) must continue to conduct an incredible amount of research for human space exploration. Human beings can not easily adapt to space, and this is because of all of the health concerns that the space environment brings them. There are medical, financial, and ethical hurdles that prevent humans from living in space. This report is based on research on how space may not be safe for human exploration.

Project Objectives

In this short lesson for 11th grade students, the students will learn about the harmful environment that astronauts face. The students will complete a study on one of the subtopics searching for research on the potential harm that can be caused psychologically or physically to the space travelers. This lesson will review why space travel is considered dangerous and how space is a hostile environment for humans. The students will also play an interactive Kahoot where they answer all of the questions based on their studies.

Methods

Humans in Space face multiple dangers. Firstly, the radiation in space is especially dangerous and unnatural to humans. Beyond the protective atmosphere of Earth, astronauts are exposed to higher levels of radiation. This increases the risk of cancer and other health problems. Another danger is microgravity, which can lead to discomfort in humans. These discomforts include bone density loss, cardiovascular deconditioning, and muscle atrophy. Space debris is also a concern for humans in space. Even a small object or debris at high speeds can harm or be lethal to humans. These collisions can damage the spacecraft immensely, leading to issues of survival for humans. Isolation and confinement are another danger that these humans may face. This can lead to depression and psychological stress which can have very harmful effects on these astronauts. The students will be introduced to these concepts during the unit overview.

Results and Discussion

Overall, the students will show an understanding of the overview of space exploration and the danger many astronauts face during space travel. The students will also understand the importance of space travel and why it is relevant to our society at the end of this unit lesson.

References

https://science.nasa.gov/solar-system/exploration/

Spaghetti Satellites

Student Researcher: Ryah Moner

Advisor: Dr. Brandi Seither

Baldwin Wallace University
Department Of Education

Abstract
During this lesson students were able to learn about how NASA communicates with space through the Deep Space Network (DSN). Student were taught how the satellites work and how they need to be able to withstand the elements of the outdoors. Students then worked with a team to create their own satellite using dry spaghetti noodles and tape.

Project Objectives
By the end of the lesson students will have a general understanding of NASA's communication with space and be able to create a spaghetti satellite that can hold the weight of a large marshmallow.

Methods
1. Students were introduced to the DSN and what the satellites look like.
2. Then we discussed how the satellites need to withstand outside forces like wind and weather.
3. Students were then told that they would be building their own satellites using tape and dry spaghetti noodles.
4. Students were given full creative freedom and started to build their satellites.
5. Students were tasked with building the tallest satellite that could hold the weight of a large marshmallow at the top. The marshmallow represented the large satellite dish.

Results and Discussion
All students were successful in building a satellite. Most of the satellites were not very tall but all groups were able to hold the marshmallow. The students focused on having a strong based before they tried to make it tall.

Acknowledgments
Thank you to my cooperating teacher, Amy Murray, for allowing me to implement this in the classroom. Thank you, Dr. Seither, for your support.

References
https://www.jpl.nasa.gov/edu/learn/project/building-with-spaghetti/
https://spaceplace.nasa.gov/dsn-antennas/en/

Elements in Space: A Planetary Comparison

Student Researcher: Elizabeth Roche

Advisor: Erica Miller-Arpajian

Cleveland State University
Biology, Integrated Science; Adolescent Young Adult 7-12 Licensure

Abstract
Students will use online NASA materials to construct a presentation about the difference between the planets in our solar system. This project will focus on the different elements present in the planets and will go along with the HS-PS-1 Ohio learning standard. Students may choose two or more planets to explore and will work in groups to foster collaboration. The presentations will be media of the students' choice (slide show, trifold poster, video, webpage, blog, etc.). Students will be directed to NASA's Spaceplace webpage as a starting point to familiarize themselves with the planets (students have wide range of prior scientific knowledge). Students will be required to use NASA's online image database to find pictures of the planets to include in their presentations. Required in the presentation will be: the most common elements found on the planets, characteristics of the elements (atomic number, number of subatomic particles, etc.), and atmospheric characteristics. Students will also display at least two other interesting facts. When the projects are completed, the students will present to their peers so the whole class may learn more about the chemical composition of our solar system.

Project Objectives
This lesson was an introductory lesson to review content the students learned in physical science as freshman. The project objectives were to investigate the chemical makeup of the solar system and review knowledge on atomic characteristics, namely protons, neutrons, and electrons. The students were reviewing their knowledge of energy levels and atomic structure. When completing this project, the students were able to combine this standard chemistry knowledge while also learning about the universe and solar system.

Methods
This project began with an introduction with the expectations of the project and a short tutorial of how to find and how to use NASA's materials. I then placed my students in strategic groups and they chose whichever form to make their project that they felt would best portray their material. They had two 90-minute blocks to work on this project. During these two work days, I circulated the classroom and had thorough check-ins with the students on their work. The students then presented their projects to the whole class.

Results and Discussion
I evaluated my students on their content, creativity, and presentation skills. They did a good job creating projects that had accurate content, but struggled with creativity and presentation skills.. It was not a surprise that they handled the content well, as this was a review of content they learned in a previous class. However, the lack of creativity is not an uncommon issue with urban education. Every group except for one made a rather simple PowerPoint presentation. This lack of creativity got better throughout the semester with repeated exposure to creative project requirements. The same was true with their presentation skills. I made sure to give specific and manageable feedback to the students to help them get better at presenting while still pushing them to be better.

References

https://spaceplace.nasa.gov/
https://www.nasa.gov/images/

The Water Cycle

Student Researcher: Nathan Samblanet

Advisor: Brandi Seither

Baldwin Wallace University
Department of Education

Abstract
Water is such a vital resource in our world today and it is important to understand the cycle that water goes through. Water cycles through many places on earth and it is important to keep all those places free of pollution to ensure clean water. During these lessons, my students discussed the path that water takes and how keeping water clean helps out humans. We came to the conclusion that water is not only important for use to drink but it helps grow food and so much more. My students discussed the water cycle and the importance of keeping water clean.

Project Objectives
By the end of this lesson students will be able to:
- Describe the Water cycle.
- Describe the importance of water.
- Chart their data for the water cycle dice activity.

Methods
Experiment Procedure:
- Each student received a cup of water with shaving cream on top.
- Then, the teachers added food coloring to the top, and students observed what happened.
- Students then recorded their observations.
- Then, the class discussed how this experiment showed the precipitation step of the water cycle.
- Finally, students discussed the importance of precipitation and how it helps us.

Activity Procedure:
1. Explain that students will play a game; they will role-play water as it moves throughout Earth. Ask students where water exists on Earth and how it gets there. Display OVERHEAD: “Water Cycle.”
2. Distribute the STUDENT WORKSHEET: “Water Cycle Game.” Divide students into pairs, pairing an older student with a younger student if possible. Divide pairs evenly among the stations.
DESK CONFIGURATION
Animal Plant Clouds
Lake Soil
Surface Glaciers
River Ocean Ground
3. Explain that when the signal is given, students will roll the die at the station. If more than one student is at a station, students will need to take turns rolling the die. Students should read the number on the die and match it to the chart on the sheet on the table. The chart will indicate where to go next. For example, if a student rolls a 3 at the Soil Surface Station, he or she will move to the Ground Water station next.
4. As students move from station to station, they should chart their paths on their STUDENT WORK-SHEETS.

5. At the next station, the student should roll the die and move according to the chart at the new station. Each station will have a different chart.
6. Sometimes the chart will indicate that a student should stay at that station. In that case, the student should mark an X on that location on his or her chart and roll again. By the end of the game, a student may have several X's next to a particular station. At the end of the game, students will share paths with each other.
7. Play a mock round to make sure students understand the rules.
8. Indicate that students should begin and assist as necessary. Allow students to play for 10-15 minutes. (NOTE: Level I students may require more play time.)
9. Draw a replica of the blank STUDENT WORKSHEET: "Water Cycle Game" on the board or use the OVERHEAD: "Water Cycle." Invite students to share the path they took. Compare students' paths.
10. If needed, introduce the term "water cycle." Explain that a cycle is something that repeats over and over. For example, the year is a cycle. The twelve months of the year repeat over and over every year. Water moves on Earth in a cycle as well. Even though water moves in a variety of ways, it always returns to its original position.
11. Ask students to answer the following questions based on the paths that were taken during the water cycle game. List student ideas on the board and discuss as a class. Where can water from a plant go? How does water get to a river? Where can water go from a glacier? How does water get to a cloud?

Results and Discussion

This lesson was a huge success in my classroom. It sparked students to think more about we use water and how it is not just for drinking. My students also learned through the dice activity the paths in which water can take to help reinforce the importance of keeping those areas clean. Through the experiment my students grasped the understanding of precipitation and the other steps of the water cycle. Overall, these lessons greatly helped my students understand the water cycle and the importance of water.

Acknowledgments

I want to thank the OSGC for allowing me to come in and learn how to incorporate NASA products and steam into my classroom. I also want to thank Dr. Brandi Seither for her support during this project.

References

"Water Cycle Dice Game." *NASA*, NASA, gpm.nasa.gov/education/interactive/water-cycle-dice-game. Accessed 21 Mar. 2024.

"Rain Cloud in a Jar." *The Stem Laboratory*, 31 Mar. 2022, thestemlaboratory.com/rain-cloud-jar/.

A Lesson in Ocean Ecology: The Intersection of the Carbon Cycle, Climate Change, and Ocean Biota

Student Researcher: Grace A. Turcotte

Advisor: Dr. William Jones

Cedarville University
AYA Science Comprehensive Education

Abstract
The purpose of this lesson is to educate students on how biochemical cycles function and how these cycles contribute to environmental change. This lesson connects the importance of the carbon cycle with the real-world issue of climate change. It is important for the students to be able to make this connection so that they are inspired to learn of how the actions of humans and other organisms impact the Earth's climate. This lesson on ocean ecology is a cooperative-based learning activity using the resources provided on NASA's website. Digital tools provide interactive models that allow for students to experience a more direct approach with understanding the carbon cycle. After learning from these models, students will be divided into groups and allowed to choose a topic that must then be approved for their presentation. This group activity will allow students to present organized information with their peers and broaden the classes understanding of this subject. The expectation for this project is that students would build collaborative skills as they conduct research and organize their findings. Peers are expected to evaluate all presentations to develop lifelong skills in assessing and providing feedback to others.

Methodology Used
This multi-day activity is based on cooperative-based learning. Cooperative learning is an instructional task design that engages students actively in achieving learning outcomes through their own efforts and the efforts of the members of their small learning team. The students work together in groups to answer a research question that is focused on the relationship between the hydrosphere and atmosphere. This activity was created using ideas from the NASA online lab titled "Climate Change Online Lab". Students will present their work to the class and discuss how different topics relate to one another. This form of instruction has been linked with increases in student achievement, critical thinking, group interaction, and self-esteem. Interdependent learning ensures all students are accountable for their learning.

Lesson
This lesson is part of a unit meant to educate students on the role carbon has in keeping our world habitable. This lesson focuses on how carbon dioxide is absorbed and released in relation to the hydrosphere. An experiment will be done in class that demonstrates how water absorbs CO_2, which alters the pH balance of the solution. Students are then expected to choose a topic that demonstrates they understand how carbon interacts with the Earth's Ocean. Examples of appropriate topics include how carbon dioxide levels relate to ocean levels rising, what causes ocean acidification, the rise of ocean temperatures, and how El Nino events affect the pace the ocean absorbs carbon dioxide. All these potential topics allow for students to research real-world concerns using resources provided by NASA. Lesson objectives:

1. Students can analyze data collected by NASA to determine how carbon emissions have influenced the health of the ocean.

2. Students can use interactive models to develop an explanation for why changes in global temperatures and ocean chemistry have taken place.
3. Students can identify how carbon is transferred between different spheres of the earth.
4. Students can use NASA resources to compare changes in CO2 concentration, biochemical cycles, and global temperatures and explain why recording these variables allows humans to make informed ecological decisions.

Discussion Questions:

1. Are the impacts of excess carbon emissions limited to changes in the ocean?
2. How has collecting data on carbon emissions helped researchers interpret recent trends concerning ocean acidity?
3. Why does NASA invest time and resources in studying the amount of carbon on Earth?
4. What impact does the carbon cycle have on your life? What would you predict the future looks like for future generations considering the trends you found?

Results

I have not been able to formally implement this lesson in a classroom setting. However, this lesson was intentionally designed to work for a high school level classroom and should serve as a valuable resource for my future classes. Classrooms that have fostered a higher level of independence would lend themselves well to this lesson, whereas classrooms that heavily rely on direct instruction may need additional scaffolding to ensure students are actively learning. I hope to have the opportunity to use this lesson and expose future generations to how NASA resources can be used for understanding current events.

Conclusion

This lesson was designed to share resources with students and promote active learning. Students need to consider real-world scenarios and form questions based on what they interpret from legitimate sources. The resources provided by NASA are an entry way for students to learn how data can be used to draw conclusions on what is being analyzed. This enables students to take ownership of their learning and invest in lifelong skills. The group setting replicates what students will experience in their future careers while the cooperative learning style ensures all students take accountability for their work. Students are able to demonstrate what they have found in a concise manner and learn from their peers.

Acknowledgments and References

Mohr, K. (n.d.). *Ocean*. NASA. https://earth.gsfc.nasa.gov/ocean

NASA. (2023, May 25). *Home – climate change: Vital signs of the planet*. NASA. https://climate.nasa.gov/%C2%A0%C2%A0/

NASA. (n.d.-a). *Climate change inquiry lab*. NASA. https://gpm.nasa.gov/education/lesson-plans/climate-change-inquiry-lab

NASA. (n.d.-b). *Climate change online lab*. NASA. https://gpm.nasa.gov/education/lesson-plans/climate-change-online

NASA. (n.d.-c). *CMS*. NASA. https://carbon.nasa.gov/cms/data.html

NASA. (n.d.-d). *Eyes on the Earth*. NASA. https://ocov2.jpl.nasa.gov/eyes-on-the-earth//